ABSTRACT

Title of Dissertation:	TRACING THE FORMATION AND MERGER-DRIVEN GROWTH OF MASSIVE BLACK HOLES WITH THE ZWICKY TRANSIENT FACILITY
	Charlotte Alison Ward Doctor of Philosophy, 2022
Dissertation Directed by:	Dr. Suvi Gezari Department of Astronomy

The dawning of low–frequency gravitational wave (GW) astronomy via pulsar timing arrays and space–based GW interferometry will provide new opportunities for the study of the supermassive black hole (SMBH) binaries which form as galaxies merge through cosmic time. The onset of observational GW studies has coincided with the expansion of wide–field optical time–domain surveys such as the Zwicky Transient Facility (ZTF), which provide a complementary way to detect and analyze SMBHs when they accrete gas and emit at optical wavelengths. In this thesis I describe how high cadence surveys like ZTF can be used to discover rare populations of massive black holes which inform our understanding of early massive black hole seeding channels and their subsequent growth through mergers to produce the SMBH populations we see today.

In the first part of this thesis I present a search for variable active galactic nuclei (AGN) which are spatially offset from their host galaxies using time-resolved imaging

data from ZTF and deeper, higher resolution imaging data from the Legacy Surveys. I present a population of 52 variable AGN in merging galaxies in addition to 9 candidates for gravitational wave recoil of remnant SMBHs which may be used to constrain SMBH binary merger rates and spin alignment efficiencies. I also examine the dramatic rebrightening of a previous recoiling SMBH candidate SDSS1133, and conclude from spectroscopic follow–up that it is more likely an outbursting luminous blue variable star.

In the second part of the thesis, I present a population of 190 low–mass AGN in dwarf galaxies discovered by their optical or mid–infrared variability in deep ZTF difference imaging and forward–modeled photometry of *WISE* image stacks. These intermediate mass black hole (IMBH) candidates can be used to constrain the low–mass end of the $M_{BH} - \sigma_*$ relation and dwarf galaxy occupation fractions in order to better understand the origins of the first massive black holes. Only 9 candidates from my search had been detected previously in radio, X-ray, and variability searches for dwarf galaxy AGN. I find that spectroscopic approaches to AGN identification would have missed 81% of my ZTF IMBH candidates and 69% of my *WISE* IMBH candidates, showing the promise of variability searches for discovery of otherwise hidden low–mass AGN.

In the third part of this work, I present 299 variable AGN in ZTF which have double–peaked Balmer broad lines from the motion of gas in their accretion disk, increasing the number of known double–peaked emitters (DPEs) by a factor of $\sim$2. DPEs can arise as false positive candidates in both spectroscopic and variability–based searches for SMBH binaries, so it is important to characterize the properties of their spectra and light curves. I find that 16% of variable broad line AGN in ZTF are DPEs and that $\sim$50% of the DPEs display dramatic changes in the relative fluxes of their red and blue peaks over long $10 - 20$ year timescales. I show that a number of DPEs exhibit apparently periodic and chirping signals in the optical and mid–infrared and discuss how this arises naturally from their power spectra. I show that DPE light curves have slightly steeper power spectra than their standard broad line counterparts and are $\sim$1.5 times more likely to have a low frequency turnover. I compare the variability and spectroscopic properties of the ZTF DPE population with the recently discovered inspiraling SMBH binary candidate SDSSJ1430+2303 (ZTF18aarippg) and conclude that the variable velocity–offset broad lines and periodic behavior of ZTF18aarippg are not unusual compared to other DPEs, and it is therefore more likely to be a single AGN rather than an SMBH binary.

I conclude this thesis by outlining how the transient detection and image forward–modeling techniques presented in this thesis can be used to find populations of low accretion rate, off–nuclear AGN with the upcoming Legacy Survey of Space and Time at the Vera Rubin observatory in order to produce much better constraints on massive black hole seeding channels and GW recoil rates. I also discuss how these techniques can be applied to new science cases, such as the analysis of strongly gravitationally lensed supernovae and quasars, for cosmological studies with LSST.

TRACING THE FORMATION AND MERGER-DRIVEN GROWTH OF MASSIVE BLACK HOLES WITH THE ZWICKY TRANSIENT FACILITY.

by

Charlotte Alison Ward

Dissertation submitted to the Faculty of the Graduate School of the
University of Maryland, College Park in partial fulfillment
of the requirements for the degree of
Doctor of Philosophy
2022

Advisory Committee:
Dr. Suvi Gezari, Chair/Advisor
Dr. Peter Nugent, Co-Advisor
Professor M. Coleman Miller
Professor Richard Mushotzky
Professor Peter Shawhan

Preface

A version of Chapter 2 was published in *The Astrophysical Journal* as "AGNs on the Move: A Search for Off-nuclear AGNs from Recoiling Supermassive Black Holes and Ongoing Galaxy Mergers with the Zwicky Transient Facility" (Ward et al., 2021a). A version of Chapter 3 was submitted to *The Astrophysical Journal* as "Variability-selected intermediate mass black hole candidates in dwarf galaxies from ZTF and WISE" (Ward et al., 2021b). The referee suggested minor revisions which have been implemented in Chapter 3. A version of Chapter 4 is currently under review by the Zwicky Transient Facility black holes working group and will be submitted to *The Astrophysical Journal* as "Optically variable double-peaked emitters in ZTF: Understanding the AGN populations which mimic SMBH binary behavior" (Ward et al., in prep) after implementation of any revisions suggested by the publication board. Each chapter is presented with minor modifications from the article version to ensure continuity throughout the thesis.

Dedication

For my parents

Acknowledgments

This thesis would not have been possible without the dedicated support of my research advisors. I first and foremost want to say a huge thank you to Suvi Gezari for being such an enthusiastic and patient advisor throughout my PhD. Suvi has always directed me towards the most exciting science topics and her passion for astronomy constantly reminds me to enjoy my day-to-day research. I have been incredibly lucky to have an advisor who is so thoroughly invested in the success of her students. I would absolutely not be where I am today without her guidance, and I'm very grateful for all the time she has invested in mentoring me and for the many incredible opportunities she's given me over the last few years!

I would next like to express my gratitude to Peter Nugent for stepping in as co-advisor midway through my PhD and for all his encouragement and support to investigate new avenues of research. Before starting my PhD I would never have imagined I would become so interested in high performance computing. Thanks to Peter I have obtained valuable experience in this area, beginning with a very stimulating and enjoyable summer at LBNL. Peter's enthusiasm for ambitious computing projects is contagious, and his confidence in me to get such projects done was essential to the success of this thesis. Peter has also been an incredible source of career advice and I'm very grateful for all his guidance and support as my second advisor!

I would next like to express my gratitude to Cole Miller and Richard Mushotzky for being such enthusiastic and encouraging thesis committee members. Thanks for always drawing my attention to important papers and concepts and for being so supportive of my research. Every committee meeting left me feeling very enthusiastic about my research and I'm really grateful for those extra boosts of motivation. I'd also like to thank Cole for becoming my official UMD advisor during the final years of my PhD and for all his administrative assistance with my student visa. Thanks also to Peter Shawhan for serving as Dean's Representative on my PhD thesis committee!

I would also like to thank a number of UMD faculty and staff who have supported me in different ways throughout the last 5 years. I wanted to say a particular thanks to Stuart Vogel for the time he has invested in supporting my career and for his work enabling UMD's involvement with GROWTH, ZTF and LDT – all of which were absolutely essential to this thesis! I also wanted to say thanks to Brad Cenko for his LDT and Keck observing advice, and to Andy Harris for all his support and assistance throughout my PhD. I wanted to mention the incredible work of administrative staff Susan Lehr, Dorinda Kimbrell, Natalie Rowe, Olivia Dent, Lauren Miles and Barbara Hansborough who have helped me manage the various funding sources for my PhD, enabled a lot of conference travel, and made sure I jumped through all the administrative hoops to the point of graduation. Last but not least, I wanted to say thanks to Derek Richardson for organizing so many fun department birdwatching expeditions – these were much–needed stress relief throughout my PhD and as a bonus I now have a lifelong hobby!

I would not have made it through my PhD without the support and kindness of my fellow graduate students. I particularly want to express my gratitude to Sara Frederick for

all her support – if I was ever stuck on a scientific or technical problem Sara was always there to help, and her dedication to astronomy has been a constant source of inspiration. I could not have done this without her guidance and friendship and it's been an honor to work together in Suvi's group! I also wanted to say thank you to Tiara Hung for sharing all her time-domain experience and knowledge with me in the first couple of years of my PhD – I would have been off to a much slower start if it weren't for her patience and assistance! Thank you also to Erica Hammerstein for being such an wonderful collaborator and co-observer – it's been so much fun working together on ZTF transients and follow–up over the last few years! I wanted to say thank you to Tomás Ahumada and Ginny Cunningham, as well as Sara and Erica, for all the fun times we've shared on conferences and observing trips. I will always remember our many wonderful experiences in the world of time–domain astronomy. I wanted to say thanks to Liz Tarantino for being such an kind and lovely office mate throughout the years as well – I'm glad we could share so many experiences, from class assignments to postdoc applications, together! I also particularly wanted to express my appreciation for GRAD-MAP leads and co-leads Amy Steele, Milena Crnogorčević, and Andrew Guo for the enormous efforts they put into the program. Thank you for being such incredible people to work with!

I would like to express my appreciation for the external collaborators who have invested so much time expanding my technical knowledge and answering my numerous questions about image modeling and photometry: Dustin Lang, Martin Landriau, Danny Goldstein, and Michael Medford. I'd like to thank Matthew Graham, Frank Masci, Andrew Drake, and other members of the ZTF collaboration who have provided very useful feedback on my papers. I also want to thank Umaa Rebbapragada and Ashish

Mahabal for teaching me so much about machine learning in the early days of ZTF. Thanks also to Maayane Soumagnac for her friendship and support during my time at LBNL!

Going back to the time before my PhD, I wanted to thank Tara Murphy and George Hobbs for first kindling my love for astronomy during my undergraduate and honors research. I would not be where I am today if it were not for the incredible experiences I had in their research groups! Thanks also to my high school physics teacher Paul Stokes, who inspired me to take up physics in the first place. Every teacher and researcher who has encouraged and supported me since primary school has enabled my path to this PhD, and I'm grateful for the work of every one!

I want to thank my parents and my brother for always encouraging me to pursue what I love and for providing emotional support every step of the way. And of course, I absolutely could not have made it without the love and support of my partner Matthew, who is always there to encourage me when I need it most.

Table of Contents

Preface ii

Dedication iii

Acknowledgements iv

Table of Contents viii

List of Tables xi

List of Figures xii

List of Abbreviations xvi

Chapter 1: Introduction 1

1.1 Massive black holes and their host galaxies 1

1.1.1 Massive black hole seeding channels 2

1.1.2 Observational constraints on seeding channels 4

1.2 Active galactic nuclei 7

1.2.1 Black hole accretion 7

1.2.2 Accretion onto IMBHs and consequences for dwarf galaxy active fractions 8

1.2.3 Narrow emission line diagnostics 10

1.2.4 Disk–wind structure of AGN 11

1.2.5 Double–peaked broad emission from the accretion disk 13

1.2.6 Optical and X-ray variability 20

1.3 Supermassive black hole binaries 22

1.3.1 Formation of gravitationally bound systems 22

1.3.2 Observable signatures of accreting SMBH binaries 23

1.3.3 Gravitational wave recoil as a tracer of SMBH binary spin alignment 29

1.4 Searching for rare AGN populations with time–domain data 32

1.4.1 Introduction to image differencing and alert streams with the Zwicky Transient Facility 34

1.4.2 Introduction to forward modeling techniques for joint survey analysis 38

1.5 Scope of the dissertation 39

Chapter 2: A search for off–nuclear AGN from recoiling SMBHs and ongoing galaxy mergers with the Zwicky Transient Facility 41
2.1 Overview . . . 41
2.2 Introduction . . . 42
2.3 Sample selection . . . 50
2.3.1 The Zwicky Transient Facility . . . 50
2.3.2 Selection of variable AGN in ZTF . . . 51
2.3.3 Selection of AGN spatially offset from their host galaxy . . . 54
2.3.4 Morphological classification of AGN hosts . . . 62
2.3.5 Spectroscopic analysis of ZTF broad line AGN . . . 64
2.4 Results . . . 67
2.4.1 AGN in galaxy mergers . . . 67
2.4.2 Chance coincidences of AGN and background galaxies . . . 74
2.4.3 AGN spatially offset from the center of disturbed galaxies . . . 77
2.4.4 SDSS1133 (ZTF19aafmjfw) . . . 92
2.5 Conclusions . . . 95
2.6 Supplementary Material . . . 96

Chapter 3: Variability–selected intermediate mass black hole candidates in dwarf galaxies from ZTF and *WISE* 101
3.1 Overview . . . 101
3.2 Introduction . . . 102
3.3 Dwarf galaxy sample selection . . . 110
3.4 ZTF photometry of dwarf galaxies . . . 112
3.5 Selection of variable IMBH candidates . . . 114
3.6 Spectroscopic and multi–wavelength properties of the ZTF–selected IMBH candidates . . . 124
3.7 ZTF variability of previously reported PTF–selected IMBH candidates . . . 128
3.8 *WISE* single epoch forced photometry . . . 129
3.9 Properties of the *WISE*–selected variable IMBH candidates . . . 131
3.10 Discussion . . . 135
3.11 Conclusions . . . 141

Chapter 4: Optically variable double–peaked emitters in ZTF: Understanding the AGN populations which mimic SMBH binary behavior 150
4.1 Overview . . . 150
4.2 Introduction . . . 151
4.3 Methods and Results . . . 155
4.3.1 Selection of variable AGN in ZTF with visible Balmer broad lines 155
4.3.2 Spectroscopic selection of DPE sub–sample . . . 157
4.3.3 Variability properties of DPEs and other broad line AGN . . . 168
4.3.4 Spectroscopic monitoring of DPEs . . . 184
4.3.5 Radio emission from DPEs . . . 192
4.4 Discussion . . . 192
4.5 Summary and conclusions . . . 197

4.6 Supplementary Material 200

Chapter 5: Summary and Future Work 207
5.1 Summary 207
5.2 Future Work 211
5.2.1 Multi–wavelength and spectroscopic follow–up of off–nuclear AGN 211
5.2.2 Searching for rare transients with The Legacy Survey of Space and Time 212

Chapter 6: Facilities and Software 219
6.1 Facilities 219
6.2 Existing software applied to research presented in this thesis 220
6.3 New software developed for this thesis 221

Bibliography 225

List of Tables

2.1 Offset cutoffs (arcseconds) selected for classification of off–nuclear AGN based on their peak magnitude. 60
2.2 Breakdown of the complete sample of 251 offset AGN into 5 galaxy morphology–based classifications. 63
2.3 Morphological and spectroscopic properties of the 52 AGN in galaxy mergers. 70
2.4 Spectroscopic and morphological properties of the sample of AGN spatially offset from disturbed host galaxies. 78
2.5 X-ray and radio properties of the sample of AGN spatially offset from disturbed host galaxies. 79
2.6 Best fit accretion disk parameters for the 5 off–nuclear double peaked emitters. 87
2.7 X-ray and radio properties of the 52 ZTF AGN in galaxy mergers. 99

3.1 Spectroscopic properties and BH masses derived from various methods for the 44 AGN candidates with significant and correlated g and r band variability found in ZTF. 119
3.2 Spectroscopic properties and host galaxy masses for the 36 supernova candidates found in ZTF. 122
3.3 Properties of the 14 SN candidates found in forward modeled *WISE* light curves. 143
3.4 Properties of the 148 AGN candidates with significant and correlated W1 and W2 variability found in forward modeled *WISE* light curves. 144

4.1 Spectroscopic and wavelength properties of the 299 variable DPE candidates in ZTF. 160
4.2 Fractions of DPE and AGN populations with $> 2\sigma$ evidence for an extra component in the power spectra model. 176

6.1 Best fit accretion disk parameters for circular and elliptical models of two double–peaked emitters from ZTF. 223

List of Figures

1.1 Schematic of three proposed seeding channels for the first massive black holes and the effects of each channel on BH–galaxy scaling relations . . . 3
1.2 Observed relations between BH mass vs galaxy stellar bulge mass, and BH mass vs galaxy stellar velocity dispersion. 6
1.3 Effects of BH mass on high energy X-ray photon flux and BPT narrow line ratios 12
1.4 Schematic of cloud trajectories in an AGN accretion disk based on cloud density. 14
1.5 Double–peaked mean Hα emission line profiles and rms spectra from canonical double–peaked emitters Arp 102B and 3C 390.3. 17
1.6 Illustration of the effects of disk parameters on the shape of the double–peaked profile 18
1.7 Diagram of binary AGN broad line regions and dusty tori for 3 regimes of differing orbital separation, Hill radii and BLR radii. 26
1.8 Diagram of a possible accretion disk structure of an SMBH binary and the mechanisms by which its optical emission could vary with orbital period. . 28
1.9 The distribution of projected spatial offset vs line of sight velocity for off–nuclear and active recoiling AGN from a population of simulated mergers. 31
1.10 Zwicky Transient Facility image cutouts of a supernova and a variable star, showing the reference image, the single epoch science image, and the subtraction. 37
1.11 `Tractor` modeling example of a low resolution WISE image forward modeled from a high resolution SDSS image. 39

2.1 Distribution of spatial offsets between AGN and their host galaxy nuclei from the ZTF AGN sample. 59
2.2 Example of the ZTF image subtraction of a variable AGN, and the corresponding Tractor model of the host galaxy and point source. 61
2.3 Distribution of physical spatial offsets between AGN and the closest galaxy nucleus for a variable AGN population, a population of AGN in mergers, and 9 off–nuclear AGN. 65
2.4 Distribution of Balmer broad line velocities relative to narrow emission lines for all ZTF AGN with broad lines. 66
2.5 Spectrum of AGN ZTF18aaxvmpg and its offset companion galaxy. . . . 73
2.6 BPT classifications of AGN ZTF18aaxvmpg and its companion galaxy. . . 74

2.7 X-ray luminosity for 27 AGN with known spectroscopic redshifts as a function of physical galaxy separation. 75
2.8 Peak luminosity change relative to the reference image amongst the 27 AGN in mergers and a control sample of single AGN. 75
2.9 ZTF light curves in g, r and i-band for the sample of 9 offset AGN and the known recoiling SMBH candidate in SDSS1133 80
2.10 For the 9 off–nuclear AGN: Coadded Legacy Survey Images, models of the images produced by forward modeling with `The Tractor`, and the residuals, with radio contours overlaid. 81
2.11 Optical spectra of the 9 off–nuclear AGN. 82
2.12 Hα and Hβ broad line regions for the off–nuclear AGN candidates. 85
2.13 Best fit accretion disk models of double–peaked Hα accretion disk emission in 5 off–nuclear AGN candidates. 86
2.14 Spectrum of the flare ZTF19aafmjfw from SDSS1133. 94
2.15 Magnitude–weighted AGN–host offsets obtained from r-band ZTF difference images. 97
2.16 Magnitude–weighted AGN–host offsets obtained from g-band ZTF difference images. 98

3.1 Pearson r correlation coefficient and χ^2/N in g- and r-band calculated from ZTF light curves of the dwarf galaxy sample for 3 different binning timescales. 116
3.2 Three examples of ZTF light curves which passed the variability criteria and were classified as variable AGN candidates. 117
3.3 Three examples of ZTF light curves which passed the variability criteria and were classified as supernova candidates. 118
3.4 Galaxy mass and redshift distributions of variable IMBH candidates and supernova candidates from ZTF compared to the parent dwarf galaxy sample. 125
3.5 BPT diagram showing emission line classification of IMBH and supernova candidates from ZTF. 127
3.6 Pearson r correlation coefficient and χ^2/N in W1 and W2 band calculated from *WISE* forward modeled light curves of dwarf galaxies and a control AGN sample. 132
3.7 Six examples of *WISE* forward modeling light curves which passed the variability criteria and were classified as IMBH candidates. 133
3.8 Galaxy mass and redshift distributions of variable IMBH candidates from WISE compared to the parent dwarf galaxy sample. 135
3.9 BPT diagram showing emission line classification of IMBH and supernova candidates from ZTF. 136
3.10 Legacy survey cutouts of 3 *WISE* IMBH candidates (a–c) and 2 ZTF IMBH candidates (d–e) with host masses $M_* < 10^{8.2}\mathrm{M}_\odot$ and the candidate with a FIRST radio detection (f, radio position overlaid in green circle). Blue circles show the central position for *WISE* or ZTF forced photometry. 137

4.1 Distribution of redshifts, maximum g-band magnitudes and estimated virial masses for the DPE sample and the broad line AGN control sample. 169
4.2 Optical and mid–IR light curves of selection double–peaked emitters. . . . 171
4.3 Power spectra and model fits of 4 DPEs. 177
4.4 Distribution of power law index and power spectral density amplitude for the DPE and control AGN samples. 178
4.5 Power spectra and model fits of 4 DPEs with low frequency cutoffs. 179
4.6 Cumulative distribution functions for the Δ log likelihood when comparing the PL (power law), WN (power law + white noise), BPL (broken power law + white noise) and Gauss (power law + Gaussian bump) models of DPE and AGN power spectra. 180
4.7 Distribution of damped random walk parameters τ (characteristic timescale) and σ (high frequency noise amplitude) from MCMC modeling of g-band ZTF light curves of the DPE and control AGN samples. 182
4.8 Distributions of power spectral density amplitude and power law index vs estimated virial mass for the DPE sample and the broad line AGN control sample. 183
4.9 Distributions of virial black hole mass and damped random walk parameters σ and τ from MCMC modeling of DPE and a mass–matched control AGN sub–sample. 185
4.10 Comparison of Balmer broad line structures from recent and > 13 year old archival spectra of 10 DPEs. 187
4.11 Time variability in Hα and $H\beta$ profiles of 3 new DPEs from ZTF. 188
4.12 Distribution of velocities of red and blue shoulders in broadline profiles from multi–Gaussian fitting of archival SDSS spectra of ZTF DPEs compared to other samples in the literature. 190
4.13 Distribution of the power law spectral index of the optical continua of the DPE and broad line AGN control samples. 191
4.14 Examples of multi–Gaussian fits to the Hα spectra of the 33 DPEs with the brightest double–peaked broad lines relative to the flux of the Hα narrow line. 201
4.15 Examples of multi–Gaussian fits to the Hα spectra of the 33 DPEs with the brightest double–peaked broad lines relative to the flux of the Hα narrow line (continued). 202
4.16 Examples of multi–Gaussian fits to the Hα spectra of the 33 DPEs with the brightest double–peaked broad lines relative to the flux of the Hα narrow line (continued). 203
4.17 ZTF and WISE optical and mid–IR light curves of the 26 DPEs with the brightest double–peaked broad lines relative to the flux of the Hα narrow line. 204
4.18 ZTF and WISE optical and mid–IR light curves of the 26 DPEs with the brightest double–peaked broad lines relative to the flux of the Hα narrow line (continued). 205

4.19 ZTF and WISE optical and mid–IR light curves of the 26 DPEs with the brightest double–peaked broad lines relative to the flux of the Hα narrow line (continued). 206

5.1 Predicted LSST light curve of dwarf galaxy NGC4395 215
5.2 BH occupation fraction as a function of halo mass and stellar mass according to cosmological simulations. 215
5.3 For IMBH populations in cosmological simulations: distributions of distances from halo centers and nuclear fractions as a function of BH mass. 216
5.4 Examples of simulated gLSNe in LSST images and histograms of the minimum angular separations between multiply–imaged gLSNe in the simulated populations. 217

6.1 Examples of circular and elliptical accretion disk model fits to a flaring double–peaked emitters from iPTF. 224

List of Abbreviations

2MASS	Two Micron All-Sky Survey
AGN	Active Galactic Nucleus
AMPEL	Alert Management, Photometry and Evaluation of Lightcurves
BASS	Beijing-Arizona Sky Survey
BH	Black Hole
BPT	Baldwin, Phillips and Terlevich
CLASS	Cosmic-Lens All Sky Survey
CSS	Catalina Sky Survey
DECaLs	Dark Energy Camera Legacy Survey
DECam	Dark Energy Camera
DESI	Dark Energy Spectroscopic Instrument
DPE	Double−Peaked Emitter
DR	Data Release
DRW	Damped Random Walk
GROWTH	Global Relay of Observatories Watching Transients Happen
IMBH	Intermediate Mass Black Hole
iPTF	intermediate Palomar Transient Factory
LBV	Luminous Blue Variable
LDT	Lowell Discovery Telescope
LSST	Legacy Survey of Space and Time
pPXF	Penalized Pixel Fitting
LISA	Laser Interferometer Space Antenna
MzLS	Mayall z-band Legacy Survey
NEOWISE	Near-Earth Object Wide-field Infrared Survey Explorer
NSA	NASA-Sloan Atlas
PTF	Palomar Transient Factory
QSO	Quasar
SDSS	Sloan Digital Sky Survey
SMBH	Supermassive Black Hole
SN	Supernova
VLA	Karl G. Jansky Very Large Array
VLASS	Karl G. Jansky Very Large Array Sky Survey
WISE	Wide-field Infrared Survey Explorer
ZTF	Zwicky Transient Facility

Chapter 1: Introduction

In this chapter I provide an introduction to the physics of massive black hole (MBH) formation and growth. I summarize the various possible origins for the first massive black hole seeds, and how these origins could result in observable differences in the MBH–host galaxy relationships we see today. I describe the multi-wavelength emission produced by MBHs as they accrete gas, and relate this to the physical structure of MBHs and their environment. I discuss how MBH binaries form when galaxies merge, and how gravitational wave recoil may occur as a consequence of MBH binary mergers. I introduce the open questions we currently have about MBH formation and growth to motivate the research presented in the following chapters. Finally, I describe how time–domain survey data enables the study of MBHs via their variable optical and infrared emission.

1.1 Massive black holes and their host galaxies

The vast majority of massive galaxies host an MBH of mass $10^3 < M_{\rm BH} < 10^{10} M_\odot$ in their nucleus (Magorrian et al., 1998). When MBHs interact with their surrounding environment by accreting gas and emitting radiation, they can be observed as active galactic nuclei (AGN). Most observed AGN are accreting supermassive black holes (SMBHs), which we define as having mass $M_{\rm BH} > 10^6 M_\odot$, but some AGN arise from intermediate mass black holes (IMBHs) of mass $10^3 < M_{\rm BH} < 10^6 M_\odot$. AGN can be identified via their multi–wavelength emission and spectroscopic signatures. Their optical, infrared and X-ray brightness often changes over time, allowing them to be detected via their variability in time–domain surveys (Geha et al., 2003; MacLeod et al., 2011; Schmidt et al., 2010; Smith et al., 2018; Ulrich et al., 1997).

1.1.1 Massive black hole seeding channels

There are multiple proposed channels for the formation of the first massive black hole seeds which grew into the SMBHs we see today (Figure 1.1; see Greene et al., 2020, for a review). It is likely that most massive black holes originated as $\sim 10 M_\odot$ BHs from core-collapse supernovae at redshifts $z < 10$ which grew over time via gas accretion to become supermassive. However, for some high–mass and high–redshift SMBHs, this is only viable for lower radiative efficiencies than are typically assumed ($L < 0.1\dot{M}c^2$) or if periods of super-Eddington accretion (see Section 1.2.1) are allowed. Other MBH formation channels have therefore been proposed in order to explain the range of observed SMBH masses and redshifts. In one channel, the massive and low metallicity stars at $z > 10$ (Pop III stars) collapsed into more massive black hole seeds of $M_{\rm BH} \sim 100 M_\odot$ (Fryer & Kalogera, 2001), producing approximately one MBH per high–density peak (Madau et al., 2014; Madau & Rees, 2001). If this channel produced the first MBHs, we would therefore expect the fraction of galaxies hosting an MBH (the galaxy occupation fraction) to be close to 1. In the second proposed channel, gas clouds collapsed directly to MBHs of $M_{\rm BH} \sim 10^4 - 10^6 M_\odot$ while avoiding the typical phases of stellar evolution, producing

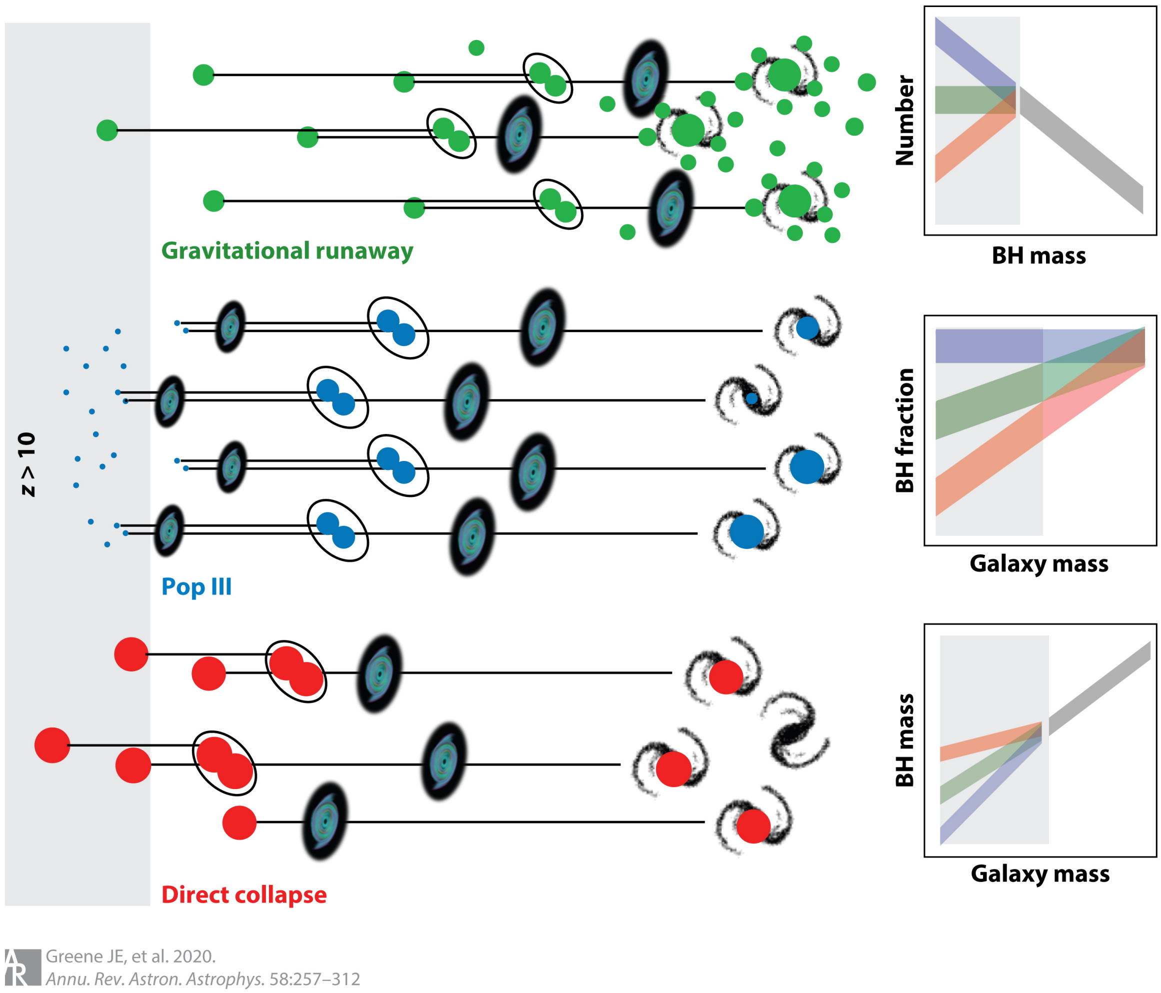

Figure 1.1: Schematic of three proposed seeding channels for the first massive black holes and the effects of each channel on BH–galaxy scaling relations, from Greene et al. (2020). Initial seeds are shown as filled circles in the left gray column, where the radius indicates the relative mass of the initial seeds. Merger events are indicated by unfilled black ovals while accretion events are shown by filled ovals containing an accretion disk image. The final occupation fractions in low redshift galaxies and relative masses are indicated on the right side of the schematic. The observable effects of each seeding channel on present–day scaling relations (the BH mass distribution, the BH occupation fraction as a function of galaxy mass, and the BH mass–galaxy bulge mass relation) are shown on the right. Reproduced by permission of the authors and Annual Reviews.

occupation fractions of 0.2–1.0 depending on galaxy mass (e.g. Begelman et al., 1980; Lodato & Natarajan, 2006; Loeb & Rasio, 1994). This could only have occurred at $z > 15$ when the gas was pristine enough to avoid cooling and fragmentation into smaller units (Habouzit et al., 2016). In the third channel, collisional runaway of stellar–mass BHs and neutron stars as dynamical friction pulled them into high density galaxy nuclei produced seed MBHs of $\sim 10^4 - 10^6 M_\odot$ (Boco et al., 2020; Miller & Hamilton, 2002; Portegies Zwart & McMillan, 2002; Sicilia et al., 2022). This thesis aims, in part, to discover populations of MBHs whose properties may help us distinguish between these alternative seeding channels.

1.1.2 Observational constraints on seeding channels

SMBHs grow as their host galaxies merge with other galaxies over time, producing a correlation between SMBH mass and host galaxy stellar bulge mass M_* (Kormendy & Ho, 2013). The relationship between $M_{\rm BH}$ and M_* extending down to dwarf galaxies of stellar mass $M_* \sim 10^7 M_\odot$ is:

$$\log\left(M_{\rm BH}/M\odot\right) = \alpha + \beta \log\left(M_{\rm bulge,*}/10^{11} M_\odot\right) \tag{1.1}$$

with $\alpha = 8.80 \pm 0.085$ and $\beta = 1.24 \pm 0.081$ (Figure 1.2; Schutte et al., 2019). Galaxy mass can be approximated by the velocity dispersion of its stars σ_*, producing the $M_{\rm BH} - \sigma_*$ relation:

$$\log\left(M_{\rm BH}/M\odot\right) = \alpha + \beta \log\left(\sigma_*/200 \rm km\ s^{-1}\right) \tag{1.2}$$

with $\alpha = 8.37 \pm 0.05$ and $\beta = 5.31 \pm 0.33$ (Woo et al., 2013). Dwarf galaxies of stellar mass $M_* < 3 \times 10^9 M_\odot$ are therefore the best places to find low–mass black holes.

The low–mass end of the galaxy occupation fraction, and the slope and scatter of the $M_{\rm BH} - \sigma_*$ relation at low galaxy masses, will vary depending on the formation mechanism of early black hole seeds. For example, Pop III stars will produce a population of undermassive BHs in low redshift galaxies with stellar dispersion $\sigma_* < 100$ km/s while direct collapse mechanisms will produce heavier black holes, resulting in a flattening of the $M_{\rm BH} - \sigma_*$ relation around masses of $10^5 M_\odot$ (Volonteri & Natarajan, 2009). The fraction of IMBHs in dwarf galaxies which are wandering in their galaxy haloes, rather than occupying the nucleus, may also constrain BH seed formation mechanisms. The wandering fraction will be substantially higher if massive black holes were produced by gravitational runaway due to the high frequency of IMBH ejection during these interactions (Holley-Bockelmann et al., 2008; Volonteri & Perna, 2005).

The observed $M_{\rm BH} - \sigma_*$ relation has only 15 black holes in galaxies of $M_* < 3 \times 10^9 M_\odot$ with well–measured BH and galaxy masses (Figure 1.2; Baldassare et al., 2020a), so to see if this relation holds at lower masses we would benefit from having more BHs at $M_* < 3 \times 10^8$. This motivates the development of strategies to detect low–mass AGN in dwarf galaxies, which tend to have low accretion luminosities (Bellovary et al., 2018) and are frequently missed by traditional AGN search criteria using infrared color cuts (Latimer et al., 2021), X-ray luminosities (Mezcua et al., 2018), or the optical emission line ratios (e.g. Reines et al., 2013) due to the harder spectral energy distributions (SEDs) and lower accretion rates of low–mass AGN (Sections 1.2.2 and 1.2.3).

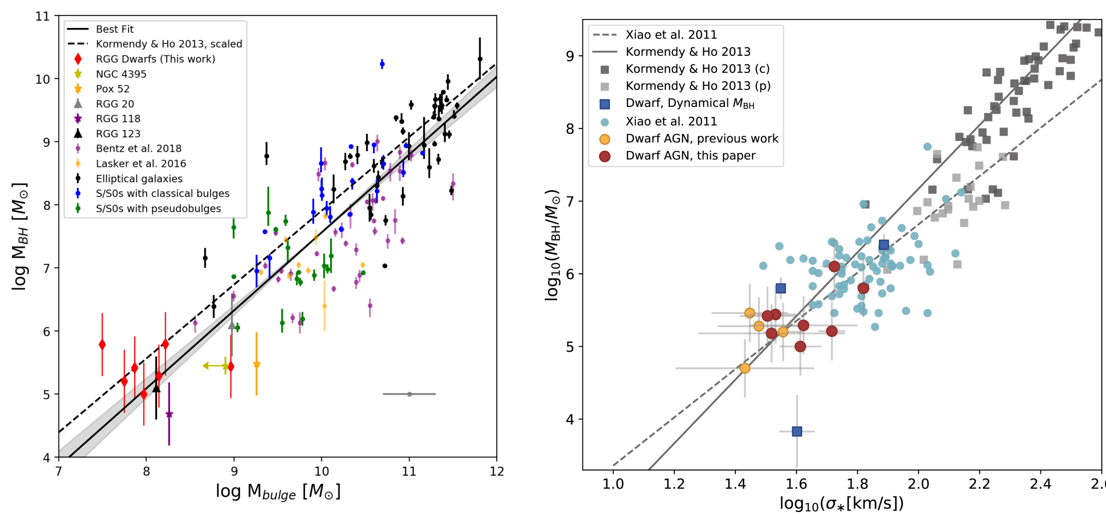

Figure 1.2: **Left**: BH mass vs stellar bulge mass, including some dwarf galaxies, from Schutte et al. (2019). Bulge masses were derived from color–dependent mass-to-light ratios, while BH masses were derived from a mixture of dynamical and virial broad line measurements. Reproduced by permission of the authors and AAS. **Right:** Black hole mass versus stellar velocity dispersion, from Baldassare et al. (2020a). Dark gray squares show galaxies with classical bulges and light gray squares show galaxies with pseudo–bulges. Dwarf galaxies with dynamical BH mass estimates are shown as dark blue squares while the red, yellow and light blue circles indicate AGN in dwarf galaxies with virial BH mass measurements. Reproduced by permission of the authors and AAS.

1.2 Active galactic nuclei

1.2.1 Black hole accretion

AGN are produced by gas accretion onto an SMBH in a galaxy nucleus, which converts energy from the gravitational potential to light. In a simple model where an SMBH undergoes spherically symmetric accretion of gas of density $\rho(r)$ and emits radiation which is also spherically symmetric, we can find the maximum luminosity for a black hole where the radiation force is smaller than the gravitational force on the gas so that the gas is not dispersed quickly (the Eddington luminosity):

$$L_{\rm Edd} \equiv \frac{4\pi G c}{\kappa} M_{\rm BH} \sim 1.28 \times 10^{46} M_8 \, {\rm erg \; s^{-1}} \tag{1.3}$$

where M_8 is the BH mass in units of $10^8 M_\odot$ and κ is the opacity. Assuming fully ionized hydrogen and Thomson scattering this corresponds to a maximum accretion rate given by

$$\dot{M}_{\rm Edd} = \frac{L_{\rm Edd}}{\epsilon_r c^2} \approx 2.2 M_8 \left(\frac{\epsilon_r}{0.1}\right)^{-1} M_\odot \, {\rm yr^{-1}}. \tag{1.4}$$

where ϵ_r is the conversion efficiency of accreted mass to radiation defined by $\epsilon_r \equiv \frac{L}{\dot{M}_{\rm BH} c^2}$. Super–Eddington accretion is, however, possible if mass accretion occurs in a disk while radiation escapes from the polar zones (Abramowicz et al., 1988). A number of high redshift ($z > 6$) quasars with bolometric luminosities greater than their estimated Eddington luminosities have been observed, providing some evidence that super-Eddington accretion may have occurred at early times (e.g. Bañados et al., 2021).

The gas accreted onto an SMBH has angular momentum and therefore has a structure close to a Keplerian disk. This disk has temperature structure approximated by

$$T(R) \sim 6.3 \times 10^5 \left(\frac{\dot{M}_{\rm BH}}{\dot{M}_{\rm Edd}}\right)^{1/4} M_8^{-1/4} \left(\frac{r}{r_S}\right)^{-3/4} \mathrm{K} \tag{1.5}$$

assuming that $\epsilon = 0.1$, where $r_S = \frac{2GM_{\rm BH}}{c^2}$ is the Schwarzchild radius of the BH. Thermal emission from accretion disks with this temperature structure is responsible for the 'blue bump' at $\sim 10^{15} - 10^{16}$ Hz in UV/visible spectra of quasars. Additional features include a mid–IR bump due to thermal emission from warm dust at $T < 1000$K. Dust echoes in the mid–IR can provide information on the geometry and environment of AGN. The X-ray spectra of AGN can be decomposed into a power law over frequency ν given by $S_\nu \propto \nu^{-\alpha}$ where $\alpha \sim 0.7$, a soft excess and a high energy hump. These features arise from Comptonization and reflection of photons within a high temperature corona above the optically thick part of the accretion disk.

1.2.2 Accretion onto IMBHs and consequences for dwarf galaxy active fractions

Numerical modeling of accretion onto $z \sim 10$ BH seeds finds that there are two distinct accretion modes onto MBHs: an efficient 'feeding–dominated' regime, and an inefficient 'feedback–limited' regime with intermittent duty cycles and regular outflow episodes (Pacucci et al., 2015). Three conditions are required for the efficient mode to occur (Begelman & Volonteri, 2017; Inayoshi et al., 2016; Pacucci et al., 2018, 2015).

The conditions depend on the BH mass, the gas number density n_B at the Bondi radius $R_B = 2GM_{\rm BH}/c_s^2$ where c_s is the sound speed, and the angular momentum content of the gas at R_B: $\lambda_B = l_B/(GM_{\rm BH}R_B)^{1/2}$, where l_B is the angular momentum content per unit mass of gas. For efficient accretion on small scales ($r \ll R_B$), we require

$$M_{\rm BH} \gtrsim 10^{-11} \left(\frac{n_B}{1\rm cm^{-3}}\right)^2 M_\odot \tag{1.6}$$

caused by the size of the 'transition radius' which determines where radiation pressure dominates the accretion flow. For efficient accretion on large scales ($r \gtrsim R_B$) we require

$$M_{\rm BH} \gtrsim 10^{9} \left(\frac{n_B}{1\rm cm^{-3}}\right)^{-1} M_\odot \tag{1.7}$$

which reflects the size of the of the ionized region around the BH compared to R_B. The final condition is determined by the need for infalling gas to have sufficient angular momentum to be accreted, given by:

$$M_{\rm BH} \gtrsim 2.2 \times 10^{19} \left(\frac{\lambda_B}{10^{-1}}\right)^{24/13} M_\odot \tag{1.8}$$

The result of these conditions is that higher mass BHs have larger ranges of gas density which meet the requirements for the efficient mode (Pacucci et al., 2018). From the point of view of BH seed growth, this means that seeds of mass $10^{3-4} M_\odot$ primarily evolve in the 'feedback–limited' regime and grow slowly, while massive seeds $\gtrsim 10^{5-6} M_\odot$ grow in the 'feeding–dominated' regime and accrete mass more quickly (Pacucci et al., 2015).

An important effect of these accretion conditions is that the active fraction (the fraction of galaxies containing AGN with accretion duty cycles close to ~ 1 and with Eddington ratios $f_{\text{Edd}} \gtrsim 0.1$) is predicted to be lower for lower mass galaxies: Pacucci et al. (2021) predict an active fraction of 5% for dwarf galaxies of stellar mass $10^7 M_\odot$, compared to 20% of galaxies of stellar mass $10^{10} M_\odot$.

1.2.3 Narrow emission line diagnostics

Many AGN exhibit strong narrow lines of width $\sim 100 - 400$ km s^{-1} over the UV to near–IR wavelength range due to 'forbidden' transitions which can only arise in low density gas, typically $n_e \sim 10^4\,\text{cm}^{-3}$. The narrow line region has a characteristic temperature of 15,000 K and extends up to 100 pc from the SMBH. The relative fluxes of forbidden emission lines are tracers of the ionizing radiation spectrum and the density and temperature of the gas. In particular, the [O III]λ5007/Hβ ratio gives an indication of average ionization and temperature in the gas, while the [O I]λ6300/Hα, the [S II]$\lambda\lambda$6717,6713/Hα and the [N I]λ6583/Hα ratios are indicators of contributions from a large partially ionized zone arising from high–energy photoionization (Osterbrock, 1989).

Active galaxies and star forming galaxies can be distinguished via their emission line ratios using the Baldwin, Phillips and Terlevich diagram (BPT; Baldwin et al., 1981; Veilleux & Osterbrock, 1987). This diagram was developed by modeling emission lines excited by ionizing radiation fields from combined stellar continua and AGN emitting a power law spectrum. It was found that pure star formation can be identified by the condition:

$$\log(\mathrm{O\,[III]}/\mathrm{H}\beta) < 0.61/\log(\mathrm{N\,[II]}/\mathrm{H}\alpha) - 0.05) + 1.3 \tag{1.9}$$

(Kauffmann et al., 2003), while the extreme starburst demarcation condition is given by

$$\log(\mathrm{O\,[III]}/\mathrm{H}\beta) < 0.61/\log(\mathrm{N\,[II]}/\mathrm{H}\alpha - 0.47) + 1.19 \tag{1.10}$$

(Kewley et al., 2001).

Recent studies have considered the impact of black hole mass on AGN emission line ratios and have found that the BPT classifications do not hold at masses $M_{BH} \lesssim 10^7 M_\odot$ Cann et al. (Figure 3.5; 2019). This arises due to the harder SED of low–mass AGN accretion disks. When BHs have masses $< 10^7 M_\odot$, the dominant ionization states of oxygen change from O^+ and O^{2+} to higher ionization states, up to O^{8+} for a $10^2 M_\odot$ BH. In low–mass AGN, the greater fraction of X-ray photons at high energies which penetrate the cloud more effectively produces an extended partially ionized zone where H^+ is produced but O^{2+} is not. The effect of these combined factors is that O [III]/Hβ is reduced for low–mass AGN and their line ratios fall in the starforming region of the BPT diagram described by equation 1.9. Classical spectroscopic diagnostics are therefore biased against low–mass AGN.

1.2.4 Disk–wind structure of AGN

Seyfert galaxies, which are active galaxies with quasar–like cores, have historically been classified by their spectra into Type I Seyferts, which have broad Balmer emission

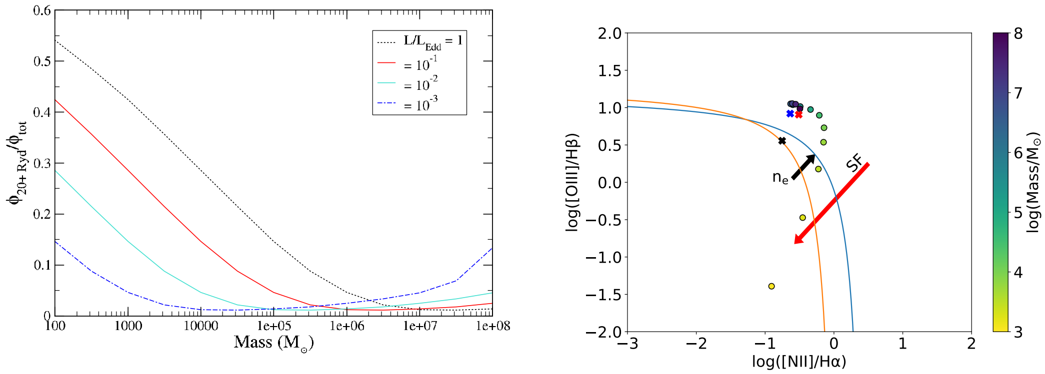

Figure 1.3: **Left**: Fraction of X-ray photon flux of energy > 20 Ryd (equivalent to 272.1 eV) over total photon flux vs BH mass for 4 different Eddington ratios, from (Cann et al., 2019). The fraction of high energy X-ray photons is larger for lower BH masses. **Right:** BPT diagram showing AGN emission line ratios for a range of BH masses, obtained from photoionization modeling at constant $\log U = -2$, $n_H = 300\text{cm}^{-3}$ and $\dot{m}/\dot{m}_{\text{Edd}} = 0.1$, from Cann et al. (2019). The solid lines indicate the conditions from equations 1.9 and 1.10. Reproduced by permission of the authors and AAS.

lines of width $\sim 100 - 1000$ km s^{-1} in addition to narrow emission lines, and Type II Seyferts, which have only narrow emission lines.

AGN are surrounded by a continuous distribution of clouds whose composition changes at the dust sublimation radius $R_d \simeq 0.4L_{45}^{1/2}$pc, where $L_{45} = L_{\text{bol}}/10^{45}$erg s^{-1}. A 'dusty torus' forms beyond the dust sublimation radius which reprocesses the ultraviolet and optical continuum emission to the infrared (Barvainis, 1992; Hönig & Kishimoto, 2011, 2017; Koshida et al., 2014). Depending on the viewing angle and the opening angle of the torus, optical broad line emission from high velocity gas close to the AGN may be blocked by the dust, explaining the differences between Seyfert 1 and Seyfert 2 galaxies in the 'AGN unification' scheme (Antonucci, 1993).

There also exists a class of 'true Type II' Seyfert galaxies, which intrinsically lack broad emission lines, and a class of intermediate types which have some broad line emission, but at lower broad-to-narrow flux ratios than observed for the majority of Type I Seyfert galaxies. Findings that most Type I AGN appear as intermediate type at low luminosity (Stern & Laor, 2012) and findings that lower Eddington ratio AGN have higher obscuration fractions in samples of X-ray selected AGN (Ricci et al., 2017) have led to the realization that the intrinsic AGN classification evolves from Type I to Type II as accretion rate decreases.

The disk–wind model of AGN describes how there exists a two–component broad line region separated according to the density of gas clumps relative to a critical density dependent on radiative efficiency ϵ_r and luminosity L_{45} according to:

$$N_{\text{crit}}(R_d) \sim 4.3 \times 10^{22} \frac{1}{100\epsilon_r} \left(\frac{L_{45}}{M_7^{2/3}} \right)^{3/4} \text{cm}^{-2} \tag{1.11}$$

(Elitzur & Ho, 2009). In this scenario, outflows of subcritical density clouds tend to follow streamlines outward (and produce Gaussian broad line emission) and supercritical clouds remain close to the disk surface. The dependence of the critical density on luminosity may therefore explain the smooth transition between Type I and true Type II (Figure 1.4; Bon et al., 2009; Elitzur et al., 2014; La Mura et al., 2009; Popović et al., 2004).

1.2.5 Double–peaked broad emission from the accretion disk

Double–peaked broad emission lines are observed in a fraction of AGN in the permitted H and He lines. The double peaked structures span velocities up to 10,000 km s^{-1} and are understood to arise from the outer regions of the AGN accretion disk, which

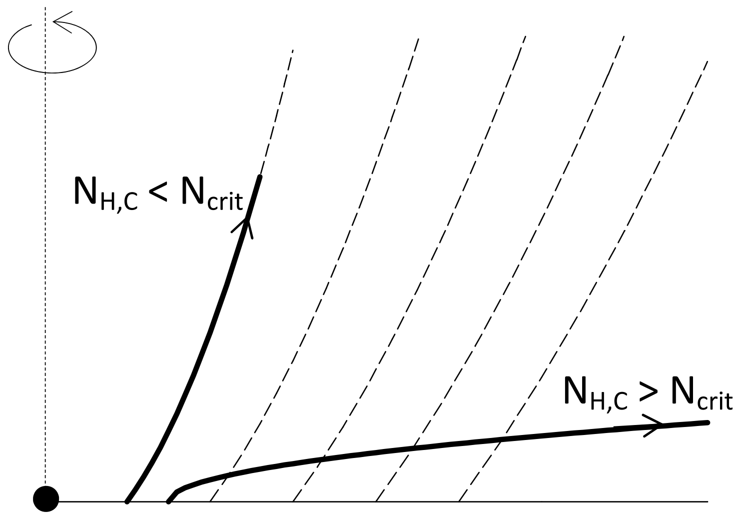

Figure 1.4: Schematic of cloud trajectories in an AGN accretion disk, from Elitzur et al. (2014). Clouds with column density $N_{H,c} < N_{\text{crit}}$ follow the streamlines generated by wind ram pressure, while clouds with column density $N_{H,c} > N_{\text{crit}}$ tend to move across the streamlines and stay near the disk surface. Reproduced by permission of the authors.

stretches from a few gravitational radii to a few thousand. The shapes of these broad lines are often well described by a model in which an inner thick, hot ion torus illuminates a thin outer disk of ionized gas, which has a power law relation between emissivity and radius (Chen & Halpern, 1989). Balmer lines are broadened by electron scattering in the T$< 10^5$K atmosphere of the thin disk which is photoionized.

This model depends on the dimensionless gravitational radius $\xi = r/M$ for black hole mass M and distance from the black hole r. We also define $X = \nu/\nu_0 - 1$, where ν is the observed frequency. The specific intensity is then given as a function of radius by:

$$I(\xi, \nu_e) = \frac{\epsilon_0}{4\pi} \frac{\xi^{-q}}{\sqrt{2\pi}\sigma} e^{(\nu_e - \nu_0)^2/2\sigma^2} \tag{1.12}$$

$$= \frac{\epsilon_0}{4\pi} \frac{\xi^{-q}}{\sqrt{2\pi}\sigma} \exp\big[- \frac{(1 + X - D)^2 \nu_0^2}{2\sigma^2 D^2} \big] \tag{1.13}$$

where the exponential term arises from local turbulent broadening σ, ν_e is the emitted frequency and ν_0 is the rest frequency. The Doppler factor is given by:

$$D = \sqrt{1 - 3/\xi}(1 + \xi^{-1/2}\text{sin } i \text{ sin } \phi)^{-1} \tag{1.14}$$

for the weak field approximation, where ϕ is the azimuthal angle on the disk and i is the inclination angle where 0 degrees is face on and 90 degrees is edge on.

The observed line profile is given by:

$$F_x = \frac{\eta M^2 \nu_0 \text{cos} i}{d^2} \int_{\xi_1}^{\xi_2} \int_{-\pi/2}^{\pi/2} \xi I(\xi, \nu_e) D^3 g(D) d\phi d\xi \tag{1.15}$$

where

$$g(D) = 1 + \xi^{-1}\Big[\frac{2D^2}{D^2 \text{cos} i^2 + \xi(D - \sqrt{1 - 3/\xi})^2} - 1\Big] \tag{1.16}$$

An elliptical variation to the circular disk model was described by Strateva et al. (2003). This adds two parameters: ellipticity e and disk orientation ϕ_0. The distance between disk particles and the black hole has an angular dependence given by:

$$\xi(\phi) = \frac{\xi_0(1 + e)}{1 - e\cos(\phi - \phi_0)} \tag{1.17}$$

for the elliptical case, where ξ_0 is the mean radius. $g(D)$ from the circular model is replaced with:

$$\Psi(\xi, \phi) = 1 + \xi^{-1}\frac{1 - \text{sin} i \,\text{cos}\phi}{1 + \text{sin} i \,\text{cos}\phi} \tag{1.18}$$

The Lorentz factor is:

$$\gamma = 1 - [\frac{e^2 \sin(\phi - \phi_0) + (1 - 2/\xi)(1 - e\cos(\phi - \phi_0))^2}{\xi(1 - 2/\xi)^2(1 - e\cos(\phi - \phi_0))}]^{-1/2} \tag{1.19}$$

and the impact parameter b relating the apparent position of a photon in the observer's frame to its initial trajectory in the disk is given by:

$$\frac{b}{r} \approx \sqrt{1 - \sin^2 i \cos^2\phi}[1 + \frac{1}{\xi}(\frac{1 - \sin i \cos\phi}{1 + \sin i \cos\phi})] \tag{1.20}$$

such that the Doppler factor is given by:

$$\begin{aligned}\frac{1}{D} = \gamma \Bigg[& (1 - \frac{2}{\xi})^{-1/2} - \frac{e \sin(\phi - \phi_0)\sqrt{1 - (b/r)^2(1 - 2/\xi)}}{\sqrt{\xi(1 - 2/\xi)^3[1 - e\cos(\phi - \phi_0)]}} \\ & + \frac{\sin i \sin\phi (b/r)\sqrt{1 - e\cos(\phi - \phi_0)}}{\sqrt{\xi(1 - 2/\xi)(1 - \sin^2 i \cos^2\phi)}} \Bigg]\end{aligned} \tag{1.21}$$

D and g(D) in equation 1.15 can then be replaced to obtain the flux profile as a function of ν for the elliptical model.

Examples of the double–peaked Hα spectra of canonical DPEs Arp 102B and 3C 390.3, and the corresponding RMS spectra, are shown in Figure 1.5. The effects of inclination, disk size and ellipticity on the observed profile are illustrated in Figure 1.6.

Spectroscopic monitoring of DPEs over months to years has revealed that the relative intensity and shape of the blue and red peaks can vary on the dynamical timescale of the accretion disk (Gezari et al., 2007; Jovanović et al., 2010; Lewis et al., 2010; Popovic, 2011; Sergeev et al., 2002; Shapovalova et al., 2013; Storchi-Bergmann et al.,

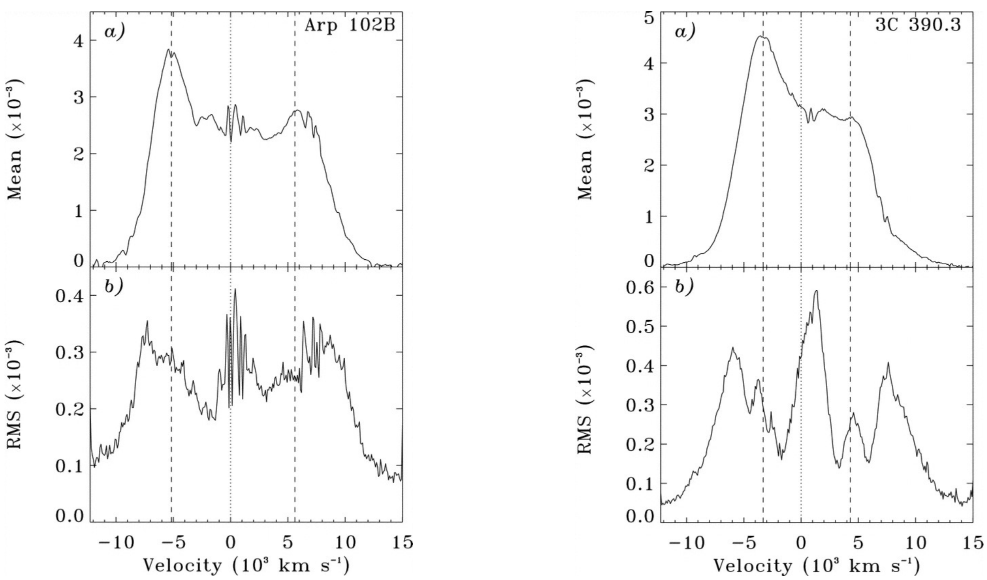

Arp 102B

3C390.3

Figure 1.5: Mean and RMS broad Hα emission line profiles from canonical double–peaked emitters Arp 102B (left) and 3C 390.3 (right), from Gezari et al. (2007). The dashed lines show the central velocities of the red and blue peaks derived from the mean profile. Reproduced by permission of the authors and AAS.

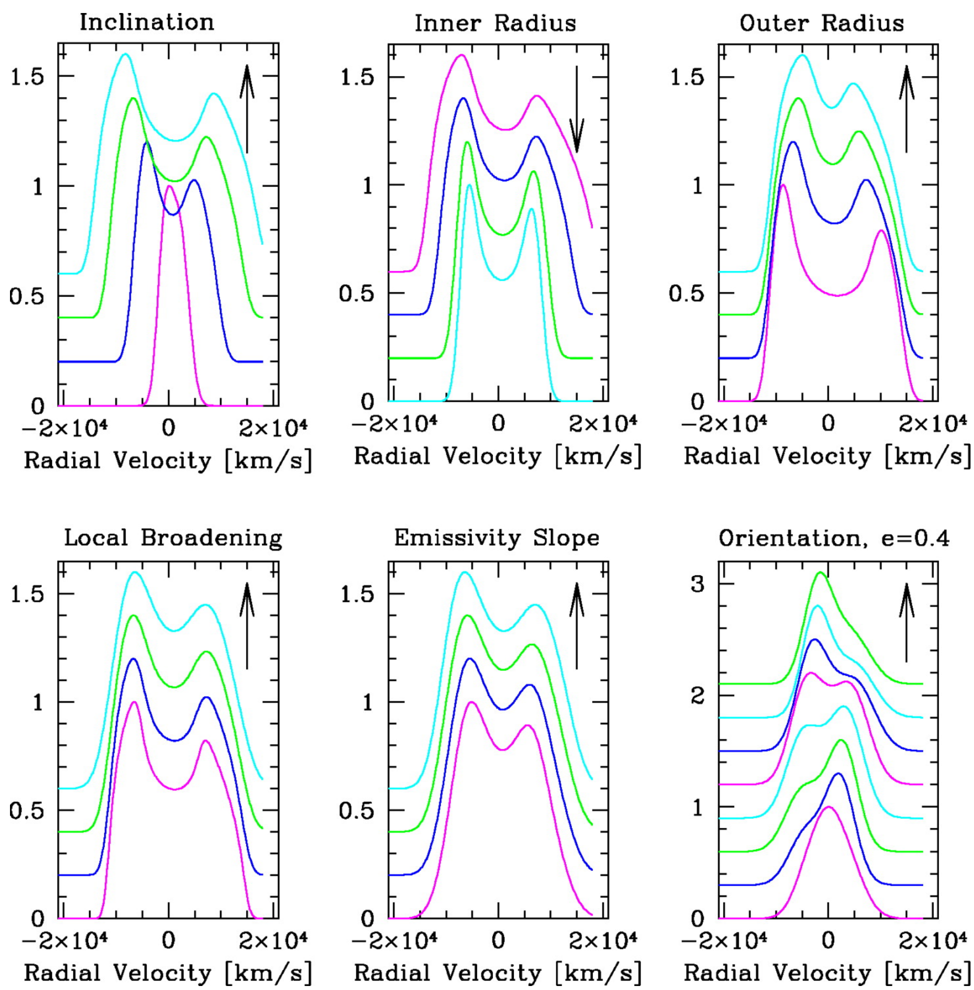

Figure 1.6: Illustration of the effects of disk parameters on the shape of the double–peaked profile, from Strateva et al. (2003). Reproduced by permission of the authors and AAS.

2003). Estimates of DPE fractions amongst the wider broad line AGN population range from $\sim 3 - 30\%$ (Eracleous & Halpern, 1994; Ho et al., 1997; Strateva et al., 2003). Double–peaked profiles are most commonly visible in low luminosity, low–accretion rate AGN (Eracleous & Halpern, 1994; Ho, 2008; Ho et al., 2000), where emission from a central broad line region cannot mask the dip between the peaks. Storchi-Bergmann et al. (2016) predict that double peaked profiles are ubiquitous in broad line AGN, but are only observed when the inclination angle is $> 20°$ so that the separate peaks of the accretion disk are observable, but $\lesssim 37°$ so that the accretion disk emission is not blocked by the obscuring torus. As Gaussian broad lines will also only be observed at inclination angles $\lesssim 37°$, we would therefore expect that 60% of broad line AGN would have visible disk emission, but other factors may reduce this fraction. For example, if the double–peaked component is too weak to be observed when contaminated by star formation emission or the AGN is in a high accretion state so that the contribution from non–disk clouds dominates the broad line emission and fills the dip between the peaks.

In the two–component disk–wind model, it is outflows of subcritical density clouds which produce Gaussian broad line emission while supercritical clouds close to the disk surface produce double–peaked emission. Disk–wind models which explain the observability of double–peaked profiles are supported by reverberation mapping of Seyfert 1 nuclei, which shows that even when the Hβ profiles are not double–peaked, the rms spectra are, implying that the most variable, innermost broad line gas is always in a disk even if we cannot see it in the optical spectra (Denney et al., 2010; Schimoia et al., 2017; Storchi-Bergmann et al., 2016). The disk–wind model may also explain the higher relative luminosity of double–peaked structures to broad line gas in low–luminosity AGN compared to standard Seyfert 1 nuclei (Elitzur et al., 2014; Storchi-Bergmann et al., 2016).

1.2.6 Optical and X-ray variability

The optical and X-ray fluxes of AGN vary stochastically such that light curves of flux vs time can be used to identify and characterize AGN. The power spectral density of optical variability generally follows an f^{-2} power law with a low frequency turnover to white noise at the 'characteristic timescale' or 'damping timescale' denoted τ (Kelly et al., 2009; Kozłowski et al., 2010; MacLeod et al., 2010; Simm et al., 2016; Suberlak et al., 2021), although some AGN optical PSDs exhibit larger power law indices down to $\alpha = -3.3$ (Mushotzky et al., 2011).

The characteristic timescale has been shown to correlate with BH mass according to:

$$\tau = 107^{+11}_{-12}\text{days}\left(\frac{M_{\rm BH}}{10^8 M_\odot}\right)^{0.38^{+0.05}_{-0.04}} \tag{1.22}$$

for BHs in the mass range of $10^4 < M_{\rm BH} < 10^{10}$ and this relation has been found to extend down to the optical variability timescales of accreting $\sim 1 M_\odot$ white dwarfs (Burke et al., 2021).

This relationship between mass and characteristic variability timescale can be understood in terms of the orbital time and the time it takes to restore thermal equilibrium in the accretion disk. These are both dependent on the radius from the BH, and its mass, according to:

$$t_{\rm orb} = 100\left(\frac{M_{\rm BH}}{10^8 M_\odot}\right)\left(\frac{R}{100 R_S}\right)^{3/2} \text{days} \tag{1.23}$$

$$t_{\text{th}} = 1680 \left(\frac{\alpha}{0.01}\right)^{-1} \left(\frac{M_{\text{BH}}}{10^8 M_\odot}\right) \left(\frac{R}{100 R_S}\right)^{3/2} \text{days} \tag{1.24}$$

where $R_S = 2GM_{\text{BH}}/c^2$ and α is the viscosity parameter (Burke et al., 2021). For a constant accretion rate and radiative efficiency, we would expect the effective emitting radius for a given wavelength to scale with mass according to $R \propto M_{\text{BH}}^{2/3}$ and therefore the two timescales to scale with mass as $t_{\text{orb,th}} \propto M_{\text{BH}}^{1/2}$. The location of the disk which drives optical variability is likely at the radius were the UV emission originates (Burke et al., 2021).

In comparison to the optical, AGN X-ray variability is much faster and scales with mass with a slope of ~ 1 (González-Martín & Vaughan, 2012; Körding et al., 2007; McHardy et al., 2006). This likely arises because the X-ray emitting corona is much closer to the SMBH than the UV–emitting accretion disk segment. If the X-ray emission is determined by the orbital and thermal timescales at the innermost stable orbit of the BH, which scales linearly with mass, this would explain the $\tau_{\text{X-ray}}$ vs M_{BH} slope. The relationships between variability timescale and BH mass may provide a way to estimate BH mass via well–sampled optical and X-ray light curves when other methods are not viable.

1.3 Supermassive black hole binaries

1.3.1 Formation of gravitationally bound systems

The efficient formation of a gravitationally bound SMBH binary following the merger of the host galaxies is a key step in understanding BH–galaxy co–evolution. There are a few confirmed active galactic nuclei (AGN) pairs at separations of tens of parsecs to kiloparsecs (dual AGN; see De Rosa et al., 2019, for a summary). It takes a long time for dissipative interactions (such as circumbinary disk torques, stellar slingshots, and dynamical friction) to reduce the SMBH separation from kpc to sub–pc scales (Begelman et al., 1980). Once SMBH binaries reach sub–pc separations, they can coalesce after a short time and are therefore expected to be intrinsically rare. Simulations by Volonteri et al. (2009) predict a density of ~ 0.01 deg^{-2} binaries at $z < 1$, corresponding to a fraction of $< 0.1\%$ of quasars. Sub–pc SMBH binaries are also difficult to detect: a binary of 0.01 pc separation at 100 Mpc would require 0.1 mas angular resolution to resolve. There are only two promising candidate binaries at pc to sub–pc separations where the SMBHs are likely gravitationally bound to one another: radio galaxy 0402+379 with an SMBH separation of 7.3 pc (Bansal et al., 2017; Rodriguez et al., 2006), and the blazar OJ 287 which may be explained by an eccentric SMBH binary with a 0.05 pc semi–major axis (Dey et al., 2019b; Sillanpaa et al., 1988; Stockton & Farnham, 1991; Valtonen, 2007; Valtonen et al., 2008). There are, however, no confirmed binaries at separations of $< 10^{-2}$ pc, the regime where gravitational wave (GW) emission drives sufficient angular momentum loss to lead to SMBH coalescence (Kelley et al., 2017; Merritt &

Milosavljević, 2005; Milosavljević & Merritt, 2003; Rajagopal & Romani, 1995).

SMBH binaries with total masses 10^5–$10^7 M_\odot$ emit GWs within the $\sim 10^{-4}$–1 Hz range where they will be detectable by the *Laser Interferometer Space Antenna* (*LISA*). Holley-Bockelmann et al. (2010) predict that mergers between intermediate–mass BHs and SMBHs at $z < 2$ will be the most common source of SMBH merger signatures in LISA, although mergers between two $\sim 10^5$ IMBHs will also be detectable. Predicted detection rates vary from 0.1 to 175 observed events per year, with more recent studies preferring rates < 1 yr^{-1}, and depend heavily on BH seeding mechanisms, accretion prescriptions, and dynamical binary formation efficiency (Banks et al., 2022; Holley-Bockelmann et al., 2010; Klein et al., 2015; Salcido et al., 2016). Other observational constraints on these factors will assist in making informed predictions for LISA merger rates. Populations of SMBH mergers will also be detectable over the next few years by pulsar timing arrays (Burke-Spolaor et al., 2019; Kelley et al., 2018; Rosado et al., 2015; Taylor et al., 2016). Comparisons of gravitational wave background rates derived from PTAs and GW background rates implied by optically–selected SMBH binary populations can assist in characterizing false positive rates for optical candidates (Sesana et al., 2018).

1.3.2 Observable signatures of accreting SMBH binaries

SMBH binaries may be spectroscopically identifiable if broad Hα and Hβ emission produced by the accretion disks around the individual SMBHs appears at orbital velocities of hundreds to thousands of km s^{-1} relative to the narrow emission line velocity, indicating the presence of orbiting SMBHs. Whether there are one or two velocity–

offset peaks depends on whether one or both SMBHs have detectable broad line gas emission. The velocities and magnitudes of the broad peaks depend on the semimajor axis, mass ratio, eccentricity and phase of the binary (Bogdanović et al., 2008; Nguyen & Bogdanović, 2016; Nguyen et al., 2018). Searches for SMBH binaries with velocity–shifted broad lines in spectroscopic surveys have yielded almost 100 candidates (Boroson & Lauer, 2009; Ju et al., 2013; Shen et al., 2013; Tsai et al., 2013; Wang et al., 2017). However, fitting of orbital models to long term broad line velocity changes has ruled out the binary hypothesis for a substantial fraction of candidates (Doan et al., 2020; Eracleous et al., 1997a; Guo et al., 2019; Liu et al., 2016b, 2014; Runnoe et al., 2015; Wang et al., 2017).

Recent analysis of the population of Illustris binaries of mass between 10^6 and $10^{10} M_\odot$ at $z < 2$ suggests that only 0.5% of binaries will have detectable velocity–offset broad lines, assuming sensitivity to $> 10^3$ km s^{-1} offsets (Kelley, 2020). Given the estimated AGN fraction in binaries of $10^{-2} - 10^{-3}$ (Volonteri et al., 2009), Kelley (2020) estimated that <1 in 10^4 AGN will have have kinematic binary signatures. Low kinematic detectability fractions arise from the trade–off between having sufficiently large orbital velocities for spectroscopic detection and large enough SMBH separations for the broad line gas to remain associated with each individual SMBH (Figure 1.7; Kelley, 2020). This trade–off can be understood as follows. The radius of the individual BH broad–line region is related to its mass and accretion rate by

$$R_{\rm BLR} \sim 0.16 {\rm pc} \left(\frac{M_i}{10^8 M_\odot} \frac{f_{\rm Edd}}{0.1} \right)^{0.59} \tag{1.25}$$

The effective Hill radius of each individual BH, which defines where the gravitational influence of the individual BH dominates over the effect of the companion, is approximated by:

$$\frac{R_{\text{Hill},2}}{a} = 3^{-2/3}\mu_i^{1/3} \tag{1.26}$$

where $\mu_i \equiv M_i/(M_1+M_2)$. Thus we can estimate the minimum binary semi–major axis for the preservation of the smaller black hole's broad line region (BLR):

$$a_{\text{min},2} \equiv 3^{2/3} R_{\text{BLR},2}\mu_2^{-1/3} \tag{1.27}$$

$$\sim 1.9\times 10^{-1}\text{pc}\left(\frac{\mu_2}{0.1}\right)^{0.38}\left(\frac{f_{\text{Edd}}}{0.1}\right)^{0.88} \tag{1.28}$$

and a corresponding minimum orbital period (Kelley, 2020):

$$p_{\text{min}} \sim 770\text{yr}\left(\frac{M}{10^8 M_\odot}\frac{\mu_2}{0.1}\right)^{0.38}\left(\frac{f_{\text{Edd}}}{0.1}\right)^{0.88} \tag{1.29}$$

While spectroscopic searches have looked for velocity–offset and time–varying broad lines as kinematic signatures of a binary, searches for optical periodicity have aimed to find SMBH binaries based on flux modulation alone. Hydrodynamical simulations have shown that torques exerted on the circumbinary gas disk by binary motion modulate the accretion rate, producing observable changes in luminosity depending on the mass ratio of the SMBHs (D'Orazio et al., 2013; Farris et al., 2014; MacFadyen & Milosavljević, 2008; Ragusa et al., 2016; Roedig et al., 2012; Shi & Krolik, 2015). For approximately equal mass ratio binaries, an inner cavity forms at a radius of $\sim 2a$ and an overdensity of material develops at the outer edge of the cavity (D'Orazio et al., 2013; Farris et al., 2014;

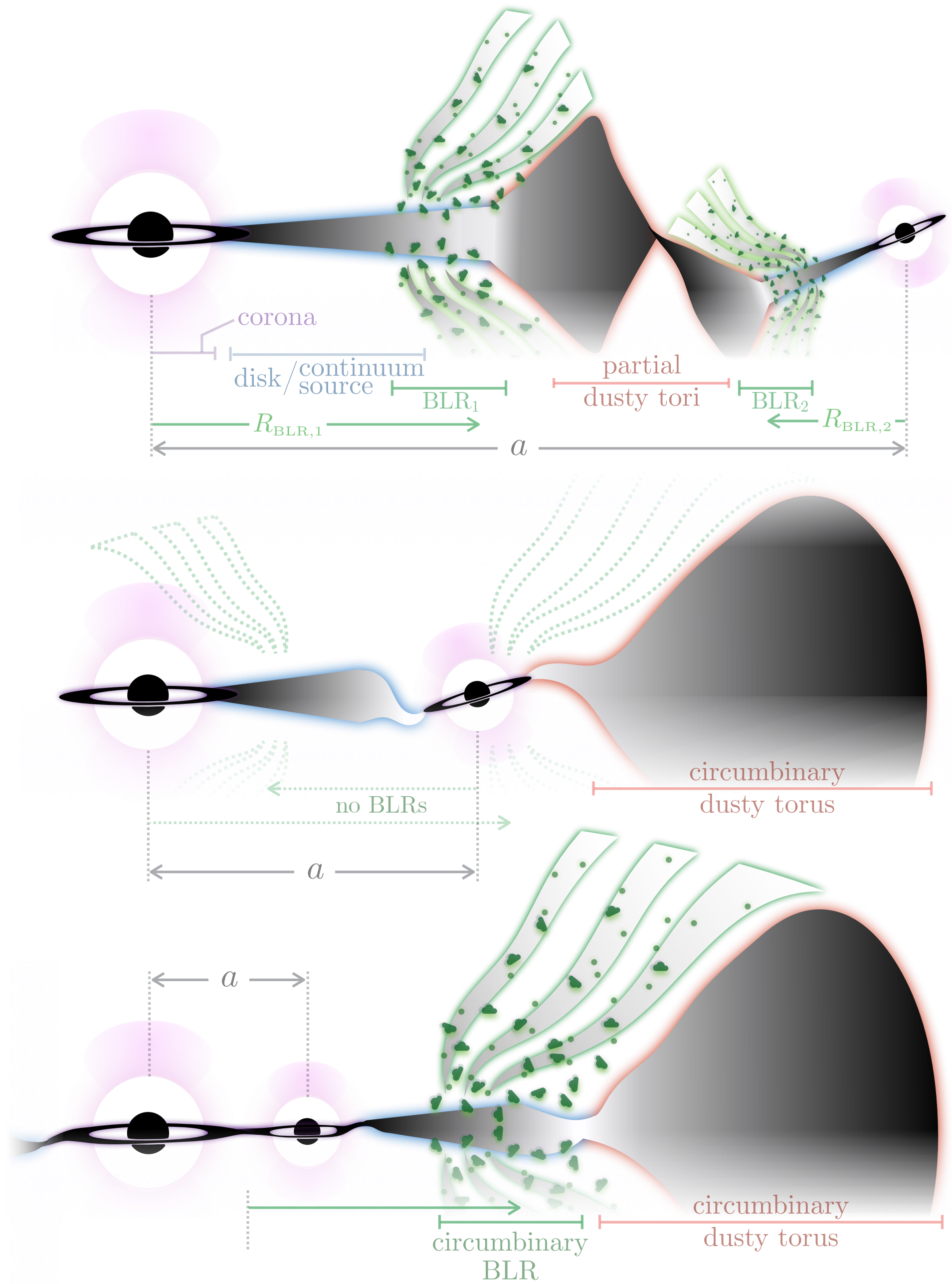

Figure 1.7: Diagram of binary AGN broad line regions and dusty tori in 3 different regimes, from Kelley et al. (2019). Above: When $R_{\mathrm{BLR}} < R_{\mathrm{Hill}} < a$, the BLRs move with the AGN while the dusty tori near the hill radii are partially disrupted. This is the only configuration where velocity–offset BLRs can be detected. `Center:` $R_{\mathrm{Hill}} < R_{\mathrm{BLR}} \approx a$: one or both BLRs can be disrupted by the companion SMBH, and the dusty torus forms part of the circumbinary disk. `Below:` $R_{\mathrm{BLR}} > R_{\mathrm{Hill}}$ where the BLRs and torus make up the circumbinary disk and are not carried with the orbital motion of the individual SMBHs. Reproduced by permission of the authors.

MacFadyen & Milosavljević, 2008; Noble et al., 2012; Shi et al., 2012). The modulation period is set by the Keplerian orbital period at the radius of this overdensity, so is predicted to be 3–8 times the orbital period of the binary (D'Orazio et al., 2013; Kelley et al., 2019). Hydrodynamic variability is expected to produce a sawtooth–shaped light curve (Duffell et al., 2020; Farris et al., 2014; Kelley et al., 2019). Doppler boosting due to large orbital velocities along the line of sight may also produce sinusoidal modulation on the same timescale as the binary orbital period (Charisi et al., 2018; D'Orazio et al., 2015; Kelley et al., 2019). These processes are illustrated in Figure 1.8.

Variability from SMBH binaries may also be observable at infrared wavelengths. Delayed infrared reverberation is observed from normal optically variable AGN when dust in the torus and polar regions reprocesses the ultraviolet and optical continuum emission (Barvainis, 1992; Hönig & Kishimoto, 2011, 2017; Koshida et al., 2014). Similar IR echoes may be observed in the case of SMBH binaries, with the phase and amplitude of IR emission depending on the ratio of dust light crossing time to the optical variability period, the torus inclination, and the opening angle (D'Orazio & Haiman, 2017; Jun et al., 2015). X-ray outbursts are also predicted to occur during pericentric passages (Bogdanović et al., 2008).

The expected optical variability of SMBH binaries on timescales comparable to the orbital timescale has motivated a number of searches for periodic AGN in time domain surveys such as the PanSTARRS Medium Deep Survey, the Catalina Sky Survey and the Palomar Transient Factory. These searches have each yielded tens of candidates with light curves which are better fit by a sinusoidal model than a damped random walk (DRW) model describing typical quasar stochastic variability (Charisi et al., 2016; Graham

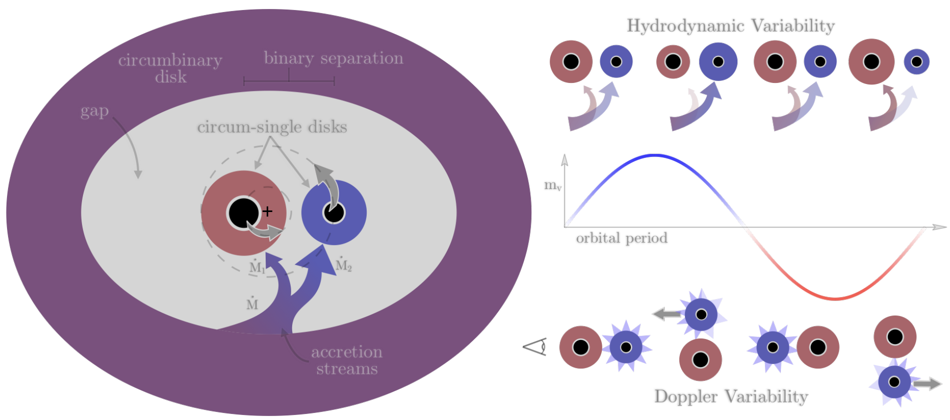

Figure 1.8: `Left:` Diagram of an SMBH binary with single disks around individual SMBHs and a shared circumbinary accretion disk. A gap of radius $\sim 2a$ is formed between the binary and the circumbinary disk. The secondary SMBH receives a larger share of the accretion rate as it is further from the center of mass and passes closer to the circumbinary accretion disk. `Right:` Diagrams of the two possible mechanisms for variability observed over a single orbit. Hydrodynamic variability may arise as relative accretion rates onto the primary and secondary change over orbital phase. Doppler boosting of the faster moving secondary may also produce variability for observers near the orbital plane. Figure from Kelley et al. (2019). Reproduced by permission of the authors.

et al., 2015a,b; Liu et al., 2015, 2016b). Unfortunately, continued monitoring of these candidates tends to provide evidence against the periodic models fitted from the initial few cycles (e.g. Liu et al., 2018a). A number of studies have shown from simulated red noise light curves that 3–4 'false' cycles can frequently arise, and that careful calculation of false positive rates is required to confirm variability–selected binary candidates (Barth & Stern, 2018; Goyal et al., 2018; Liu et al., 2018a; Vaughan et al., 2016). PTA limits suggest that a large fraction of variability survey candidates are false positives (Sesana et al., 2018), as do population estimates based on analysis of the detectable SMBH binary parameter space (Kelley et al., 2019; Krolik et al., 2019).

1.3.3 Gravitational wave recoil as a tracer of SMBH binary spin alignment

Gravitational radiation emitted by merging black hole binaries can induce a recoil velocity on the merged remnant which is given by:

$$\vec{V}_{\text{recoil}}(q,\vec{\alpha}) = v_m\hat{e}_1 + v_\perp(\cos(\epsilon)\hat{e}_1 + \sin(\epsilon)\hat{e}_2) + v_\parallel\hat{e}_\parallel \tag{1.30}$$

$$v_m = A\frac{q^2(1-q)}{(1+q)^5}\left(1 + B\frac{q}{(1+q)^2}\right) \tag{1.31}$$

$$v_\perp = H\frac{q^2}{(1+q^2)^5}\left(\alpha_2^\parallel - q\alpha_1^\parallel\right) \tag{1.32}$$

$$v_\parallel = K\cos(\Omega-\Omega_0)\frac{q^2}{(1+q)^5}|\vec{\alpha}_2^\perp - q\vec{\alpha}_1^\perp| \tag{1.33}$$

where $\hat{a}_i = \hat{S}_i/m_i^2$, $\vec{S}_i$ and m_i are the spin and mass of BH i, q is the mass ratio of the smaller to larger BH, the indices $\parallel$ and $\perp$ describe the components of the orbital angular momentum at merger, $\hat{e}_1$ and $\hat{e}_2$ are the orthogonal unit vectors in the orbital plane, and the constants are $A = 1.2 \times 10^4$ km/s, $B = -0.93$, and $H = (7.3 \pm 0.3) \times 10^3$ km s^{-1} (Campanelli et al., 2007b). Ω is the angle between the in–plane component of $\vec{\Delta} \equiv m(\vec{S}_2/m_2 - \vec{S}_1/m1)$ and the infall direction at merger, and ϵ is the angle between the 'unequal mass' and 'unequal spin' contributions to the recoil velocity in the orbital plane. ϵ depends strongly on the configuration but is $90°$ for head–on collisions. As such, large recoils can occur for mass ratios close to 1 with maximally spinning BHs with spins counteraligned and in the orbital plane. 'Superkick' configurations with BH spins partially aligned to the orbital angular momentum can produce even larger recoil velocities up to 5000 km/s (Lousto & Zlochower, 2011). Simulations of remnant orbits after recoil for a range of velocities indicate that the remnants may orbit outside the potential well for $10^6 - 10^9$ years before falling to the center, and may occasionally be ejected from the host galaxy entirely (Blecha & Loeb, 2008).

The broad line gas around the SMBH with a higher orbital velocity than the recoil velocity is expected to be carried away with the SMBH. The radius of the region containing this gas is given by:

$$\frac{GM_{\rm BH}}{V_{\rm recoil}^2} \sim 1{\rm pc} M_8 \sigma_{200}^{-2} \left(\frac{v_{\rm gas}}{V_{\rm recoil}} \right)^2 \tag{1.34}$$

where M_8 is the BH mass in units of $10^8 M_\odot$ and σ_{200} is the nuclear velocity dispersion in units of 200 km s^{-1} (Campanelli et al., 2007a). When the recoil velocity to escape velocity ratio is $v_{\rm recoil}/v_{\rm esc} < 0.6$–$0.8$, Bondi–Hoyle accretion dominates, but for larger recoil kicks, the gas disk ejected with the SMBH is the main source of gas which will

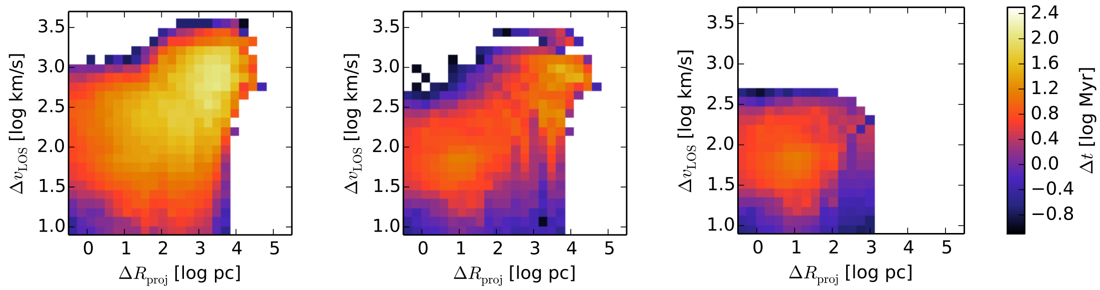

Figure 1.9: The distribution of projected spatial offset vs line of sight velocity for off–nuclear and active recoiling AGN from a population of simulated mergers, from Blecha et al. (2016). The color scale indicates the time the population spends at each spatial offset and velocity. Results are shown for three different spin alignment scenarios: randomly distributed spin alignment (left), a realistic mixture of aligned and misaligned spins (middle) and perfectly aligned spins (right). Velocities > 1000km/s and offsets > 1 kpc are preferred when SMBH spins are randomly aligned, but are not observed when spins are always efficiently aligned. Reproduced by permission of the authors.

be accreted (Blecha et al., 2011). The AGN will be most luminous immediately after a high–velocity recoil or during pericentric passages through a gas–rich remnant, and AGN with kicks > 800 km s^{-1} are expected to be active for a period of $\sim 10^6$ years after recoil (Blecha et al., 2011; Blecha & Loeb, 2008).

As binaries with perfectly aligned spins can produce maximum recoil velocities of only 200 km s^{-1}, while binaries with misaligned spins can produce kicks up to 5000 km s^{-1}, the observed velocities and spatial offsets of a population of recoiling AGN could be used to constrain spin alignment efficiency in populations of SMBH binaries (Figure 1.9; Blecha et al., 2016). A population of recoiling black holes would therefore inform simulations of SMBH spin alignment based on torques in the circumbinary gas disk (Bogdanović et al., 2007; Lodato & Facchini, 2013) and stellar interactions during inspiral (Berczik et al., 2006). As SMBHs which have undergone recoil kicks of $> 0.5v_{\rm esc}$

accrete substantially less mass than SMBHs which remain in their galaxy nuclei, the observed black hole occupation fraction and $M_{\rm BH} - \sigma_*$ relations will be affected by GW recoil if it occurs regularly (Blecha et al., 2011; Volonteri, 2007; Volonteri et al., 2010). It is therefore important to understand how often recoil events occur and what spatial offsets they can produce between ejected SMBHs and their host nuclei.

1.4 Searching for rare AGN populations with time–domain data

The state of the field summarized thus far has introduced a number of open questions about the formation and growth of massive black holes leading to the populations we see today:

- Were the original massive black hole seeds produced by Pop III star, direct collapse, or gravitational runaway channels?
- How efficiently did the initial MBH seeds grow via mergers and accretion to produce the BHs we see today?
- How are disk–emitting AGN different from other broad line AGN, and can they be explained by two–component disk–wind AGN models?
- What fraction of SMBH binaries reach sub–pc separations where GW radiation emission leads to SMBH coalescence?
- How efficiently do SMBH spins align and how often do high velocity gravitational wave recoil events result from mergers?

- Can SMBH binaries be detected via kinematic signatures from broad line gas and optical periodicity, and how often do single disk–emitting AGN arise as false positives in SMBH binary searches?

Answers to these questions are limited by the very small sizes of confirmed populations of low–mass BHs in dwarf galaxies and SMBHs which are cases of GW recoil. They are also limited by biases in the spectroscopic selection of low–mass, off–nuclear and disk–emitting AGN. Time domain data available from ZTF imaging provides a way to address these limitations. Identification of AGN via their variability avoids many biases against low–mass and off–nuclear AGN which are inevitable in spectroscopic surveys, and provides a way to study the accretion states of low–mass AGN, DPEs, and off–nuclear AGN compared to their more typical AGN counterparts.

In this section, I describe how time–domain surveys such as the Zwicky Transient Facility (ZTF) can identify variable objects such as AGN via difference imaging and forward modeling of multi–epoch datasets. By using alert filtering, difference image photometry and forward modeling to make the most of ZTF and other complementary imaging data, this thesis aims to develop strategies for the systematic discovery of populations of rare AGN relevant to the aforementioned questions via their variability. It also aims to study the spectroscopic, multi–wavelength, and optical variability properties of these important AGN populations.

1.4.1 Introduction to image differencing and alert streams with the Zwicky Transient Facility

In the last two decades a number of wide–field time–domain surveys such as the Catalina Real–Time Survey (CRTS; Drake et al., 2009), Palomar Transient Factory (PTF/iPTF; Law et al., 2009), Panoramic Survey Telescope and Rapid Response System (Pan-STARRS; Kaiser, 2004), All Sky Automated Survey for SuperNovae (ASAS-SN; Shappee et al., 2014), and Asteroid Terrestrial–impact Last Alert System (ATLAS; Tonry et al., 2018) have discovered a range of new transient astronomical phenomena within and beyond our galaxy. ZTF is the latest in this series and is an important precursor to the Legacy Survey of Space and Time (LSST) at Vera C. Rubin observatory (Ivezić et al., 2019).

ZTF contains two telescope systems: a wide–field imager on the Palomar 48–inch Oschin (Schmidt) telescope and an integral field unit spectrograph (IFUS) on the Palomar 60–inch telescope (Graham et al., 2019). The new 576 megapixel camera deployed for the ZTF wide–field imager provided a 47 deg^2 field of view, allowing ZTF to observe 3760 deg^2 per hour. It has a 5σ detection limit of 20.5 mag in r- and g-band and 20.0 mag in i-band during single 30 s exposures. The IFUS allows for prompt follow–up and classification of bright transients of magnitude $r < 19$. ZTF averages 300 annual visits per source and a nightly transient detection rate of 1 million alerts, corresponding to a nightly data rate of 1.4TB (Masci et al., 2019; Patterson et al., 2019). The data scale of ZTF is approximately 10% of the upcoming LSST, making it an ideal testing ground for large scale identification and follow–up of the transient sky in preparation for the next decade.

ZTF detects time–varying astronomical phenomena by comparing nightly observations with a static 'reference' image of the sky. A reference image consists of a coadd, or stack–average, of single exposures. In the main ZTF pipeline, reference images are made up of $15-40$ CCD–quadrant images selected to have high quality photometric and astrometric calibrations, good point–source FWHM, and well–estimated pixel noise and background levels which satisfy filter–dependent criteria. While the acceptable FWHM range was set to $2.''0 <$ FWHM $< 3.''5$ to ensure most inputs are better than Nyquist–sampled, lower FWHM images are prioritized so that most input images range from $2.''0 <$ FWHM $< 2.''4$.

ZTF reference images are produced as follows. Global median background levels are subtracted from single epoch images. The images are mapped and resampled onto a footprint with optimal geometry and orientation using `SWarp` (Bertin et al., 2002). The science images are gain–matched by rescaling the photometric zero–points of each image to a fixed target zero–point for each filter. Bad pixels caused by temporary detector artifacts and cosmic rays are removed using outlier–trimmed averaging on each individual pixel stack. A position–dependent point spread function (PSF) is determined for the coadd using `DAOPhot` (Stetson, 1987), which is then applied to detect sources and produce photometry via PSF fitting. `SExtractor` (Bertin & Arnouts, 1996) is then used to generate aperture and isophotal photometry, and a catalog of aperture to PSF–fit photometry corrections is stored. A more detailed description of reference image generation for ZTF can be found in Masci et al. (2019).

Once a reference image is available for a particular CCD–quadrant, image differencing can be applied to single epoch (science) images to search for transient events. Image differencing first requires matching of sources from the PSF–fit photometry catalogs of the reference and science images so that the reference image can be resampled and interpolated onto the science image using `SWarp`. Bad pixels are masked and a smoothly varying differential background image is computed and subtracted from the science image. The `ZOGY` algorithm (Zackay et al., 2016) is then performed for PSF–matching and subtraction of the reference image from the science image. This produces a difference image as well as a match–filtered S/N image which can be used for point–source detection. Detection can be applied to both positive (science − reference) and negative (reference − science) difference images. Examples of two reference, science and difference image trios are shown in Figure 1.10.

When sources are detected from the `ZOGY` data products, an 'alert packet' containing information about the detection is produced for the ZTF Alert Distribution System (Patterson et al., 2019). Each 'packet' contains an alert name, metrics specific to the detected sources, image metadata (including quality metrics), the closest known solar–system object, details about the 3 closest PanSTARRS1 sources and the closest *Gaia* DR1 catalog source, information about previous events detected within the last 30 days within 1.5" of the alert position, and three 63×63 pixel cutouts from the reference, science and difference image. These alert packets are sent to a series of alert 'brokers' which can select alert packets based on criteria about the information they contain (e.g. Nordin et al., 2019a). Selected sources may then become the subject of spectroscopic and multi–wavelength follow–up.

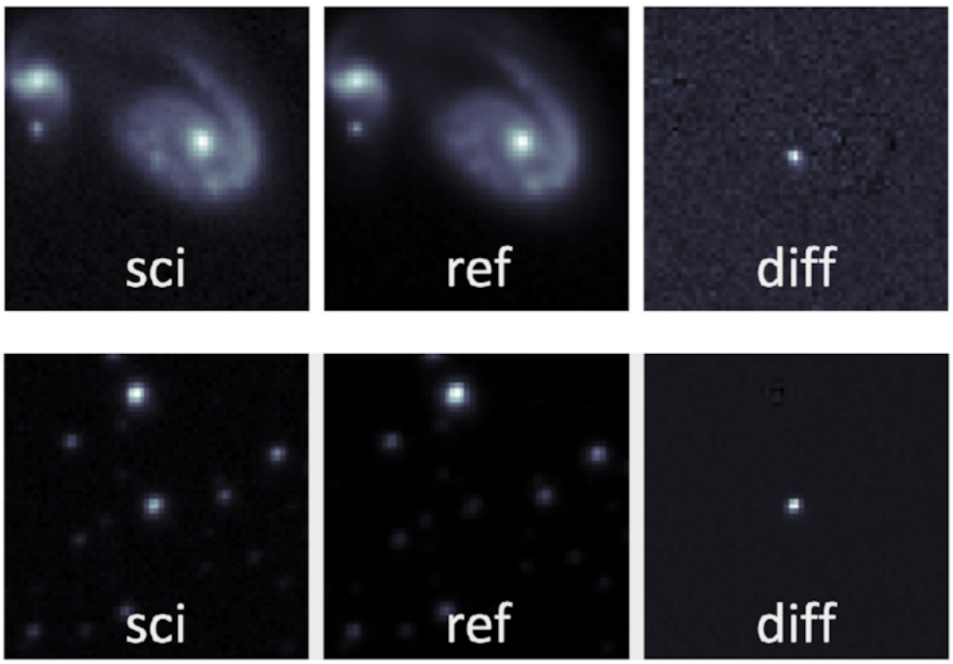

Figure 1.10: Zwicky Transient Facility 63 × 63 pixel cutouts showing the reference image, the single epoch science image, and the subtraction of the two, for a supernova (above) and a variable star (below), from Duev et al. (2019). Reproduced by permission of the authors.

1.4.2 Introduction to forward modeling techniques for joint survey analysis

Forward modeling is an alternative approach to image differencing for the detection of sources and determination of their fluxes. `The Tractor` (Lang et al., 2016) is a piece of software which implements this approach by producing models of pixel–level data for optimized source extraction and characterization. `The Tractor` produces a full generative model that includes image calibration parameters such as the PSF shape and the sky background along with the parameters of the sources in the images (their positions, shapes, and fluxes). If the model is correct, the resulting pixel–space prediction of the images should differ from the images only by noise. Assuming independent noise between pixels, the log–likelihood of the observed data given the model is the negative chi–squared difference: (image – model) / noise. By minimizing this log–likelihood, the software can generate models of images and infer properties of the sources they contain.

The forward modeling approach offered by `The Tractor` allows for the generation of source models from images of differing PSFs and pixel sizes. It was used to produce models from combined BASS, MzLS, DECaLS and WISE data making up the Legacy Surveys, allowing for rigorous treatment of the differing imaging data (Dey et al., 2019a). It was also used for photometry of 400 million objects in low resolution mid–IR *WISE* imaging using high resolution source catalogs derived from optical SDSS data (Figure 1.11; Lang et al., 2014). In the combined WISE–SDSS analysis, `The Tractor` was able to measure the mid–IR flux of sources with W1 magnitudes $17 < W1 < 25$, where the efficiency of the ALLWISE catalog drops

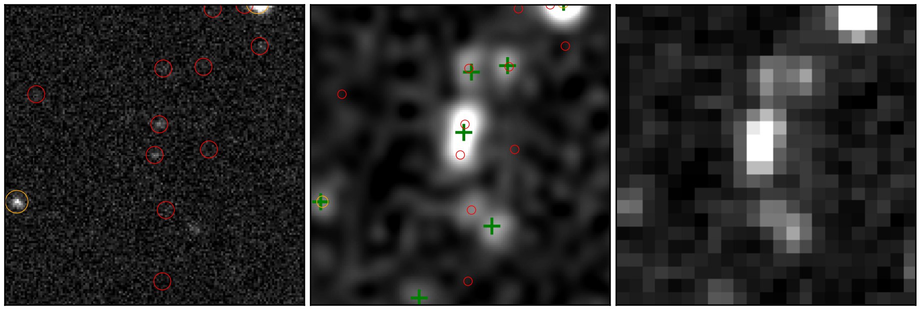

Figure 1.11: Example of an SDSS image (left), the smoothed model for the WISE image produced by `The Tractor` using an initial source catalog derived from the SDSS model (middle), and the corresponding WISE image (right), demonstrating how `The Tractor` can use forward modeling to fit the fluxes of blended sources, from Lang et al. (2014). Red circles show the positions of sources identified in the original SDSS image. Reproduced by permission of the authors and AAS.

sharply. Generative forward modeling of images from multiple surveys is a powerful tool for deblending in crowded fields (Melchior et al., 2021, 2018). Advanced deblending techniques for photometry will become particularly important as surveys become more sensitive: the depth of LSST is such that 63% of galaxies will have overlapping objects affecting their photometry (Melchior et al., 2021). This thesis therefore aims, in part, to demonstrate the utility of forward modeling techniques adapted for time–domain survey data.

1.5 Scope of the dissertation

This thesis sets out to search for rare and important AGN which can inform our understanding of MBH seeding and merger–driven growth amongst the larger AGN population using time–domain data from the Zwicky Transient Facility. In Chapter 2, I present a systematic search for off–nuclear AGN in ZTF in order to find active AGN in galaxy mergers and candidates for gravitational wave recoil from SMBH binaries. In

Chapter 3, I present a search via optical and mid–IR variability for low–mass AGN in dwarf galaxies which can distinguish between alternative MBH seeding channels, and compare the effectiveness of variability selection to other spectroscopic approaches. In Chapter 4, I present a population of variable double–peaked disk–emitting AGN from ZTF and analyze their kinematic signatures and time–domain power spectra within the context of SMBH binary search strategies and a previously discovered DPE which was considered to be an imminent SMBH merger. In Chapter 5, I discuss how the analysis applied to ZTF data in this thesis lays the groundwork for vastly more sensitive searches for off–nuclear and low–mass AGN with the Legacy Survey of Space and Time over the next decade. In Chapter 6, I summarize the observational and computing facilities which enabled this thesis work, and describe software developed and implemented for this research.

Chapter 2: A search for off–nuclear AGN from recoiling SMBHs and ongoing galaxy mergers with the Zwicky Transient Facility

2.1 Overview

A supermassive black hole (SMBH) ejected from the potential well of its host galaxy via gravitational wave recoil carries important information about the mass ratio and spin alignment of the pre–merger SMBH binary. Such a recoiling SMBH may be detectable as an active galactic nucleus (AGN) broad line region offset by up to 10 kpc from a disturbed host galaxy. In this chapter, I describe a novel methodology using forward modeling with `The Tractor` to search for such offset AGN in a sample of 5493 optically variable AGN detected with the Zwicky Transient Facility (ZTF). I present the discovery of 9 AGN which may be spatially offset from their host galaxies and are candidates for recoiling SMBHs. Five of these offset AGN exhibit double–peaked broad Balmer lines which may arise from unobscured accretion disk emission and four show radio emission indicative of a relativistic jet. The fraction of double–peaked emitters in our spatially offset AGN sample is significantly larger than the 16% double–peaked emitter fraction observed for ZTF AGN overall. In our sample of variable AGN we also identified 52 merging galaxies, including a new spectroscopically confirmed dual AGN.

Finally, we detected the dramatic rebrightening of SDSS1133, a previously discovered variable object and recoiling SMBH candidate, in ZTF. The flare was accompanied by the re–emergence of strong P–Cygni line features indicating that it may be an outbursting luminous blue variable star.

2.2 Introduction

Supermassive black holes (SMBHS) reside in the center of most galaxies (Ferrarese & Ford, 2005; Kormendy & Richstone, 1995). As I described in Chapter 1, galaxy growth via hierarchical mergers therefore results in the formation of SMBH binaries. The time taken for these SMBH binaries to merge depends on the nature of their host galaxies. While binaries in gas–poor galaxies may stall at 1 pc separations (e.g. Milosavljević & Merritt, 2001), SMBH binaries in gas–rich environments may merge on timescales of $10^6 - 10^7$ years (Escala et al., 2005).

A consequence of SMBH mergers in gas–rich environments may be the gravitational wave recoil of coalesced SMBHs after merger (Section 1.3.3). In this process, the asymmetric emission of gravitational waves during SMBH coalescence imparts momentum to the coalesced black hole, ejecting it from the central potential well to wander about the galaxy halo for 10^6 to 10^9 years (Blecha & Loeb, 2008; Campanelli et al., 2007b; Loeb, 2007; Volonteri & Madau, 2008; Volonteri & Perna, 2005). The 'recoiling black hole' is expected to carry broad line gas with it and continue to undergo regulated accretion, allowing it to be observable as an active galactic nucleus (AGN) spatially offset from the center of its host galaxy (Blecha & Loeb, 2008). Simulations by

Volonteri & Madau (2008), for example, show that an AGN with a 500 km/s kick velocity could still be accreting and observable as an off–center quasar at 30 kpc from its host center.

Other observable signatures of a recoil event include evidence of recent galaxy merging activity. Since the recoiling AGN may continue to accrete for a 10^6 year timescale after recoil (Blecha & Loeb, 2008), tidal structures may still be visible while the recoiling SMBH is active and detectable. The ejected AGN could also leave behind a trail of feedback evidence in the form of enhanced Hα emission leading to the galaxy centre (Loeb, 2007).

Simulations show that the recoil velocity and maximum host–AGN spatial offset of the recoiling SMBH depends on the mass ratio and spin alignment of the black hole binary prior to merger (Blecha et al., 2016; Campanelli et al., 2007b). Binaries with perfectly aligned spins can produce a maximum recoil velocity of only 200 km s^{-1}. A binary with misaligned spins can produce kicks up to 5000 km s^{-1}. A population of recoiling black holes would therefore provide strong constraints on the distribution of masses and spins in SMBH binaries. This would, in turn, inform simulations of SMBH spin alignment (Berczik et al., 2006; Bogdanović et al., 2007; Lodato & Facchini, 2013).

A confirmed sample of recoiling SMBHs could be used to test the predictions of numerical relativity simulations on the fraction of massive black holes ejected via recoil from their host galaxies at different redshifts and the effects of this on observed black hole occupation fractions and the $M_{\rm BH} - \sigma_*$ relation (Blecha et al., 2011; Volonteri, 2007; Volonteri et al., 2010). Such a sample would also allow us to study the effect of displaced AGN feedback on the evolution of merger remnants, such as the expected increase in star formation rates and lengthening of the starburst phase (Blecha et al., 2011).

Despite the many motivations to search for recoiling SMBHs, only a few good candidates have been found to date. One such object is the radio–loud QSO 3C 186 which has an 11 kpc spatial offset from its host galaxy and a -2140 ± 390 km s^{-1} velocity offset between the broad and narrow emission lines (Chiaberge et al., 2017). The tidal features of the host galaxy indicate recent merger activity. Integral field spectroscopy was performed to study the complex kinematics and determine if the velocity offset could result from a peculiar outflow (Chiaberge et al., 2018). The results were consistent with the recoiling SMBH scenario but final confirmation will require both James Webb Space Telescope IFU spectroscopy to map the Hβ region with 0.1” resolution and deep imaging from HST to rule out the presence of a second low–mass galaxy (Chiaberge et al., 2018).

SMBH recoil may also be the origin of the variable object SDSS J113323.97+550415.8 (SDSS1133) (Koss et al., 2014). This object is 800 pc from the center of a low redshift dwarf galaxy and has displayed AGN–like stochastic variability over > 63 years. However, AGN–like variability can be mimicked by long–lived stellar transients (Burke et al., 2020b) and giant stellar outbursts or supernovae such as SN2009ip (Maza et al., 2009) and UGC 2773 OT2009–1 (Boles, 2009). Spectra of SDSS1133 show the presence of blue–shifted Balmer absorption lines and [Fe II] λ7155 and [Ca II] $\lambda\lambda$ 7291, 7324 forbidden emission lines which are highly unusual for an AGN. It is therefore possible that SDSS1133 is a luminous blue variable (LBV) star continuing to demonstrate non–terminal outbursts (Koss et al., 2014).

The lack of many recoiling SMBH candidates has motivated a number of systematic searches for offset AGN using different techniques. A Gaia analysis of a sample of low redshift, unobscured broad line AGN from SDSS showed that at least 99% were within 1 kpc of the host, 90% within 500pc and 40% within 100 pc (Shen et al., 2019). This study used a technique called varstrometry (Hwang et al., 2020) to measure AGN–host spatial offsets via the astrometric jitter of the photocenter induced by the AGN flux variability, allowing them to rule out the existence of a substantial offset AGN population on 10 pc to 1 kpc scales at redshifts $0.3 < z < 0.8$.

From this study, it appears that unobscured, accreting, recoiling SMBHs with $>$ 10 pc separations must be very rare at low redshifts, if they exist. This may be because SMBH spin alignment is always very efficient, inducing only small velocity recoils with small maximum separations. Recoiling black holes may also be more common in the early universe due to higher merger rates and lower galaxy masses. Cold gas inflow during merger may increase the required escape velocity for many galaxies and gas drag could play a role in keeping recoiling black holes close to the galaxy center (Blecha et al., 2016). The level of accretion may be too small for recoiling SMBHs to be detectable and offset AGN may be frequently obscured by the gas environment induced by the merger (Shen et al., 2019).

While these results appear discouraging, another systematic search by Lena et al. (2014) undertook careful isophotal modeling of archival HST images of 14 nearby core elliptical galaxies and found that 10 of the 14 had small $\sim 1 - 10$ pc displacements between the AGN and host galaxy center, 6 of which were considered confident detections because the galaxy profiles were not asymmetric. 4 of the 6 galaxies showed alignment between the AGN–photocenter displacements and the radio jet axis. This correlation is predicted for gravitational recoil of SMBHs but may instead indicate that the spatial offset was induced by radio jet acceleration of the SMBH. This radio axis correlation would not be produced by interactions with massive perturbers or orbital motion prior to SMBH binary coalescence (Lena et al., 2014).

Other searches have used a multi–wavelength approach to successfully find offset AGN candidates. Skipper & Browne (2018) searched for radio–optical spatial offsets in a sample of 345 SDSS galaxies with nearby compact radio sources detected in the Cosmic–Lens All Sky Survey (CLASS) catalogue, finding 3 sources with offsets greater than 0.6 arcseconds. Condon et al. (2017) found one offset AGN candidate amongst 492 radio point sources from the NRAO VLA Sky Survey (VLASS; Condon et al., 1998) when crossmatched to extended sources in the Two Micron All–Sky Survey (2MASS) Extended Source Catalog (Jarrett et al., 2000).

A recent study by Reines et al. (2020) found that the majority of a sample of 13 radio AGN in dwarf galaxies were off–nuclear, likely because the lower escape velocities in dwarf galaxies make it easier for black holes to wander from the central potential. Kim et al. (2017) found a recoiling SMBH candidate in a systematic search for spatially offset X-ray AGN in a sample of 2542 sources with optical/near–infrared counterparts in archival HST images from the *Chandra* Source Catalogs – Sloan Digital Sky Survey Cross–match Catalog (Evans et al., 2010; Rots & Budavári, 2011).

Even though these search strategies have yielded some recoiling SMBH candidates, there are many challenges to confirming the nature of these objects. Candidates with broad line gas at $> 1000\,\mathrm{km\ s^{-1}}$ velocities relative to narrow emission lines but no observable AGN–host spatial offset can often be explained by outflowing winds (Allen et al., 2015; Robinson et al., 2010), scattered broad line emission from an SMBH binary

(Robinson et al., 2010), asymmetric double–peaked emission from an elliptical accretion disk (Steinhardt et al., 2012), or two superposed AGN (Shields et al., 2009a,b).

When confirming that AGN which are spatially offset from their host galaxy nuclei have undergone GW recoil, it must be ruled out that they are not in fact AGN with a barely visible, undermassive host which is undergoing a merger with the larger galaxy (Chiaberge et al., 2017). In this case, the true host galaxy may be on the lower end of the luminosity – SMBH mass scaling relation (McLure & Dunlop, 2002) and very compact such that the extended galaxy emission around the QSO is not detectable, resulting in a false association with the brighter, offset companion galaxy in a merging system. This can occur when the AGN's host galaxy was tidally stripped as it merged with the larger galaxy (Bellovary et al., 2010) and has been proposed as the nature of the Jonker et al. (2010) recoiling SMBH candidate and the origin of a number of off–nuclear ultraluminous X-ray sources such as HLX–1 (Farrell et al., 2009). Compact dwarf galaxies hosting SMBHs may be very common at low redshifts. Four ultra–compact dwarf galaxies with masses $M > 10^7 M_\odot$ in the Virgo and Fornax clusters have been shown to host SMBHs through analysis of their velocity dispersion and mass profiles (Afanasiev et al., 2018; Ahn et al., 2017, 2018; Seth et al., 2014). These systems were likely produced through tidal stripping of a larger galaxy hosting an SMBH. Voggel et al. (2019) estimate that such stripped nuclei may host 8% to 32% of local SMBHs.

AGN in merging galaxies also have typical relative velocities of $10 - 400$ km s^{-1} (Comerford & Greene, 2014; Comerford et al., 2009; Liu et al., 2018b) and these velocities are comparable to the predicted velocities of recoiling SMBHs from spin–aligned binaries. Comerford & Greene (2014) estimate that 4% to 8% of Type 2 AGNs are in galaxy mergers, so these systems may be quite common. Triple SMBH systems, in which a merger with a third galaxy occurs before the initial SMBH binary forms, can also be difficult to distinguish from recoiling SMBHs (Civano et al., 2010; Kalfountzou et al., 2017).

Offset AGN in merging galaxies are nonetheless important to find because they provide a way to study AGN fueling by galaxy merger triggered gas inflows (Canalizo & Stockton, 2001; Surace et al., 1998; Treister et al., 2012). The increased incidence of galaxy mergers amongst X-ray selected AGN and increasing X-ray luminosity with decreasing AGN separation in dual AGN suggests that black hole accretion peaks during the merging process (Koss et al., 2012). Comerford & Greene (2014) also found that the fraction of AGN in galaxy mergers increases from 0.7% to 6% over the AGN bolometric luminosity range of $43 < \log(L_{bol})$[erg/s] < 46 which suggests that galaxy mergers trigger high luminosity AGNs. High–resolution hydrodynamical simulations by Van Wassenhove et al. (2012) predict that AGN triggering and the likelihood of dual AGN activity is strongest at < 10 kpc separations and that most merger–triggered AGN activity is non–simultaneous such that 90% of SMBHs in mergers appear as single or offset AGN instead of dual AGN at $L_{\rm bol} > 10^{44}$ erg s^{-1} and separations $> 1 - 10$ kpc. These predictions are supported by observations of the relative occurrence of offset vs dual AGN (e.g. Comerford et al., 2009). Discoveries of AGN in tidally stripped dwarf galaxies in mergers may also yield IMBH candidates which can be used to constrain models of BH seed formation in the early universe (e.g. Reines & Comastri, 2016; Volonteri & Natarajan, 2009).

Discoveries of AGN in mergers have occurred both serendipitously and in targeted searches. Binary AGN were found in X-ray imaging spectroscopy of ultraluminous infrared galaxy NGC 6240 (Komossa et al., 2003) and Mrk 739, a galaxy with two optically distinguishable bulges (Koss et al., 2011). A search for AGN companions to a sample of ultra–hard X–ray–selected AGNs from the all–sky Swift Burst Alert Telescope (BAT) survey with Chandra, XRT and XMM imaging combined with emission line diagnostics with SDSS and Gemini spectroscopy revealed 16 dual AGN (Koss et al., 2012).

Many searches for AGN in mergers on $< 10\,$kpc scales have looked for double peaked narrow [O III] λ5007 emission lines in large spectroscopic datasets such as SDSS (e.g. Liu et al., 2010; Smith et al., 2010; Wang et al., 2009; Xu & Komossa, 2009). Comerford & Greene (2014) found 351 offset AGN candidates amongst a sample of 18,314 Type 2 AGNs by measuring velocity offsets between the forbidden and Balmer emission lines relative to the stellar absorption lines. Fu et al. (2011a) found 16 dual AGN candidates with high–resolution near–infrared images of 50 double–peaked [O III] λ5007 AGNs and one of these was confirmed as a kpc scale binary AGN with high resolution radio images (Fu et al., 2011b).

Searches for dual AGN via X-ray, radio, and optical imaging suffer from different selection effects, and there are ongoing efforts to understand the affects of AGN obscuration by gas and dust during merger (Glikman et al., 2015; Kocevski et al., 2015; Koss et al., 2011). Koss et al. (2018) found that obscured luminous black holes, with X-ray emission but not visible broad $H\beta$ lines, were significantly more likely be in a later stage nuclear merger than a comparable sample of inactive galaxies.

The lack of a large sample of dual AGN and even a small sample of confirmed recoiling SMBHs motivates the development of new search strategies to find AGN offset from their host galaxies and from companion galaxies. A large transient survey which identifies offset AGN candidates via their variability provides one such approach.

In this chapter we present a new method for a systematic search for offset AGN – both recoiling SMBHs and AGN in galaxy mergers – using the Zwicky Transient Facility (ZTF; Bellm et al., 2019a; Dekany et al., 2020; Graham et al., 2019). In Section 2.3, we present our techniques for filtering ZTF transients to make a sample of 5493 optically variable AGN. We present a new version of `The Tractor` forward modeling software for confirmation of AGN–host spatial offsets and describe the candidate selection strategy used to obtain 9 offset AGN candidates and 52 AGN in mergers. In Section 2.4, we describe the multi–wavelength and spectroscopic properties of these new samples and present the rebrightening of the previously discovered recoiling SMBH candidate SDSS1133.

2.3 Sample selection

2.3.1 The Zwicky Transient Facility

The Zwicky Transient Facility (ZTF; Section 1.4.1) is a wide–field optical transient survey which provides three important advantages in a systematic search for off–nuclear AGN via their variability. Firstly, ZTF enables us to discover new AGN by applying light curve modeling techniques to new transients and identifying AGN–like stochastic variability. Light curve modeling of variable sources to find previously undiscovered AGN has been demonstrated for SDSS Stripe 82 difference imaging and for transients in the Palomar Transient Factory (Baldassare et al., 2018, 2020b).

Secondly, image subtractions containing the AGN can be used to locate the position of AGN–like variability relative to the host galaxy. Because spectroscopic surveys tend to have large plate sizes (for example, the SDSS spectroscopic plate size is 1.49”), it can be difficult to confirm that the location of the AGN broad lines is associated with an offset point source. By detecting AGN–like variability from an offset point source, we can confirm the spatially offset nature of AGN candidates.

Finally, the sky coverage of ZTF allows us to search a very large area for offset AGN, which is important given the apparent rarity of $> 10\,\mathrm{pc}$ spatial offset recoiling SMBHs at low redshifts.

2.3.2 Selection of variable AGN in ZTF

We obtain our sample of variable AGN using data from the ZTF alert stream (Patterson et al., 2019). The ZTF pipeline produces approximately 100,000 alerts every night, so we implement a filter with the alert broker and analysis framework `AMPEL` (Alert Management, Photometry and Evaluation of Lightcurves; Nordin et al., 2019a) to detect variable AGN amongst other transient phenomena.

Our method to filter out poor subtractions, moving sources and variable stars and find only extragalactic transients is similar to the approach used in the Tidal Disruption Event (TDE) filter of van Velzen et al. (2021). We apply a liberal cut of < 0.8 on the star–galaxy score (Tachibana & Miller, 2018) to find transients associated with galaxies, and a cut of < 0.3 on the real–bogus score (Duev et al., 2019; Mahabal et al., 2019) to remove bogus transients. We remove objects in busy stellar fields by crossmatching to the Gaia and PanSTARRS catalogs with `catsHTM` (Soumagnac & Ofek, 2018) to ensure that there are no more than 30 Gaia objects and 100 PanSTARRS objects within a 15" radius. We also require at least 3 significant detections > 0.01 days apart and a minimum flux increase of 2.5 magnitudes.

This filtering strategy primarily finds two kinds of common extragalactic transient: supernovae and variable AGN. To select AGN and remove supernovae within the `AMPEL` filter, we require that our transients either match an object in a series of AGN catalogs or have variability which is more characteristic of an AGN than a supernova. We use `catsHTM` and `Extcats`[1] look for a 2" crossmatch with objects in The Million Quasar Catalog (Flesch, 2015), a machine learning based catalog of photometric AGN candidates (Brescia et al., 2015), and a catalog of 720,961 variable sources from the Palomar Transient Factory (PTF) and intermediate Palomar Transient Factory (iPTF) found between 2009 and 2016 which were not classified as a star (Miller et al., 2017) and had > 5 detections over > 24 hours.

For sources which do not have an AGN catalog crossmatch, we model their full ZTF light curve history within the `AMPEL` filter. We use the `SNCOSMO` supernova modeling tool (Barbary et al., 2016) to fit the 'salt2' SN Ia model to the g and r band light curves and extract the reduced χ^2_{SN} goodness of fit for the best fit SN Ia model.

For comparison to the SN Ia goodness of fit, we implement the Butler & Bloom (2011) quasar modeling routine. This routine calculates the structure function for input light curves and compares this to the ensemble quasar structure function for Sloan Stripe

[1]https://github.com/MatteoGiomi/extcats

82 g- and r-band AGN light curves. The goodness of fit of the ensemble structure function model χ^2_Q gives a measure of how likely the ZTF light curve shows AGN–like variability.

The Butler & Bloom (2011) routine also calculates the reduced χ^2 for the null hypothesis that the source shows non–AGN like variability (such as from a variable star). We denote this as χ^2_{Q0}. For the purposes of separating AGN from supernovae, we found that AGN generally have much lower χ^2_{Q0} values than χ^2_{SN}, so this variability statistic was also effective at separating SN from AGN.

Our filter accepted any source where either the g- or r-band light curve had a χ^2_Q or χ^2_{Q0} value less than the SN Ia goodness of fit χ^2_{SN}. Based on tests with a sample of 111 spectroscopically classified supernovae with > 20 ZTF epochs, we determined that this method removes approximately 95% of SN Ia and 60% of Type II supernovae. With a sample of 166 spectroscopically confirmed AGN with $20 - 100$ ZTF epochs, we were able to classify 80% correctly.

Objects which pass either the AGN crossmatch criteria or light curve fitting criteria pass the `AMPEL` filter and are pushed to the GROWTH Marshal science portal for arrangement of spectroscopic followup (Kasliwal et al., 2019). The AGN candidates are then confirmed either with existing SDSS spectroscopy, follow–up spectroscopic observations with the DeVeny spectrograph on the Lowell Discovery Telescope, or by their WISE color or variability history. To classify AGN based on their WISE W1–W2 color we use the criteria:

$$W1 - W2 > 0.662 \exp\{0.232(W2 - 13.97)^2\} \tag{2.1}$$

from Assef et al. (2013), and to classify AGN based on significant variability in their WISE light curve we require the χ^2 relative to a flat light curve to satisfy $\chi^2/\mathrm{dof} > 10$.

We apply this procedure to ZTF alerts from a 2.5 year period between 2018-01-01 to 2020-07-06 and obtain a sample of 5493 AGN. This constitutes our final sample of strongly variable ZTF AGN with spectroscopic or WISE color/variability confirmation.

2.3.3 Selection of AGN spatially offset from their host galaxy

2.3.3.1 Image modeling with `The Tractor`

In order to model the positions of the variable AGN relative to their host galaxy, we apply `The Tractor` (Lang et al., 2016) to forward model the host galaxy profile and transient point source emission across ZTF images. `The Tractor` forward models in pixel space by parametrizing the astrometry solution, sky noise and point spread function of each image and modeling this simultaneously with the shape, flux and position of each source across images in multiple bands and surveys.

We developed a version of `The Tractor` to fit a host galaxy profile and an overlapping point source with a position in or around the host. The point source position and the host galaxy shape, flux and position are assumed constant over all epochs, while the point source flux may vary across single epochs. The version of `The Tractor` that we apply determines the best fitting one of two galaxy profile models: a pure de Vaucouleurs profile described by $I(r) = I_0 \exp(-7.67[(r/r_e)^{1/4}])$ and a pure exponential profile described by $I(r) = I_0 \exp(-1.68r/r_e)$. `The Tractor` is a highly advantageous tool for this analysis because it allows for forward modeling across images of different bands and different instruments. ZTF images taken when the transient is bright can be simultaneously modeled with higher resolution, deeper images from a different telescope to improve modeling of the host galaxy. Subtraction of the model from the coadded data can also help to reveal irregularities in galaxy structure in the residuals.

We model 3422 out of the sample of 5493 AGN with `The Tractor`. Due to limitations with archival storage of ZTF images on our filesystem and the availability of overlapping Legacy Survey (Dey et al., 2019a) and PanSTARRS (Chambers et al., 2016) images for astrometric source matching, we do not model the remaining 2071. As the AGN are isotropically distributed in the sky, choosing to model a subset of the full sample with `The Tractor` does not introduce any biases with respect to the distribution of host–AGN offsets.

We remove 126 of the 3422 AGN because they are duplicates of existing AGN in the sample. The ZTF alerts for particular transients sometimes demonstrate such a large scatter in position that they are considered to be 2 or 3 different transients with separate ZTF names by the alert pipeline. As such, the alerts associated with a single transient can be distributed across 2 or 3 different transient objects. By applying an 8" cone search to all AGN which pass our `AMPEL` AGN filter, we find transients which are associated with one another and select the transient ID with the most alert packets containing real detections.

We model the sample of 3296 unique AGN by selecting the 30 ZTF g- and r-band images taken closest to peak magnitude. This allows us to reach a median depth in AB magnitude of 22.4 in the r-band and 22.2 in the g band. We chose to model only 30 ZTF images due to computational and time constraints, but future work could model the whole sample with `The Tractor` to greater depths by modeling larger numbers of ZTF images and including higher resolution, deeper DECam imaging.

Of our 3296 AGN, 186 do not have sufficient S/N in the 30 ZTF images to model a host galaxy and point source with `The Tractor` above the limiting magnitude. This leaves 3110 objects with measured AGN–host offsets.

2.3.3.2 Determination of statistically significant spatial offsets

Since the ZTF camera has 1" pixels but much of the simulated recoiling black hole population is only observable at sub–arcsecond AGN–host spatial offsets, it is important to understand the positional accuracy that can be obtained from ZTF image subtractions.

In order to determine which AGN–host spatial offsets are statistically significant, we studied the distribution of offsets from the sample of 3110 objects with host galaxy and point source positions determined by simultaneously modeling 30 g- and r-band ZTF images with `The Tractor` (see Section 2.3.1). If the uncertainties in observed RA and Dec of the host galaxies are normally distributed with standard deviation σ_{ref}, and the uncertainties in observed RA and Dec of the variable point sources are normally distributed with standard deviation σ_{sci}, the radial distribution of spatial offsets between them will follow a Rayleigh distribution with $\sigma_{\mathrm{R}}^2 = \sigma_{\mathrm{ref}}^2 + \sigma_{\mathrm{sci}}^2$.

In a study of radio AGN from the Cosmic–Lens All Sky Survey (CLASS) catalogue, Skipper & Browne (2018) found that the population of offsets between the radio AGN and optical galaxies in SDSS followed a mixture distribution consisting of a Rayleigh component and an exponential tail component, where the latter component may represent real AGN–host spatial offsets. Similarly, we find that the shape of our offset distribution from `Tractor` modeling of the ZTF AGN sample is described by the expected Rayleigh distribution at offsets $\lessapprox$ 1" and at offsets $\gtrapprox$ 1" the distribution is better described by a decaying exponential.

We therefore model our AGN–host spatial offset distributions by splitting the AGN sample into 3 different sub–samples based on the peak difference magnitude of the AGN. The ranges in peak–magnitude used to produce the sub–samples are 15–18, 18–19.5, and 19.5–23. These ranges were selected to ensure that each sample was large enough to model the Rayleigh and exponential tail components. The offset distributions of these sub–samples are shown in Figure 2.1 a) c) and e). We fit a mixture distribution consisting of a Rayleigh component $\alpha(x)$ and an exponential component $\epsilon(x)$:

$$P_x = C\alpha(x) + (1 - C)\epsilon(x) \tag{2.2}$$

$$= C\frac{x}{\sigma_{\mathrm{R}}^2}\mathrm{exp}\big(-\frac{x^2}{2\sigma_{\mathrm{R}}^2}\big) + (1 - C)\tau e^{-\tau x} \tag{2.3}$$

for offsets x, mixture coefficient C, Rayleigh width σ_R and exponential decay parameter τ. We do this by directly minimizing the log likelihood between the model distribution and the data.

We first model the exponential decay parameter τ to fit only offsets $x > 1.0$" so that the fit is not heavily biased by low–offset sources which dominate the distribution. We then fix the value of τ and fit the mixture distribution to the whole sample to find σ_R and C. The fits are shown in Figure 2.1 a), c) and e), where we can see the Rayleigh component explaining the portion of the distribution which arises from positional uncertainty, and the exponential tail component showing the portion of the distribution which may contain physically real AGN–host offsets. For a given AGN–host offset x, we can calculate the probability that an offset $\geq x$ is drawn from the Rayleigh component as:

$$P_\alpha(x > R) = \frac{C \int_R^\infty \alpha(x)}{C \int_R^\infty \alpha(x) + (1 - C) \int_R^\infty \epsilon(x)} \tag{2.4}$$

This is shown as a function of offset x in Figure 2.1 b), d) and f). The probability function shows that as the offset increases, it is less likely to be explained by the Rayleigh distribution arising from positional uncertainties and more likely to be part of an exponential tail consisting of possibly real offsets. The spatial offset at which the probability of being drawn from the exponential component of the mixture distribution is 0.3% is marked by the dashed line in Figure 2.1 b), d) and f).

Using the probability functions to determine an offset cutoff for the 3 sub–samples, we determine 3σ offset cutoffs shown in the first column of Table 2.1. We select a cutoff of 0.511" for AGN with a peak magnitudes between 15 and 18, 0.773" for AGN with peak magnitudes between 18–19.5, and 0.976" for AGN with peak magnitudes between 19 and 23.

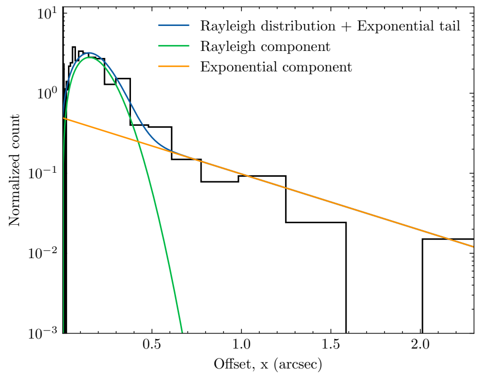

(a) AGN with a peak difference magnitude between 15 and 18.

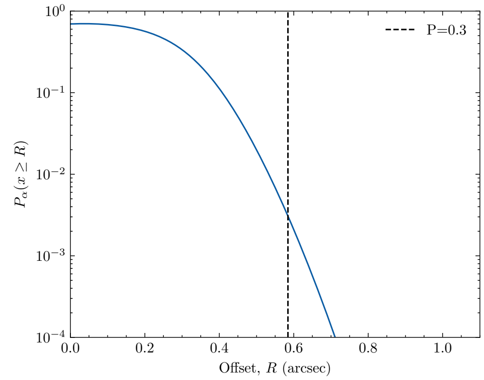

(b) 3σ offset = 0.574”.

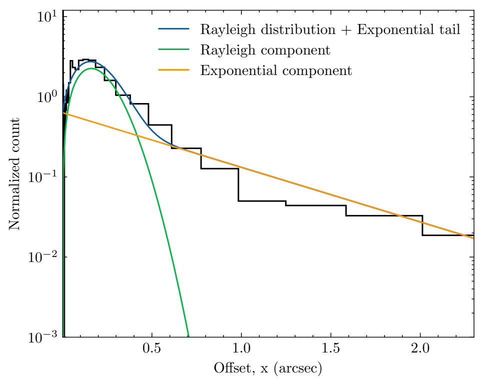

(c) AGN with a peak difference magnitude between 18 and 19.5.

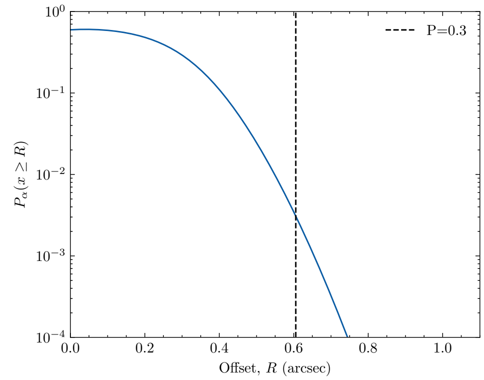

(d) 3σ offset = 0.605”.

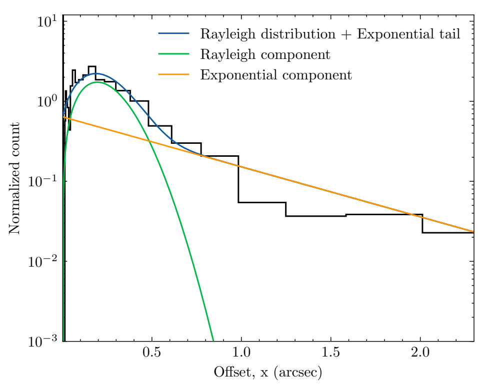

(e) AGN with a peak difference magnitude between 19.5 and 23.

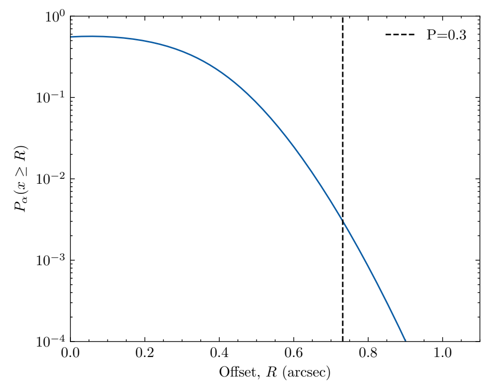

(f) 3σ offset = 0.732”.

Figure 2.1: **Left**: Normalized histogram with logarithmic bins for AGN–host offsets obtained from `Tractor` modeling. The best–fit model of a mixture distribution with Rayleigh and exponential components are shown. **Right:** Probability that an offset greater than R is drawn from the Rayleigh component of the mixture distribution shown in (a) instead of the exponential component. The offset where this probability is 0.3% is shown with a dashed line.

Table 2.1: Offset cutoffs (arcseconds) selected for classification of off–nuclear AGN based on their peak magnitude. The first column shows the peak magnitude bin. The second column shows the $> 3\sigma$ cutoff for a significant AGN–host offset derived by `The Tractor`. The third and fourth columns show the uncertainty on the magnitude–weighted transient position derived from ZTF alert packets for r-band and g-band respectively. The fifth column shows the number of AGN which have $> 3\sigma$ `Tractor` offsets and match the magnitude–weighted transient position using these cutoffs.

Peak magnitude	`Tractor` modeling	g-band subtraction	r-band of AGN	Number
19.5–23	0.732	0.946	0.976	64
18–19.5	0.605	1.009	0.773	164
15–18	0.574	0.959	0.551	23

2.3.3.3 Matching of transient positions from `The Tractor` and ZTF difference images.

In order to confirm that the best–fit point source position from `The Tractor` modeling is consistent with the position of the transient in the ZTF difference images, we calculate the magnitude–weighted position of the transient from the ZTF alert packets containing information about the position and magnitude of each single epoch difference image detection. The weights $1/\sigma^2_{\text{offset}}$ for the magnitude–weighted transient position are calculated using equation 3 from van Velzen et al. (2019):

$$\sigma_{\text{offset}} = 0.24 + 0.04(m_{\text{diff}} - 20) \tag{2.5}$$

In order to determine the uncertainty in the magnitude–weighted transient position from the ZTF alert packets, we undertake the same offset distribution modeling procedure

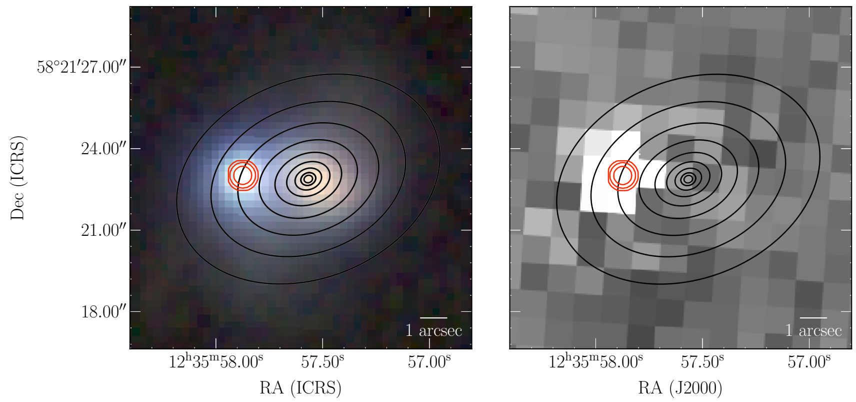

Figure 2.2: *Left:* Coadded g, r and z-band Legacy Survey images of ZTF18aaxvmpg. *Right:* ZTF image subtraction of ZTF18aaxvmpg when the AGN was close to peak magnitude. Overlaid contours show the best fit `Tractor` galaxy profile (black) and point source model (red) for a theoretical seeing of 1" derived from ZTF image modeling.

as we do for the `Tractor` AGN–host offsets. The modeling results for each magnitude binned sub–sample are shown in Figures 2.15 and 2.16 in Section 2.6. As the distribution of magnitude–weighted offsets is substantially different for g-band images and r-band images, due to the differing contributions of the AGN towards the reference image in different bands, we find cutoffs for the two bands separately. Using the probability functions to determine an offset cutoff for the 3 sub–samples, we determine 3σ offset cutoffs shown in Table 2.1. When checking that the `Tractor` point source positions are consistent with the magnitude–weighted transient position from the alert packets, we require a match within these selected cutoffs.

Figure 2.2 shows an example ZTF image subtraction for ZTF18aaxvmpg with the `Tractor` model overlaid. For this object, the `Tractor` point source position shown in the red contours was consistent with the ZTF transient seen in the image subtraction. This object was therefore considered to be an offset AGN candidate.

We find that 251 AGN have $> 3\sigma$ AGN–host offsets found by `Tractor` modeling which are consistent with the magnitude–weighted transient position from the alert packets. The breakdown of candidates from each peak magnitude bin is shown in the last column of Table 2.1.

2.3.4 Morphological classification of AGN hosts

In order to confirm the host–AGN offset found in ZTF images and classify the 251 offset AGN based on their morphology we undertook `Tractor` modeling with deeper, higher resolution images. For this task, we used archival images from the DESI Legacy Imaging Surveys (Dey et al., 2019a). The combined DECam Legacy Survey, Mayall z-band Legacy Survey and Beijing–Arizona Sky Survey were taken between 2014 and 2019 and cover declinations from $-18 < \delta < +84$, offering 0.262"/pix resolution and depths of 24.7 , 23.9 and 23.0 for g, r and z bands respectively

We modeled the high resolution coadded g and r and z band Legacy Survey images of each system with a single galaxy profile and an offset point source. We then visually examined the images, `Tractor` models and residuals to determine if each offset AGN was well modeled as a point source or if there was excess unmodeled emission indicating the presence of a second host galaxy in the system which is centered on the AGN. We separated the sample into 5 categories. The number of objects in each category is shown in Table 2.2.

When the residuals of the galaxy and offset point source model showed a clear stellar bulge surrounding the offset AGN, it was considered likely that there are two galaxies in the system rather than one. If the residuals also showed morphological

Table 2.2: Breakdown of the complete sample of 251 offset AGN into 5 galaxy morphology–based classifications. The first row is the number of AGN which have extended galaxy emission around them and appear to be interacting and merging with a second galaxy. The second row shows the number of AGN which are not surrounded by a stellar bulge and appear to be spatially offset from the center of a galaxy with indications of recent merging activity. The third row shows the number of AGN in disturbed, post–merger systems where the stellar bulge is offset from the center of the extended galaxy profile and aligned with the AGN. The fourth row shows the number of AGN which appear to be point sources spatially offset from a undisturbed galaxy and are therefore more likely to be chance coincidences with background galaxies. The fifth row shows the number of AGN where the ZTF position could not be confirmed in archival Legacy Survey images.

Classification	Number
AGN in galaxy mergers	52
AGN offset from the stellar bulge of disturbed galaxy	9
AGN aligned with the stellar bulge of disturbed galaxy	21
AGN offset from an undisturbed galaxy	29
AGN without position confirmation in Legacy Survey modeling	140

evidence of merging activity such as tidal structures, we considered the AGN to be part of a galaxy merger. These objects will be discussed further in Section 2.4.1.

When the system was well modeled by a single galaxy profile and offset point source and there were no tidal structures indicating recent merging activity it was considered likely to be chance coincidence of an AGN and an unrelated background galaxy. These AGN are discussed in Section 2.4.2.

For AGN which were well modeled by an offset point source and showed morphological evidence of recent merging activity in the host galaxy residuals, we considered that the AGN may be a candidate for a recoiling SMBH. We consider these objects as recoiling SMBH candidates because the recoiling AGN is expected to be visible for a period of 10^6 years after recoil while the host galaxy will still show evidence of previous merging activity in its morphology (Blecha et al., 2016). These objects are discussed in Section 2.4.3.

When the AGN was in a disturbed, irregularly–shaped host galaxy with a stellar bulge which was offset from the photometric center of the extended galaxy profile and the AGN was aligned with this stellar emission, we did not consider the AGN to be a recoiling SMBH candidate.

The remainder of the 251 objects did not have point source emission from an AGN present in the Legacy Survey images used for `Tractor` modeling. For these objects, confirmation of the spatial offset discovered in ZTF images requires follow–up with deeper, higher resolution imaging taken when the AGN emission is visible.

The distribution of physical offsets in kpc for the whole sample, the AGN in mergers, and the off–nuclear AGN is shown in Figure 2.3. The complete AGN sample shows a tail extending beyond 40 kpc due to chance coincidences with background galaxies.

2.3.5 Spectroscopic analysis of ZTF broad line AGN

In order to model the distribution of broad line velocity offsets in the ZTF AGN sample as a whole, we modeled all 2422 ZTF AGN which had archival SDSS spectra and were classified as broad line AGN by the SDSS DR14 pipeline with Penalized Pixel Fitting (pPXF) (Cappellari, 2017; Cappellari & Emsellem, 2004). This method finds the velocity dispersion of stellar absorption lines using a large sample of high resolution templates of single stellar populations adjusted to match the spectral resolution of the

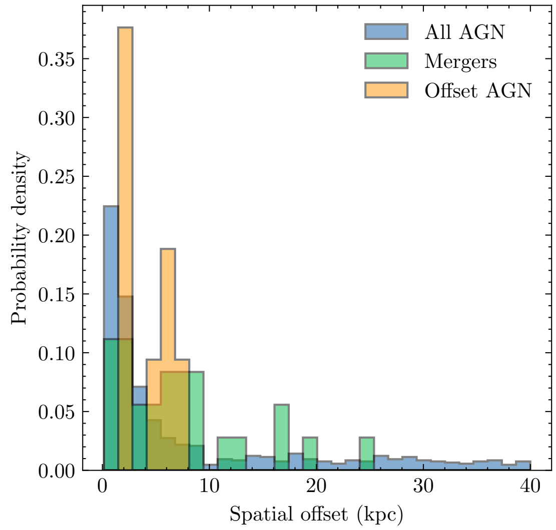

Figure 2.3: Distribution of physical spatial offsets between AGN and their closest galaxy for 3 samples: 898 AGN from the `Tractor` modeled sample with available spectroscopic redshifts, 27 of the 52 AGN in mergers with spectroscopic redshifts, and the 9 off–nuclear AGN. A tail of spatial offsets > 10 kpc can be seen in the blue histogram due to the presence of background galaxies.

input spectrum. We simultaneously fit the narrow Hα, Hβ, Hγ, Hδ, [S II] λ6717, 6731, [N II] λ6550, 6575, [O I] λ6302, 6366 and [O III] λ5007, 4959 emission lines during template fitting. The emission line fluxes are each fit as free parameters but the line widths of the Balmer series are tied, as are the line widths of the forbidden lines.

In these fits the velocity of whichever broad Hα, Hβ, Hγ, Hδ lines were available within the SDSS spectroscopic wavelength range were allowed to vary up to 3000km s^{-1} from the narrow lines. The velocity of each Balmer broad line was tied to the other Balmer broad lines.

We find that the ZTF AGN broad line velocities have a mean displacement of 143 km s^{-1} with a standard deviation of 126 km s^{-1} when the central component is fit with a Gaussian (Figure 4.12). Our distribution of broad line velocities for variable ZTF AGN is similar to the distribution of Hβ broad line velocities found by Bonning et al. (2007) with

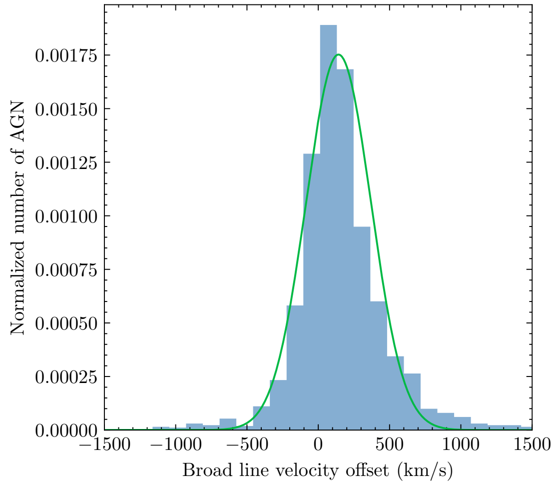

Figure 2.4: Distribution of Balmer broad line velocities relative to [S II] λ6717, 6731, [N II] λ6550, 6575, [O I] λ6302, 6366 and [O III] λ5007, 4959 emission line velocities found by fitting of archival SDSS spectra with `pPXF`. Velocities are shown for the 2422 AGN with broad Balmer lines in archival SDSS spectra out of the complete ZTF AGN sample of 5542 objects.

a sample of 2598 SDSS AGN where they found a mean displacement of 100km s^{-1} and a standard deviation of 212 km s^{-1}.

Our velocity distribution shows a substantial tail population with velocities up to ± 2500 km s^{-1}. The fraction of AGN f_ν with velocity magnitudes greater than 1000, 1500 and 2000 km s^{-1} are $f_{1000} = 0.025$, $f_{1500} = 0.009$ and $f_{2000} = 0.003$. These values are comparable to those found in the Bonning et al. (2007) sample, where they find fractions of $f_{1000} = 0.0035$, $f_{1500} = 0.0012$ and $f_{2000} = 0.0008$. It therefore appears that a variability selected AGN sample shows a broad line velocity distribution which is typical of a spectroscopically selected AGN sample.

2.4 Results

2.4.1 AGN in galaxy mergers

52 of our spatially offset AGN were determined to be in a merger with a second galaxy based on the presence of two galaxy nuclei and an interacting morphology visible in Legacy Survey images. The galaxy separations from `Tractor` modeling of Legacy Survey images ranged from $0.4 - 9$", which for the 33 AGN with known redshifts, corresponded to physical separations of 0.54 to 24.65 kpc.

For 14 of these AGN with available SDSS spectra of both galaxies, only ZTF18aacjltc had narrow emission lines consistent with an AGN in both galaxies. The remaining 12 were single AGN, where the companion galaxy did not show narrow AGN emission line ratios. The observed fraction of dual vs offset AGN is consistent with the predictions of Van Wassenhove et al. (2012).

18 galaxy mergers had only one archival SDSS spectrum available, with the fiber centered on the variable AGN. Follow–up spectra of the companion galaxies will be required to determine if these mergers contain one or two AGN. 15 galaxy mergers have no archival SDSS spectra available, as the variable object was classified as an AGN based on optical ZTF and infrared WISE variability. Follow–up spectra of both the AGN and companion galaxy will be required to spectroscopically confirm the presence of one or two AGN.

Aside from appearing in a range of multi–wavelength AGN sample papers, a fraction of our sample of AGN in merging galaxies have been studied in more detail in the literature. ZTF18aasxvyo is a well studied X-ray bright BL Lac object (Halpern et al., 1986) and ZTF18aaqjcxl is also a known BL Lac (Plotkin et al., 2008). ZTF18acegbsb is a known double peaked emitter (Strateva et al., 2003) in a merger, which has been studied in the context of AGN photoionization of companion galaxies (Keel et al., 2019). ZTF18aamfuhc appeared in the same cross–ionization study. ZTF18abhpvvr is a known dual AGN (Huang et al., 2014) and ZTF18aawwfep and ZTF18aajnqqv are also a known AGN pairs from Liu et al. (2011).

ZTF18aaifbku, an AGN in the double–lobed galaxy Mark 783, was imaged with the Karl G. Jansky Very Large Array (JVLA) at 5 GHz on September 6 2015 and showed radio emission from a compact core component and an extended component which was 26 kpc long (Congiu et al., 2017). The lack of jet emission led the authors to conclude that the radio emission was a relic of previous AGN activity before it entered a quiescent state. This AGN was first observed in ZTF on June 5 2018 and has shown continued variability to r-band magnitudes of 17.07 since then, suggesting that the AGN activity has turned on since on since the radio observations were made in 2015.

In order to determine if ZTF18aaxvmpg was a dual AGN, we undertook more detailed spectroscopic follow–up. The SDSS spectrum of ZTF18aaxvmpg taken on 2006-05-21 with the fiber centered on the AGN shows the presence of broad Balmer lines but the companion galaxy at 5.5 kpc from the AGN did not have an archival spectrum. We took a new spectrum of both the host galaxy and the AGN on 2019-10-29 with the DeVeny spectrograph on the Lowell Discovery Telescope using a 1.5” slit, central wavelength of 5700 Å, a spectroscopic coverage of 3600–8000 Å and a total exposure time of 3200s. The spectrum of the AGN and the companion galaxy is shown in figure 2.5.

Using the best–fit line fluxes from pPXF modeling of the spectrum, we determine the AGN and host galaxy types using the [O III] λ5007, Hβ, [N II] λ6573 and Hα line amplitudes. The emission line ratios of the AGN and companion galaxy and their classifications on the BPT diagram are shown in Figure 2.6. We find that the variable AGN has narrow line emission consistent with a Seyfert, while the host galaxy narrow line emission falls into the Composite/LINER category. Since LINER emission can be produced by either AGN or hot old stars on galactic scales we must distinguish between the two using a WHAN diagram, which classifies LINERs with a narrow Hα equivalent width $>$ 3 Å and a $\log_{10}$([N II] λ6573/ Hα) flux ratio > -0.4 as AGN (Cid Fernandes et al., 2011; Mezcua & Domínguez Sánchez, 2020). With `pPXF` we measure the equivalent width of narrow Hα to be 3.54 ± 0.11 Å and the $\log_{10}$([N II] λ6573/ Hα) flux ratio to be -0.165 ± 0.097. This places the spectrum in the 'weak AGN' class of the WHAN diagram, suggesting that the system does indeed host a second AGN. We therefore conclude that ZTF18aaxvmpg is part of a dual AGN.

6 of the 27 broad line AGN in mergers for which we have archival SDSS spectra showed double–peaked broad Balmer emission from an unobscured accretion disk, corresponding to 22% of the sample. The classifications of broad line region shapes of each AGN in a merger is shown in Table 2.3. It will be shown in Section 2.4.3.1 that 16% of the broad line ZTF AGN are double–peaked emitters. It is therefore possible that AGN in mergers are more likely to have double–peaked broad lines than normal ZTF AGN.

Table 2.3: Morphological and spectroscopic properties of the 52 AGN in galaxy mergers.The host–AGN spatial offset and g-band AGN/host galaxy flux ratio is derived from `Tractor` modeling of Legacy Survey images. The 8th column lists the number of AGN in the system, confirmed by either spectroscopic narrow emission line ratios or the presence of WISE variability. The second number in this column indicates whether neither the AGN or host galaxy have a spectrum (0), only the AGN has a spectrum (1), or whether there is a spectrum of the host galaxy centroid available as well (2). The last column shows the classification of the shape of the broad line region where we adopt the scheme of Strateva et al. (2003): prominent red shoulder (RS), prominent blue shoulder (BS), two prominent peaks (2P), two blended peaks (2B), complex multi–Gaussian structure (MS). We denote a Gaussian broad line with a 'C' and AGN with no broad line emission with 'None'. If there are no SDSS spectra available for the source or the source does not have broad emission lines, we indicate this with a '–'.

ZTF name	z	RA (hms)	Dec (dms)	Host–AGN dist. (")	Host–AGN dist. (kpc)	AGN flux/ gal. flux	# AGN/ # spec	BLR shape
ZTF18aaxvmpg	0.212	12:35:57.810	58:21:21.726	1.296 ± 0.002	5.477 ± 0.008	21.25	1/2	C
ZTF18abamzru	-	17:23:27.486	42:21:22.683	5.231 ± 0.001	–	3.20	1/0	-
ZTF18aasxvyo	0.23635	14:17:56.535	25:43:21.506	5.068 ± 0.001	19.162 ± 0.004	24.24	1/2	-
ZTF18aaieguy	0.213	13:25:18.144	41:10:09.717	0.676 ± 0.007	2.88 ± 0.03	0.48	1/1	C
ZTF19aakjemw	0.147	15:50:07.939	27:28:10.996	5.435 ± 0.002	16.184 ± 0.006	1.16	1/2	2B
ZTF18aaifbku	0.067	13:2:58.854	16:24:27.806	0.985 ± 0.002	1.371 ± 0.003	1.75	1/1	C
ZTF18aampabj	0.216	16:52:58.864	44:48:45.540	3.118 ± 0.001	13.416 ± 0.004	15.31	1/2	C
ZTF19aaagygp	-	01:07:13.787	-11:36:2.998	3.969 ± 0.002	–	0.34	1/0	-
ZTF18abujubn	-	19:08:12.617	45:32:49.643	8.562 ± 0.002	–	25.97	1/1	MG
ZTF18acegbsb	0.037	09:04:36.964	55:36:02.772	9.027 ± 0.009	6.992 ± 0.007	2.14	1/2	RS
ZTF19aaozpdm	-	13:37:01.086	20:25:14.343	1.682 ± 0.013	–	0.88	1/0	-
ZTF18aacjltc	0.189	08:12:52.208	40:23:47.253	3.192 ± 0.001	12.091 ± 0.004	6.06	2/2	C
ZTF18abtpite	-	23:18:35.915	41:08:0.284	3.262 ± 0.007	–	0.41	1/0	-
ZTF18abvwrxu	-	22:04:07.944	-08:57:24.505	1.011 ± 0.003	–	5.87	1/0	-
ZTF19abaktpb	-	16:42:19.074	03:45:53.037	8.164 ± 0.008	–	8.5	1/0	-
ZTF18aaqjcxl	0.099	07:58:47.235	27:05:16.379	3.314 ± 0.001	6.712 ± 0.002	5.54	1/1	None

ZTF18abyoivl	-	00:22:52.018	08:24:0.757	0.391 ± 0.007	–	0.97	1/0	-
ZTF18aabdiug	0.062	12:31:52.060	45:04:43.273	0.572 ± 0.002	0.738 ± 0.003	11.13	1/2	C
ZTF19aaviuyv	-	18:56:20.579	37:12:36.076	2.651 ± 0.014	–	3.48	1/0	-
ZTF18aabxczq	0.063	10:38:33.425	46:58:06.741	0.413 ± 0.003	0.54 ± 0.004	1.69	1/2	C
ZTF18acvwlrf	0.233	12:50:16.219	04:57:45.074	1.271 ± 0.005	5.887 ± 0.023	0.99	1/1	MG
ZTF19aasejqv	0.233	14:13:29.817	26:44:35.232	1.57 ± 0.009	7.261 ± 0.042	2.85	1/1	2B
ZTF18aazogyo	0.081	14:56:27.421	30:53:40.225	5.442 ± 0.001	9.123 ± 0.002	13.33	1/1	2B
ZTF18aceypvy	0.163	09:51:12.391	31:35:37.084	2.406 ± 0.003	7.913 ± 0.01	9.89	1/1	C
ZTF18acbweyd	0.189	10:20:38.565	24:37:12.421	4.24 ± 0.002	16.125 ± 0.008	11.47	1/1	C
ZTF18acablce	-	16:30:55.490	72:26:43.352	1.37 ± 0.008	–	1.77	1/0	-
ZTF18abhpvvr	-	00:38:33.041	41:28:53.681	3.595 ± 0.003	–	9.29	1/0	-
ZTF19abfqmjg	-	22:56:41.062	23:02:32.510	7.402 ± 0.003	–	48.85	1/0	-
ZTF18abmqwgr	-	20:27:53.382	14:08:50.604	1.539 ± 0.012	–	1.33	1/0	-
ZTF19aadgbih	0.196	12:46:33.522	45:34:21.773	0.381 ± 0.006	1.494 ± 0.024	1.82	1/1	C
ZTF19aalpfan	0.075	13:27:51.414	06:42:49.854	0.627 ± 0.003	0.964 ± 0.005	6.86	1/1	2B
ZTF18aawwfep	0.197	08:54:41.735	30:57:54.759	1.37 ± 0.003	5.424 ± 0.012	2.22	1/2	C
ZTF19aavxims	-	12:48:55.053	-06:59:54.802	4.735 ± 0.001	–	31.52	1/0	-
ZTF19aaaplct	-	14:57:28.940	08:34:22.879	2.835 ± 0.039	–	0.97	1/0	-
ZTF18aajnqqv	0.081	12:57:41.050	20:23:47.747	1.747 ± 0.004	2.901 ± 0.007	2.83	1/2	C
ZTF18abszfur	0.291	22:07:16.099	12:11:03.278	4.322 ± 0.002	24.646 ± 0.011	5.16	1/0	-
ZTF19abucbkt	0.16239	01:36:04.252	21:37:25.882	4.60 ± 0.01	12.935 ± 0.03	4.47	1/1	C
ZTF18adbhlyb	0.212	11:17:59.188	20:15:19.078	4.508 ± 0.001	19.075 ± 0.004	4.19	1/1	MG
ZTF18acxhoij	-	01:12:07.783	-21:04:28.682	1.099 ± 0.045	–	2.66	1/0	-
ZTF18acajwep	-	01:04:05.280	21:22:31.946	2.906 ± 0.001	–	7.08	1/0	-
ZTF19abipoqj	-	22:43:14.796	80:59:27.375	0.499 ± 0.005	–	0.57	1/0	-
ZTF19abpkoou	-	02:34:16.170	05:18:42.732	3.524 ± 0.001	–	8.38	1/0	-
ZTF18abztovy	-	08:29:24.624	34:50:45.655	1.719 ± 0.011	–	0.86	1/0	-
ZTF18acsllgd	-	03:45:45.495	22:23:58.156	1.041 ± 0.025	–	4.59	1/0	-
ZTF19aanxrki	0.114	15:32:27.165	04:19:22.283	3.557 ± 0.064	8.304 ± 0.149	1.29	1/2	C

ZTF18aamfuhc	0.086	13:42:34.214	19:13:34.184	4.845 ± 0.001	8.608 ± 0.002	28.39	1/1	MG
ZTF18aadwvyr	0.126	08:29:44.346	32:52:21.163	0.984 ± 0.003	2.53 ± 0.008	2.15	1/1	C
ZTF19abauzsd	0.285	15:54:32.681	21:43:48.220	0.483 ± 0.007	2.699 ± 0.039	1.03	1/1	RS
ZTF18abufbsq	-	23:46:15.513	12:47:07.733	0.891 ± 0.003	–	1.14	1/0	-
ZTF18abzuzrg	0.178	16:55:16.540	32:15:55.145	1.369 ± 0.007	4.908 ± 0.025	1.11	1/2	MG
ZTF18abtmcdb	-	01:20:12.473	07:12:58.251	0.535 ± 0.003	–	3.81	1/0	-
ZTF18aauhnby	0.09	12:04:15.954	56:02:58.100	1.092 ± 0.002	2.02 ± 0.004	1.39	1/1	C

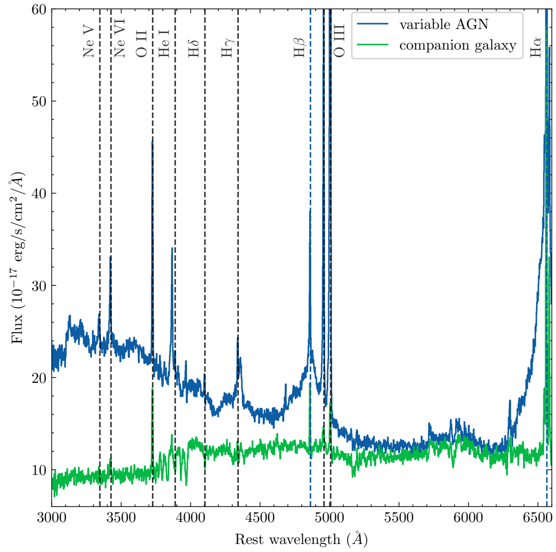

Figure 2.5: Spectrum of ZTF18aaxvmpg and its offset companion galaxy taken on 2019-10-29 with the DeVeny spectrograph on the Lowell Discovery Telescope. Broad Balmer features can be seen in the AGN spectrum but only narrow emission lines are visible from the companion galaxy.

In order to determine the X-ray luminosities of the sample, we crossmatched with a 60" radius to the second ROSAT All Sky Survey catalog (Boller et al., 2016). 31 of the 52 AGN had X-ray detections. The X-ray fluxes for the 31 AGN, along with luminosities for those with a known redshift, are shown in Table 2.7. 9 of the AGN in mergers had 20cm radio detections in FIRST. 6 of the 10 AGN with detected radio emission were also X-ray bright. The smaller fraction of radio AGN compared to X-ray AGN may be due to delayed triggering of radio emission during the merger (Shabala et al., 2017; Skipper & Browne, 2018).

The relationship between galaxy separation and X-ray luminosity is shown in Figure 2.7. We do not find a correlation between galaxy separation and X-ray luminosity in the range of 1–19 kpc separations represented by our sample. While Koss et al. (2012) found that the X-ray luminosity of AGN pairs decreased with increasing separation up to

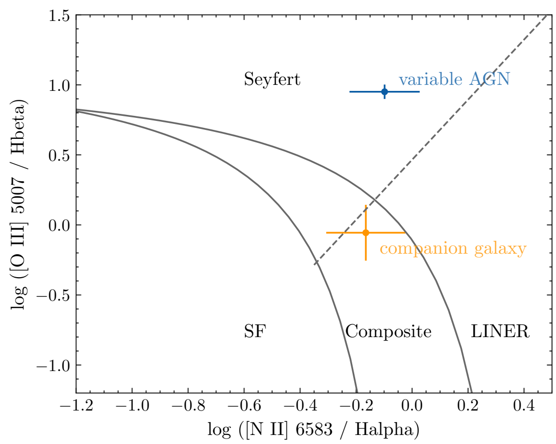

Figure 2.6: [O III] λ5007, Hβ, [N II] λ6573 and Hα narrow emission line ratios from pPXF fitting of DeVeny spectra taken of the variable AGN ZTF18aaxvmpg and its companion galaxy overlaid on the AGN classification regions. The ZTF AGN is classified as a Seyfert while the offset galaxy has a combination of star forming and LINER emission.

90 kpc, they also did not find a strong correlation at < 20 kpc.

In order to compare the variability of the AGN in mergers with the complete AGN sample, we determined the maximum flux change between the ZTF reference image and single epoch science images for the AGN with spectroscopic redshifts, and determined the corresponding change in luminosity. The distribution of peak luminosity change is shown in Figure 2.8 for the merger sample and for a larger sample of 689 ZTF AGN, controlled for the quality cuts used to produce the merger sample. The two samples show a similar distribution of peak luminosity. Implementing a K–S test to compare the two samples confirms they are drawn from the same distribution with a p–value of 0.64.

2.4.2 Chance coincidences of AGN and background galaxies

In our sample of offset AGN we find 29 AGN which are offset from an undisturbed galaxy with a symmetrically shaped profile. While many of these objects are likely to

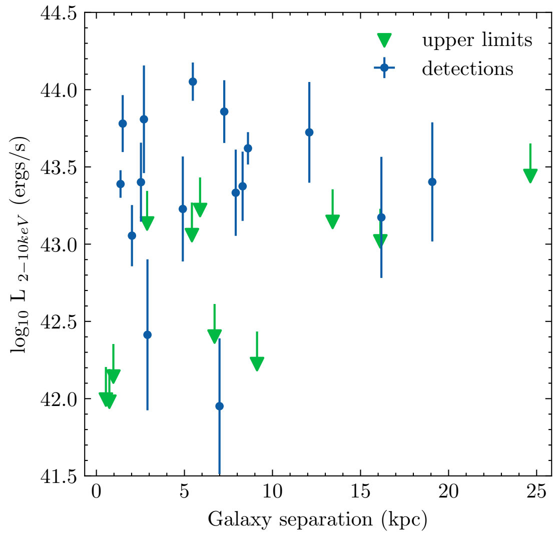

Figure 2.7: 2–10 keV luminosity for 27 AGN with known spectroscopic redshifts as a function of physical galaxy separation. 16 were detected in the second ROSAT All Sky Survey catalog and 11 have non–detections.

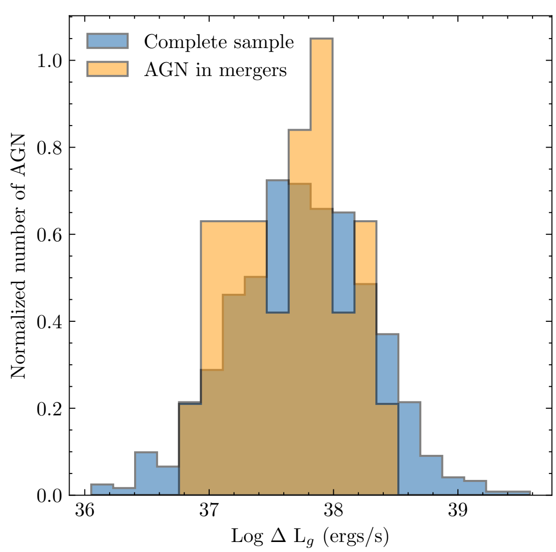

Figure 2.8: Peak luminosity change relative to the reference image amongst the 27 AGN in mergers and a larger sample of 689 variable AGN which had spectroscopic redshifts available. The larger sample was controlled to undergo the same quality cuts as the merger sample.

be quasars coinciding with background galaxies, it is possible that a fraction of them are AGN with a real association to the spatially offset host. We therefore calculate the approximate number of chance coincidences with background galaxies that we expect for the sample of 3110 AGN which were modeled by `The Tractor`.

To determine the density of background galaxies, we use `Casjobs` to query the SDSS DR16 catalog to find the number of galaxies with g-band model magnitudes between 15 and 22.8. We choose a g-band limiting magnitude of 22.8 because it is the median effective depth of each set of 30 ZTF images used for `Tractor` modeling for the AGN sample. We note that the choice of the median limiting magnitude is a significant approximation because there is a wide distribution in effective depths for the `Tractor` models of the AGN. Future work should take a more systematic approach to reach a consistent limiting magnitude for all objects.

We find that there are 119,364,394 galaxies in the SDSS survey area of 14,555 deg^2 within this magnitude range, corresponding to a density of 6.328×10^{-4} per arcsec^2. This means that we expect 1.789×10^{-2} background galaxies in a 3” radius circle around a given AGN. For our sample of 3110 AGN with `Tractor` modeled offsets, we therefore expect 56 AGN to have unassociated background galaxies within 3 arcseconds.

As we do not have an excess of AGN which are intrinsically offset from undisturbed host galaxies beyond the estimated number of chance coincidences, we do not have evidence that any of these objects could be recoiling SMBH candidates. The AGN falling under this category require spectra to confirm the host galaxy redshift and provide evidence that they are not chance coincidences.

2.4.3 AGN spatially offset from the center of disturbed galaxies

Our morphological classification scheme finds 9 AGN which are variable point sources spatially offset from a potential host galaxy and do not show evidence of a second stellar bulge around the AGN. The properties of the 9 offset AGN are summarized in Tables 2.4 and 2.5. Their ZTF light curves are shown in Figure 2.9. We show the coadded g-, r- and z-band Legacy Survey images, the best–fit Tractor model and the residuals for each object in Figure 2.10. The residuals all show asymmetric, tidal structures indicative of previous merging activity. Spectra of the offset AGN are shown in Figure 2.11.

Table 2.4: Spectroscopic and morphological properties of the sample of AGN spatially offset from disturbed host galaxies. The redshifts are based on the position of O III lines in the archival SDSS spectrum of the AGN. The spatial offsets are obtained from modeling of point source and galaxy profile positions in the Legacy Survey images with `Tractor`. For the 3 AGN with Gaussian broad lines the broad line velocities are found by modeling of a Gaussian Balmer broad line series with `pPXF`. For objects which are poorly modeled by a Gaussian and well–modeled by a double–peaked accretion disk model (Chen & Halpern, 1989) we instead classify the shape of the broad line by adopting the scheme of Strateva et al. (2003): prominent red shoulder (RS), prominent blue shoulder (BS), two prominent peaks (2P), two blended peaks (2B). If a central Gaussian broad line is required in addition to the double–peaked accretion disk model we indicate this with '+C'.

ZTF name	z	RA (hms)	Dec (dms)	Host–AGN dist. (arcseconds)	Host–AGN dist. (kpc)	BLR vel. (km s^{-1})
ZTF19aautrth	0.208	16:30:41.964	30:36:2.448	1.076 ± 0.003	4.48 ± 0.012	BS+C
ZTF19aadgijf	0.262	14:26:14.312	27:29:55.98	1.197 ± 0.005	6.195 ± 0.026	-462.0 ± 0.3
ZTF18aaxmrom	0.347	16:09:11.257	17:56:16.271	1.057 ± 0.01	7.089 ± 0.067	RS+C
ZTF19aayrjsx	0.215	23:32:54.463	15:13:5.407	1.329 ± 0.003	5.695 ± 0.013	2P+C
ZTF18aalsidi	0.348	15:53:57.736	47:52:32.015	0.901 ± 0.004	6.051 ± 0.027	RS+C
ZTF18accptjn	0.214	22:12:17.117	3:50:40.531	0.648 ± 0.005	2.767 ± 0.021	344.3 ± 0.3
ZTF18absvcae	0.755	20:49:07.593	5:13:17.362	1.679 ± 0.004	22.035 ± 0.052	–
ZTF18aaoeobb	0.270	12:48:53.9	34:24:29.448	0.429 ± 0.004	2.284 ± 0.021	2B+C
ZTF19aadggaf	0.266	13:42:06.57	5:05:23.898	0.488 ± 0.004	2.554 ± 0.021	608.2 ± 0.3

Table 2.5: X-ray and radio properties of the sample of AGN spatially offset from disturbed host galaxies. The X-ray detection column shows which objects have detections within 1.0' of the AGN position in the a ROSAT All Sky Survey catalog, and the radio detection column shows the 20cm flux density or upper limit if it was within the coverage of the FIRST radio survey (Helfand et al., 2015). The radio loudness is indicated in the last column.

ZTF name	X-ray	Radio flux (mJy/beam)	R
ZTF19aautrth	✓	< 0.98	< 1.56
ZTF19aadgijf	✓	< 1.24	< 2.05
ZTF18aaxmrom	✓	444.48	1760
ZTF19aayrjsx	✓	–	–
ZTF18aalsidi	✓	< 0.88	< 10.32
ZTF18accptjn	×	1.12	0.87
ZTF18absvcae	×	4.97	51.6
ZTF18aaoeobb	✓	< 0.93	< 0.95
ZTF19aadggaf	✓	3.80	2.89

2.4.3.1 Broad line region properties

The details of the Hα and Hβ broad line regions of the spatially offset AGN are shown in Figure 2.12. We do not have Hα and Hβ spectra for ZTF18absvcae due to its higher redshift. 3 of the 8 AGN for which we do have spectra of the Hα or Hβ lines (ZTF19aadgijf, ZTF18accptjn and ZTF19aadggaf) have Gaussian broad lines. The broad line velocity offsets determined from `pPXF` fitting are shown in Table 2.4. Because of the large distribution of velocity offsets in the overall ZTF AGN sample (Figure 4.12) and the fact that the ZTF AGN which have extreme $> 1500\mathrm{km\,s^{-1}}$ velocities do not show any evidence of a spatial offset, we do not make any conclusions from the velocities of 200–600 km $^{-1}$ magnitude observed for these 3 AGN.

The remaining 5 of the 8 AGN (ZTF18aalsidi, ZTF19aautrth, ZTF18aaxmrom,

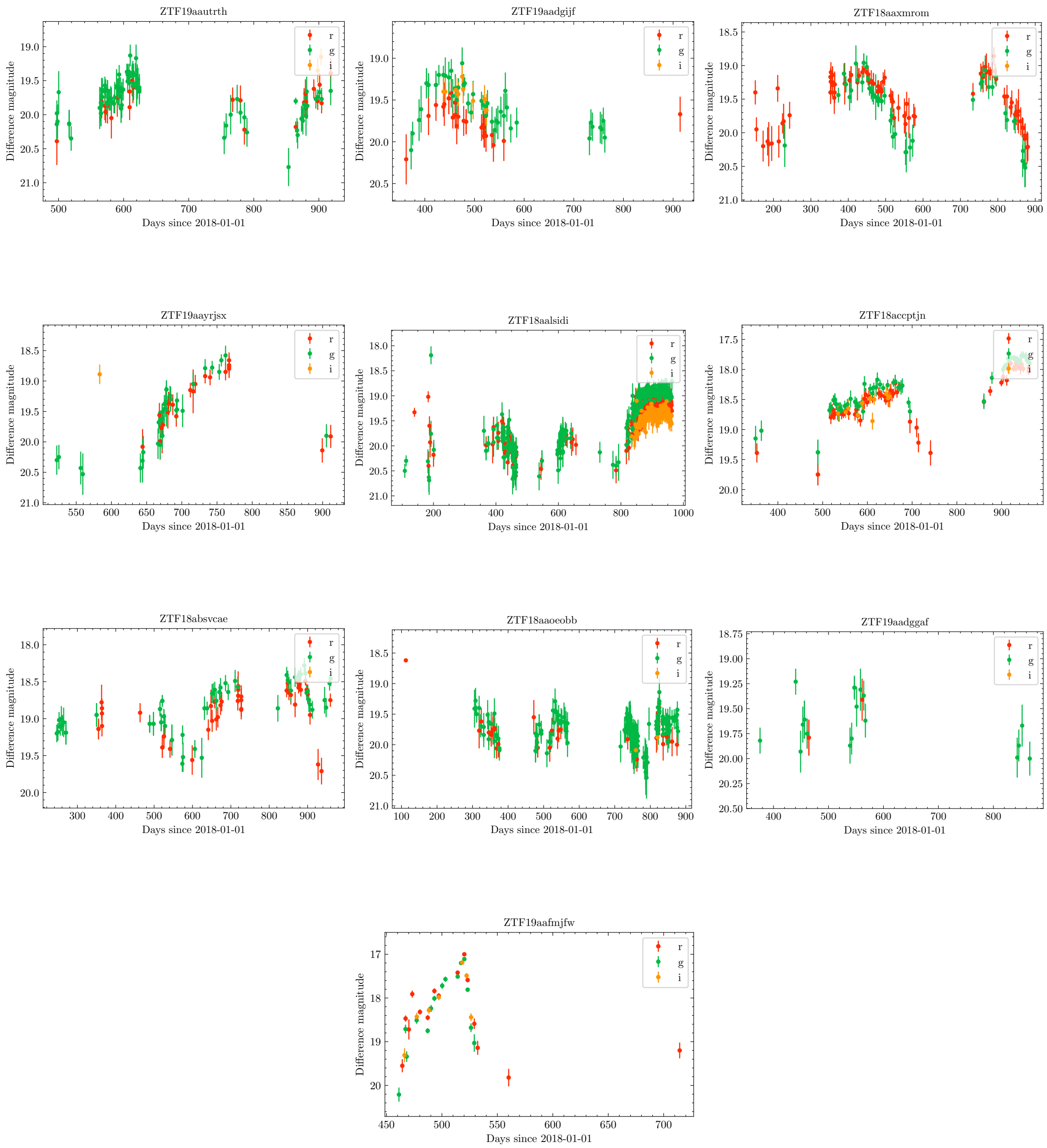

Figure 2.9: ZTF light curves in g, r and i-band for the sample of 9 offset AGN and the known recoiling SMBH candidate in SDSS1133 which rebrightened in ZTF (ZTF19aafmjfw). We show only the $> 3\sigma$ detections.

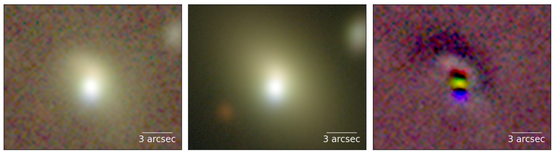

(a) ZTF19aautrth

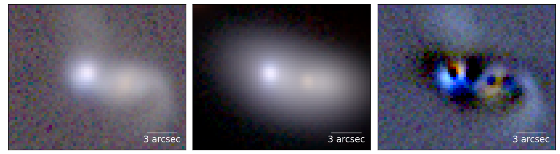

(b) ZTF19aadgijf

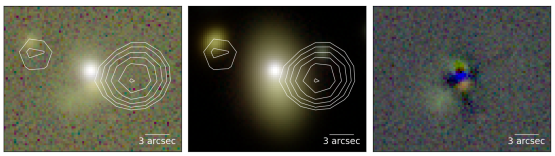

(c) ZTF18aaxmrom

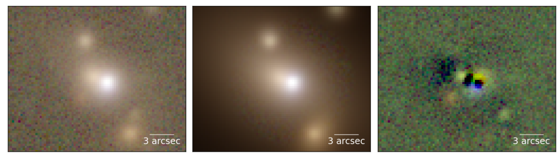

(d) ZTF19aayrjsx

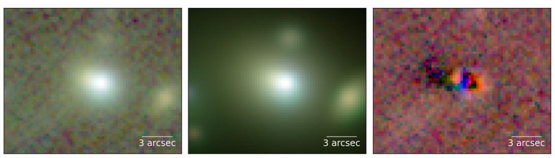

(e) ZTF18aalsidi

(f) ZTF18accptjn

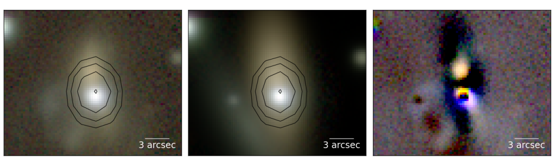

(g) ZTF18absvcae

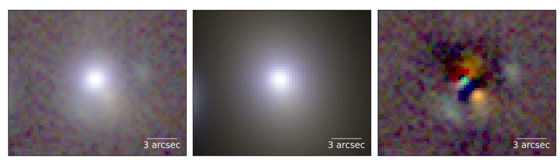

(h) ZTF18aaoeobb

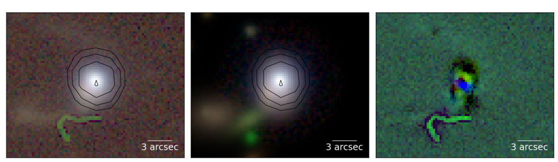

(i) ZTF19aadggaf

Figure 2.10: For each offset AGN: *Left:* Coadded g, r and z band Legacy Survey Images. *Middle:* Corresponding coadded `Tractor` model. *Right:* Image–model residuals showing galaxy tidal structures. For the 4 AGN with 20cm detections in FIRST (ZTF18aaxmrom, ZTF18accptjn, ZTF18absvcae, ZTF19aadggaf) we overlay contours of the FIRST image.

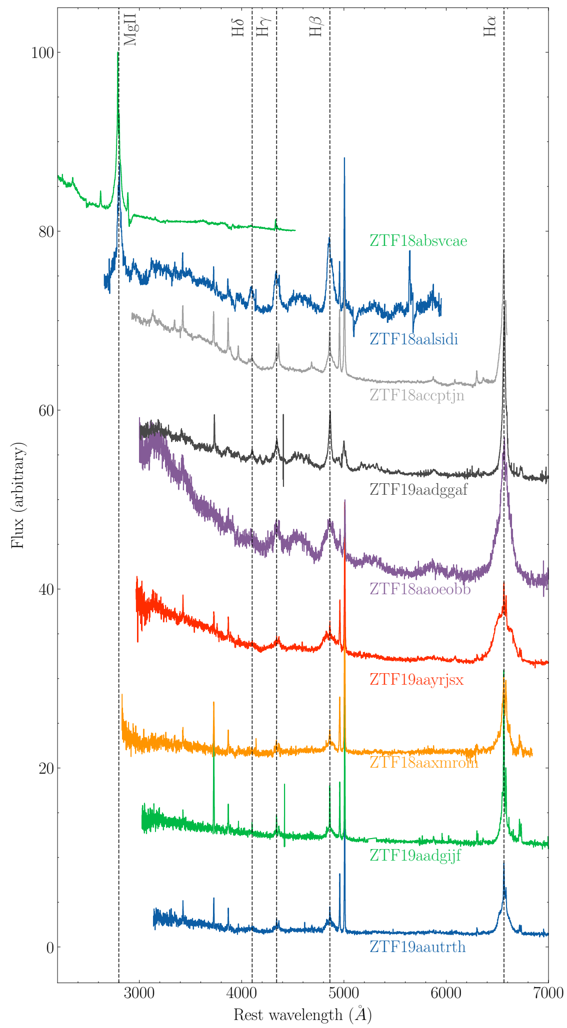

Figure 2.11: Spectra of the off–nuclear AGN, all from the SDSS archive except for ZTF18absvcae, ZTF18accptjn and ZTF18aalsidi which were observed with the DeVeny spectrograph on LDT on 2020-09-13, 2020-09-15 and 2020-10-11 respectively. In all SDSS spectra, the fiber was centered on the AGN rather than the photometric center of the offset host galaxy. The Balmer series is shown with dotted lines.

ZTF19aayrjsx and ZTF18aaoeobb) for which we have spectra of the Hα or Hβ lines have asymmetric Balmer broad line regions which are poorly fit by a Gaussian. Adopting the classification scheme of Strateva et al. (2003) we note that ZTF18aalsidi and ZTF18aaxmrom have prominent red shoulders, ZTF18aautrth has a prominent blue shoulder, ZTF19aayrjsx has two prominent peaks which are red and blue–shifted, and ZTF18aaoeobb has two blended peaks which are red and blue–shifted. These classifications are displayed in Table 2.4. Such asymmetric structures can arise due to double–peaked emission from an unobscured, relativistic Keplerian accretion disk (Chen & Halpern, 1989; Eracleous & Halpern, 1994).

To determine if the velocity–offset peaks observed in the broad Balmer lines of ZTF19aautrth, ZTF18aaxmrom, ZTF19aayrjsx, ZTF18aaoeobb and ZTF18aalsidi can be accounted for by accretion disk emission, we model the broad lines with an elliptical accretion disk model where an inner thick, hot ion torus illuminates a thin outer disk of ionized gas, which has a power law relation between emissivity and radius given by slope q (Chen & Halpern, 1989; Strateva et al., 2003). The model depends on the inner and outer dimensionless gravitational radii of the disk ϵ_1 and ϵ_2, local turbulent broadening parameter σ, azimuthal angle ϕ, inclination angle i where 0 degrees is face–on and 90 degrees is edge–on, ellipticity e and disk orientation ϕ_0. We bound the inner radius to $0 < \epsilon_1 < 1000$, the outer radius to $0 < \epsilon_2 < 8000$, the emissivity slope to $0 < q < 5$ and the local broadening to $0 < \sigma < 0.01$, to ensure that we could find good fits to the data with disk shape parameters consistent with the known double–peaked emitter population from Strateva et al. (2003). All four objects required a central Gaussian broad line in addition to the accretion disk model to produce a good fit to the data, which is not uncommon for double–peaked emitters (Strateva et al., 2003).

The best fit disk parameters from the Hα and Hβ fits of the 5 sources are shown in Table 2.6 and the models are shown in Figure 2.13. We note that our simple log likelihood minimization procedure for disk model fitting may not explore the whole parameter space and find the most optimal disk parameters. However, it serves to illustrate that accretion disk emission models can account for the extra flux which is not well described by a Gaussian model. More rigorous fitting with MCMC could be used to better determine disk shape parameters and their uncertainties in the future.

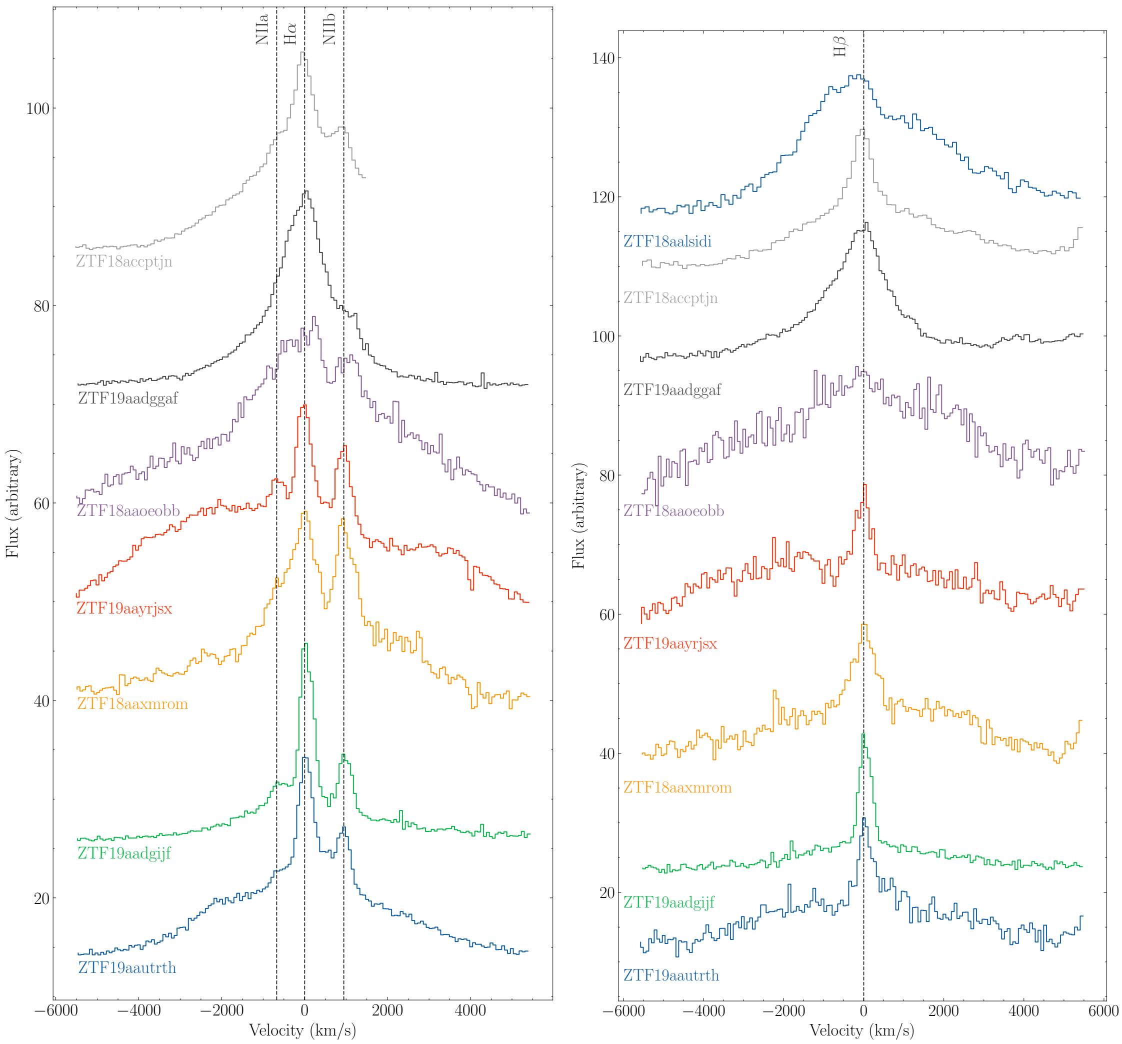

Figure 2.12: *Left:* Hα broad line regions and *Right:* Hβ broad line regions for the off–nuclear AGN candidates. 5 of the 8 off–nuclear AGN for which we have spectra of either the Hα or Hβ lines show asymmetric or double–peaked broad Balmer structures (ZTF18aaoeobb, ZTF19aayjrsx, ZTF18aaxmrom, ZTF19aautrth, ZTF18aalsidi). The other three show standard Balmer broad lines (ZTF18accptjn, ZTF19aadggaf, ZTF19aadgijf).

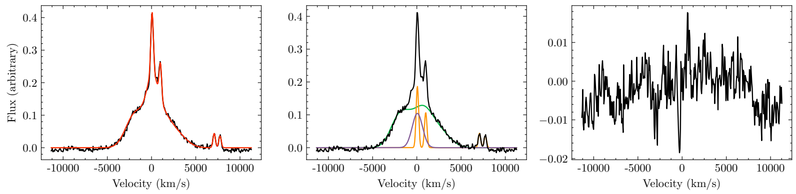

ZTF19aautrth

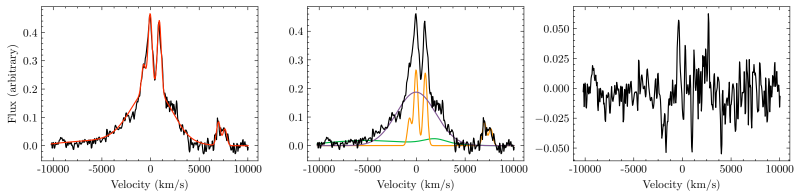

ZTF18aaxmrom

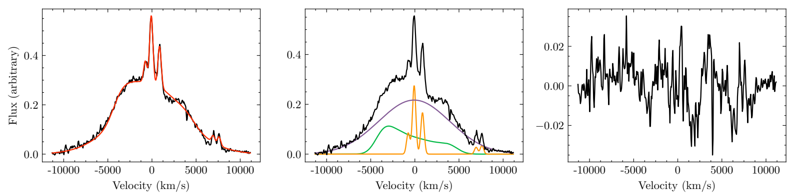

ZTF19aayrjsx

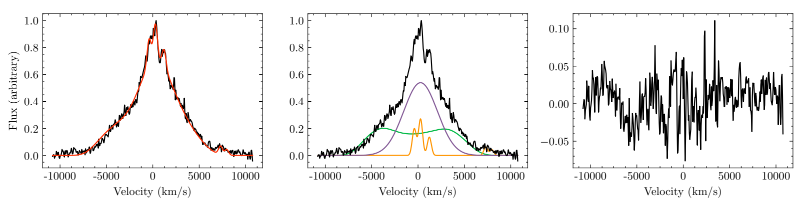

ZTF18aaoeobb

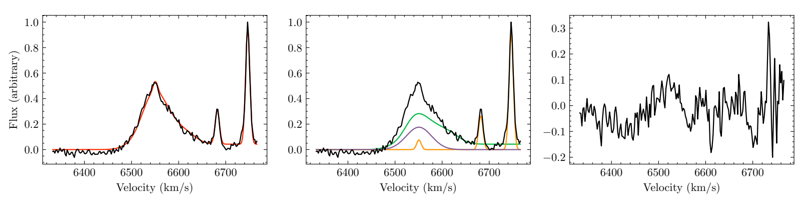

ZTF18aalsidi

Figure 2.13: Best fit models of double–peaked Hα accretion disk emission in off–nuclear AGN candidates ZTF19aautrth, ZTF18aaxmrom, ZTF19aayrjsx and ZTF18aaoeobb and Hβ disk emission in ZTF18aalsidi after subtracting a stellar continuum model derived from pPXF. On the left we show the continuum subtracted data in black and the best fit narrow emission line and accretion disk model in red. The middle plots show the separate narrow line (green), accretion disk (orange) and central broad line (purple) components of the fit. The rightmost plots show the error weighted flux residuals after subtracting the best fit model.

Table 2.6: Best fit accretion disk parameters for the 5 off–nuclear double peaked emitters from modeling of the Hα (ZTF19aadgijf, ZTF19aautrth, ZTF18aaxmrom and ZTF19aayrjsx) and Hβ (ZTF18aalsidi) broad lines after subtracting a stellar continuum model derived from pPXF. Disk parameters were derived from a simple log likelihood minimization fit to illustrate that accretion disk emission models can describe the observed broad line shapes well.

Disk parameter	ZTF19aautrth	ZTF18aaxmrom	ZTF19aayrjsx	ZTF18aaoeobb	ZTF18aalsidi
Central component required	Yes	Yes	Yes	Yes	Yes
Inner radius (ϵ)	252	813	70	997	21
Outer radius (ϵ)	608	6800	7995	3841	2255
Inclination (degrees)	13.6	84.9	14.0	47.6	12.8
Turbulent broadening (c)	0.0035	0.0007	0.007	0.0019	0.0042
Ellipticity	0.46	0.54	0.91	0.17	0.93
Disk orientation (degrees)	18.2	36.6	39.0	31.6	357.1 height

In order to determine if the double–peaked emitter fraction of 63% amongst spatially offset AGN is substantially different from the entire variable ZTF AGN sample, we applied a multi–Gaussian fitting procedure to the 1923 variable AGN with archival SDSS spectra of the Hα region which had broad Balmer lines to search for double–peaked emitters. We used the `pPXF` fitting procedure described in Section 2.3.5 to fit two different models. In the first model the spectrum was fit with a single broad Balmer line free to have a velocity offset to the narrow Balmer lines. This was fit at the same time as the narrow emission lines and stellar continuum. In the second model the spectrum was fit with 3 broad lines: one with central velocity tied to the narrow Balmer lines, one with a velocity up to 6000 km s^{-1} relative to the narrow lines, and one with a velocity down to –6000 km s^{-1}. The widths of the 3 broad lines were not tied to each other.

To find double–peaked emitters from the fits of these two models, we required the χ^2 improvement from the multiple broad line model compared to the single broad line model to be > 250. Then to be considered a double–peaked emitter candidate the 2 velocity offset Hα broad lines were each required to have peak flux densities of $> 33\%$ of the narrow Hα line and to have a velocity > 500 km s^{-1} from the narrow line velocity. As the effectiveness of this criteria depended on the relative brightness of narrow and broad lines, and the width of the broad line region, we visually inspected the 275 candidates found via this criteria and rejected 82, leaving 193 double–peaked emitters. We then visually inspected the remaining 1648 spectra to find any objects which may have missed by the criteria. We found 106 double–peaked spectra which were missed by the automatic classification scheme.

We therefore estimated that 299 of 1923, or 16%, of the variable AGN sample are double peaked emitters. This is much larger than the 3.6% fraction found for SDSS AGN by Strateva et al. (2003) with spectroscopic principal component analysis, suggesting that either variable AGN are more likely to be double–peaked emitters, or that our classification scheme is more likely to classify asymmetric broad line regions as double–peaked emitters than classification schemes used in previous studies. The 16% fraction of variable ZTF AGN with double–peaked broad Balmer lines is substantially smaller than 63% fraction seen in the spatially offset AGN sample.

2.4.3.2 Multi–wavelength properties

7 of the 9 offset AGN were detected in the ROSAT All Sky Survey and 4 AGN (ZTF18aaxmrom, ZTF18accptjn, ZTF18absvcae, ZTF19aadggaf) were detected at 20cm wavelengths in the FIRST radio survey, which uses the VLA to image a footprint largely coincident with SDSS to a detection sensitivity of 1 mJy (Helfand et al., 2015). The radio fluxes for these 4 AGN, as well as upper limits for another 4 which were within FIRST survey coverage but were not detected, are shown in Table 2.5. The contours of FIRST radio imaging are overlaid in Figure 2.10. ZTF18aaxmrom shows two radio lobes on either side of the galaxy which are likely the result of synchrotron emission from a jet. The other 3 AGN show radio point sources which coincide with the position of the ZTF AGN. The radio loudness[2] is also shown in Table 2.4. Two AGN with radio emission are classified as radio–loud ($R > 10$, Kellermann et al. (1989)), 2 are radio–moderate, and 4 others have upper limits indicating that they are not radio loud.

The recoiling SMBH candidates from Chiaberge et al. (2017) and Lena et al. (2014)

[2] $R = \frac{L_{5\mathrm{GHz}(\nu)}}{L_{4400\text{Å}}(\nu)}$

also demonstrate radio emission. As noted by Chiaberge et al. (2017), radio emission from a recoiling SMBH is not surprising given that the rapid spin needed to produce a relativistic jet can be produced by a binary black hole merger (Hemberger et al., 2013; Schnittman, 2013) and that there is a link between radio loud AGNs and major galaxy mergers (Chiaberge et al., 2015; Ivison et al., 2012). Assuming that the radio jet axis matches the spin axis of the recoiling SMBH, we would also expect recoil velocity to be preferentially aligned with the radio jet (Lena et al., 2014).

2.4.3.3 Confirming the nature of the offset AGN

There are two main alternative explanations for the nature of these offset AGN. Firstly, they may be chance coincidences with disturbed background galaxies. Secondly, they may be AGN in mergers with compact or undermassive host galaxies such that extended emission around the AGN is very faint. Given the predicted frequency of SMBHs in tidally stripped nuclei which may appear as offset AGN (Voggel et al., 2019), it would not be surprising if a large fraction of our objects are in fact AGN in compact galaxies merging with a larger galaxy.

If the distribution of expected velocity and spatial offsets of the recoiling SMBH population follows the simulated distribution of Blecha et al. (2016), we would expect the velocity offsets of our sample to range from 300 to 3000 km s^{-1} given their large spatial offsets. Spectroscopic fitting (Section 2.4.3.1) shows that the 3 AGN with Gaussian broad lines have velocity offsets ranging from 344–608 km/s (see Table 2.4) and the remainder of the sample with double–peaked emission have spectra consistent with a broad line region and accretion disk close to rest velocity (Figure 2.13). It is possible for large separation recoiling SMBHs to show small line of sight velocities, depending on their orbital trajectory at the time. However, if our objects are indeed all recoiling SMBHs, it is surprising that a fraction of the 9 do not have larger > 600 km/s line of sight velocities. The observed velocities therefore argue against the recoil hypothesis for these objects.

Much further work is therefore required to confirm the recoiling SMBH hypothesis for any of these offset AGN. To rule out the main alternative scenario – that the off-nuclear AGN are hosted by an undermassive host galaxy undergoing a merger with the larger galaxy – Hubble Space Telescope (HST) IR imaging could be used to search for a second extended region of old stellar emission around the offset AGN. HST imaging would be well complemented by IFU observations to map the positions of the narrow line emission relative to the AGN broad line emission (Chiaberge et al., 2018).

Chandra X-ray imaging to search for a second obscured AGN (e.g. Comerford et al., 2017) would also be essential for these candidates. If we observe just one X-ray point source, we can produce upper limits on the X-ray luminosity of a second AGN and show that they rule out the presence of an obscured AGN using the [O III] flux from the host center. This would strongly favor the recoiling black hole hypothesis.

As spatial offsets greater than 1.5 kpc are only possible in simulations where misaligned SMBH binary spins can occur (Blecha et al., 2016), if even a subset of our candidates could be confirmed as recoiling SMBHs, their extreme spatial offsets could demonstrate the existence of SMBH binaries with misaligned spins.

2.4.4 SDSS1133 (ZTF19aafmjfw)

SDSS1133, a variable object and recoiling SMBH candidate discovered by Koss et al. (2014) was identified by our search pipeline during a dramatic flare in ZTF, labeled ZTF19aafmjfw. This object has a long history of variability and the alternative scenarios proposed for its origin include: an LBV which exploded as a type IIn supernova in 2001, an LBV which continues to exhibit giant eruptions, or an offset AGN with flaring and stochastic variability (Koss et al., 2014). It was first observed in 1950 with the 103aO DSS plate at a magnitude of 18.6 and was again observed at comparable magnitudes in 1994 and 1999. It was then discovered to be flaring to $g = 16.4$ in SDSS on 2001-12-18 and 2002-04-01 but had faded to $g = 18.7$ by 2003-03-09. It was observed at a minimum of $g = 20.18$ with PS1 on 2012-02-22 after which it brightened to $g = 19.3$ on 2014-01-20 (Koss et al., 2014).

We searched for this object in archival data from the Catalina Real–time Transient Survey (Drake et al., 2009) and found that this object demonstrated another small scale flaring event in 2014. After showing no detectable V–band activity between 2006-02-03 and 2014-05-12, it brightened by V=0.22 between 2014-04-28 and 2014-06-05. After a gap in observations it had faded again by 2014-12-27.

This object showed no evidence of variability in ZTF prior to 2019-04-07, when it became detectable at $m_g = 20.21$ on 2019-04-07, flared to $m_g = 17.00$ on 2019-06-05, and faded again by 2019-12-16. The ZTF flare ZTF19aafmjfw is shown in Figure 2.9. The 3 magnitude change in brightness seen in ZTF was of comparable scale to the SDSS flare in 2001. The ZTF rebrightening of this object suggests that the transient emission from 2001 to 2013 was not from a Type IIn supernova with a variable star progenitor.

We obtained a spectrum of ZTF19aafmjfw with the DeVeny spectrograph on LDT on 2019-05-29 when the object was bright. The spectrum showed the return of broad Hα and Hβ absorption lines blue–shifted over a 2000 to 8000 km s^{-1} range (Figure 2.14), as had been observed in December 2013 and January 2014 (Koss et al., 2014). It also showed the return of [Fe II] λ7155 and [Ca II] $\lambda\lambda$ 7291, 7324 lines – features which have been seen only occasionally in AGN (e.g. Phillips (1976)) spectra, late–time supernovae spectra (e.g. Filippenko, 1997; Pastorello et al., 2019) and outbursting LBVs (Solovyeva et al., 2019).

The 100 day timescale, 3–4 magnitude flux change and high velocity absorption lines make this outburst comparable to the transient SN2009ip, a supersonic stellar explosion from a $> 60\text{M}_\odot$ star (Foley et al., 2011; Smith et al., 2010). The presence of broad Balmer, He I and Na D lines and a very blue continuum also links ZTF19aafmjfw to SN2009ip. However, SN2009ip did not show the forest of Fe group lines and [Ca II] $\lambda\lambda$ 7291, 7324 emission lines which we observe in ZTF19aafmjfw. Such Fe and Ca features were observed in the stellar outburst UGC 2773 OT2009–1, which is likely to be either a giant LBV eruption or extreme S Dor variability with circumstellar dust eruption (Foley et al., 2011; Smith et al., 2010). However, UGC 2773 OT2009–1 had a cooler temperature and weaker Balmer emission than SN2009ip, suggesting that it was a subsonic outburst rather than an explosion.

As ZTF19aafmjfw has spectroscopic features in common with SN2009ip which could indicate a high velocity explosion (blueshifted Balmer absorption lines, bright and broad Balmer emission and a blue continuum) and other spectroscopic features in

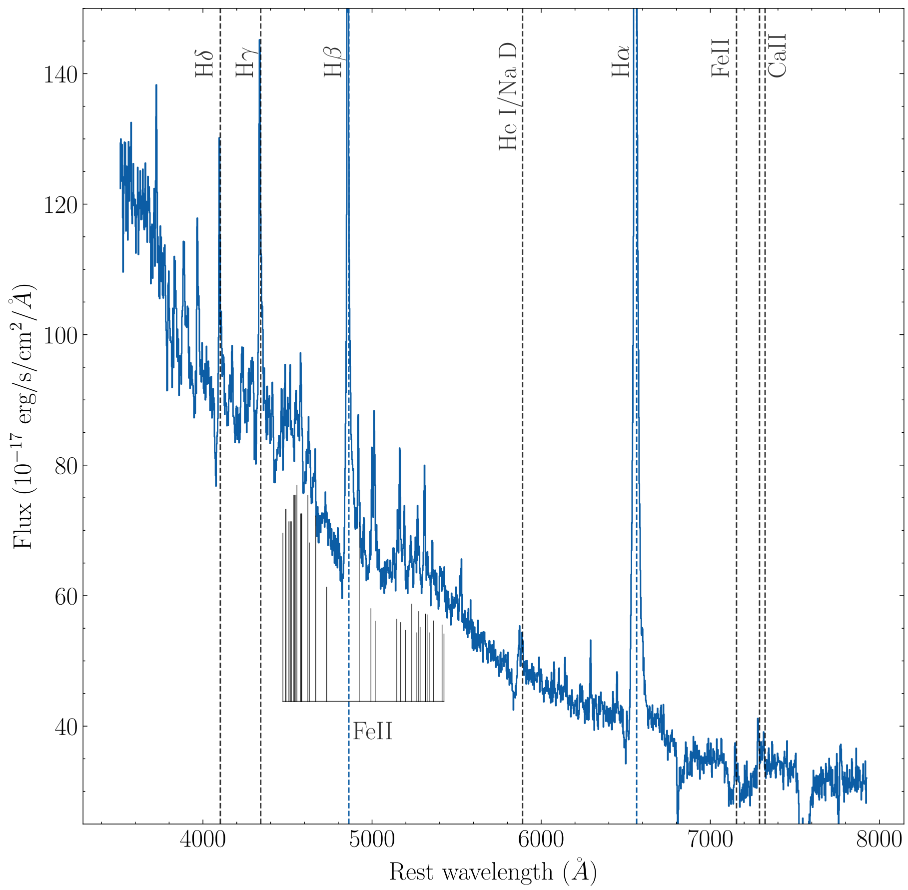

Complete spectrum

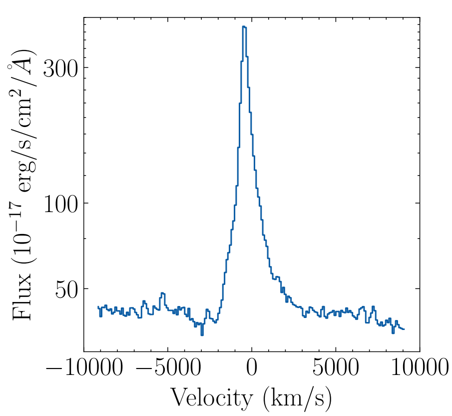

Hα broad line region.

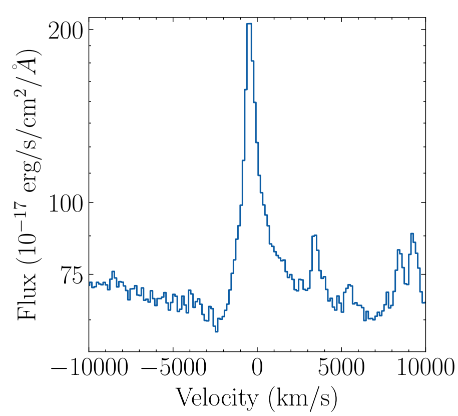

Hβ broad line region.

Figure 2.14: Spectrum of the flare ZTF19aafmjfw from SDSS1133 taken on 2019-05-29 with the DeVeny spectrograph on the Lowell Discovery Telescope. Subplot (a) shows the complete spectrum, while (b) and (c) show close–ups of Hα and Hβ in log scale to emphasize the P–cygni profile structure.

common with UGC 2773 OT2009–1 which could indicate a stellar outburst within a circumstellar dust envelope (FeII and CaII emission lines), the observed spectroscopic features may be due to a non–terminal, supersonic LBV outburst in a dusty circumstellar environment.

We note, however, that the presence of such a rare and massive star in a dwarf galaxy which does not show recent star formation in Keck adaptive optics and HST imaging is very unlikely (Koss et al., 2014), and while the observed combination of spectroscopic features would be unusual for a standard AGN, they may be induced by a recoil event. We therefore cannot yet completely rule out the recoil hypothesis in favor of an LBV or supernova imposter explanation.

2.5 Conclusions

We have described a novel search strategy for the discovery of spatially offset AGN from recoiling SMBHs and ongoing galaxy mergers. This strategy uses ZTF difference imaging to find variable AGN and `Tractor` forward modeling to determine the AGN position across multiple ZTF epochs and in deep, high resolution Legacy Survey images.

We have found a sample of 52 AGN in galaxy mergers and a sample of 9 AGN which may be spatially offset from their host galaxies. 5 of the 8 offset AGN for which we have spectra of the Hα or Hβ broad line regions show irregularly shaped broad Balmer lines with velocity offset broad peaks. These structures may arise due to emission from an unobscured, relativistic Keplerian accretion disk around the AGN. The 63% fraction of double–peaked emitters in the offset AGN sample is much larger than the 16% observed for the whole ZTF AGN sample. The remaining 3 offset AGN with spectra have Gaussian broad lines with velocities ranging in magnitude from 200 to 600 km/s relative to the narrow emission lines.

Our search strategy detected the variable object and recoiling SMBH candidate SDSS1133 (Koss et al., 2014) when it re–brightened by 3 magnitudes in ZTF. Follow–up spectra showed the return of a blue continuum, blue–shifted absorption lines and [Fe II] λ7155 and [Ca II] $\lambda\lambda$ 7291, 7324 forbidden lines, suggesting that the source may be either a luminous blue variable star which continues to show non–terminal outbursts or a recoiling AGN which continues to show variability.

Further multi–wavelength follow–up is required to confirm that our recoiling SMBH candidates are not AGN with undermassive hosts in mergers or chance coincidences with disturbed background galaxies. If even a subset of our offset AGN candidates are confirmed to be recoiling black holes, their large spatial offsets could show that SMBH binaries with misaligned spins are able to form. Such binaries may be detectable at a later stage of evolution by the Laser Interferometer Space Antenna (LISA) and would provide strong constraints on models of SMBH binary formation. The success of our variability–based search strategy with ZTF suggests that future searches for offset AGN with the Vera Rubin Observatory (Ivezić et al., 2019) may yield large populations of recoiling SMBH candidates and AGN in mergers.

2.6 Supplementary Material

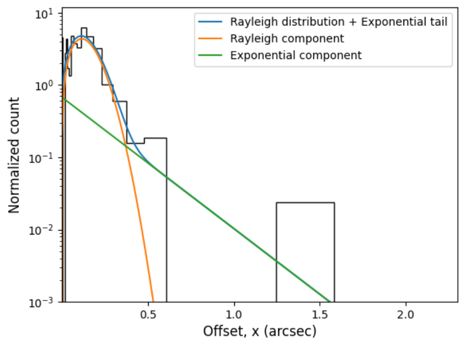

(a) AGN with a peak difference magnitude between 15 and 18.

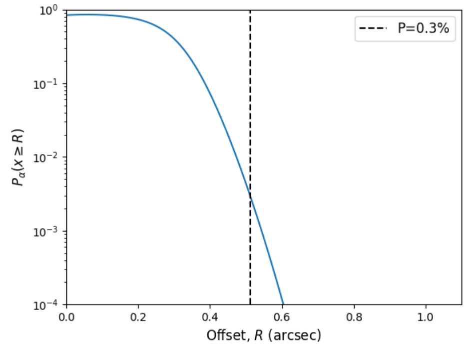

(b) 3σ offset = 0.551”.

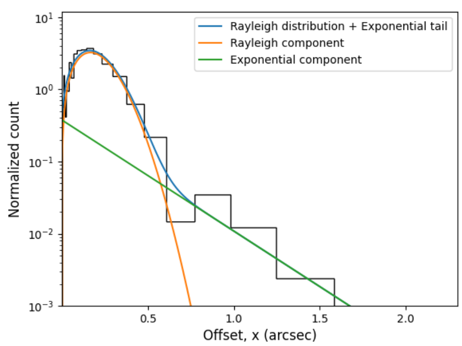

(c) AGN with a peak difference magnitude between 18 and 19.5.

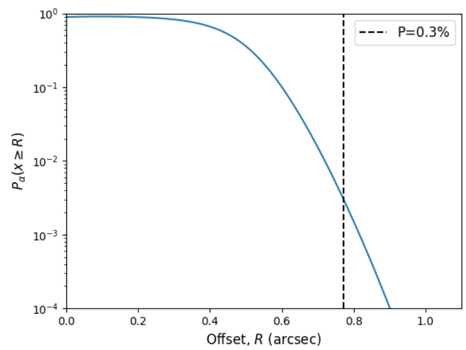

(d) 3σ offset = 0.773”.

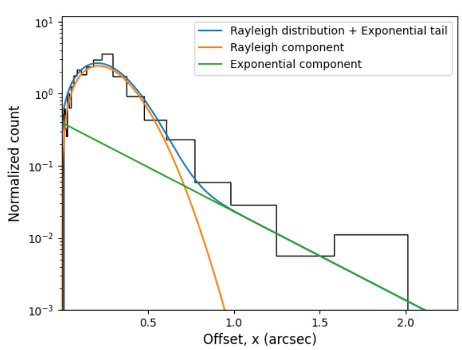

(e) AGN with a peak difference magnitude between 19.5 and 23.

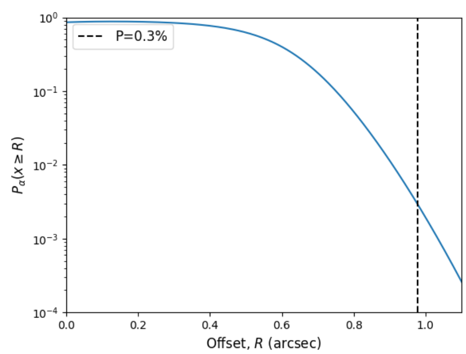

(f) 3σ offset = 0.976”.

Figure 2.15: **Left**: Normalized histogram with logarithmic bins for magnitude weighted AGN–host offsets obtained from r-band ZTF difference images. The best–fit model of a mixture distribution with Rayleigh and exponential components are shown. **Right:** Probability that an offset greater than R is drawn from the Rayleigh component of the mixture distribution shown in (a) instead of the exponential component. The offset where this probability is 0.3% is shown with a dashed line.

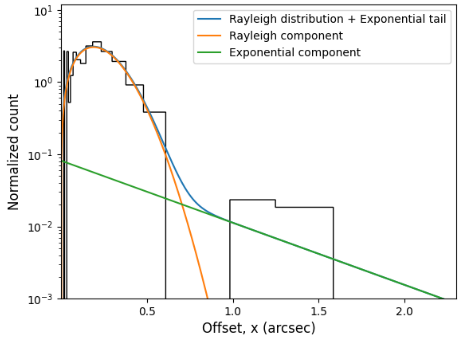

(a) AGN with a peak difference magnitude between 15 and 18.

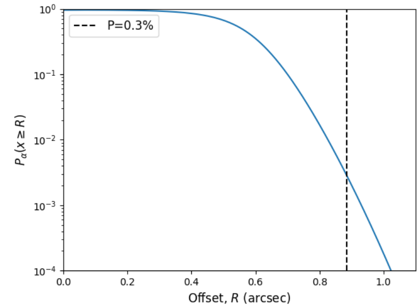

(b) 3σ offset = 0.959”.

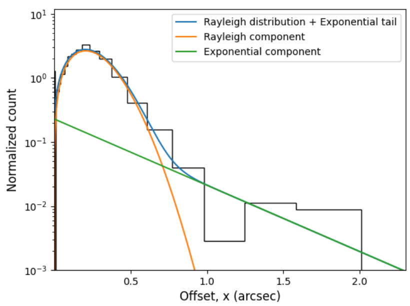

(c) AGN with a peak difference magnitude between 18 and 19.5

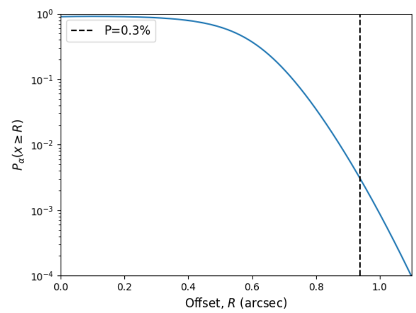

(d) 3σ offset = 1.009”.

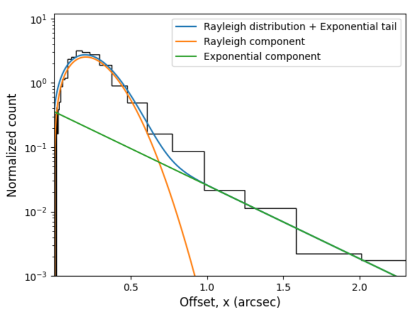

(e) AGN with a peak difference magnitude between 19.5 and 23.

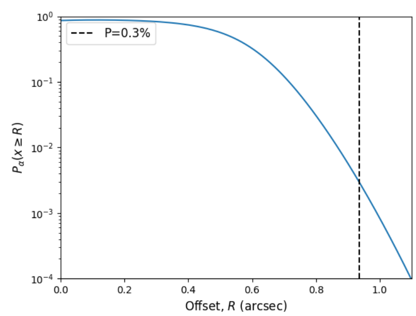

(f) 3σ offset = 0.946”.

Figure 2.16: **Left**: Normalized histogram with logarithmic bins for magnitude weighted AGN–host offsets obtained from g-band ZTF difference images. The best–fit model of a mixture distribution with Rayleigh and exponential components are shown. **Right:** Probability that an offset greater than R is drawn from the Rayleigh component of the mixture distribution shown in (a) instead of the exponential component. The offset where this probability is 0.3% is shown with a dashed line.

Table 2.7: X-ray and radio properties of the 52 ZTF AGN in galaxy mergers. We show the 2–10keV flux in cts/s for the AGN with detections in the second ROSAT All–Sky Survey and conversions to luminosity for those with a spectroscopically confirmed redshift. We also indicate the 20cm flux from the FIRST survey, including upper limits where available, and the corresponding luminosities.

ZTF name	ROSAT flux (cts/s)	$L_{2-10\mathrm{keV}}$ ($\times 10^{44}$ ergs/s)	FIRST flux ($\times 10^{24}$ ergs/cm^2/s)	$L_{5\mathrm{GHz}}$ ($\times 10^{55}$ ergs/s)
ZTF18aaxvmpg	0.196 ± 0.022	1.126 ± 0.129	< 1.39	< 18.552
ZTF18abamzru	< 0.05	–	< 1.33	–
ZTF18aasxvyo	1.728 ± 0.06	–	24.3 ± 1.36	–
ZTF18aaieguy	< 0.05	–	< 1.54	< 20.944
ZTF19aakjemw	0.031 ± 0.011	0.149 ± 0.054	< 1.46	< 8.666
ZTF18aaifbku	0.302 ± 0.025	0.245 ± 0.02	185.3 ± 1.5	208.297 ± 1.686
ZTF18aampabj	< 0.05	–	24.1 ± 1.34	335.637 ± 18.662
ZTF19aaagygp	0.04 ± 0.012	–	–	–
ZTF18abujubn	< 0.05	–	–	–
ZTF18acegbsb	0.034 ± 0.014	0.009 ± 0.004	12.8 ± 0.97	4.206 ± 0.319
ZTF19aaozpdm	< 0.05	–	< 1.39	–
ZTF18aacjltc	0.051 ± 0.015	0.529 ± 0.159	< 1.76	< 18.156
ZTF18abtpite	0.024 ± 0.01	–	–	–
ZTF18abvwrxu	0.163 ± 0.03	–	< 1.42	–
ZTF19abaktpb	< 0.05	–	–	–
ZTF18aaqjcxl	< 0.05	–	< 1.47	< 3.706
ZTF18abyoivl	< 0.05	–	< 1.1	–
ZTF18aabdiug	< 0.05	–	37.4 ± 1.43	35.732 ± 1.366
ZTF19aaviuyv	0.051 ± 0.01	–	–	–
ZTF18aabxczq	< 0.05	–	< 1.45	< 1.43
ZTF18acvwlrf	< 0.05	–	11.6 ± 1.51	192.822 ± 25.1
ZTF19aasejqv	0.086 ± 0.016	0.721 ± 0.135	< 1.34	< 22.161
ZTF18aazogyo	< 0.05	–	< 1.44	< 2.41
ZTF18aceypvy	0.047 ± 0.012	0.215 ± 0.055	< 1.39	< 10.349
ZTF18acbweyd	< 0.05	–	< 1.36	< 14.168
ZTF18acablce	0.022 ± 0.005	–	–	–
ZTF18abhpvvr	0.072 ± 0.014	–	–	–
ZTF19abfqmjg	< 0.05	–	–	–
ZTF18abmqwgr	0.077 ± 0.015	–	–	–
ZTF19aadgbih	0.092 ± 0.016	0.603 ± 0.102	24.9 ± 1.5	279.113 ± 16.814
ZTF19aalpfan	< 0.05	–	< 1.48	< 2.056
ZTF18aawwfep	< 0.05	–	< 1.39	< 15.897
ZTF19aavxims	0.041 ± 0.015	–	< 1.52	–
ZTF19aaaplct	0.165 ± 0.025	–	< 1.48	–
ZTF18aajnqqv	0.02 ± 0.009	0.026 ± 0.012	36.5 ± 1.47	59.825 ± 2.409
ZTF18abszfur	< 0.05	–	< 1.5	< 41.386
ZTF19abucbkt	< 0.05	–	–	–

ZTF18adbhlyb	0.036 ± 0.013	0.253 ± 0.09	< 1.34	< 17.931
ZTF18acxhoij	0.086 ± 0.016	$-$	$-$	$-$
ZTF18acajwep	< 0.05	$-$	$-$	$-$
ZTF19abipoqj	< 0.05	$-$	< 1.05	$-$
ZTF19abpkoou	0.043 ± 0.016	$-$	< 1.08	$-$
ZTF18abztovy	< 0.05	$-$	< 1.54	$-$
ZTF18acsllgd	0.031 ± 0.012	$-$	$-$	$-$
ZTF19aanxrki	0.068 ± 0.014	0.237 ± 0.049	< 1.44	< 4.96
ZTF18aamfuhc	0.341 ± 0.033	0.417 ± 0.04	< 1.42	< 2.693
ZTF18aadwvyr	0.06 ± 0.014	0.252 ± 0.059	< 1.02	< 4.353
ZTF19abauzsd	0.027 ± 0.009	0.643 ± 0.206	< 1.5	< 39.366
ZTF18abufbsq	0.048 ± 0.013	$-$	21.5 ± 1.39	$-$
ZTF18abzuzrg	0.028 ± 0.009	0.169 ± 0.053	< 1.45	< 13.173
ZTF18abtmcdb	0.032 ± 0.01	$-$	< 1.11	$-$
ZTF18aauhnby	0.1 ± 0.018	0.113 ± 0.021	< 1.53	< 3.168

Chapter 3: Variability–selected intermediate mass black hole candidates in dwarf galaxies from ZTF and *WISE*

3.1 Overview

While it is difficult to observe the first black hole seeds in the early Universe, we can study intermediate mass black holes (IMBHs) in local dwarf galaxies for clues about their origins. In this chapter I present a sample of variability–selected AGN in dwarf galaxies using optical photometry from the Zwicky Transient Facility (ZTF) and forward–modeled mid–IR photometry of time–resolved Wide–field Infrared Survey Explorer (*WISE*) coadded images. We found that 44 out of 25,714 dwarf galaxies had optically variable AGN candidates, and 148 out of 79,879 dwarf galaxies had mid–IR variable AGN candidates, corresponding to active fractions of $0.17 \pm 0.03\%$ and $0.19 \pm 0.02\%$ respectively. We found that spectroscopic approaches to AGN identification would have missed 81% of our ZTF IMBH candidates and 69% of our *WISE* IMBH candidates. Only 9 candidates have been detected previously in radio, X-ray, and variability searches for dwarf galaxy AGN. The ZTF and *WISE* dwarf galaxy AGN with broad Balmer lines have virial masses down to $10^{5.5} M_{\odot}$ and for the rest of the sample, BH masses predicted from host galaxy mass range between $10^{5.2} M_{\odot} < M_{\rm BH} < 10^{7.3} M_{\odot}$. We found that only 5 of

152 previously reported variability–selected AGN candidates from the Palomar Transient Factory in common with our parent sample were variable in ZTF. We also determined a nuclear supernova fraction of $0.05 \pm 0.01\%$ year^{-1} for dwarf galaxies in ZTF. Our ZTF and *WISE* IMBH candidates show the promise of variability searches for the discovery of otherwise hidden low–mass AGN.

3.2 Introduction

It is challenging to determine how the very first massive black holes formed because they have grown over time as galaxies merge and their black holes accrete (Volonteri & Begelman, 2010). High redshift black hole (BH) seeds are very difficult to detect due to their low luminosities (Volonteri & Reines, 2016) so we can instead constrain models of BH seed formation by studying the least massive black holes in local galaxies (Reines & Comastri, 2016). These low–mass analogs to black hole seeds are called intermediate mass black holes (IMBHs) and have masses in the range $100 < M_{BH} < 10^6 M_\odot$. Dwarf galaxies of stellar mass $M_* < 10^{9.75} M_\odot$ are the best place to find low–mass black holes because galaxy mass and black hole mass are correlated (e.g. Kormendy & Ho, 2013; Woo et al., 2013). Supernova–driven stunting of black hole growth in dwarf galaxies also makes these black holes comparable to early BH seeds (Anglés-Alcázar et al., 2017; Habouzit et al., 2017).

The low–mass end of galaxy population relations such as the black hole occupation fraction and the slope and scatter of the relationship between black hole mass and the stellar velocity dispersion of the host bulge ($M_{\rm BH} - \sigma_*$, Ferrarese & Merritt (2000)) will vary depending on the formation mechanism of early black hole seeds (see Greene et al., 2020, for a review). For example, Pop III stars will produce a population of undermassive BHs in low redshift galaxies with stellar dispersion $\sigma_* < 100$ km/s while direct collapse mechanisms will produce heavier black holes, resulting in a flattening of the $M_{\rm BH} - \sigma$ relation around masses of $10^5 M_\odot$ (Volonteri & Natarajan, 2009). Although the potential for low–mass black hole populations to constrain BH seed formation histories may be limited by uncertainties in accretion prescriptions (Ricarte & Natarajan, 2018) it nonetheless motivates the discovery of a large population of black holes in low–mass galaxies. A recent effort by Baldassare et al. (2020a) to fill in the low–mass end of the $M_{\rm BH} - \sigma_*$ relation doubled the number of black holes with measured virial masses and stellar velocity dispersions in dwarf galaxies of $M_* < 3 \times 10^9 M_\odot$ to 15 and the results were in agreement with an extrapolation of the linear relationship observed for high–mass galaxies. However, larger numbers of low–mass AGN, particularly in galaxies of mass $M_* < 3 \times 10^8$, are needed to more fully constrain seed models.

The fraction of IMBHs in dwarf galaxies which are wandering in their galaxy haloes, rather than occupying the nucleus, may also constrain BH seed formation mechanisms. The wandering fraction is dependent on galaxy merger history but will be substantially higher if massive black holes were produced by gravitational runaway of massive star remnants (Miller & Hamilton, 2002; Portegies Zwart & McMillan, 2002) due to the high frequency of IMBH ejection during these interactions (Holley-Bockelmann et al., 2008; Volonteri & Perna, 2005). Ricarte et al. (2021b) found that a substantial population of wandering black holes exist in the ROMULUS cosmological simulations and make up 10% of black hole mass in the local universe. Studies of IMBHs of mass

$3.8 < \log M_{\rm BH}(M_\odot) < 7.0$ in cosmological zoom–in simulations suggest that 50% of IMBHs in dwarf galaxies are wandering within 7 kpc of the galaxy center due to historical galaxy mergers (Bellovary et al., 2018, 2021). This is supported by radio observations of dwarf galaxy AGN (Reines et al., 2020). Observational constraints on the wandering fraction of IMBHs in dwarf galaxies will help to test the accuracy of cosmological merger simulations, the effects of gravitational wave recoil on black holes in low–mass galaxies and the feasibility of the gravitational runaway black hole seed formation mechanism.

A major challenge for both the search for IMBHs and for estimating the occupation and wandering fractions is that the predicted accretion rates are very low, particularly for non–nuclear AGN. Black hole accretion may be bimodal in its efficiency, causing low–mass black holes $< 10^5 M_\odot$ to grow more slowly (Pacucci et al., 2018). Bellovary et al. (2018) found that most simulated IMBHs reach a maximum bolometric luminosity of $\log L_{\rm bol}$(erg/s) < 41 and are therefore very difficult to detect. Pacucci et al. (2021) used a theoretical model based on galaxy mass and the angular momentum available in nuclear regions to estimate an active fraction of 5–22% of AGN in dwarf galaxies which increases with host mass. The level of activity likely depends on the merger history of the dwarf galaxy. Kristensen et al. (2021) find that inactive dwarf galaxies in the `Illustris` simulations tend to have been residing in dense environments for long times, while active galaxies had commonly been in a recent ($\leq$ 4 Gyr) minor merger.

Discovery of AGN activity in dwarf galaxies will also help us to test predictions on the importance of AGN feedback in the low–mass regime. While Geha et al. (2012) found that dwarf galaxies in SDSS with no active star formation are extremely rare and that more massive neighboring galaxies were the cause of star formation quenching, Penny et al.

(2018) and Dickey et al. (2019) have found evidence for internal AGN–driven quenching in a small number of dwarf galaxies. Simulations suggest that dwarf galaxies hosting overmassive black holes have lower central stellar mass density, lower H I gas content and lower star formation rates than dwarf galaxies with undermassive counterparts, suggesting that internal feedback in dwarf galaxies can quench star formation only for higher mass black holes (Sharma et al., 2019). Simulations by Koudmani et al. (2019) found that AGN outflows in dwarf galaxies only have a small effect on regulating global star formation rates compared to supernovae and sustained high–luminosity AGN with isotropic winds.

Detailed observational studies of small dwarf galaxy samples have painted a different picture. GMOS IFU observations of 8 dwarf galaxies by Liu et al. (2020) discovered the presence of high velocity outflows in 7 out of 8, with some outflows capable of expelling a portion of outflowing material from the galaxy and enriching the surrounding circumgalactic medium. Coronal line emission inconsistent with shocks was also detected from 5 of these objects Bohn et al. (2021). Larger samples of AGN in dwarf galaxies will allow for further searches for signatures of AGN feedback such as high velocity and large scale outflows.

A range of approaches have been used to obtain samples of AGN candidates in dwarf galaxies. Some studies have taken a spectroscopic approach by looking for the emission line signatures of AGN in low–mass galaxies. Reines et al. (2013) found that 151 dwarf galaxies with masses $10^{8.5}M_{\odot} < M_{*} < 10^{9.5}M_{\odot}$ amongst a sample of 25,000 had [O III] λ5007/Hβ and [N II] λ6550/Hα narrow emission line ratios indicative of AGN activity. Mezcua & Domínguez Sánchez (2020) found a sample of 37 dwarf galaxies with 'hidden' AGN ionization lines by spatially resolving emission from star forming regions and nuclear AGN within each dwarf galaxy using MaNGA integral field unit spectroscopy. Molina et al. (2021) used [Fe X] λ6374 coronal line emission as a signature of AGN accretion to find 81 dwarf galaxies with possible IMBHs.

Multi–wavelength approaches have also been successful in the identification of AGN in dwarf galaxies. Mezcua et al. (2018) identified 40 AGN in dwarf galaxies with stellar masses $10^7 M_\odot < M_* < 3 \times 10^9 M_\odot$ via their X-ray emission in the *Chandra* COSMOS–Legacy Survey, finding an AGN fraction of ∼0.4% for redshifts less than 0.3. Reines et al. (2020) found that 39 of 111 dwarf galaxies had compact radio sources at 8–12 GHz with the Karl G. Jansky Very Large Array (VLA) and determined that 13 of these could confidently be classified as AGN. They also found that 10 of the 13 radio AGN detected were spatially offset from their optical galaxy nuclei.

A new approach to the detection of IMBH candidates has been to search for AGN–like stochastic variability from low–mass galaxies as a signature of the presence of a central BH. Baldassare et al. (2018) found 135 galaxies with AGN–like variability on yearly timescales when constructing light curves of ~ 28000 galaxies with SDSS spectra, including 12 from dwarf galaxies with stellar masses $M_* < 3 \times 10^9 M_\odot$. They therefore estimated a variability fraction of 0.1% for AGN in dwarf galaxies. A similar study in 2020 used light curves from the Palomar Transient Factory (Law et al., 2009) to search for variable AGN in 35,000 galaxies with stellar mass $M_* < 10^{10} M_\odot$, identifying variability in 102 galaxies with masses $M_* < 3 \times 10^9 M_\odot$ (Baldassare et al., 2020b).

As some low–mass AGN vary on hourly timescales, very high cadence surveys have proved effective for the discovery of variability from dwarf galaxy AGN. For example, Burke et al. (2020a) produced a 30 minute cadence, one month long light curve of the

AGN in the archetypal dwarf galaxy NGC 4395 using data from the Transiting Exoplanet Survey Satellite (TESS). The $\sim\ 10^5 M_\odot$ black hole was variable with a characteristic timescale of $1.4^{+1.9}_{-0.5}$ days. Martínez-Palomera et al. (2020) used data from the HiTS imaging survey, which undertook one week of high cadence (4 times per night) and high coverage (120–150 deg^2) observations with the Dark Energy Camera each year for three years, to search for short timescale IMBH variability. They identified 500 galaxies with hourly, small amplitude variation in their week–long light curves. They estimated that 4% of dwarf galaxies contained an IMBH based on their results. Shaya et al. (2015) monitored ~500 galaxies with the Kepler telescope (Borucki et al., 2010) and found that while 4% showed bright AGN activity, many other galaxies exhibited faint (down to 0.001 magnitude) variability which may also have been due to the presence of a low–mass AGN.

Recently, Secrest & Satyapal (2020) undertook a search for variable AGN in the mid–IR. This was motivated by the sensitivity of mid–IR studies to low luminosity AGN which are frequently optically obscured and Compton–thick (Annuar et al., 2017; Ricci et al., 2016) and frequently unobservable in the soft X-rays (Polimera et al., 2018), along with the low contamination rates of supernovae due to weak mid–IR emission (Smitka, 2016). To produce mid–IR light curves, Secrest & Satyapal (2020) used multi–epoch photometry from the Wide–field Infrared Survey Explorer (Wright et al., 2010, *WISE*). *WISE* mapped the sky in the W1 (3.4μm) and W2 (4.6μm) bands with 6 month cadence over an 8 year baseline between the initial observations in 2010, the Near–Earth Object Wide–field Infrared Survey Explorer mission from 2010–2011 (*NEOWISE*; Mainzer et al., 2011a) and the reactivation mission beginning in 2013 (*NEOWISE*–R; Mainzer et al., 2014). Secrest & Satyapal (2020) found a sample of 2,199 dwarf galaxies of stellar mass $M_* < 2 \times 10^9 M_\odot$ and redshift $0.02 < z < 0.03$ from the NASA–Sloan Atlas which had corresponding sources in the All*WISE* catalog. Amongst this sample, only 2 (0.09%) showed significant variability in light curves produced by the All*WISE* Multiepoch Photometry Table and the *NEOWISE*–R Single Exposure Source Table.

Variability–based search strategies have been particularly good at finding AGN candidates in dwarf galaxies which are optically obscured or unidentifiable by their spectroscopic signatures. For example, only 25% of the optically variable AGN candidates in galaxies of mass $M_* < 10^{10} M_\odot$ found in PTF were classified as AGN or Composite galaxies based on their narrow emission lines (Baldassare et al., 2020b). This is likely due to a combination of star formation dilution of AGN emission lines and the hardening of the accretion disk SED around lower mass BHs which extends the partially ionized zone and reduces the emission line ratios normally used for AGN classification (Cann et al., 2019). Variability–based strategies therefore have an important place for finding AGN which would otherwise be missed due to biases in other selection techniques.

Previous searches for active IMBH candidates in dwarf galaxies with spectroscopic, radio, X-ray and mid–IR observations have not provided a complete, unbiased census of the IMBH occupation fraction because different strategies are hindered by high star formation rates, obscuration and low accretion luminosities. Therefore, despite the discoveries of these large samples of dwarf AGN candidates, there are very few confirmed IMBHs with well–sampled SEDs and measured virial black hole masses which we can use to occupy the sparsely populated low–mass ends of a number of black hole–galaxy scaling relations. This motivates the development of effective search strategies for identifying substantially larger samples of IMBH candidates. This will provide more opportunities for careful confirmation and multi–wavelength characterization of the best candidates, especially those with broad Balmer lines.

In this chapter we present a comprehensive search for AGN–like variability from a large sample of dwarf galaxies in the optical and mid–IR in order to build upon the previous successes of Baldassare et al. (2018, 2020b) and Secrest & Satyapal (2020) with SDSS, PTF and *WISE*. For our optical search we have used observations from the Zwicky Transient Facility (ZTF; Bellm et al., 2019a; Dekany et al., 2020; Graham et al., 2019), a new and ongoing optical survey which began in March 2018 and achieves single epoch limiting magnitudes of ~ 20.5 in g-, r- and i-band over a survey footprint of 23,675 deg^2. The Northern Sky Survey of ZTF Phase I (Mar 2018 – Sep 2020) had an average cadence of 3 days and this was supplemented by higher cadence sub–surveys with hourly to 1 day cadences (Bellm et al., 2019b). The ongoing ZTF Phase II (Oct 2020 – present) Northern Sky Survey has a 2 day cadence. By comparison, PTF had a footprint of ~ 8000 deg^2 and a ~ 5 day cadence. To expand upon the mid–IR variability search of Secrest & Satyapal (2020), we have made use of new forward modeled photometry catalogs of time–resolved *WISE* coadds to produce more sensitive photometry of a larger dwarf galaxy sample. We do this work in preparation for the upcoming Legacy Survey of Space and Time (LSST) at Vera C. Rubin Observatory (Ivezić et al., 2019) which will provide a more complete census of variable IMBHs over the next decade due to its expected single visit limiting magnitude of g ∼25 at a 3 day cadence spanning ∼10 years.

In Section 3.3 we describe our dwarf galaxy sample selection process. In Section 3.4 we describe our procedure for ZTF forced photometry of the dwarf galaxy sample.

In Section 3.5 we describe our selection strategy for finding the optically variable AGN. In Section 3.6 we present our sample of IMBH candidates and supernovae from ZTF and describe their multiwavelength and spectroscopic properties. In Section 3.7 we describe our selection of variable AGN in *WISE* based on forward modeled photometry of time resolved coadds and in Section 3.8 we discuss the multi–wavelength and spectroscopic properties of the *WISE*–selected IMBH candidates. In Section 3.9 we discuss the merits of the two selection strategies and the properties of the IMBH candidates in further depth.

3.3 Dwarf galaxy sample selection

We selected a sample of dwarf galaxies using the NASA–Sloan Atlas (NSA) version v1_0_1 [1]. The NSA produced stellar mass estimates for galaxies by fitting 5 templates derived from stellar population synthesis models (Blanton & Roweis, 2007; Bruzual & Charlot, 2003) to SDSS images of galaxies after subtracting the sky background (Blanton et al., 2011). We used this catalog of stellar masses to allow for more direct comparison to other AGN variability searches which classify dwarf galaxies using stellar masses from this catalog (e.g. Baldassare et al., 2018, 2020b; Reines et al., 2013; Secrest & Satyapal, 2020).

When compiling our list of dwarf galaxies from the NSA we required redshifts of $0.02 < z < 0.35$ and elliptical Petrosian masses of $M_* < 3 \times h^{-2} 10^9 M_\odot$. We selected an h value of 0.73 for consistency with Reines et al. (2013) and Secrest & Satyapal (2020) such that our mass cutoff corresponds to $M_* < 10^{9.75} M_\odot$. After finding some high redshift quasars listed in the catalog with erroneous redshifts and underestimated stellar

[1] https://www.sdss.org/dr16/manga/manga-target-selection/nsa

masses, we required the NSA redshift to be derived from an SDSS spectrum (described by the `ZSRC` column in the NSA table). This resulted in a final sample of 81,462 dwarf galaxies.

For the ZTF photometry, we also required that the objects overlap with > 100 high quality g and r band ZTF images over a > 1 year baseline. Due to computational limitations, we selected a random subset of the parent light curve sample consisting of 25,714 dwarf galaxies for our ZTF variability search. For our *WISE* variability search we required there to be > 5 epochs over a > 3 year baseline and this resulted in a final sample of 79,879 objects for the mid–IR search.

We produced a control sample of optically variable AGN with host galaxies of mass $M_* > 10^{9.75} M_\odot$ from a parent sample of 5,493 variable ZTF AGN found by Ward et al. (2021a). This AGN sample was obtained from the ZTF alert stream (Patterson et al., 2019) using the AMPEL alert broker `AMPEL` (Alert Management, Photometry and Evaluation of Lightcurves; Nordin et al., 2019a) to crossmatch ZTF transients to AGN catalogs using `catsHTM` (Soumagnac & Ofek, 2018) and check for AGN–like variability with the Butler & Bloom (2011) quasar modeling routine. We matched the AGN from this sample to the NASA–Sloan Atlas with a 5” radius and found 1,053 objects with measured galaxy masses. Both the control sample and the dwarf galaxy sample were processed by the following photometry pipeline.

3.4 ZTF photometry of dwarf galaxies

Difference imaging to detect variability requires the production of reference images, which are co–added stacks of exposure images to support image differencing downstream. To produce new ZTF forced photometry with custom, deeper references than the main ZTF alert pipeline we implemented the ZUDS photometry pipeline[2] on our dwarf galaxy and AGN control samples. We generated reference images for each field, CCD, quadrant and filter from ZTF single epoch science images by selecting up to 60 images as close as possible in time which met the following criteria established by Masci et al. (2019) for the main ZTF alert pipeline:

1. Seeing within the range $2.''0 \leq$ FWHM $\leq 5.''0$, with priority given to images with lower seeing values.
2. Quality status $= 1$
3. Magnitude zeropoints given by $25.3 \leq$ MAGZP(g) ≤ 26.5 or $25.3 \leq$ MAGZP(r) ≤ 26.5 for filters g and r respectively.
4. Color coefficients given by $-0.20 \leq$ CLRCOEFF(g) ≤ 0.15 or $-0.05 \leq$ CLRCOEFF(r) ≤ 0.22 for filters g and r respectively.
5. Limiting magnitudes given by MAGLIM(g) ≥ 19.0 or MAGLIM(r) ≥ 19.0 for filters g and r respectively.
6. Global pixel median ≤ 1900 DN or ≤ 1600 for filters g and r respectively.

[2] https://github.com/zuds-survey/zuds-pipeline

7. Global robust pixel RMS ≤ 100 DN.

8. Acquired after camera reinstallation on February 5, 2018 UT.

When there were multiple field, CCD and quadrants containing the source for a particular filter, we selected the reference image containing the largest number of high quality ZTF science images in the coadd to be the reference image. We produced 1000"x1000" cutouts of each single epoch science image and reference image, produced subtractions, then undertook aperture photometry with a 3".0 radius. We then applied the aperture to PSF correction factors produced by the main ZTF image pipeline to produce PSF photometry light curves. We measured the baseline flux of each object in the reference image and added this to the fluxes measured from the image subtractions.

In order to improve our sensitivity to low S/N variability from faintly varying AGN and prepare the data for calculation of the Pearson correlation coefficient between g- and r-band photometry, we binned the data in temporal bins. We first applied zeropoint corrections, then undertook error–weighted binning in flux space using bins of 5, 10 and 20 day increments. Therefore, each galaxy had 3 light curves with different bin sizes for the calculation of variability statistics. This binning procedure may have reduced our sensitivity to objects with optical variability only on timescales <20 days and therefore may have introduced biases against particularly low–mass AGN. However, we determined that binning was necessary to both allow for the calculation of the Pearson r correlation coefficient whilst confidently identifying light curves with correlated variability over a range of timescales, as expected from AGN power spectra (Burke et al., 2021; Kelly et al., 2009; MacLeod et al., 2011) With this procedure we generated light curves of

25,714 dwarf galaxies and the 1,053 AGN from the high–mass galaxy control sample.

3.5 Selection of variable IMBH candidates

In order to detect real variability amongst the sample of dwarf galaxy light curves we trialed a number of variability statistics including the Pearson correlation coefficient (as used by Secrest & Satyapal (2020)), the goodness of fit of the light curves to the quasar structure function (using `qsofit` (Butler & Bloom, 2011), as used in Baldassare et al. (2018, 2020b); Ward et al. (2021a)), the excess variance (Martínez-Palomera et al., 2020; Sánchez et al., 2017) and the χ^2/N in g and r bands. We found that a combination of the Pearson correlation coefficient and χ^2 produced the best separation between the AGN control sample and the majority of the non–variable dwarf galaxy population.

The Pearson correlation coefficient r between the binned g and r band fluxes was calculated as:

$$r = \frac{C_{f_g,f_r}}{\sigma_{f_g}\sigma_{f_r}} \tag{3.1}$$

where C_{f_g,f_r} is the covariance between g and r bands given by

$$C_{f_g,f_r} = \frac{1}{N-1}\sum_{i}^{N}(f_{g,i} - \langle f_g \rangle) \times (f_{r,i} - \langle f_r \rangle) \tag{3.2}$$

and σ_{f_g} and σ_{f_r} are the g and r band variability amplitudes given by:

$$\sigma_f^2 = \frac{1}{N-1}\sum_{i}^{n}(f_i - \langle f \rangle)^2 \tag{3.3}$$

and the expectation value $\langle f \rangle$ was given by the median flux.

We also calculated the χ^2/N of the light curves in g and r bands:

$$\chi^2/N = \frac{1}{N}\sum_{i}^{N}\frac{(f_i - \langle f\rangle)^2}{\sigma_i^2} \tag{3.4}$$

The distribution of the Pearson correlation coefficient r and the χ^2/N values for g and r bands for the dwarf galaxy and control AGN light curves with 5, 10 and 20 day bin sizes is shown in Figure 3.1. We applied cutoffs of $r > 0.2$, $r > 0.3$, and $r > 0.4$ for 5, 10 and 20 day bin sizes respectively, and $\chi^2/N > 3$ in both filters for all bin sizes, to classify dwarf galaxies as variable. Each dwarf galaxy was required to meet this cutoff in all 3 binning timescales to ensure that correlations and variance was not produced as artifacts of bin phase and size.

We then manually inspected the light curves and subtractions to remove light curves with high variance due to poor quality photometry and to determine which light curves contained single flares with reddening consistent with supernovae. 36 supernovae–like flares were found, corresponding to a nuclear SN rate of $0.14 \pm 0.02\%$ ($0.05 \pm 0.01\%$ year^{-1}) for dwarf galaxies in ZTF Phase I.

This process produced a final sample of 44 dwarf galaxies ($0.17 \pm 0.03\%$) with variability consistent with AGN activity. These constitute our set of optically variable IMBH candidates. The properties of this sample are summarized in Table 3.1. Examples of ZTF light curves of 3 dwarf galaxies with AGN–like variability are shown in Figure 3.2 and examples of 3 supernova light curves are shown in Figure 3.3.

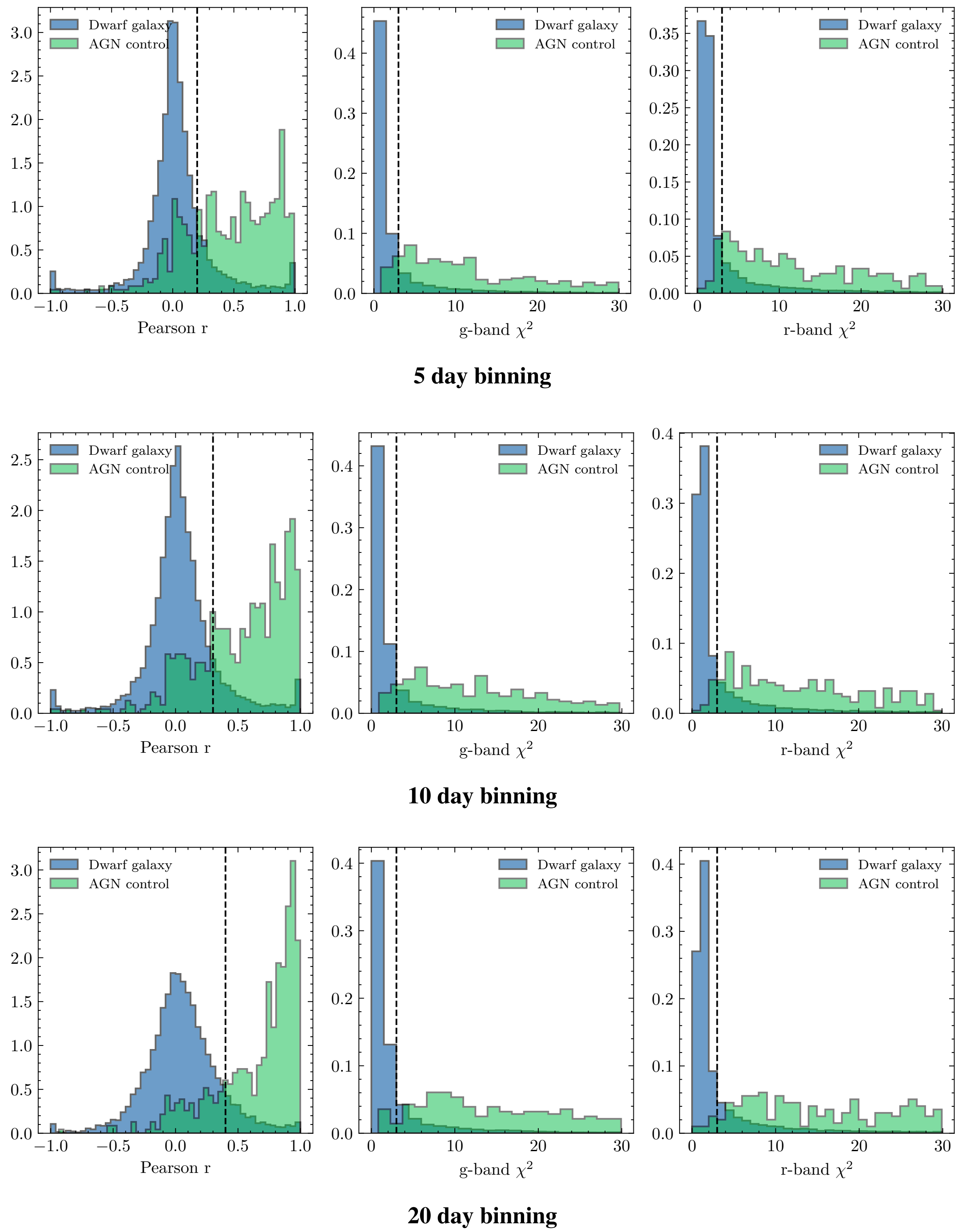

Figure 3.1: Pearson r correlation coefficient and χ^2/N in g- and r-band calculated from ZTF light curves for 3 different binning timescales. We show the entire dwarf galaxy population with ZTF photometry in blue and the AGN control sample (from host galaxies of stellar mass $M_* > 3 \times 10^{9.75} M_\odot$) in green. The cutoffs used for AGN candidate selection are shown in black dotted lines for each statistic. We required the 3 statistics to satisfy the cutoffs for all 3 binning timescales in order for a candidate to be selected.

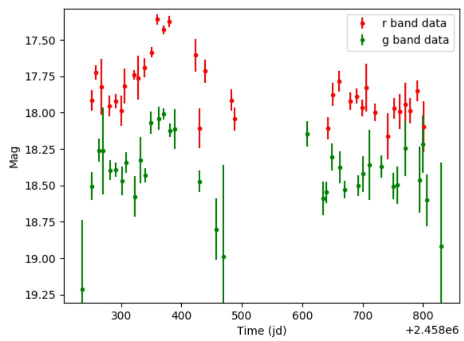

NSA189758

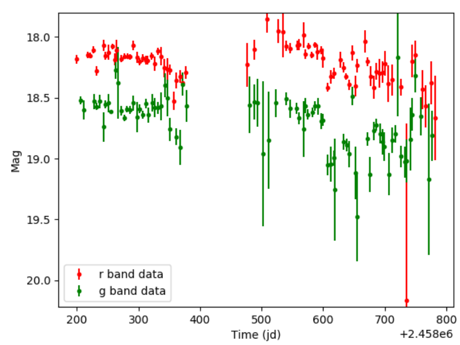

NSA212423

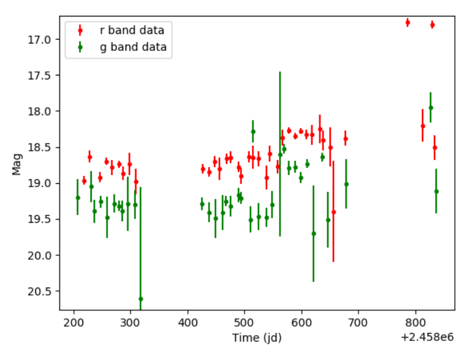

NSA158589

Figure 3.2: Three examples of ZTF light curves which passed the variability criteria and were classified as variable AGN candidates.

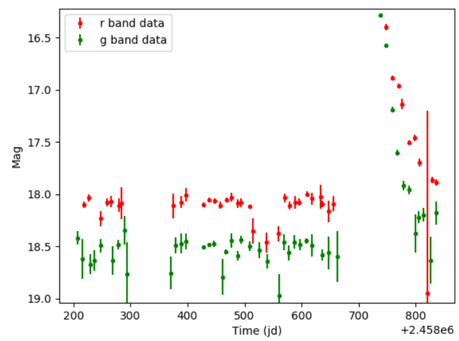

NSA164967

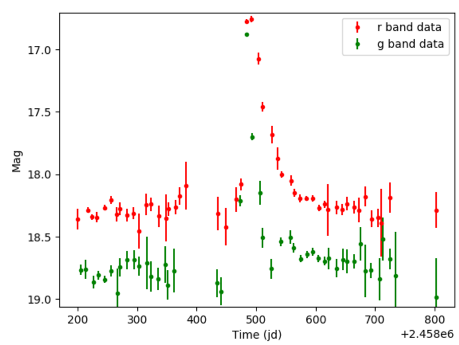

NSA136891

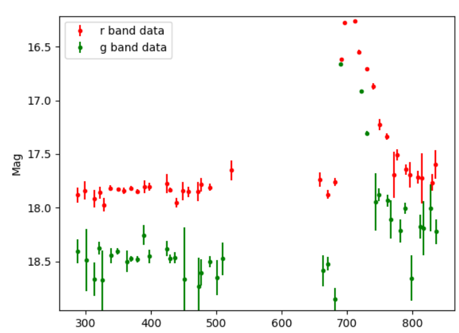

NSA33420

Figure 3.3: Three examples of ZTF light curves which passed the variability criteria and were classified as supernova candidates.

Table 3.1: Properties of the 44 AGN candidates with significant and correlated g and r band variability found in ZTF. The IDs, positions, redshifts and host galaxy stellar masses are those from the NSA catalog version $\mathrm{v1\_0\_1}$. In the first $\log_{10}M_{BH}$ column we show the estimated black hole mass based on the $M_* - M_{BH}$ from Schutte et al. (2019) which has a scatter of 0.68 dex. The presence of Balmer broad lines is indicated in the BLR column. Virial masses were calculated for broad line AGN by Ho & Kim (2015) based on the width of the Hα broad lines.

NSA ID	RA (hms)	Dec (dms)	z	$\log_{10}M_*$ ($M_\odot$)	$\log_{10}M_{BH}$ ($M_\odot$)	BPT class	Broad lines	$\log_{10}M_{BH,vir}$ ($M_\odot$)
8479	12:31:07.418	00:27:47.447	0.0214	9.51	6.95	SF	×	-
19864	12:36:43.723	-3:01:15.176	0.0082	8.12	5.23	SF	×	-
20245	12:42:32.662	-1:21:02.583	0.0037	8.75	6.01	SF	×	-
23518	16:21:41.608	01:02:53.989	0.0324	9.57	7.03	SF	×	-
30890	23:18:28.463	00:20:47.845	0.0341	9.66	7.14	Composite	×	-
32653	00:09:26.408	00:19:32.182	0.1138	9.74	7.24	Seyfert	✓	7.048
35747	01:10:59.314	00:26:01.103	0.0188	9.7	7.19	Seyfert	✓	7.561
37197	01:44:32.794	00:57:15.492	0.0716	9.59	7.05	SF	×	-
42027	00:43:38.702	14:38:29.188	0.0766	9.74	7.24	SF	×	-
43101	01:06:29.847	14:58:17.054	0.0393	9.54	6.99	SF	×	-
44934	02:11:58.218	14:16:09.393	0.0264	9.45	6.88	SF	×	-
46229	07:47:06.104	37:36:55.296	0.0364	9.54	6.99	SF	×	-
49405	08:29:12.677	50:06:052.41	0.0432	9.54	6.99	SF	✓	6.363
52237	09:16:08.642	55:59:22.952	0.0721	9.67	7.15	SF	×	-
78310	09:05:10.183	50:42:10.045	0.0369	9.74	7.24	SF	×	-
83637	10:19:48.118	03:31:18.466	0.0324	9.05	6.38	SF	×	-
95377	15:23:50.527	56:48:15.474	0.0511	9.41	6.83	SF	×	-
97216	16:05:40.674	50:45:16.842	0.0129	8.2	5.33	SF	×	-
115553	02:54:57.457	00:25:55.471	0.1077	9.47	6.9	SF	×	-
117445	22:16:19.958	-7:20:55.229	0.0591	9.15	6.51	SF	×	-

127775	00:17:18.375	15:49:06.185	0.0603	9.36	6.77	SF	×	-
132743	09:49:53.016	60:53:25.584	0.0828	9.57	7.03	SF	×	-
133634	11:00:44.374	60:20:05.121	0.0171	8.46	5.65	SF	×	-
138748	14:55:45.198	57:20:49.518	0.0795	9.56	7.01	SF	×	-
142229	15:57:46.352	47:17:47.018	0.0316	9.35	6.75	SF	×	-
142571	16:20:58.965	45:10:54.736	0.0542	9.51	6.95	Composite	×	-
158589	11:30:27.424	52:18:13.171	0.0483	9.37	6.78	SF	×	-
159003	11:41:52.296	52:38:24.914	0.0191	8.91	6.21	SF	×	-
164884	09:28:01.292	49:18:17.303	0.1143	9.71	7.2	SF	✓	6.961
168943	13:45:010.34	-3:01:20.764	0.0469	9.42	6.84	SF	×	-
181600	13:06:15.181	58:57:0033.1	0.0292	9.64	7.11	Seyfert	✓	6.732
183841	11:09:18.046	49:47:53.629	0.0466	9.3	6.69	SF	×	-
188282	17:15:34.141	31:31:45.348	0.0229	9.61	7.08	SF	×	-
189758	21:05:04.972	00:01:010.03	0.0312	9.46	6.89	Composite	×	-
197553	10:57:14.371	54:10:56.999	0.072	9.34	6.74	SF	×	-
198091	11:32:00.219	53:42:50.763	0.0268	9.62	7.09	SF	×	-
202748	21:24:056.67	00:38:45.601	0.048	9.19	6.56	SF	×	-
212423	16:18:03.954	35:08:08.626	0.033	9.59	7.05	SF	×	-
272369	11:38:55.181	44:19:031.64	0.0321	9.45	6.88	Composite	×	-
277358	14:52:32.685	36:24:47.857	0.0542	9.52	6.96	SF	×	-
298494	12:19:51.136	47:50:37.875	0.0384	9.71	7.2	Seyfert	×	-
301868	13:25:45.394	46:07:01.166	0.0365	9.25	6.63	SF	×	-
451469	14:14:05.019	26:33:36.804	0.0358	9.66	7.14	SF	✓	6.303
545880	13:37:02.948	18:10:13.979	0.0265	8.82	6.1	SF	×	-

The distributions of the redshifts and host galaxy stellar masses of the optically variable dwarf galaxies are shown in Figure 3.4. All but 6 of the IMBH candidates were in galaxies of mass $M_* > 10^9 M_\odot$. By comparison, a larger fraction of supernovae were observed in low–mass galaxies and most were found in a narrow redshift range of $0.02 < z < 0.055$.

We checked both the supernova and AGN candidate samples for spectroscopic classification on the Transient Name Server[3]. 25 of the 36 supernova candidates had published spectroscopic classifications. One of these was classified as a supernova but was not typed. 17 out of the remaining 24 (71%) were classified as SNIa, SNIc or SNIc–BL. 7 out of 24 (29%) were classified as SNII or SNIIn. These classifications are shown in Table 3.2. We note that the remaining 11 SN without spectroscopic classifications can only be classified as SN candidates, as they may be AGN outbursts (Drake et al., 2019). None of the AGN candidates had spectroscopic classifications published on TNS.

[3]https://www.wis-tns.org/

Table 3.2: Properties of the 36 supernova candidates with significant and correlated g and r band variability found in ZTF. The IDs, positions, redshifts and host galaxy stellar masses are those from the NSA catalog version $\mathrm{v}_{1\_0\_1}$. The presence of Balmer broad lines is indicated in the BLR column. The last column shows the spectroscopic classification made published by ZTF on the Transient Name Server.

NSA ID	RA (hms)	Dec (dms)	z	$\log_{10}M_*(M_\odot)$	BPT class	Broad lines	Classification
6971	12:00:49.206	-1:15:01.297	0.021	8.55	SF	$\times$	None
8600	12:35:43.642	00:13:25.722	0.0231	9.43	Seyfert	$\times$	None
14878	14:48:27.429	00:12:04.871	0.0269	8.94	SF	$\times$	None
33420	00:28:51.572	-1:04:22.318	0.0333	9.25	SF	$\times$	SNIa
38750	02:33:46.936	-1:01:28.378	0.0489	9.51	SF	$\times$	None
41092	03:35:26.631	00:38:11.445	0.0232	8.23	SF	$\times$	None
47343	08:00:26.505	42:49:16.255	0.0408	9.58	SF	$\times$	SNIa
60574	10:26:03.501	64:50:10.285	0.0368	9.47	SF	$\times$	SNIa
60660	10:40:58.604	65:30:54.366	0.0108	8.25	SF	$\times$	SNIc
70478	13:02:24.185	03:22:032.91	0.0234	9.25	SF	$\times$	None
77819	08:35:16.365	48:19:01.178	0.0429	9.55	SF	$\times$	SNIc
81368	08:55:49.031	03:38:32.333	0.0274	9.59	SF	$\times$	SNIIn
90779	11:11:03.618	64:14:46.086	0.0352	9.46	SF	$\times$	SNII
121437	21:51:07.575	12:25:36.661	0.0285	9.46	SF	$\times$	SNIc-BL
126810	23:58:48.168	14:44:29.893	0.0274	8.95	SF	$\times$	SNII
136564	13:21:28.156	62:52:029.91	0.0413	9.66	SF	$\times$	SNIa
136891	13:29:31.023	61:26:000.53	0.0313	9.25	SF	$\times$	None
137293	14:02:21.316	59:25:08.501	0.0321	9.61	SF	$\times$	None
137916	14:17:15.746	59:16:39.876	0.0365	9.24	SF	$\times$	SNIa
141203	03:26:45.983	01:11:01.017	0.0485	9.13	SF	$\times$	SNIa
146295	11:19:04.838	03:42:53.379	0.0273	8.74	SF	$\times$	None
164967	09:35:11.377	48:43:08.652	0.0244	8.9	SF	$\times$	SNIa
183178	10:43:31.995	48:26:37.354	0.0413	9.44	SF	$\times$	SNIa

191873	09:36:08.603	06:15:25.511	0.008	8.43	SF	$\times$	SN
208509	14:20:52.371	50:31:28.532	0.0446	9.52	SF	$\times$	SNII
211965	16:12:50.281	36:01:18.328	0.0314	9.09	SF	$\times$	None
214163	02:36:15.641	-1:11:59.948	0.0471	9.2	SF	$\times$	SNIa
216212	00:13:45.056	00:51:05.651	0.0322	8.55	SF	$\times$	None
220206	14:49:48.132	54:48:46.962	0.0448	9.47	SF	$\times$	SNIa
224290	16:57:15.706	31:57:50.583	0.0377	9.3	SF	$\times$	SNII
229236	09:04:08.208	39:40:35.155	0.028	9.5	SF	$\times$	SNIa
249950	15:08:50.831	40:42:44.478	0.0305	9.38	SF	$\times$	SNII
269844	10:23:20.137	41:23:40.255	0.0515	9.6	SF	$\times$	SNIa
271156	11:02:16.807	44:20:06.661	0.0246	9.64	Composite	$\times$	SNII
289679	10:15:29.897	37:59:02.588	0.054	8.93	SF	$\times$	SNIa
298529	12:22:36.827	47:58:08.744	0.0499	9.5	SF	$\times$	SNIa

In order to estimate the black hole masses of our IMBH candidates based on their host galaxy stellar mass we used the updated relationship between black hole mass and bulge mass derived by Schutte et al. (2019). This study found a linear relationship based on a sample of galaxies with carefully measured black hole and bulge masses including 8 dwarf galaxies with stellar masses $\log(M_*) < 8.5 M_\odot$:

$$\log(M_{\rm BH}/M_\odot) = \alpha + \beta \log(M_*/10^{11} M_\odot) \tag{3.5}$$

$$\alpha = 8.80 \pm 0.085; \beta = 1.24 \pm 0.081$$

The relation has a scatter of 0.68 dex. The black hole mass estimates for the IMBH candidates are shown in Table 3.1.

3.6 Spectroscopic and multi–wavelength properties of the ZTF–selected IMBH candidates

In order to determine the spectroscopic class of the IMBH candidates on the Baldwin, Phillips and Terlevich diagram (Baldwin et al., 1981; Veilleux & Osterbrock, 1987) we fit the narrow emission line ratios with Penalized Pixel Fitting (pPXF) (Cappellari, 2017; Cappellari & Emsellem, 2004). This method finds the best fit stellar continuum and absorption model using a large sample of high resolution templates of single stellar populations adjusted to match the spectral resolution of the input spectrum. We simultaneously fit the narrow Hα, Hβ, Hγ, Hδ, [S II] λ6717, 6731, [N II] λ6550, 6575, [O I] λ6302, 6366 and [O III] λ5007, 4959 narrow emission lines as well as the best

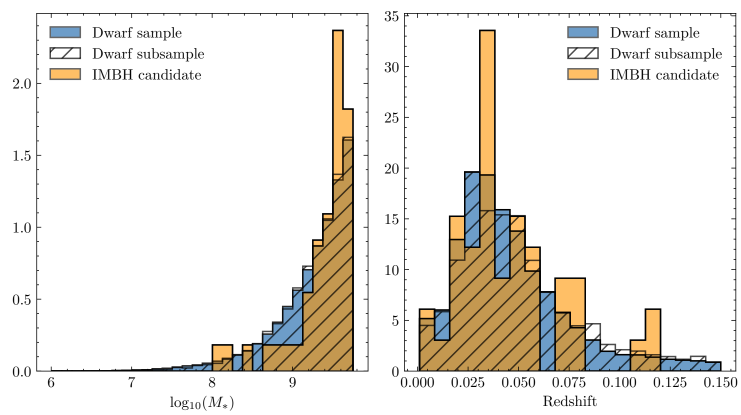

AGN candidate sample

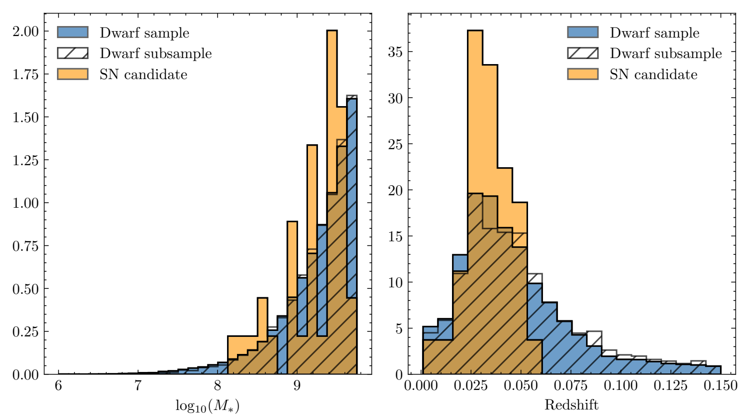

Supernova sample

Figure 3.4: Normalized galaxy mass and redshift distributions of variable IMBH candidates (top) and supernova candidates (bottom) shown in green and the parent dwarf galaxy sample shown in blue. The subset of the parent dwarf galaxy for which ZTF photometry was produced for the optical IMBH search is shown in the hatched histogram. Redshifts and host galaxy mass measurements were derived from the NSA.

fit stellar continuum spectrum during template fitting.

The classification of the IMBH candidates on the [O III] λ5007/Hβ – [N II] λ6583 /Hα BPT diagram is shown in Figure 3.5. 35 objects (81%) are classified as star forming while 4 objects (9%) are in the composite region and 4 (9%) are classified as Seyferts. For comparison, we also show the density of the original 81,462 dwarf galaxy parent sample on the BPT diagram using emission line ratios quoted in the NSA catalog. From the grey contours it can be seen that the majority of the dwarf galaxy population is star forming but a small population extends out to AGN and LINER regions of the BPT classification scheme. Our typical star forming IMBH candidates lie at higher emission line ratios than this population, in part because our `pPXF` modeling considers stellar absorption of those lines.

The classification of the supernova host galaxies on the [O III] λ5007/Hβ – [N II] λ6583 /Hα BPT diagram is also shown in Figure 3.5. 34 host galaxies (94%) are classified as star forming while 1 object (3%) was in the composite region and 1 (3%) in the Seyfert region.

We crossmatched our ZTF–selected IMBH candidates to the active dwarf galaxies from the Secrest & Satyapal (2020) mid–IR variability search, the Baldassare et al. (2018, 2020b) optical variability searches, the Molina et al. (2021) [Fe X] λ6374 coronal line emission search, the Mezcua & Domínguez Sánchez (2020) IFU spectroscopy search, the Mezcua et al. (2018) Chandra X-ray search, the Latimer et al. (2021) mid–IR color selection box search and the Reines et al. (2013) optical emission line search. We found that only 7 objects had been detected in previous optical variability searches (Baldassare et al., 2018, 2020b), where they have different IDs due to the use of NSA

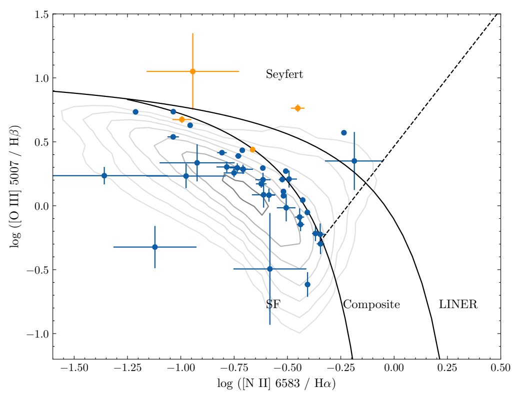

AGN candidates

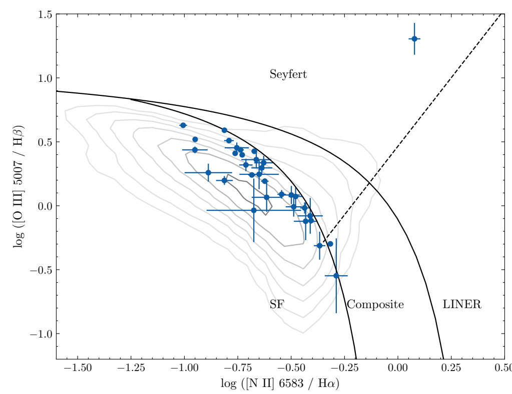

Supernova candidates

Figure 3.5: BPT diagram showing narrow line ratios derived from `pPXF` fitting of archival SDSS spectra of the ZTF–selected IMBH candidates (left) and supernova candidates (right). Orange points show line ratios for IMBH candidates with broad Balmer lines in archival spectra and blue points show those with narrow emission lines only. Grey contours show the population density with log scaling of the entire parent dwarf galaxy sample for line ratios derived from the NASA–Sloan Atlas. Classification regions are labeled in black text. We note that because `pPXF` determines narrow emission line strength after accounting for stellar absorption of those same lines, fluxes may appear to be slightly larger in the BPT diagram compared to the NSA–derived emission lines fluxes of the dwarf galaxy population.

version $v_{0\_1\_2}$: NSA32653 (SDSS), NSA49405 (PTF), NSA115553 (SDSS), NSA181600 (PTF), NSA202748 (PTF), NSA451469 (PTF) and NSA545880 (PTF). No other multi–wavelength detections of our candidates from previous IMBH searches were found.

NSA32653, NSA35747, NSA49405, NSA164884, NSA464884, NSA181600 and NSA451469 were the only objects in our IMBH sample to exhibit broad Balmer lines in archival SDSS spectra. These objects previously had their virial black hole masses estimated using the width of the Hα broad lines by Ho & Kim (2015) and Liu et al. (2019). These virial masses ranged between $10^{6.3} M_{\odot}$ and $10^{7.6} M_{\odot}$ and are shown in Table 3.1.

3.7 ZTF variability of previously reported PTF–selected IMBH candidates

After discovering that 5 objects from the variability selected AGN sample from PTF (Baldassare et al., 2020b) were also variable in ZTF according to our selection thresholds, we decided to determine if the remaining AGN candidates in dwarf galaxies from PTF had ZTF variability which was missed by our selection criteria.

We first found that our parent dwarf galaxy sample had 152 objects which overlapped with the variable PTF sample. We then visually inspected the `zuds-pipeline` light curves we made of the 152 common dwarf galaxies and confirmed that no other dwarf galaxy had apparent variability. We then used the ZTF forced photometry service (Masci et al., 2019) to obtain alternative photometry of the sources with the original ZTF reference images. After removing poor quality images by requiring the `procstatus` flag be $= 0$, we measured the baseline flux from the reference images, applied zeropoints and combined the baseline and single epoch fluxes to produce the light curves of the 152 objects. We then visually inspected the candidates to look for any signs of variability. The alternative pipeline confirmed that only 5 candidates from our overlapping samples showed statistically significant variability in ZTF.

3.8 *WISE* single epoch forced photometry

As we aimed to search for mid–IR variability from a large sample of dwarf galaxies which may have been too faint to appear in the search of the original All*WISE* catalog by Secrest & Satyapal (2020), we made use of forward modelled photometry of time–resolved *WISE* coadds (Meisner et al., 2018) made available through Data Release 9[4] of the DESI imaging Legacy Survey (Dey et al., 2019a). This approach was previously implemented by Lang et al. (2014) to produce forced photometry of 400 million SDSS sources with the deep un*WISE* coadds (Lang, 2014; Meisner et al., 2017). Lang et al. (2014) used `The Tractor` (Lang et al., 2016) to use deeper, higher resolution source models from SDSS to produce photometry of blended and faint objects in the un*WISE* coadds. They were able to report fluxes and uncertainties from 3σ and 4σ detections which were not included in the original *WISE* catalog. More recently, they implemented this technique to produce time–resolved *WISE* photometry (Meisner et al., 2018). As *WISE* revisits each field at a ∼6 month cadence, with an increased cadence towards the poles, and takes ~ 10 exposures each visit, they coadded the exposures from each visit to produce forced photometry on each coadd. This therefore provided light curves with

[4] https://www.legacysurvey.org/dr9/catalogs/

approximately 15 fluxes measured over ~ 8 years.

We crossmatched the SDSS galaxy positions of our dwarf galaxy sample to the un*WISE* source catalog and pulled the single epoch *WISE* photometry for the closest un*WISE* source. Some light curves showed an oscillation behaviour when multiple sources were contained within the large *WISE* PSF and the *WISE* flux was distributed across the multiple sources differently in each epoch. To overcome this, we combined the total flux of the sources within a radius of 3 *WISE* pixels (3x2.75") to ensure that all dwarf galaxy variability was captured within the combined fluxes. We removed light curves where an erroneously high flux ($f - \langle f \rangle > 5\sigma$) in both W1 and W2 bands produced a r and χ^2/N above the cutoffs. We also removed light curves where source confusion within the *WISE* PSF size still resulted in an oscillating behaviour using the following criteria. If the summed difference between every adjacent W1 flux measurement was greater than twice the summed difference between every W1 flux offset by two epochs, the light curve was flagged as bad quality. We produced *WISE* light curves of the AGN control sample with the same procedure.

For each source we calculated the Pearson correlation coefficient r between the W1 and W2 bands and the χ^2/N for each band. The distribution of these statistics for the two samples is shown in Figure 3.6. We required that dwarf galaxies have $r > 0.75$ and $\chi^2/N > 1.0$ in W1 and W2 to be considered a variable AGN candidate.

Of the 79,879 dwarf galaxies for which *WISE* single epoch forced photometry was available, 124 were removed due to light curve quality flags. Of the remaining 79,755 light curves, we found that 165 had fluxes which met our variability criteria. One dwarf galaxy, NSA253466, was detected by our variability criteria due to the well–studied Type IIn supernova SN 2010jl (Stoll et al., 2011) which has had detailed follow–up in the near–IR, X–ray and radio (e.g. Chandra et al., 2015; Fransson et al., 2014) showing interaction with the dense circumstellar medium. We removed this object from our AGN candidate sample. We removed 3 other objects with supernovae visible in both WISE and ZTF data: NSA559938 (ZTF18aamftst: an SNIIn), NSA143427 (ZTF18acwyvet, an SNIIL), and NSA230430 (ZTF20aaupkac: an SNIa). We removed 14 other galaxies with light curves showing single flares, often with color changes characteristic of SNe: NSA20892, NSA32356, NSA143207, NSA236644, NSA250558, NSA253466, NSA274965, NSA340533, NSA355173, NSA379733, NSA475418, NSA502699, NSA528212, NSA548379. The properties of these supernova host galaxies are summarized in Table 3.3.

The properties of the remaining final sample of 148 AGN candidates (corresponding to $0.19 \pm 0.02\%$ of the dwarf galaxy sample) are summarized in Table 3.4 and 6 examples of variable *WISE* light curves are shown in Figure 3.7.

3.9 Properties of the *WISE*–selected variable IMBH candidates

The distributions of the redshifts and host stellar masses of the mid–IR variable dwarf galaxies are shown in Figure 3.8. We exclude NSA64525 from the histogram because the estimated mass provided by the NASA–Sloan Atlas ($10^{5.39} M_{\odot}$) is inconsistent with the stellar dispersion velocity of 193 ± 8 km/s measured by the SDSS spectroscopic pipeline. This dispersion velocity indicates that the BH itself likely has a mass of $\sim 10^7 M_{\odot}$ according to the $M - \sigma_*$ relation (Kormendy & Ho, 2013) and the host

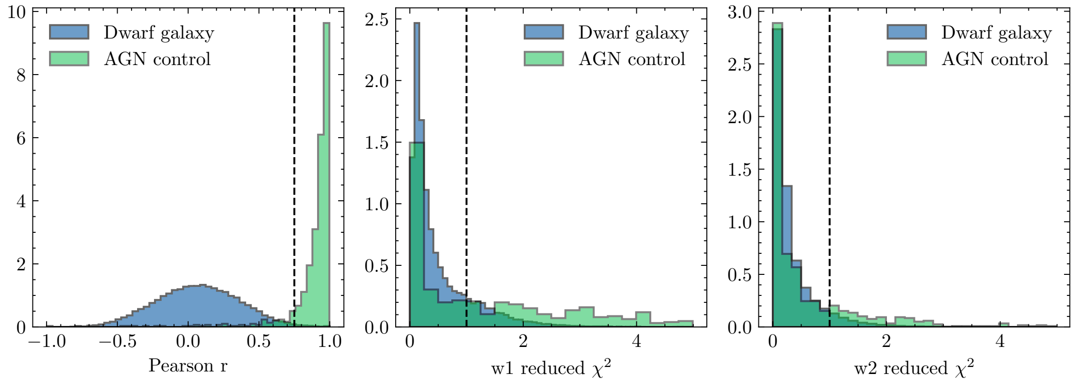

Figure 3.6: Pearson r correlation coefficient and χ^2/N in W1 and W2 band calculated from *WISE* forward modeling light curves. We show the entire dwarf galaxy population with *WISE* photometry in blue and the AGN control sample (from host galaxies of stellar mass $M_* > 3 \times 10^{9.75} M_\odot$) in green. The cutoffs used for AGN candidate selection are shown in black dotted lines for each statistic. We required the 3 statistics to satisfy the cutoffs in order for a candidate to be selected.

galaxy therefore has mass comparable to $\sim 10^{9.5} M_\odot$ based on the $M_{\rm BH} - M_*$ relation (Schutte et al., 2019). The mid–IR variability selection finds a higher fraction of variable AGN at low redshifts compared to the overall dwarf galaxy sample and shows a slight preference for higher mass galaxies.

The classification of the mid–IR IMBH candidates on the [O III] λ5007/Hβ – [N II] λ6583 /Hα BPT diagram is shown in Figure 3.9. 100 objects (69%) are classified as star forming while 32 objects (22%) are in the composite region, 3 (2.1%) were classified as LINERs and 10 (6.9%) as Seyferts. 12 of the IMBH candidates (8.1%) have broad Balmer lines. These objects also had their virial black hole masses estimated using the width of the Hα broad lines by Ho & Kim (2015) and Liu et al. (2019). These virial masses range between $10^{5.5} M_\odot$ and $10^{8.2} M_\odot$ respectively and are shown in Table 3.4.

In order to determine how many *WISE*–selected IMBH candidates were also

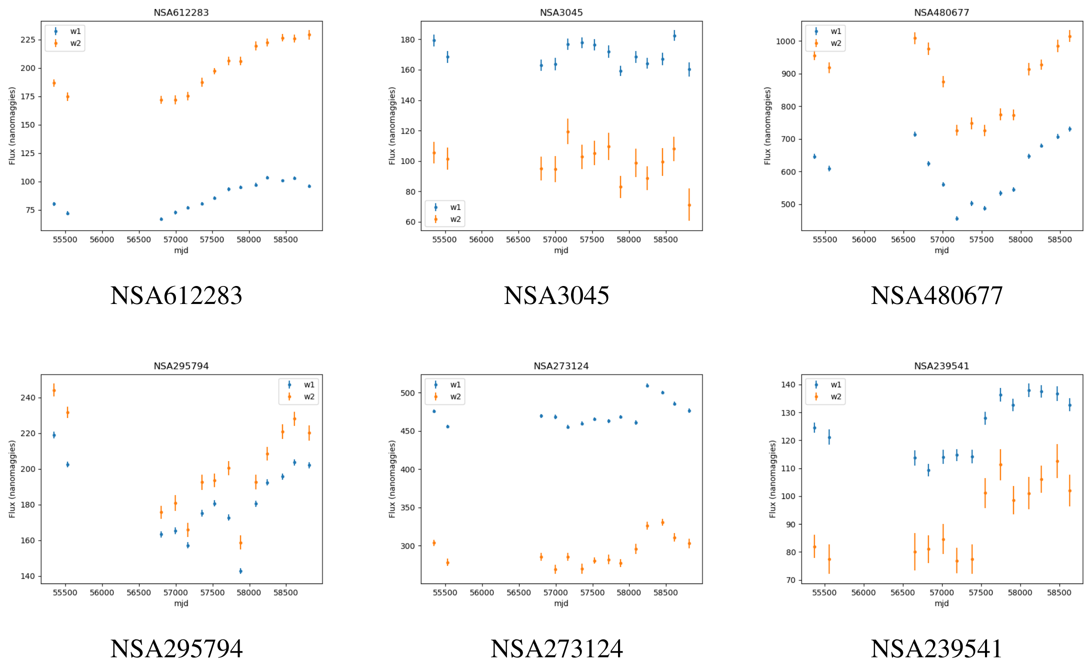

Figure 3.7: Six examples of *WISE* forward modeling light curves which passed the variability criteria and were classified as IMBH candidates.

optically variable, we produced ZTF photometry of the remainder of the 148 dwarf host galaxies which were not included in the original ZTF search. We found that 15 out of 148 (10%) met the optical variability criteria for ZTF outlined in Section 3.5. 7 of the 15 AGN which were variable at both wavelengths had visible broad lines in their spectra, and amongst these broad line AGN, the virial masses ranged between $M_{\rm BH} = 10^{6.3} M_{\odot}$ and $M_{\rm BH} = 10^{8.2} M_{\odot}$. Only two of these sources (NSA164884 and NSA451469) were found in the original ZTF sample, due to the smaller sample of dwarf galaxies for which we produced optical photometry. The AGN with both mid–IR and optical variability are indicated in the last column of Table 3.4.

NSA451469 had also been found in PTF by Baldassare et al. (2020b). We crossmatched our mid–IR selected IMBH candidates to the active dwarf galaxies from the

Secrest & Satyapal (2020) mid–IR variability search, the Baldassare et al. (2018, 2020b) optical variability searches, the Molina et al. (2021) [Fe X] λ6374 coronal line emission search, the Mezcua & Domínguez Sánchez (2020) IFU spectroscopy search, the Mezcua et al. (2018) Chandra X-ray search, the Latimer et al. (2021) mid–IR color selection box search and the Reines et al. (2013) optical emission line search. Only 2 objects had been found in previous AGN searches.

One object, NSA638093, had previously been found in the *WISE* variability search by Secrest & Satyapal (2020) and in the mid–IR color selection box by Latimer et al. (2021) (object number 11, listed with NSAID 151888 from version $\mathrm{v}_{1\_1\_2}$ of the NSA), where they used *Chandra* to find X-ray emission which may have been consistent with X-ray binaries instead of AGN activity. NSA386591 appears in the Reines et al. (2013) spectroscopic search for BPT AGN and Composites and the Latimer et al. (2021) mid–IR color selection search (ID number 6) where it was found to have an X-ray luminosity consistent with AGN activity and too large to be produced by X-ray binaries.

We undertook a search for radio emission from the IMBH candidates in the Karl G. Jansky Very Large Array Sky Survey (VLASS; Lacy et al., 2020). This survey covers a total of 33,885 deg^2 in the 2–4 GHz range with an angular resolution of $\sim$ 2".5 and will obtain a coadd 1σ sensitivity of 1 μJy/beam by survey end in 2024. We searched for crossmatches within 10" in Table 2 of the VLASS Epoch 1 Quick Look Catalogue which contains $\approx 700,000$ compact radio sources with > 1 mJy/beam detections associated with mid–IR hosts from the un*WISE* catalog (Gordon et al., 2020). We found that one IMBH candidate, NSA87109, had a corresponding radio point source at a separation of 0.0038" from the optical NASA–Sloan Atlas galaxy position with a flux of 17.55 ± 0.27

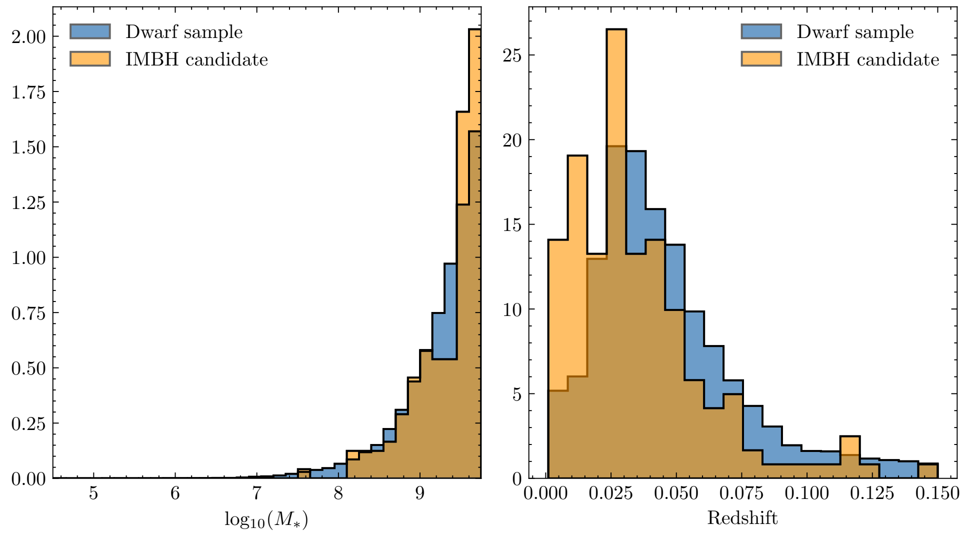

Figure 3.8: Normalized galaxy mass and redshift distributions of *WISE* IMBH candidates shown in orange and the parent dwarf galaxy sample shown in blue. Redshifts and host galaxy mass measurements are derived from the NSA.

Jy. This object is a known BL Lac which has also been detected in 0.1–2.4 keV X-rays (Massaro et al., 2009).

We show cutouts from the DESI Legacy Imaging Surveys (Dey et al., 2019a) of 3 *WISE* candidates and 2 ZTF candidates with host masses $M_* < 10^{8.2} M_\odot$ and the object with a VLASS radio detection (NSA87109, with stellar mass $\log_{10} M_* = 9.66$) in Figure 3.10. The radio source and one other low–mass IMBH candidate are in compact, blue galaxies while the other 4 low–mass IMBH candidates reside in galaxies with complex morphologies and multiple stellar overdensities.

3.10 Discussion

The number of dwarf galaxies which were variable in *WISE* corresponded to a $0.19 \pm 0.02\%$ variability fraction, while the optical variability fraction that we find

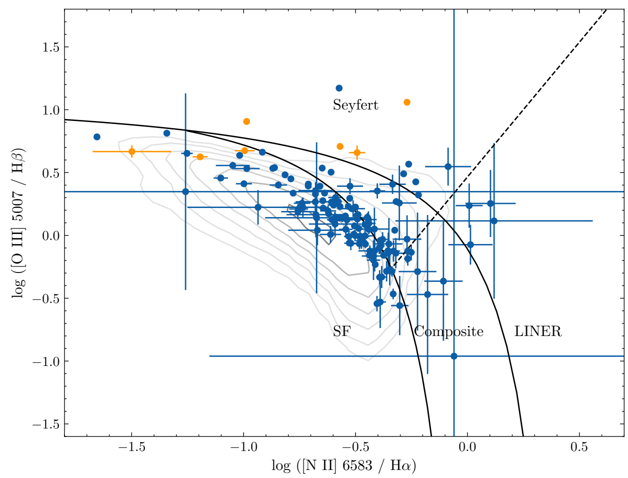

Figure 3.9: BPT diagram showing narrow line ratios derived from pPXF fitting of archival SDSS spectra of the *WISE*–selected IMBH candidates. Orange points show line ratios for IMBH candidates with broad Balmer lines in archival spectra and blue points show those with narrow emission lines only. Grey contours show the population density with log scaling of the entire parent dwarf galaxy sample for line ratios derived from the NASA–Sloan Atlas. Classification regions are labeled in black text.

from the ZTF AGN candidates is $0.17 \pm 0.03\%$. Our results therefore suggest that the two methods are similarly effective for identifying IMBH candidates with the current sensitivities and baselines available for mid–IR and optical photometry of dwarf galaxies. This, however, will change with the improved optical sensitivities and baselines offered by the LSST survey over the next decade.

Our mid–IR active fraction was larger but within the uncertainty range of the active fraction found by Secrest & Satyapal (2020) ($0.09^{+0.20}_{-0.07}\%$) in a much smaller sample of 2197 dwarf galaxies with the main *WISE* photometry catalog. The optical variability fraction that we find is also consistent with the active fraction of $0.15 \pm 0.07\%$ found for dwarf galaxies of the same mass in PTF (Baldassare et al., 2020b).

The 90% fraction of *WISE*-selected AGN candidates which are variable in the mid-

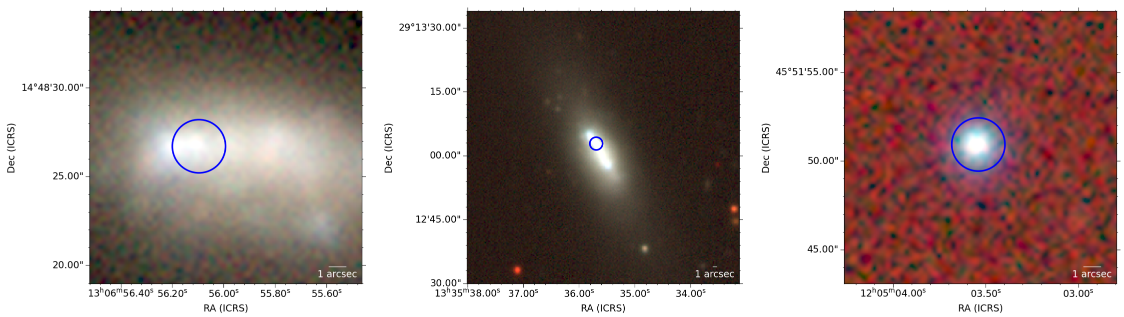

(a) NSA370005 (b) NSA418763 (c) NSA612283

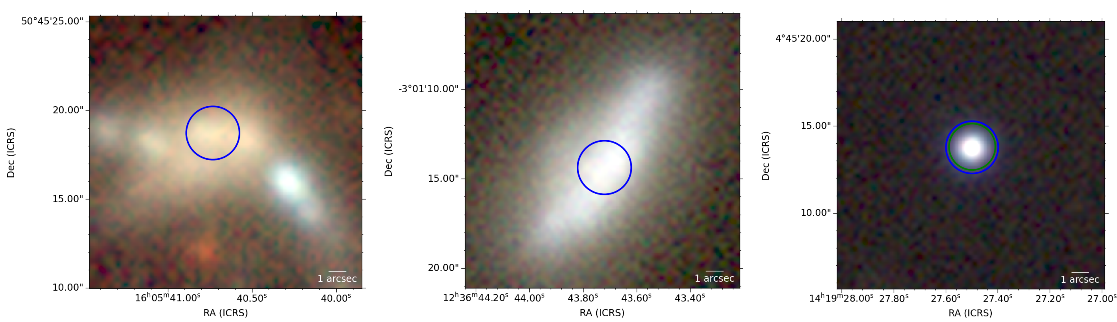

(d) NSA97216 (e) NSA19864 (f) NSA87109

Figure 3.10: Legacy survey cutouts of 3 *WISE* IMBH candidates (a–c) and 2 ZTF IMBH candidates (d–e) with host masses $M_* < 10^{8.2}\mathrm{M}_\odot$ and the candidate with a FIRST radio detection (f, radio position overlaid in green circle). Blue circles show the central position for *WISE* or ZTF forced photometry.

IR but not the optical likely arises from a combination of line-of-sight obscuration of nuclear optical emission due to the dusty torus and global obscuration from the host galaxy. Obscuration of nuclear optical emission from AGN with detectable mid–IR signatures has been observed for many Seyfert 2 galaxies (e.g. Annuar et al., 2015, 2017; Goulding et al., 2011; Ricci et al., 2016). It is possible that the majority of our mid–IR variable AGN in dwarf galaxies are Seyfert 2s with obscured optical variability which are also not picked up by the BPT diagram due to the effects of their lower masses on the optical emission line ratios. Line-of-sight obscuration of optical emission of *WISE* candidates is supported by the fact that 7 of the 12 *WISE*–selected IMBH candidates with bright BLRs were variable in both the mid–IR and the optical.

We note that only 5 of the 152 dwarf galaxies in common with the Baldassare et al. (2020b) AGN candidate sample from PTF were variable in ZTF. This may be because of the use of differing statistical criteria for variability classification. It may also be the case that the longer 7 year baseline of the combined PTF and iPTF light curves in Baldassare et al. (2020b) improved their sensitivity to AGN which vary on longer timescales compared to shorter timescales. They indeed find that longer baseline data has a much higher detectable variability fraction, increasing by a factor of 4 from 0.25% for light curves with < 2 year baselines to 1% for light curves with > 2 year baselines. By comparison, our procedure of using deep references and stacking to detect fainter variability in more evenly–sampled, ~ 3 year baseline light curves may make us more sensitive to variability on month to year long timescales, but may miss AGN with flux changes over longer 2–7 year timescales. An alternative explanation may be that a large fraction of low–mass AGN are state–changing AGN (e.g. Frederick et al., 2019) which can switch their optical variability on and off over the decade–long timescale of the PTF and ZTF surveys. Indeed, Martínez-Palomera et al. (2020) found that the majority of IMBH candidates with optical variability on hourly to daily timescales from the SIBLING survey were not variable when observed again the following year.

81% of the ZTF–selected IMBH candidates were star–forming on the BPT diagram and only 7 have been identified as AGN via their Balmer broad lines. Only 7 had been identified in previous dwarf galaxy AGN searches and these were all via their optical variability in SDSS or PTF. The non–AGN spectroscopic classifications of the majority of the sources indicates that optical variability selection can find AGN in dwarf galaxies which would be missed by other selection strategies.

Similarly, 100 (69%) of *WISE*–selected IMBH candidates were star–forming on the BPT diagram and therefore would have been missed by classic spectroscopic selection methods. 12 (8.1%) can be identified as AGN due to the presence of broad lines, 1 (0.63%) could have been found via radio emission alone, another 2 (1.27%) via the mid–IR selection box and 1 (0.63%) via X-ray emission. We therefore see that $\sim$ 70% of candidates from mid–IR variability selection could likely not have been found through other selection techniques. A higher fraction of the *WISE*–selected candidates are BPT–AGN compared to optically–selected candidates, perhaps indicating that the AGN emission lines of galaxies with mid–IR variability are less likely to be diluted by star formation.

Both the ZTF–selected and *WISE*–selected AGN candidate host galaxies tend to have higher masses and lower redshifts compared to the overall distributions of the host galaxy sample, likely due to the higher luminosities of these AGN. However, our selection method is still capable of detecting AGN variability from dwarf galaxies with redshifts up to $z \sim 0.15$ and stellar masses down to $M_* = 10^{7.52} M_\odot$. The virial masses for the AGN candidates with broad lines go down to $M_{\rm BH} = 10^{5.485} M_\odot$ and in most cases are lower than the BH masses estimated from the $M_{\rm BH} - M_*$ relation, indicating that our search may have found MBHs which are undermassive for their hosts. We therefore conclude that our variability–selection approach is useful for selecting AGN which can populate the poorly sampled lower end of the $M_{\rm BH} - \sigma_*$ relation. Future work should take high resolution spectra of our IMBH candidates for fitting of the velocity dispersion from the stellar absorption lines to provide another independent estimate of the BH mass.

The discovery of 36 nuclear supernova candidates shows the usefulness of applying simple statistics to ZTF forced photometry of large galaxy samples to find supernovae candidates in dwarf galaxies. There are many motivations to study rates of supernovae in dwarfs such as explaining the increase in the rate ratio of superluminous supernovae to core collapse supernovae in low–mass galaxies and whether the increased metallicity or specific star formation rates in dwarfs are the driving factor for this trend (Taggart & Perley, 2021). It has also been found that the emerging class of fast blue optical transients like AT2018cow are preferentially hosted by dwarf galaxies (Perley et al., 2021). Our finding that 0.14% of dwarf galaxies contained nuclear supernovae during ZTF Phase–I (corresponding to 0.05% per year) and that most SN were within redshifts of $0.02 < z < 0.055$ may provide insights into these questions.

3.11 Conclusions

In this paper we have presented a search for IMBH candidates by looking for variable AGN in dwarf galaxies of stellar mass $M_* < 10^{9.75} M_\odot$ in the optical and mid–IR. We applied a new ZTF forced photometry pipeline to produce deep, high quality reference images for image subtraction and made g- and r- band light curves of 25,714 dwarf galaxies. These light curves were stacked in a range of time bins to improve sensitivity to faint variability. We applied statistical cutoffs to find significant and correlated variability between the two bands and found 36 supernova candidates and 44 AGN candidates. The supernova fraction was $0.05 \pm 0.01\%$ year^{-1} and the optically variable AGN fraction was $0.17 \pm 0.03\%$.

To search for mid–IR variability we used `Tractor` forward modelled photometry of time–resolved *WISE* coadds. We found 148 dwarf galaxies with significant and correlated variability in the W1 and W2 bands after removing 14 supernovae. The mid–IR variable AGN fraction was $0.19 \pm 0.02\%$.

We found that 81% of our ZTF AGN candidates would have been missed with classical spectroscopic classification on the BPT diagram. Of our *WISE* candidates, 69% would have been missed with spectroscopic classification and only 4 would have been detected via radio or X-ray detection or the mid–IR color selection box. While our candidates were slightly biased to low redshifts and high galaxy masses compared to the parent dwarf galaxy sample, they were effective in identifying AGN with virial masses as low as $M_{\rm BH} = 10^{5.485} M_\odot$ and in dwarf galaxies with stellar masses $10^{7.5} < M_* < 10^{8.5} M_\odot$. We therefore conclude, in accordance with previous variability searches, that optical and mid–IR variability selection is effective for finding low–mass AGN in dwarf galaxies which would be missed by other spectroscopic selection techniques.

After checking the ZTF photometry of the 152 dwarf galaxies in common between our parent sample and the variability–selected AGN candidates from PTF (Baldassare et al., 2020b) we found that only 5 continue to show variability in ZTF. The lack of variability in our ZTF light curves may be due to the different baselines and sensitivities of the two search strategies and the differing methods for finding AGN–like variability.

With more detailed imaging and spectroscopic analysis, our variability–selected AGN candidates could help to populate the sparsely sampled end of the $M_* - \sigma$ relation and provide insights into black hole seed formation mechanisms, dwarf galaxy–black hole co–evolution and the accretion states of low–mass AGN. Future work on these candidates will include forward modeling of ZTF and DECam images to determine their positions relative to their host galaxy nuclei and determine the off-nuclear fraction. The potential for forward modeling of ZTF images to determine the position of a variable point source relative to its host galaxy was demonstrated in Ward et al. (2021a) for recoiling SMBH candidates and will provide a way to confirm the positions of IMBH candidates without X-ray or radio detections.

These candidates are just the tip of the iceberg in the search for optically variable AGN in dwarf galaxies, which will be greatly enhanced by the capabilities of the Legacy Survey of Space and Time (LSST) at Vera C. Rubin Observatory (Ivezić et al., 2019) over the next decade. The capacity of LSST to find fainter and more distant IMBHs in dwarf galaxies via their variability will tighten the constraints we can place on black hole seeding channels and the efficiency of massive BH growth.

Table 3.3: Properties of the 14 SN candidates found in forward modeled *WISE* light curves. The IDs, positions, redshifts and host galaxy stellar masses are those from the NSA catalog version $\mathrm{v}_{1\_0\_1}$. In the first $\log_{10}\mathrm{M}_{BH}$ column we show the estimated black hole mass based on the $M_* - M_{BH}$ from Schutte et al. (2019) which has a scatter of 0.68 dex. The last column shows the spectroscopic classification made published by ZTF on the Transient Name Server.

NSA ID	RA (hms)	Dec (dms)	z	$\log_{10}\mathrm{M}_*$ ($M_\odot$)	$\log_{10}\mathrm{M}_{\mathrm{BH}}$ ($M_\odot$)	BPT class	BLR?	SN Class
20892	12:59:5.105	-3:12:14.257	0.0101	7.91	4.97 ± 0.68	SF	×	None
32356	00:10:5.515	-1:05:39.795	0.0379	9.16	6.52 ± 0.68	SF	×	None
143207	16:28:31.291	41:37:12.833	0.0331	9.32	6.72 ± 0.68	SF	×	None
143427	16:32:3.899	39:36:31.289	0.0281	9.0	6.32 ± 0.68	SF	×	SNIIL
230430	07:51:8.935	22:44:27.419	0.0288	8.97	6.28 ± 0.68	-	×	SNIa
236644	11:43:39.35	09:50:18.863	0.0202	8.49	5.69 ± 0.68	SF	×	None
250558	15:31:51.855	37:24:47.41	0.0299	8.99	6.31 ± 0.68	-	×	None
253466	09:42:53.245	09:29:36.066	0.0106	8.79	6.06 ± 0.68	-	×	SNIIn
274965	13:08:19.122	43:45:25.483	0.0365	9.3	6.69 ± 0.68	-	×	None
355173	15:28:40.931	10:33:28.095	0.0887	9.43	6.85 ± 0.68	SF	✓	None
379733	13:32:18.328	07:56:26.052	0.0236	9.3	6.69 ± 0.68	SF	×	None
502699	10:08:7.779	19:17:57.808	0.0335	9.23	6.61 ± 0.68	Composite	×	None
548379	13:20:53.681	21:55:10.518	0.0224	8.35	5.51 ± 0.68	-	×	None
559938	14:31:14.719	17:11:35.152	0.0378	9.11	6.46 ± 0.68	SF	×	SNIIn

Table 3.4: Properties of the 148 AGN candidates with significant and correlated W1 and W2 variability found in forward modeled *WISE* light curves. The IDs, positions, redshifts and host galaxy stellar masses are those from the NSA catalog version $\mathrm{v1\_0\_1}$. In the first $\log_{10}\mathrm{M}_{BH}$ column we show the estimated black hole mass based on the $M_* - M_{BH}$ from Schutte et al. (2019) which has a scatter of 0.68 dex. Virial masses were calculated for broad line AGN by Ho & Kim (2015) based on the width of the Hα broad lines. In the last column, we indicate whether the WISE candidate's ZTF light curve also met the criteria for optical variability. *The estimated mass provided for NSA64525 by the NASA–Sloan Atlas ($10^{5.12}M\odot$) is inconsistent with the stellar dispersion velocity of 193 ± 8 km/s measured by the SDSS spectroscopic pipeline. This σ_* is more characteristic of a host galaxy with mass $\sim 10^{9.5} M_\odot$ and a BH with mass $\sim 10^7 M_\odot$.

NSA ID	RA (hms)	Dec (dms)	z	$\log_{10}\mathrm{M}_*$ ($M_\odot$)	$\log_{10}\mathrm{M}_{\mathrm{BH}}$ ($M_\odot$)	BPT class	BLR?	$\log_{10}M_{\mathrm{BH,vir}}$ ($M_\odot$)	Optical var.?
3045	10:39:44.299	00:51:28.625	0.0253	8.6	5.82 ± 0.68	SF	×	-	×
12740	14:06:30.104	00:19:39.525	0.1063	8.66	5.9 ± 0.68	SF	✓	6.436	×
34102	00:45:0.51	00:47:23.578	0.0568	9.35	6.75 ± 0.68	SF	×	-	×
47457	08:03:38.042	43:20:34.99	0.0153	9.08	6.42 ± 0.68	SF	×	-	×
50093	08:38:19.706	51:31:52.998	0.0166	8.75	6.01 ± 0.68	SF	×	-	×
50870	08:48:4.539	52:14:9.051	0.0403	9.33	6.73 ± 0.68	Seyfert	×	-	×
54469	03:19:26.057	-6:07:15.98	0.0076	9.17	6.53 ± 0.68	SF	×	-	×
64525*	10:11:3.771	02:31:45.452	0.1211	5.12	1.51 ± 0.68	LINER	×	-	×
71121	13:19:40.797	03:24:33.828	0.0218	8.0	5.08 ± 0.68	SF	×	-	×
73327	14:10:52.96	01:22:10.396	0.026	9.46	6.89 ± 0.68	SF	×	-	×
74770	14:58:54.268	01:59:27.33	0.0298	9.22	6.59 ± 0.68	SF	×	-	×
75025	15:05:7.305	01:59:51.121	0.008	8.46	5.65 ± 0.68	-	×	-	×
81096	08:41:34.335	02:11:19.877	0.0287	8.66	5.9 ± 0.68	SF	×	-	×
87109	14:19:27.498	04:45:13.802	0.1434	9.38	6.79 ± 0.68	LINER	×	-	✓
93256	14:02:59.68	61:45:3.942	0.0054	9.06	6.39 ± 0.68	Composite	×	-	×
95784	15:40:37.104	58:15:35.93	0.0501	9.36	6.77 ± 0.68	SF	×	-	×
98016	16:06:33.607	48:39:37.056	0.0437	9.2	6.57 ± 0.68	Composite	×	-	×

102352	20:58:22.143	-6:50:4.353	0.0738	9.45	6.88 ± 0.68	Seyfert	✓	6.432	✓
106103	00:01:11.154	-10:01:55.702	0.0489	9.38	6.79 ± 0.68	Seyfert	✓	6.372	×
107142	00:23:55.671	-9:24:22.513	0.0522	9.3	6.69 ± 0.68	Composite	×	-	×
111190	01:52:32.835	-8:25:58.66	0.0176	9.18	6.54 ± 0.68	SF	×	-	×
112816	23:09:22.927	01:00:2.16	0.0153	8.87	6.16 ± 0.68	SF	×	-	×
120721	21:30:46.71	11:12:54.805	0.0475	9.35	6.75 ± 0.68	SF	×	-	×
124852	23:26:18.717	14:11:50.593	0.0417	9.22	6.59 ± 0.68	Composite	×	-	×
128577	07:47:55.395	34:02:12.144	0.0159	8.83	6.11 ± 0.68	SF	×	-	×
129617	08:12:26.587	39:32:19.995	0.0326	9.46	6.89 ± 0.68	SF	×	-	×
130265	08:32:24.255	43:06:7.807	0.0247	8.85	6.13 ± 0.68	SF	×	-	×
135650	12:40:57.29	63:31:10.47	0.0083	9.39	6.8 ± 0.68	Composite	×	-	×
143517	16:31:24.055	41:22:44.657	0.0309	9.2	6.57 ± 0.68	SF	×	-	×
152094	13:16:59.37	03:53:19.809	0.0454	9.44	6.87 ± 0.68	Seyfert	×	-	×
155198	08:17:15.852	31:39:7.139	0.0452	9.45	6.88 ± 0.68	Composite	×	-	×
164884	09:28:1.292	49:18:17.303	0.1143	9.44	6.87 ± 0.68	SF	✓	6.961	✓
175367	09:09:33.556	38:42:38.594	0.0561	9.41	6.83 ± 0.68	SF	×	-	×
178387	10:39:28.739	56:20:58.148	0.0748	9.34	6.74 ± 0.68	Seyfert	✓	6.515	✓
180304	12:03:38.324	58:59:11.804	0.0469	9.33	6.73 ± 0.68	SF	×	-	×
185495	12:05:21.947	50:14:11.506	0.0341	8.53	5.74 ± 0.68	SF	×	-	×
186717	17:02:1.824	31:53:1.341	0.0332	9.27	6.65 ± 0.68	SF	×	-	×
189025	20:46:38.107	00:20:21.688	0.0126	9.45	6.88 ± 0.68	LINER	×	-	×
208212	14:07:2.979	50:43:14.611	0.0072	8.07	5.17 ± 0.68	Composite	×	-	×
215346	01:15:37.856	00:12:58.114	0.0453	9.22	6.59 ± 0.68	SF	×	-	×
234033	09:54:38.791	40:32:4.395	0.0673	9.25	6.63 ± 0.68	Seyfert	✓	6.657	×
235055	11:01:16.027	10:16:17.924	0.0358	9.19	6.56 ± 0.68	SF	×	-	×
239541	12:33:7.855	10:14:56.145	0.0531	9.34	6.74 ± 0.68	SF	×	-	×
241996	10:29:28.222	09:50:1.145	0.0224	8.85	6.13 ± 0.68	SF	×	-	×
249598	14:26:31.705	44:51:42.018	0.0079	8.76	6.02 ± 0.68	SF	×	-	×
250824	08:07:0.613	05:37:37.137	0.052	9.2	6.57 ± 0.68	SF	×	-	×

266623	14:15:45.723	40:06:19.138	0.0202	9.45	6.88 ± 0.68	SF	×	-	×
267136	14:42:17.705	40:02:6.81	0.0266	8.6	5.82 ± 0.68	SF	×	-	×
273124	11:59:5.594	45:49:13.767	0.024	9.29	6.68 ± 0.68	Composite	×	-	×
278949	15:36:19.446	30:40:56.33	0.0059	8.08	5.18 ± 0.68	SF	×	-	×
280953	16:11:14.252	25:11:56.413	0.0475	9.34	6.74 ± 0.68	SF	×	-	×
284032	16:02:50.886	32:08:41.391	0.0141	9.21	6.58 ± 0.68	Composite	×	-	×
286477	15:48:36.238	36:13:42.486	0.0396	9.18	6.54 ± 0.68	SF	×	-	×
295794	11:36:57.683	41:13:18.507	0.0715	9.47	6.9 ± 0.68	Seyfert	✓	6.51	×
301231	13:18:29.733	45:17:1.821	0.0358	9.39	6.8 ± 0.68	Composite	×	-	×
301767	13:35:42.788	45:55:46.505	0.0048	8.67	5.91 ± 0.68	SF	×	-	✓
315748	08:02:13.476	22:26:2.457	0.03	9.0	6.32 ± 0.68	SF	×	-	×
316044	08:19:50.791	24:47:16.158	0.0256	9.37	6.78 ± 0.68	SF	×	-	×
319190	09:54:57.968	36:05:50.942	0.0488	9.11	6.46 ± 0.68	SF	×	-	×
321176	10:43:26.474	11:05:24.227	0.0475	9.37	6.78 ± 0.68	Seyfert	✓	8.163	✓
323877	11:46:4.072	11:34:52.566	0.0099	8.91	6.21 ± 0.68	SF	×	-	×
323951	11:48:32.458	12:42:19.067	0.0146	9.24	6.62 ± 0.68	SF	×	-	×
340153	14:38:58.286	47:18:28.497	0.027	9.39	6.8 ± 0.68	SF	×	-	×
346014	13:09:15.702	13:23:8.333	0.0274	8.96	6.27 ± 0.68	Composite	×	-	×
354455	15:17:39.678	11:34:59.736	0.0652	9.22	6.59 ± 0.68	Composite	×	-	×
355963	15:43:58.996	08:07:34.691	0.0409	9.35	6.75 ± 0.68	SF	×	-	×
358934	07:44:2.155	45:30:20.646	0.0538	9.05	6.38 ± 0.68	SF	×	-	×
361340	10:07:10.915	12:39:6.079	0.0093	8.2	5.33 ± 0.68	SF	×	-	×
369885	13:07:33.823	14:00:31.128	0.0549	9.45	6.88 ± 0.68	SF	×	-	×
369924	13:07:17.443	13:38:47.968	0.0268	9.39	6.8 ± 0.68	Composite	×	-	×
370005	13:06:56.11	14:48:26.805	0.0032	7.83	4.87 ± 0.68	SF	×	-	×
370204	13:17:40.461	13:56:24.681	0.0283	8.74	6.0 ± 0.68	SF	×	-	×
376082	12:51:55.683	08:52:41.595	0.0038	8.17	5.29 ± 0.68	SF	×	-	×
376210	12:51:47.278	09:51:34.461	0.0305	9.0	6.32 ± 0.68	SF	×	-	×
376231	12:54:7.922	10:00:23.692	0.037	9.23	6.61 ± 0.68	Composite	×	-	×

376574	12:56:53.446	08:09:41.682	0.0086	8.47	5.66 ± 0.68	SF	×	-	×
376622	12:58:21.864	08:32:29.792	0.0289	9.28	6.67 ± 0.68	SF	×	-	×
377912	13:08:28.602	10:40:8.594	0.0246	9.4	6.82 ± 0.68	SF	×	-	×
385012	15:12:2.597	06:55:53.926	0.0465	9.46	6.89 ± 0.68	SF	×	-	×
385214	15:06:52.734	08:10:23.682	0.0396	8.97	6.28 ± 0.68	SF	×	-	×
386591	15:26:37.364	06:59:41.726	0.0384	9.12	6.47 ± 0.68	Composite	✓	5.485	×
389406	14:25:52.842	06:32:15.001	0.024	8.93	6.23 ± 0.68	SF	×	-	×
391212	15:04:16.147	05:49:21.806	0.0301	9.42	6.84 ± 0.68	SF	×	-	×
393092	16:03:43.582	04:32:35.996	0.0444	9.42	6.84 ± 0.68	SF	×	-	×
401713	08:02:53.694	55:17:55.692	0.03	9.14	6.49 ± 0.68	SF	×	-	×
404064	09:34:38.578	67:22:29.017	0.023	8.62	5.85 ± 0.68	SF	×	-	×
412056	09:46:23.749	34:16:52.073	0.0755	8.74	6.0 ± 0.68	SF	×	-	×
418509	13:34:5.899	27:33:40.195	0.0293	9.23	6.61 ± 0.68	Composite	×	-	×
418517	13:35:26.025	28:10:12.928	0.0633	9.35	6.75 ± 0.68	SF	×	-	×
418760	13:35:51.276	29:12:49.882	0.0212	8.89	6.18 ± 0.68	SF	×	-	×
418763	13:35:35.715	29:13:3.022	0.0028	7.92	4.98 ± 0.68	SF	×	-	×
424989	13:21:18.974	30:04:23.853	0.0912	9.39	6.8 ± 0.68	SF	✓	6.436	✓
431557	13:42:5.443	32:01:43.28	0.0156	9.19	6.56 ± 0.68	SF	×	-	×
437426	09:09:34.371	25:13:22.76	0.0078	8.7	5.95 ± 0.68	Composite	×	-	×
437561	09:17:17.051	26:26:59.206	0.0247	9.28	6.67 ± 0.68	SF	×	-	×
438165	12:03:25.676	33:08:46.147	0.0349	8.83	6.11 ± 0.68	SF	×	-	×
439902	13:39:57.611	30:42:54.223	0.042	9.38	6.79 ± 0.68	SF	×	-	×
439931	13:41:13.598	30:23:27.794	0.04	9.2	6.57 ± 0.68	SF	×	-	×
439935	13:42:43.255	30:43:39.805	0.0357	9.45	6.88 ± 0.68	Composite	×	-	×
439946	13:41:50.188	30:33:57.114	0.0264	8.84	6.12 ± 0.68	SF	×	-	✓
445385	13:28:24.676	31:09:37.833	0.0164	8.35	5.51 ± 0.68	-	×	-	×
451469	14:14:5.019	26:33:36.804	0.0358	9.39	6.8 ± 0.68	SF	✓	6.303	✓
453882	14:28:30.841	27:15:57.271	0.013	9.08	6.42 ± 0.68	SF	×	-	×
457334	14:47:17.407	24:30:19.296	0.0424	9.18	6.54 ± 0.68	SF	×	-	×

465843	15:46:53.324	17:52:21.579	0.0113	8.59	5.81 ± 0.68	SF	×	-	×
475108	11:30:26.846	30:27:52.084	0.0589	9.39	6.8 ± 0.68	Composite	×	-	×
475368	11:28:28.072	27:54:7.612	0.068	9.34	6.74 ± 0.68	Composite	×	-	×
477209	11:56:35.312	28:29:25.256	0.0117	9.01	6.33 ± 0.68	Composite	×	-	×
480677	12:29:3.509	29:46:45.995	0.0814	9.44	6.87 ± 0.68	SF	✓	-	✓
481291	12:36:12.26	26:45:22.078	0.0246	9.44	6.87 ± 0.68	SF	×	-	×
484296	13:29:39.134	25:47:50.822	0.0247	8.86	6.15 ± 0.68	SF	×	-	×
485578	08:04:18.001	15:20:38.47	0.0393	9.45	6.88 ± 0.68	Seyfert	×	-	×
487099	08:25:21.331	15:17:23.31	0.0329	9.21	6.58 ± 0.68	SF	×	-	×
487207	08:20:13.444	16:12:41.858	0.0442	9.28	6.67 ± 0.68	SF	×	-	×
488733	08:41:28.47	16:16:43.165	0.0731	9.45	6.88 ± 0.68	SF	×	-	×
501377	10:32:6.026	22:59:21.809	0.0585	8.7	5.95 ± 0.68	Composite	×	-	×
502687	10:05:23.1	19:16:18.857	0.0128	8.45	5.64 ± 0.68	SF	×	-	×
508645	09:02:50.471	14:14:8.301	0.0506	9.21	6.58 ± 0.68	-	×	-	✓
522620	11:42:50.986	20:26:31.655	0.019	9.34	6.74 ± 0.68	SF	×	-	×
538951	12:32:36.165	18:01:23.085	0.0028	8.39	5.56 ± 0.68	SF	×	-	×
540489	13:13:54.174	16:43:39.707	0.0224	9.23	6.61 ± 0.68	SF	×	-	×
540494	13:13:40.008	16:39:27.698	0.0219	8.71	5.96 ± 0.68	SF	×	-	×
548558	13:13:50.79	23:15:17.935	0.0116	8.7	5.95 ± 0.68	SF	×	-	×
548726	13:23:16.62	21:18:5.97	0.0224	9.34	6.74 ± 0.68	Composite	×	-	×
548780	13:20:42.199	20:54:37.122	0.0093	8.17	5.29 ± 0.68	SF	×	-	×
552294	13:27:59.639	23:35:50.831	0.0432	9.05	6.38 ± 0.68	SF	×	-	×
558933	14:09:28.215	17:39:43.879	0.0181	9.4	6.82 ± 0.68	SF	×	-	×
563981	14:13:13.548	20:25:25.781	0.0168	9.25	6.63 ± 0.68	SF	×	-	×
571135	15:10:24.257	19:23:47.709	0.075	9.28	6.67 ± 0.68	SF	×	-	×
572805	12:25:18.255	05:44:31.206	0.0038	8.84	6.12 ± 0.68	SF	×	-	×
576634	15:40:29.285	00:54:37.064	0.0117	8.31	5.46 ± 0.68	SF	×	-	×
583865	00:56:33.363	00:05:10.27	0.0793	9.18	6.54 ± 0.68	Seyfert	✓	6.131	×
592732	09:31:18.44	02:46:52.34	0.1148	8.56	5.77 ± 0.68	Composite	×	-	×

593159	11:04:16.043	05:16:30.756	0.1166	9.05	6.38 ± 0.68	Composite	$\times$	-	$\times$
600245	11:51:42.585	06:51:30.529	0.102	8.91	6.21 ± 0.68	Composite	$\times$	-	$\times$
612283	12:05:3.537	45:51:51.056	0.0654	7.25	4.15 ± 0.68	SF	$\times$	-	$\times$
627704	12:03:49.742	29:42:56.153	0.0105	9.18	6.54 ± 0.68	SF	$\times$	-	$\times$
638093	23:32:45.037	00:58:45.886	0.0238	9.18	6.54 ± 0.68	SF	$\times$	-	$\times$
648447	09:24:39.36	17:39:47.977	0.0136	9.32	6.72 ± 0.68	Composite	$\times$	-	$\times$
661360	11:33:23.454	55:04:20.733	0.0079	8.52	5.72 ± 0.68	SF	$\times$	-	$\checkmark$
676393	13:36:20.429	28:47:50.676	0.0268	9.23	6.61 ± 0.68	Composite	$\times$	-	$\times$
677377	13:46:22.893	29:19:2.782	0.0546	9.39	6.8 ± 0.68	SF	$\times$	-	$\times$
679695	14:07:24.993	55:06:10.896	0.0046	8.95	6.26 ± 0.68	Composite	$\times$	-	$\times$
681375	14:27:9.515	30:56:53.601	0.0137	9.32	6.72 ± 0.68	Composite	$\times$	-	$\times$
681956	14:34:37.05	59:20:18.29	0.0064	8.75	6.01 ± 0.68	SF	$\times$	-	$\times$
683356	14:48:27.022	31:47:28.383	0.0096	9.07	6.41 ± 0.68	SF	$\times$	-	$\times$
693966	12:59:20.083	09:11:13.787	0.0279	9.39	6.8 ± 0.68	Composite	$\times$	-	$\times$
694183	13:13:24.659	08:02:24.125	0.0237	9.44	6.87 ± 0.68	Composite	$\times$	-	$\times$

Chapter 4: Optically variable double–peaked emitters in ZTF: Understanding the AGN populations which mimic SMBH binary behavior

4.1 Overview

A fraction of active galactic nuclei (AGN) have double–peaked Balmer broad lines in their optical spectra thought to originate from the motion of gas in their accretion disk. It is important to characterize double–peaked emitters (DPEs) because they can mimic the kinematic and variability signatures of supermassive black hole (SMBH) binaries. In this chapter I present a sample of 299 optically variable DPEs which have light curves from the Zwicky Transient Facility (ZTF) with $>$3 year baselines. Our sample increases the number of known DPEs by a factor of $\sim$2. We find that 16% of variable broad line AGN in ZTF have double–peaked broad lines and that these are 1.6 times more likely to have detectable radio signatures at 2–4 GHz. We show that a number of optical and mid–IR DPE light curves exhibit apparently periodic behavior or chirping signals, where the frequency of sinusoidal variability increases or decreases with time, and discuss how this arises naturally from their power spectra. We show that DPE light curves have slightly steeper power spectra than their standard broad line counterparts and are $\sim$1.5 times more likely to have a low frequency turnover. We also model the ZTF time series with damped random walk models to refute previous findings that DPEs have characteristic timescales which are 2.7 times longer than standard broad line AGN. We discuss how the minor variability differences between DPEs and other broad line AGN may simply arise from the higher masses of the DPE population. Finally, we find that ∼50% of the DPEs display dramatic changes in the relative fluxes of their red and blue peaks over long $10-20$ year timescales. We also show that a larger fraction of DPEs have very steep, blue spectroscopic continua than standard broad line AGN. Finally, we compare the variability and spectroscopic properties of the ZTF DPE population with the recently discovered inspiraling SMBH binary candidate SDSSJ1430+2303 (ZTF18aarippg) and find that it is likely to be one of many single disk–emitting AGN in ZTF.

4.2 Introduction

The efficient formation of a gravitationally bound SMBH binary following the merger of the host galaxies is a key step in understanding BH–galaxy co–evolution. There are small number of active galactic nuclei (AGN) pairs at separations of tens of parsecs to kiloparsecs (see Section 1.3.1, and De Rosa et al., 2019, for a summary), providing evidence of AGN triggering by gas–rich galaxy mergers (e.g. Foreman et al., 2009; Satyapal et al., 2014, 2017; Weston et al., 2017). There are, however, no confirmed binaries at separations $< 10^{-2}$ pc, the regime where gravitational wave (GW) emission drives sufficient angular momentum loss to lead to SMBH coalescence (Kelley et al., 2017; Merritt & Milosavljević, 2005; Milosavljević & Merritt, 2003; Rajagopal

& Romani, 1995). As sub–pc SMBH separations cannot be resolved even by very long baseline interferometry (VLBI), searches for SMBH binaries in the GW emitting regime have centered on either variability at optical and X-ray wavelengths, or kinematic signatures from spectroscopy of Balmer broad line emission (see Section 1.3.2, and Bogdanović, 2015; Komossa & Zensus, 2014, for a review). Spectroscopic SMBH binary searches aim to find velocity–offset broad lines as kinematic signatures of orbiting AGN BLRs in an SMBH binary.

The majority of AGN with double–peaked broad Hα and Hβ profiles are not SMBH binaries (see Doan et al., 2020, for a review). In summary, many candidates with double–peaked Hα profiles have single–peaked Lyα lines, which would not be expected for two separately emitting single disks (Eracleous et al., 2009; O'Brien et al., 1998; Storchi-Bergmann et al., 2003); the orbital velocities are often smaller than the velocity of the gas in the single disks, which is not possible in the SMBH binary picture (Nguyen et al., 2018; Shen & Loeb, 2010); and reverberation studies find $<$3 day delays between blue and red peaks instead of the expected month to year long timescales expected for a sub–pc separation binary (Dietrich & Wagner, 1998; Shapovalova et al., 2013; Shen & Loeb, 2010). This is consistent with predictions of low rates of detectable kinematic SMBH binary signatures (Ju et al., 2013; Kelley, 2020; Pflueger et al., 2018). Asymmetric or velocity–shifted broad line profiles can also alternatively arise due to the presence of outflows and in response to fluctuations in the continuum (Barth et al., 2015; Liu et al., 2016a,c; Popovic, 2011).

DPEs are a common source of contamination in kinematic searches for SMBH binaries due to their time-varying, velocity–offset broad Balmer peaks (see Section 1.2.5).

Many DPEs show substantial changes in the relative flux of the blue and red peaks over timescales of years to decades which is well modeled by the rotation of spiral arms or hotspots in the disk (Gezari et al., 2007; Lewis et al., 2010; Schimoia et al., 2012, 2017; Storchi-Bergmann et al., 2002). Other DPEs have had double–peaked profiles materialize after being previously undetectable (Halpern & Eracleous, 1994; Storchi-Bergmann et al., 2003), perhaps due to formation of a disk after tidal disruption of a star (Bogdanović et al., 2004). Some DPEs also show transient spectroscopic phenomena such as the appearance of sharp, small peaks near the shoulders of the broad Hα and Hβ profiles (e.g. Eracleous et al., 1997a; Shapovalova et al., 2001) which may arise due to shocks or other local motions in the disk or microlensing by host galaxy stars (Abajas et al., 2002; Popović et al., 2001).

Estimates of DPE fractions amongst the wider broad line AGN population range from $\sim 3 - 30\%$ (Eracleous & Halpern, 1994; Ho et al., 1997; Strateva et al., 2003). As discussed in Section 1.2.5, double–peaked profiles are most commonly visible in low luminosity, low–accretion rate AGN (Eracleous & Halpern, 1994; Ho, 2008; Ho et al., 2000), where emission from a central broad line region cannot mask the dip between the peaks. They are also associated with large black hole mass, massive bulge, radio–loud elliptical hosts (Eracleous & Halpern, 1994). For example, Eracleous & Halpern (2003) found that 20% of 106 radio–loud AGN were DPEs, while Strateva et al. (2003) determined that double–peaked emitters are 1.6 times more likely to be radio sources. 41% of the Strateva et al. (2003) AGN were detected in the soft X-rays in the ROSAT All–Sky Survey, compared to 28% of the broad line AGN parent sample. Zhang & Feng (2017) found that that the optical variability properties of DPEs differed from other broad line AGN, having DRW characteristic timescales $2.7\times$ larger than a control sample in CSS and SDSS light curves. Two component disk–wind AGN models may explain the higher relative luminosity of double–peaked structures to broad line gas in low–luminosity AGN compared to standard Seyfert 1 nuclei (Elitzur et al., 2014; Storchi-Bergmann et al., 2016, see Sections 1.2.4 and 1.2.5).

There has been renewed interested in variability and kinematic selection of SMBH binary candidates with the discovery of SDSSJ1430+2303 (ZTF18aarippg), an AGN showing a decaying optical period over 4 cycles in a 3 year Zwicky Transient Facility (ZTF) light curve, and double–peaked broad lines with a redshifted ~ 4600 km s^{-1} and a blueshifted ~ 4000 km s^{-1} component (Jiang et al., 2022). This variable DPE has been interpreted as an uneven mass–ratio, highly eccentric SMBH binary which will merge within three years. In this chapter we present a larger sample of 299 optically variable DPEs, spectroscopically selected from a larger sample of variable AGN observed over > 3 years by ZTF. ZTF has presented us with a new opportunity to compare the variability properties of a large sample of DPEs and standard broad line AGN with a consistent, evenly sampled, long baseline data set, allowing us to better characterize the larger DPE population. This will not only shed further light on the differences between DPEs and other AGN, but help to inform best practices for false positive removal in SMBH binary searches which may be contaminated by apparently periodic DPEs.

In Section 4.3.1 we describe the selection of optically variable broad line AGN in ZTF. In Section 4.3.2 we describe the spectroscopic criteria used to identify the sub–sample of DPEs amongst the optically variable ZTF AGN. We also present three new DPEs which do not have archival spectra in SDSS. In Section 4.3.3 we characterize the variability properties of the DPEs compared to the remaining broad line AGN, showing that they have slightly steeper power spectra and longer characteristic timescales compared to standard AGN. We also show the frequent presence of dust echoes with a range of time delays, and the common occurrence of apparently periodic behavior or chirping signals (where frequency increases or decreases over time) in sections of the DPE light curves. In Section 4.3.4 we present spectroscopic monitoring of selected DPEs, showing that 50% exhibit large changes in the relative flux of the red and blue peaks over decade–long timescales. In Section 4.4, we discuss the differences between the DPE and control AGN populations in light of the viewing angle and disk–wind explanations for DPEs. We discuss the ways that DPE light curves and spectra mimic SMBH binary candidates in light of imminent merger candidate SDSSJ1430+2303 and conclude that SDSSJ1430+2303 is not likely to be special amongst the larger DPE population. We summarize our conclusions in Section 4.5.

4.3 Methods and Results

4.3.1 Selection of variable AGN in ZTF with visible Balmer broad lines

Our selection strategy to find variable AGN in ZTF was described in detail in Chapter 2 but will be summarized again here. We detected AGN variability amongst other transient phenomena in the ZTF alert stream (Masci et al., 2019; Patterson et al., 2019) by implementing a filter with the alert broker and analysis framework `AMPEL` (Alert Management, Photometry and Evaluation of Lightcurves; Nordin et al., 2019a). We applied a cut of < 0.8 on the star–galaxy score (Tachibana & Miller, 2018) to find variable objects associated with galaxies, and a cut of < 0.3 on the real–bogus score (Duev et al., 2019; Mahabal et al., 2019) to remove erroneous detections arising from poor quality images and subtractions. We removed objects in busy stellar fields by checking there were no more than 30 Gaia objects and 100 PanSTARRS objects within a 15” radius using crossmatching software `catsHTM` (Soumagnac & Ofek, 2018). We also required at least 3 significant detections > 0.01 days apart.

To select AGN and remove supernovae within the `AMPEL` filter, we required that our transients either match an object in a series of AGN catalogs or have variability more characteristic of an AGN than a supernova. We used `catsHTM` and `Extcats`[1] to crossmatch with a 2” radius to objects in The Million Quasar Catalog (Flesch, 2015), a machine learning based catalog of photometric AGN candidates (Brescia et al., 2015), and a catalog of 720,961 variable sources from the Palomar Transient Factory (PTF) and intermediate Palomar Transient Factory (iPTF) found between 2009 and 2016 which were not classified as a star (Miller et al., 2017) and had > 5 detections over > 24 hours. For sources which did not have an AGN catalog crossmatch, we modeled their full ZTF light curve history with the ‘salt2’ SN Ia model (`SNCOSMO`; Barbary et al., 2016)) and a model of the average SDSS quasar structure function (Butler & Bloom, 2011). We required that the quasar model provide a better fit to the data than the SN model based on the χ^2 statistic.

Objects which passed either the AGN catalog crossmatch criteria or the light curve fitting criteria were pushed to the GROWTH Marshal science portal for arrangement of spectroscopic followup (Kasliwal et al., 2019). The AGN candidates

[1] https://github.com/MatteoGiomi/extcats

were then confirmed either with existing SDSS spectroscopic classifications, follow–up spectroscopic observations with the DeVeny spectrograph on the Lowell Discovery Telescope, or by their WISE color or variability history. To classify AGN based on their WISE W1–W2 color we used the criteria $W1 - W2 > 0.662$ exp $\{0.232(W2 - 13.97)^2\}$ (Assef et al., 2013), and to classify AGN based on significant variability in their WISE light curve we required the χ^2 relative to a flat light curve to satisfy $\chi^2/\text{dof} > 10$.

We applied this procedure to ZTF alerts from a 2.5 year period between 2018-01-01 to 2020-07-06 and obtained a sample of 5493 strongly variable ZTF AGN with spectroscopic or WISE color/variability confirmation. We then crossmatched to the SDSS DR16 spectroscopic catalog and selected all objects of the 'GALAXY AGN BROADLINE' and 'QSO BROADLINE' class to obtain a sub–sample of 1923 optically variable AGN in ZTF with Balmer broad lines.

4.3.2 Spectroscopic selection of DPE sub–sample

In order to find the AGN with double–peaked broad lines amongst the sample of 1923 broadline AGN, we used Penalized Pixel Fitting (pPXF) (Cappellari, 2017; Cappellari & Emsellem, 2004) to model the archival SDSS spectra of the AGN. This method models the emission lines while simultaneously finding the best fit stellar continuum and absorption model using a large sample of high resolution templates of single stellar populations adjusted to match the spectral resolution of the input spectrum.

We used `pPXF` to fit two different models. In both cases we fit the narrow Hα, Hβ, Hγ, Hδ, [S II] λ6717, 6731, [N II] λ6550, 6575, [O I] λ6302, 6366 and [O III] λ5007, 4959 narrow emission lines along with a stellar continuum. In the first model the spectrum was fit with single broad Hα and Hβ lines with velocities tied to the corresponding narrow lines. In the second model the spectrum was instead fit with 3 Balmer broad lines: one with central velocity tied to the narrow Balmer lines, one with a velocity up to 6000 km s^{-1} relative to the narrow lines, and one with a velocity down to -6000 km s^{-1}. The widths of the 3 broad lines were not tied to each other.

To find double–peaked emitters from the fits of these two models, we required the χ^2 improvement from the multiple broad line model compared to the single broad line model to be > 250. Then to be considered a confident double–peaked emitter candidate the two velocity–offset Hα broad lines were each required to have peak flux densities of $> 33\%$ of the narrow Hα line and to have a velocity > 500 km s^{-1} from the narrow line velocity. As the effectiveness of this criteria depended on the relative brightness of narrow and broad lines, and the width of the broad line region, we visually inspected the 275 candidates found via this criteria and rejected 82, leaving 193 double–peaked emitters. We then visually inspected the remaining 1648 spectra to find any objects which may have missed by the criteria. We found 106 double–peaked spectra which were missed by the automatic classification scheme.

We found that 299 of 1923, or $\sim 16\%$, of the variable broad line AGN sample from ZTF are DPEs based on their archival SDSS spectra. The DPEs found by our selection criteria are shown in Table 4.1. Examples of multi–Gaussian fits to the Hα spectra of the 26 DPEs with the brightest double–peaked broad lines relative to the flux of the Hα narrow line are shown in Section 4.6. The redshifts, maximum g–band magnitudes and estimated virial black hole masses of the two samples are summarized in Figure 4.1.

The samples are similarly distributed in redshift, but DPEs reach brighter magnitudes on average than their standard broad line counterparts and have larger estimated virial masses. We will revisit the differing mass distributions in Section 4.3.3.4.

Table 4.1: Properties of the 299 variable DPE candidates in ZTF. Virial masses were calculated for broad line AGN by Ho & Kim (2015) based on the width of the Hα broad lines. The velocities of the red and blue shoulders found via multi–Gaussian fitting of DPE spectra are shown for all DPEs identified by the fitting criteria. γ shows the power law index from modeling of light curve power spectra with a power law + white noise model. The characteristic timescale and high frequency amplitude τ and σ from DRW time series modeling are shown. For objects with a detection in VLASS, the radio flux is shown in the last column.

ZTF ID	RA (hms)	Dec (dms)	z	$\log_{10}$M$_*$ ($M_\odot$)	Blue vel. (km/s)	Red vel. (km/s)	γ γ	$\log\tau$ (days)	$\log\sigma$	F$_{20cm}$ (Jy)
ZTF18aaadgxi	12:10:44.271	38:20:10.243	0.0229	8.017	−1462.0	1678.0	–	1.42	−0.32	4.2±0.38
ZTF18aaahyks	08:16:51.865	49:53:35.062	0.1587	8.04	–	–	–	5.23	−1.75	-
ZTF18aaajnly	13:05:34.477	18:19:32.916	0.1182	7.825	−949.0	1219.0	–	5.22	−1.63	-
ZTF18aaajraa	12:42:38.465	15:29:34.693	0.0703	7.417	−2481.0	669.0	–	5.03	−1.65	-
ZTF18aaaovpz	10:39:13.802	09:40:3.171	0.2171	8.689	−3542.0	1297.0	–	6.49	−1.6	-
ZTF18aabylvn	14:17:59.554	25:08:12.59	0.0163	7.535	−941.0	4754.0	–	1.44	−0.13	-
ZTF18aacajqc	10:29:46.791	40:19:13.636	0.0673	8.166	−2061.0	653.0	–	3.89	−2.18	-
ZTF18aacbjcx	12:11:17.216	24:37:11.414	0.2223	8.123	−1242.0	2215.0	–	5.01	−1.79	-
ZTF18aacbjdm	12:32:3.637	20:09:29.529	0.0636	7.701	−2766.0	860.0	–	1.45	−1.47	-
ZTF18aacdpbi	09:05:14.486	41:51:53.493	0.1764	8.653	−1475.0	1130.0	–	6.07	−1.38	-
ZTF18aacdydz	09:35:45.065	32:01:59.117	0.1013	7.817	–	–	–	5.3	−1.64	-
ZTF18aacjava	08:12:37.83	43:56:34.986	0.1821	8.284	−844.0	3015.0	–	5.46	−1.43	-
ZTF18aacjltc	08:12:52.441	40:23:48.894	0.1886	7.587	–	–	–	5.84	−1.57	-
ZTF18aacjtlo	08:29:42.682	41:54:36.885	0.1263	8.801	−2506.0	2418.0	–	6.04	−0.86	4.33±0.35
ZTF18aacrkse	09:05:14.481	41:51:53.825	0.176	8.653	−1475.0	1130.0	–	6.07	−1.46	-
ZTF18aacwjha	08:42:3.742	40:18:31.371	0.1516	8.907	−4088.0	533.0	–	6.39	−1.04	14.6±0.28
ZTF18aaellbb	08:29:42.96	28:35:21.597	0.2941	8.37	–	–	–	6.01	−1.58	-
ZTF18aaetnmr	09:01:48.203	20:36:31.954	0.115	7.203	−1916.0	505.0	–	4.63	−2.23	-
ZTF18aagfjja	08:03:27.384	08:41:52.182	0.0467	8.207	−1282.0	2525.0	–	5.86	−1.65	1.42±0.26
ZTF18aagstka	15:07:45.014	51:27:10.276	0.0459	7.391	–	–	–	1.42	−1.03	-

ZTF18aahbxie	12:42:23.359	19:47:20.884	0.1603	8.12	−1377.0	1134.0	–	3.25	−1.41	-
ZTF18aahfere	10:38:53.307	39:21:51.218	0.0548	7.81	−1547.0	954.0	–	5.75	−1.11	-
ZTF18aahfjdt	10:43:26.481	11:05:24.351	0.0475	8.163	–	–	–	4.87	−1.29	-
ZTF18aahfssj	12:30:59.742	35:45:42.828	0.1004	7.798	−2438.0	734.0	–	3.81	−1.66	-
ZTF18aahipte	11:50:26.007	26:30:38.789	0.1117	7.526	–	–	–	6.41	−0.67	-
ZTF18aahiqst	11:03:40.32	37:29:25.08	0.0736	8.61	−2521.0	2849.0	–	4.32	−2.49	2.15±0.24
ZTF18aahjbhp	13:12:59.593	26:28:24.107	0.0604	7.034	–	–	–	5.16	−1.04	-
ZTF18aahlveu	14:22:53.483	47:32:52.258	0.1991	8.563	−1885.0	2030.0	–	5.19	−1.5	-
ZTF18aahoprl	08:46:54.088	25:22:12.203	0.0508	7.927	−913.0	2105.0	–	4.13	−1.63	-
ZTF18aahsuls	12:15:47.254	29:38:30.924	0.1673	8.511	−598.0	1195.0	–	5.64	−1.07	-
ZTF18aahtnlt	11:45:10.256	30:47:17.135	0.059	6.825	–	–	–	1.43	−0.48	-
ZTF18aahujbh	12:07:22.114	38:52:15.919	0.3073	8.99	−2397.0	1328.0	–	5.39	−1.49	-
ZTF18aahuxsj	13:02:54.415	29:49:15.07	0.1836	7.638	−598.0	2015.0	–	6.16	−1.04	-
ZTF18aahxakv	12:18:48.536	30:28:29.588	0.1971	8.28	−1686.0	1108.0	–	4.48	−1.64	-
ZTF18aaiklad	15:06:20.833	29:39:56.911	0.0589	7.366	−1071.0	1275.0	–	3.23	−2.66	-
ZTF18aaiwsqa	15:56:42.838	29:48:47.552	0.0842	8.499	−774.0	1790.0	–	1.42	−0.34	-
ZTF18aajjvsu	11:21:48.293	42:47:4.788	0.1438	7.456	–	–	–	4.74	−1.82	-
ZTF18aajpluq	14:04:31.409	21:34:15.477	0.0839	8.446	−2114.0	2248.0	–	4.95	−1.37	-
ZTF18aajvtbl	17:22:39.932	30:52:52.733	0.0431	7.527	–	–	–	4.0	−1.32	4.43±0.29
ZTF18aakbsog	10:55:18.453	39:29:5.321	0.2534	8.565	−661.0	854.0	–	3.78	−2.15	1.6±0.26
ZTF18aakehue	13:45:45.371	53:32:52.216	0.1356	8.411	−1496.0	1032.0	–	2.79	−1.82	-
ZTF18aakkvuf	13:33:29.435	15:45:50.036	0.2462	9.089	−2658.0	1883.0	–	5.7	−1.5	-
ZTF18aaklvii	12:06:5.183	35:38:25.1	0.2869	7.844	−1403.0	4891.0	–	6.3	−1.15	-
ZTF18aakmfwg	11:45:26.92	33:30:44.526	0.1343	7.574	−1363.0	549.0	–	4.29	−1.89	-
ZTF18aakqzem	11:43:44.243	59:41:12.425	0.0629	7.766	−2066.0	1631.0	–	3.87	−2.18	-
ZTF18aalmrdp	09:17:28.576	27:19:51.143	0.0756	7.892	−1228.0	1863.0	–	5.65	−1.17	-
ZTF18aalrzft	16:54:35.839	33:02:51.426	0.1219	8.551	–	–	–	5.71	−1.49	-
ZTF18aalslhk	13:04:58.02	45:35:33.588	0.1831	8.549	−1731.0	1787.0	–	5.92	−1.18	-
ZTF18aambjzu	13:05:47.025	50:40:33.962	0.0551	6.86	–	–	–	4.63	−1.29	-

ZTF18aamffwm	15:12:24.264	38:51:12.765	0.2016	7.291	−643.0	571.0	–	5.23	−1.34	-
ZTF18aaoeobb	12:48:53.896	34:24:29.389	0.2703	8.764	−4076.0	592.0	–	4.71	−1.82	-
ZTF18aaqcmmu	11:44:10.16	51:58:49.911	0.2914	7.384	–	–	–	5.97	−1.25	-
ZTF18aaqcxpx	13:54:47.862	42:06:41.438	0.2318	8.137	−769.0	2168.0	–	5.9	−0.76	-
ZTF18aaqdmih	11:40:53.161	25:25:46.47	0.2988	9.194	−3938.0	2312.0	–	5.84	−0.98	-
ZTF18aaqdvwu	12:20:28.083	40:50:35.065	0.2218	8.44	−1584.0	667.0	–	4.78	−1.88	-
ZTF18aaqdxqq	11:50:19.565	53:47:24.585	0.0608	7.646	−1201.0	1102.0	–	1.42	−0.79	-
ZTF18aaqgbag	15:33:10.024	27:29:20.299	0.0719	8.575	−3292.0	2846.0	–	2.13	−1.76	1.83±0.23
ZTF18aaqjoov	12:06:18.535	23:33:39.824	0.3511	–	−2301.0	966.0	–	6.23	−1.37	-
ZTF18aaqkgwt	11:45:59.595	46:13:9.211	0.1543	8.042	−1965.0	1640.0	–	6.06	−1.08	-
ZTF18aaqlksk	14:24:24.201	59:53:0.286	0.135	8.528	−1166.0	1282.0	–	1.45	−2.0	4.88±0.22
ZTF18aaqmaet	15:20:8.243	46:16:15.21	0.1763	8.411	−914.0	1823.0	–	6.08	−0.93	-
ZTF18aarippg	14:30:16.054	23:03:44.428	0.081	–	−4600	4000	–	–	–	-
ZTF18aarlffl	11:21:51.24	40:51:46.943	0.0604	8.346	−3724.0	4888.0	–	1.43	0.32	-
ZTF18aarmerf	12:14:1.347	40:48:22.964	0.277	7.697	–	–	–	5.35	−1.59	-
ZTF18aarnfbc	12:35:54.664	15:15:34.778	0.2281	8.012	−1815.0	947.0	–	3.58	−1.48	-
ZTF18aarqlnq	17:00:46.779	29:19:26.529	0.0683	8.006	–	–	–	4.94	−1.94	-
ZTF18aarqrzt	15:52:7.185	52:53:47.168	0.3352	8.215	–	–	–	5.58	−1.75	-
ZTF18aarrwmi	16:05:2.458	33:05:45.416	0.0529	7.977	−1549.0	1565.0	–	3.15	−1.71	-
ZTF18aarywbt	12:17:9.899	07:11:29.644	0.0075	8.09	−2953.0	4635.0	–	1.55	−2.6	4.97±0.29
ZTF18aascziw	15:02:26.613	54:46:33.527	0.342	8.153	−1836.0	1374.0	–	6.1	−1.49	-
ZTF18aasrwgz	10:22:55.608	18:47:44.556	0.1766	8.463	−1827.0	798.0	–	4.59	−1.93	-
ZTF18aasukvm	12:18:22.758	38:50:43.485	0.1936	8.089	−502.0	4890.0	–	5.42	−1.48	-
ZTF18aasupgp	11:55:15.867	38:02:35.059	0.144	8.047	−3011.0	1145.0	–	3.8	−1.92	-
ZTF18aatcbcv	15:16:27.136	54:05:14.693	0.195	7.455	–	–	–	2.39	−1.69	-
ZTF18aatnuln	16:28:4.041	51:46:31.871	0.0727	–	–	–	–	1.42	−1.87	-
ZTF18aatucth	11:21:48.282	42:47:4.899	0.1438	7.456	−2346.0	742.0	–	4.87	−1.78	-
ZTF18aatxsvu	15:42:10.404	13:07:57.784	0.0928	8.004	−1035.0	1179.0	–	6.13	−0.83	-
ZTF18aauhbir	09:14:6.743	35:27:28.624	0.1364	7.869	−1655.0	699.0	–	6.22	−0.94	-

ZTF18aauiowc	11:57:12.442	18:17:40.037	0.316	8.464	–	–	–	4.75	−1.58	-
ZTF18aauvptt	13:46:28.612	17:36:59.413	0.1747	7.986	−2518.0	845.0	–	5.76	−0.42	-
ZTF18aauylsc	16:17:45.637	06:03:53.578	0.0379	7.651	−2081.0	809.0	–	5.28	−1.11	2.98±0.51
ZTF18aavjvga	15:56:42.845	29:48:47.471	0.0842	8.499	−774.0	1790.0	–	1.41	−0.42	-
ZTF18aavskhe	15:27:35.116	06:17:8.723	0.1866	8.195	−3621.0	958.0	–	5.96	−0.99	-
ZTF18aawebos	15:01:49.953	28:30:9.574	0.1409	7.633	−2337.0	764.0	–	4.86	−1.71	-
ZTF18aaweuvi	15:06:5.314	20:34:11.175	0.3044	8.467	–	–	–	6.33	−0.79	-
ZTF18aawnbyf	10:21:10.766	27:53:43.644	0.0977	7.719	–	–	–	3.99	−1.55	-
ZTF18aawnitq	11:13:59.845	31:09:12.15	0.1524	7.833	–	–	–	5.33	−1.59	-
ZTF18aawvytv	07:36:45.57	43:56:37.141	0.3164	8.303	−909.0	881.0	–	5.32	−1.41	-
ZTF18aawxnvf	11:24:5.386	44:20:47.874	0.2439	7.957	−697.0	866.0	–	6.27	−1.16	-
ZTF18aaxejis	12:23:24.132	02:40:44.462	0.0239	7.787	−2341.0	664.0	–	1.6	−1.19	-
ZTF18aaxlxwg	13:04:21.299	17:19:6.707	0.1901	8.066	−1055.0	1612.0	–	4.48	−2.09	-
ZTF18aaxlzyf	11:47:55.066	09:02:28.82	0.0687	8.364	−537.0	1340.0	–	5.47	−1.26	-
ZTF18aaxnnrx	12:07:55.843	06:04:2.745	0.1362	8.631	−1559.0	4823.0	–	6.0	−1.02	-
ZTF18aaxqprt	13:05:16.096	39:13:1.971	0.1766	8.241	−1602.0	1134.0	–	5.19	−1.78	-
ZTF18aaxrpnw	14:11:9.173	44:40:11.89	0.0946	7.465	−3387.0	941.0	–	5.47	−2.77	-
ZTF18aaxvxkz	16:05:53.754	38:25:2.323	0.2855	8.362	−505.0	4816.0	–	4.49	−1.67	-
ZTF18aaxzhgj	12:20:7.382	02:24:31.742	0.1585	8.104	−1672.0	813.0	–	5.44	−1.69	-
ZTF18aaxzqhz	10:20:44.307	49:20:46.206	0.3897	–	–	–	–	6.1	−1.34	-
ZTF18aaylbyr	15:42:13.914	18:35:0.028	0.0724	8.416	−1760.0	1358.0	–	5.01	−1.53	1.53±0.26
ZTF18aaympoe	15:27:31.773	38:43:7.616	0.3999	–	−3129.0	966.0	–	5.06	−1.82	-
ZTF18aaymybb	19:14:37.612	50:28:54.774	0.231	–	−4800	7000	–	5.01	−1.66	-
ZTF18aazhwfb	15:28:32.422	28:57:51.084	0.0633	6.945	−2381.0	667.0	–	5.66	−1.62	-
ZTF18aaziudx	14:02:0.575	42:04:41.484	0.168	8.501	−2328.0	765.0	–	5.99	−1.47	-
ZTF18aaznjgn	11:18:7.972	59:28:43.9	0.3942	–	−1301.0	1771.0	–	6.31	−1.15	2.99±0.21
ZTF18aaznkeg	10:36:33.944	62:09:39.614	0.1489	8.271	−2255.0	800.0	–	5.15	−1.79	-
ZTF18aazogyo	14:56:27.389	30:53:45.705	0.0736	8.087	−1292.0	1961.0	–	4.87	−1.92	-
ZTF18aazzfia	17:08:59.118	21:53:8.268	0.0719	8.21	−2158.0	824.0	–	4.69	−1.62	-

ZTF18abafekh	14:19:50.082	19:44:15.44	0.0772	8.167	−2479.0	643.0	–	4.99	−1.87	-
ZTF18abbppru	16:27:55.399	46:42:48.792	0.2135	8.639	−2891.0	1797.0	–	4.06	−1.52	-
ZTF18abbpwzy	15:46:6.968	03:47:57.112	0.1271	8.243	−1230.0	1296.0	–	3.8	−2.56	-
ZTF18abcypfw	15:42:41.812	22:52:53.377	0.0352	7.517	−2537.0	1537.0	–	2.4	−2.04	-
ZTF18abgjezf	21:54:13.46	27:46:51.33	0.2158	–	–	–	–	5.77	−1.15	-
ZTF18abgvcbl	13:21:5.904	51:19:43.205	0.116	7.828	−1208.0	1637.0	–	3.2	−1.94	-
ZTF18abkered	16:54:35.843	33:02:51.432	0.1219	8.551	–	–	–	5.59	−1.54	-
ZTF18abknopt	17:13:0.725	57:25:30.155	0.3602	–	–	–	–	5.83	−1.85	-
ZTF18ablqgje	14:56:31.649	00:11:14.209	0.1327	8.634	−3047.0	761.0	–	6.24	−0.55	-
ZTF18ablqhbt	13:51:51.545	21:22:11.577	0.0608	–	–	–	–	–	–	2.07±0.28
ZTF18ablqilq	13:22:35.283	50:16:44.362	0.3018	7.744	–	–	–	6.17	−1.3	-
ZTF18ablsyos	14:31:29.598	29:17:11.646	0.2554	8.002	−1746.0	1349.0	–	3.77	−2.23	-
ZTF18abthdsk	07:35:3.491	43:11:53.68	0.2621	8.224	–	–	–	6.16	−1.27	-
ZTF18abtjnci	21:31:10.506	00:35:36.949	0.1448	7.84	–	–	–	3.56	−2.51	-
ZTF18abttmvx	09:03:19.539	38:43:49.58	0.2051	7.864	–	–	–	6.54	−0.91	-
ZTF18abttnqj	08:04:11.205	43:16:40.717	0.132	–	−1714.0	2073.0	–	5.13	−1.53	-
ZTF18abuvtlx	01:29:46.713	15:04:57.253	0.3649	–	−829.0	4902.0	–	6.43	−0.73	-
ZTF18abwpfja	23:09:20.262	00:45:23.473	0.0324	7.785	−1663.0	1880.0	–	4.65	−2.34	-
ZTF18abxxohm	19:30:25.3	64:29:23.124	0.16	–	−1500	2000	–	1.42	−0.96	5.83±0.22
ZTF18abzweee	22:24:7.813	04:09:13.079	0.0975	–	−2383.0	1438.0	–	5.82	−0.94	-
ZTF18abzzror	07:56:20.08	30:45:35.483	0.2364	8.136	–	–	–	6.27	−1.13	-
ZTF18acaoyyf	09:32:57.72	47:52:49.549	0.198	8.389	−1662.0	1072.0	–	6.24	−1.03	-
ZTF18acapafh	09:56:27.058	54:04:14.959	0.207	7.689	–	–	–	6.34	−0.95	-
ZTF18accdnfn	09:43:34.209	53:34:40.495	0.0855	7.651	−1473.0	866.0	–	5.11	−2.07	-
ZTF18accnimw	11:21:51.218	40:51:47.3	0.0604	8.346	−3724.0	4888.0	–	1.42	0.35	-
ZTF18accvgos	07:26:56.082	41:01:36.139	0.1294	7.95	–	–	–	5.22	−1.68	-
ZTF18accwjod	10:22:55.621	18:47:44.49	0.1766	8.463	−1827.0	798.0	–	4.88	−1.87	-
ZTF18acdvqzz	08:53:30.282	10:58:28.021	0.2731	8.412	–	–	–	6.14	−1.61	-
ZTF18acehaci	22:24:35.289	00:11:3.72	0.0579	7.329	−1355.0	1030.0	–	4.7	−1.92	-

ZTF18aceqxwp	11:26:11.619	42:52:46.583	0.157	8.363	−1667.0	1092.0	–	6.37	−2.39	-
ZTF18aceylbs	10:57:30.693	18:21:50.437	0.232	8.999	−1503.0	4893.0	–	6.46	−1.25	-
ZTF18achbxbz	07:39:31.555	47:32:21.744	0.1353	8.348	−2084.0	852.0	–	4.8	−1.83	-
ZTF18achchge	08:38:26.513	37:19:6.815	0.2111	8.908	−1177.0	4915.0	–	5.98	−0.79	-
ZTF18aclmlqy	07:58:50.294	09:35:20.684	0.0458	7.779	−1126.0	4363.0	–	3.78	−2.65	-
ZTF18acmqplu	08:38:10.93	24:53:43.031	0.0287	7.185	–	–	–	1.46	−2.98	35.27±0.31
ZTF18acnbgnc	11:24:5.388	44:20:47.892	0.2439	7.957	–	–	–	6.28	−1.15	-
ZTF18acnneyu	13:12:22.111	29:37:47.886	0.2466	8.142	−2029.0	1116.0	–	5.38	−1.46	-
ZTF18acpcxmu	11:07:56.55	47:44:34.963	0.0727	8.24	−1056.0	529.0	–	1.57	0.87	-
ZTF18acpwodb	12:35:54.66	15:15:34.704	0.2281	8.012	−1815.0	947.0	–	3.62	−1.47	-
ZTF18acqfzeh	10:17:37.944	06:58:16.115	0.0453	–	−1774.0	1418.0	–	2.82	−1.83	-
ZTF18acqtdnj	12:37:7.422	07:40:24.859	0.132	9.199	−1975.0	4275.0	–	6.28	−1.57	-
ZTF18acqzgwt	11:22:15.922	16:03:24.166	0.1603	8.376	−538.0	909.0	–	4.46	−2.51	-
ZTF18acrnivy	13:31:38.013	01:31:51.654	0.0806	7.154	–	–	–	3.78	−1.81	2.08±0.28
ZTF18acrygbu	13:49:52.857	02:04:45.058	0.0329	7.415	–	–	–	4.48	−1.99	-
ZTF18acrygry	13:13:5.682	-2:10:39.213	0.0837	8.043	–	–	–	5.67	−1.29	-
ZTF18acvcadu	00:20:24.085	33:47:7.28	0.065	–	−2369.0	2053.0	–	2.18	−2.8	-
ZTF18acvgmng	11:03:50.619	01:19:37.358	0.1296	7.846	–	–	–	5.29	−1.79	-
ZTF18acvgnil	11:07:17.774	08:04:38.221	0.2005	8.237	−1055.0	855.0	–	5.89	−1.56	-
ZTF18acvgnqt	11:02:36.071	32:35:41.112	0.2866	8.647	−1697.0	3675.0	–	5.1	−1.39	-
ZTF18acvgvpn	12:26:41.507	05:59:6.8	0.29	8.259	–	–	–	6.27	−1.36	-
ZTF18acvgwdi	12:57:35.05	09:16:13.566	0.3711	–	–	–	–	5.43	−1.97	-
ZTF18acviafl	15:45:1.458	11:35:18.192	0.237	8.852	−670.0	4858.0	–	5.37	−1.22	-
ZTF18acvwdfc	13:43:21.378	23:20:39.265	0.1729	8.145	−1010.0	1151.0	–	4.88	−1.96	-
ZTF18acvwgao	09:39:45.912	00:29:22.308	0.1673	8.142	−1052.0	1308.0	–	5.11	−1.5	-
ZTF18acvwlrf	12:50:16.229	04:57:45.125	0.2332	8.004	−1933.0	1874.0	–	6.55	−1.05	-
ZTF18acwyxcm	13:33:12.413	01:30:23.729	0.2171	8.804	−688.0	4896.0	–	5.1	−1.16	-
ZTF18acwyzzl	15:45:47.566	12:22:1.487	0.1833	8.023	−1746.0	711.0	–	5.5	−1.88	-
ZTF18acwzaev	15:06:26.432	03:06:59.964	0.1729	7.527	–	–	–	5.94	−1.23	-

ZTF18acydjfe	14:37:1.496	26:40:19.231	0.2185	8.861	−1991.0	2617.0	–	3.78	−0.87	3.99±0.23
ZTF18aczdenj	09:38:14.808	02:00:23.566	0.1741	8.006	−609.0	963.0	–	6.09	−1.68	-
ZTF18aczeoen	11:06:49.836	10:17:38.678	0.1678	8.27	−614.0	4751.0	–	4.36	−1.91	-
ZTF18aczergd	14:23:52.461	22:47:45.505	0.2814	9.196	−4569.0	4855.0	–	4.53	−1.57	-
ZTF18aczexpu	16:03:37.055	07:08:38.795	0.1859	8.198	−806.0	1524.0	–	6.29	−1.63	-
ZTF18adachmi	14:17:58.612	09:16:9.835	0.1389	7.897	−2284.0	1081.0	–	2.87	−1.12	-
ZTF19aaafosj	13:08:39.062	16:00:7.227	0.1803	7.849	−2115.0	728.0	–	5.66	−1.16	-
ZTF19aaapujo	12:23:10.582	06:45:54.953	0.2352	–	–	–	–	–	–	-
ZTF19aacixeg	16:03:6.177	13:25:2.111	0.21	8.875	−2774.0	1289.0	–	6.22	−0.88	-
ZTF19aademoc	11:05:3.611	07:45:31.029	0.0732	7.832	−534.0	4797.0	–	5.55	−1.14	-
ZTF19aadgigp	14:47:2.866	27:37:46.547	–	9.051	−4324.0	2474.0	–	3.82	−0.66	-
ZTF19aafmqbn	12:39:54.175	07:41:53.875	0.1035	7.995	–	–	–	5.79	−1.27	-
ZTF19aagflww	15:50:53.172	05:21:12.133	0.1099	8.228	−2918.0	1022.0	–	5.75	−1.46	-
ZTF19aagwzod	04:28:38.795	00:00:39.694	0.0702	–	−1800	2400	–	5.57	−1.65	-
ZTF19aaiklvu	09:06:12.484	19:36:0.802	0.3439	–	–	–	–	6.48	−1.24	-
ZTF19aalzczk	12:59:33.521	-1:28:33.272	0.2657	7.735	–	–	–	5.74	−2.26	-
ZTF19aalzmbo	15:55:5.987	45:50:8.968	0.3777	–	–	–	–	2.08	−0.45	-
ZTF19aamgxav	11:06:40.211	05:19:5.596	0.0906	8.219	−1635.0	594.0	–	6.33	−1.25	-
ZTF19aamtdld	13:33:38.312	04:18:3.981	0.1968	8.845	−4077.0	3202.0	–	5.51	−0.99	-
ZTF19aanesnf	09:17:29.524	60:31:43.949	0.1942	7.625	–	–	–	5.07	−1.82	-
ZTF19aanikjt	14:46:37.464	31:08:47.025	0.0887	7.842	−1118.0	1187.0	–	4.72	−1.88	-
ZTF19aannwar	07:24:29.078	40:46:43.094	0.0501	–	–	–	–	6.5	−2.11	-
ZTF19aanwsuq	14:24:24.233	59:53:0.421	0.1348	8.528	−1166.0	1282.0	–	1.45	−2.07	4.88±0.22
ZTF19aaokohz	14:12:18.49	55:56:49.292	0.3167	7.878	–	–	–	5.31	−1.61	-
ZTF19aaoyjsq	12:05:30.637	16:49:41.839	0.217	–	−2341.0	4074.0	–	5.26	−1.44	-
ZTF19aapkuvx	08:21:25.374	42:19:8.549	0.2217	9.045	−3282.0	2078.0	–	5.42	−1.39	-
ZTF19aapvkcg	12:18:22.747	38:50:43.481	0.1936	8.089	−502.0	4890.0	–	5.41	−1.49	-
ZTF19aarjtww	13:49:28.538	03:59:5.54	0.2535	8.599	−1567.0	1635.0	–	5.38	−1.25	-
ZTF19aarsgzg	09:03:54.61	45:10:4.52	0.2162	7.625	–	–	–	6.21	−1.38	-

ZTF19aaseyqn	15:11:43.405	21:01:3.939	0.0805	8.209	−512.0	4148.0	–	6.58	−0.92	-
ZTF19aatlpwc	14:02:42.884	23:17:40.815	0.1824	7.806	–	–	–	–	–	-
ZTF19aawgugc	12:45:35.782	47:01:8.475	0.1511	7.4	–	–	–	5.33	−1.46	-
ZTF19aawnkup	13:02:41.516	04:07:38.605	0.1024	8.074	−1036.0	1358.0	–	4.58	−1.66	-
ZTF19aawompn	15:25:9.028	01:26:24.505	0.3	8.494	–	–	–	5.95	−1.75	-
ZTF19aawoseu	12:36:18.935	58:00:15.786	0.2088	8.226	−2691.0	1530.0	–	4.61	−2.02	-
ZTF19aayrjsx	23:32:54.459	15:13:5.477	0.2146	8.999	−1813.0	3404.0	–	6.0	−1.32	-
ZTF19aazdsch	23:54:57.103	00:42:20.053	0.2702	8.67	−1520.0	769.0	–	5.33	−1.88	-
ZTF19abaeyma	15:01:18.336	15:56:22.971	0.3254	8.543	−1215.0	1006.0	–	6.09	−2.0	-
ZTF19abauzsd	15:54:32.69	21:43:48.179	0.2848	8.306	−1618.0	714.0	–	6.3	−1.34	-
ZTF19abheonl	16:31:33.353	12:38:44.91	0.2389	7.632	–	–	–	4.95	−2.0	-
ZTF19abizomu	01:57:38.093	13:09:31.595	0.2207	8.77	−2611.0	2234.0	–	5.79	−1.46	7.9±0.55
ZTF19acbvtcx	08:34:29.292	06:03:24.998	0.1099	8.341	−1755.0	1733.0	–	5.64	−1.53	-
ZTF19acdtzdd	08:31:39.767	19:56:5.466	0.2111	7.939	−3198.0	1942.0	–	6.08	−1.49	1.61±0.29
ZTF19acszojn	13:03:23.465	01:11:2.634	0.086	7.542	−1378.0	710.0	–	5.67	−1.21	-
ZTF19adceobn	08:14:25.885	29:41:15.881	0.374	–	−3508.0	2000.0	–	6.21	−1.02	4.37±0.35
ZTF19adcfhuh	10:14:11.896	32:58:4.989	0.231	7.617	–	–	–	5.68	−0.85	-
ZTF20aabqusj	13:54:26.097	14:41:51.574	0.2141	7.994	−797.0	1082.0	–	5.18	−1.31	-
ZTF20aadccjf	16:14:39.801	19:24:20.369	0.164	8.007	−1607.0	550.0	–	5.81	−1.57	-
ZTF20aajaukh	11:50:26.005	26:30:38.782	0.1117	7.526	–	–	–	6.47	−0.64	-
ZTF20aambhbr	13:20:0.321	45:06:9.431	0.1087	–	–	–	–	3.48	−2.66	-
ZTF20aapcmmg	16:18:3.259	15:48:14.051	0.3437	8.248	–	–	–	6.04	−1.73	-
ZTF20aaunrws	15:16:27.145	54:05:14.683	0.195	7.455	–	–	–	2.38	−1.7	-
ZTF20aauvdym	12:43:24.251	01:00:28.183	0.0897	7.809	−746.0	1905.0	–	3.81	−2.45	-
ZTF20aavyedw	14:25:45.88	00:22:42.809	0.3257	7.937	–	–	–	6.18	−1.47	-
ZTF20aazgrhr	12:50:42.46	-2:49:31.34	0.0471	7.67	−1556.0	790.0	–	5.82	−2.19	-

4.3.3 Variability properties of DPEs and other broad line AGN

4.3.3.1 Construction of optical and mid–IR light curves

In order to produce light curves of the DPEs and AGN control sample using both positive and negative photometry from ZTF difference imaging, we used the ZTF forced photometry service (Masci et al., 2019). After removing poor quality images by requiring the `procstatus` flag be $= 0$, we measured the baseline flux from the reference images, applied zeropoints, and combined the baseline and single epoch fluxes to produce g- and r-band light curves of the two samples.

Notable optical light curves of selected DPEs are shown in Figure 4.2. ZTF18aarippg, the previously reported candidate for an inspiraling SMBH binary (Jiang et al., 2022) is not the only DPE light curve to display chirping signals in a section of the optical light curve. ZTF18aaznjgn also displays a ringdown signal with decreasing period and peak flux over 4 cycles during a 1300 day period. The first year of the ZTF18aaylbyr light curve shows the opposite: 3 cycles of increasing period and flux, before reverting to more complex variability. Many DPE light curves show quasi–periodic behaviour with 3–4 cycles of an approximately 8 month to 1 year period (e.g. ZTF18aalslhk and ZTF18aakehue).

The AGN and DPE samples also had mid–IR light curves available from the *WISE* mission. *WISE* mapped the sky in the W1 (3.4μm) and W2 (4.6μm) bands with 6 month cadence over an 8 year baseline between the initial observations in 2010, the Near–Earth Object Wide–field Infrared Survey Explorer mission from 2010–2011 (*NEOWISE*;

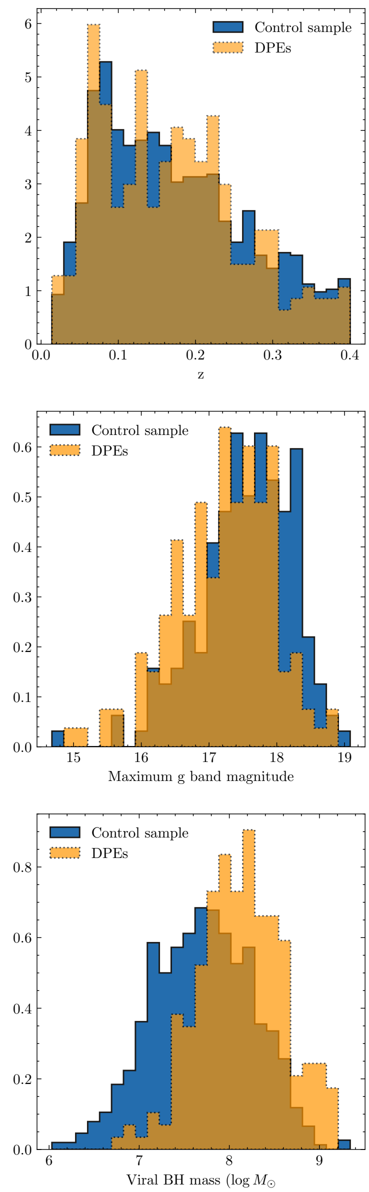

Figure 4.1: Distribution of redshift, maximum g-band magnitude from the ZTF light curve, and estimated virial mass from Ho (2008) for the DPE sample and the broad line AGN control sample. We note that the virial masses of the DPEs may be overestimated based on arguments made in Section 4.3.3.4.

Mainzer et al., 2011b) and the reactivation mission beginning in 2013 (*NEOWISE*-R; Mainzer et al., 2014). To obtain sensitive mid–IR light curves of the samples, we made use of forward modelled photometry of time–resolved *WISE* coadds (Meisner et al., 2018) made available through Data Release 9[2] of the DESI imaging Legacy Survey (Dey et al., 2019a). This provided high quality light curves of approximately 15 flux measurements in W1 and W2 measured over ~ 8 years.

The mid–IR light curves of selected DPEs are also shown in Figure 4.2. In a number of cases, the WISE light curves show the presence of mid–IR dust echoes with delays of ~ 200 days relative to the optical (e.g. ZTF18aaznjgn, ZTF18acvcadu). In other cases the delays appear to be very long, on timescales of > 1000 days (e.g. ZTF18abzweee). For a large fraction of cases, the WISE light curve follows the long term variation of the optical light curve, but does not echo shorter timescale ($<$1 year) variability (e.g. ZTF18aalslhk, ZTF18aarippg, ZTF18abxxohm).

4.3.3.2 Power spectra analysis

To prepare the light curves for power spectra production we first removed low–significance observations with uncertainties $>$10 times the median uncertainty. To reduce outliers from observations with poor photometric calibration due to cloud coverage and moon contamination, we normalized the fluxes by the best–fit linear trend and removed data which deviated by more than 7 median absolute deviations.

We next binned the data to uniform time bins with full width 7.0 d. For each bin we estimated the mean flux as the uncertainty–weighted sum of the individual fluxes. The

[2]https://www.legacysurvey.org/dr9/catalogs/

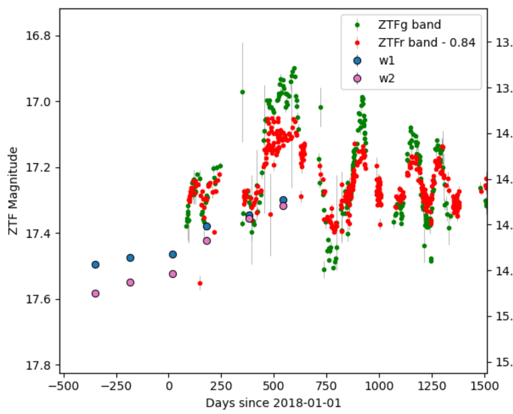

ZTF18aarippg

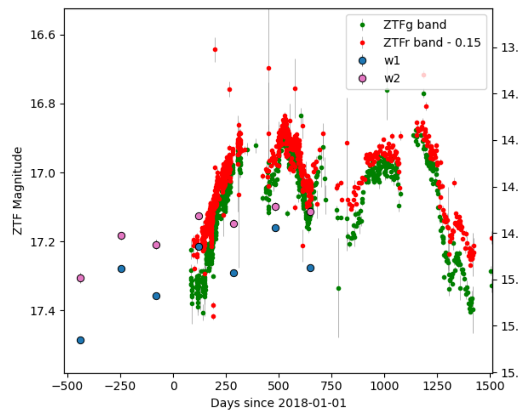

ZTF18aaymybb

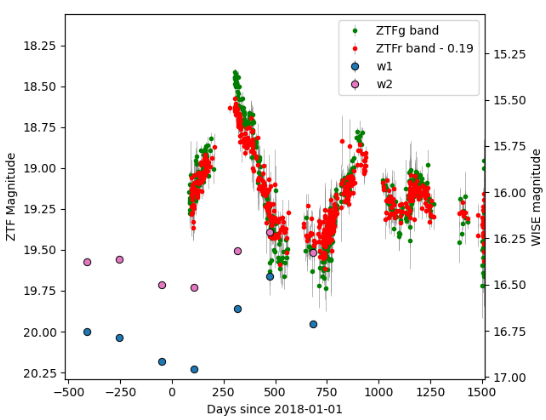

ZTF18aaznjgn

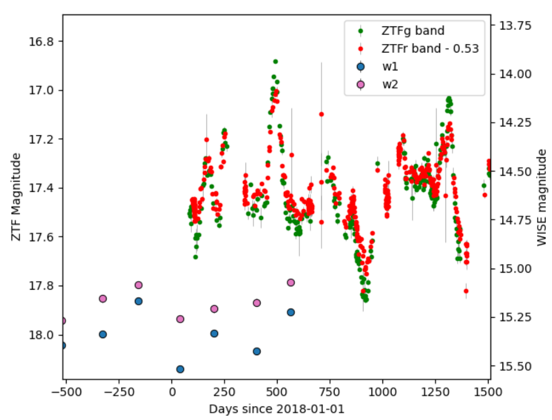

ZTF18aaylbyr

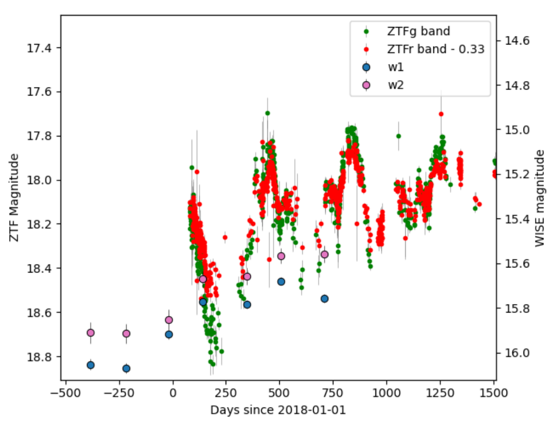

ZTF18aalslhk

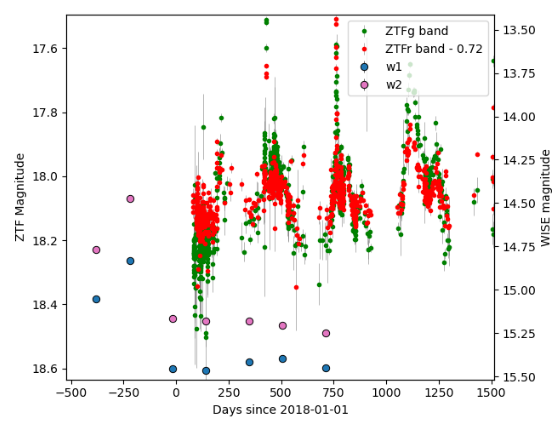

ZTF18aakehue

Figure 4.2: ZTF and *WISE* light curves of notable DPEs. The left y–axes display the ZTF magnitudes while the right y–axes display the *WISE* magnitudes.

binned measurements were more robust against single–observation outliers, so we further filtered out flux points which differed from the resulting mean values by $>5\sigma$, where σ refers to the uncertainty on the average flux obtained by propagation of uncertainty. We did this iteratively until no individual outliers remained. We next eliminated bins with large flux uncertainties, $>$ 10 times the median, typically those which contain only a single low–significance observation. To identify outlying time bins, we computed the difference in mean flux between each bin and its neighbors, computed the standard deviation of this population of differences, and removed any time bins with a difference greater than 5 standard deviations. The resulting gridded light curves generally retained $>90\%$ of the original data, and the most obvious outliers are automatically removed.

We computed the power spectral density with a generalized least squares method following the approach of Coles et al. (2011). Specifically, we adopted a model for the data in the time domain, $F(t) = F_0 + F_1(t - t_0) + \sum_k^N {}_k a_k \sin(2\pi k(t - t_0)/T) + b_k \cos(2\pi k(t - t0)/T)$, with T the total data span. The model therefore comprises a mean flux, a linear flux ramp, and a Fourier series with coefficents a_k and b_k describing the variability. To constrain the many degrees of freedom, we assumed a model for the power spectral density (PSD, P(f, λ)) and that the Fourier coefficients were distributed as a normal distribution with width $\sqrt(P)/2$. Our models for P(f) included a power law (PL), a power law with an additional white noise component (WN), a broken power law + white noise (BPL), and a power law + white noise with an additional gaussian component (Gauss). To determine the parameters of these models along with the time–domain components F_0, F_1, and the Fourier coefficients, we used generalized least squares optimization. We selected N_k, the number of Fourier components, as half of the number of data points, such that the highest frequency N_k/T was the Nyquist frequency. The resulting fit provided estimates of the PSD parameters, the PSD itself (via the Fourier components), and the total log likelihood for the model. Examples of 4 DPE light curves and their corresponding power spectra are shown in Figure 4.3. The plots show the fits of the WN, BPL and Gauss models.

For comparison, we additionally estimated a model independent power spectral density using Welch's method, based on the weighted, overlapped sum of Hann–windowed Fourier transforms. Our choice of 128 data points per segment reduced noise while retaining reasonable sensitivity to low–frequency power. The PSD estimate obtained in this way is shown in orange solid lines in the power spectra plots of Figure 4.3.

The spectra shown in Figure 4.3 demonstrate how a high frequency turnover is required in a fraction of cases in order to model an intrinsic white noise component above the noise level naturally arising from flux uncertainties in the light curve shown in gray. ZTF18aacjtlo is an example of a DPE with a clear high frequency turnover. In other cases, the power law reaches the noise level before the intrinsic AGN white noise induces a high frequency turnover. The spectral indices of the PSDs have a large range from ~ 1 to ~ 3, and whether a high frequency turnover is required depends somewhat on the spectral index. Some objects, such as ZTF18aaklvii, have steep spectral indices > 2.5 and reach the light curve's noise level at frequencies of ~ 100 year^{-1}. Others, such as quasi–periodic ZTF18aaadgxi, have very shallow power spectra with spectral indices < 2.0 and do not reach the noise level at high frequencies.

The distribution of the power law spectral indices vs the PSD amplitude at one year based on fits of the WN model to the r- and g-band power spectra of the two different populations is shown in Figure 4.4. The scatter plot shows that spectral indices tend to be steeper for objects with larger PSD amplitudes, and that the g-band power spectra have larger PSD amplitudes than the r-band power spectra. The histograms of both spectral index and PSD amplitude for the DPE population are shifted to slightly larger values relative to the histograms derived from the control AGN population, with median spectral indices $\gamma_g = 2.07 \pm 0.35$ (g-band) and $\gamma_r = 2.06 \pm 0.36$ (r-band) and median PSD amplitudes $A_g = -2.29 \pm 0.44$ (g-band) and $A_r = -2.77 \pm 0.44$, where the uncertainties are the median absolute deviations describing the range of values over the DPE population. By comparison the control AGN sample had median spectral indices $\gamma_g = 1.96 \pm 0.36$ (g-band) and $\gamma_r = 1.94 \pm 0.98$ (r-band) and median PSD amplitudes $A_g = -2.48 \pm 0.49$ (g-band) and $A_r = -2.91 \pm 0.71$ (r-band). The histograms in Figure 4.4 illustrate the shift of ~ 0.1 between the spectral indices of the two samples.

A fraction of DPE and AGN power spectra exhibited low frequency turnovers, which were sometimes associated with periodic or chirping behavior in the light curves. Examples of 4 quasi–periodic DPEs and their power spectra are shown in Figure 4.5. In most cases, the low frequency turnover was captured either by the broken power law model, where the low frequency power law component had a substantially lower spectral index than the high frequency power law component, or the Gaussian bump model, where an additional bump at frequencies < 4 yr^{-1} fitted the low frequency shelf of the power spectrum.

In order to compare the fraction of DPEs and control AGN with high and low frequency turnovers, we compared the best–fit log likelihoods of the 4 different models to find cases where there was sufficient evidence that a white noise, broken power law, or Gaussian component was required to improve the fit. The power law (PL) and PL+WN models are nested and satisfy the criteria of Wilks' Theorem such that $2\Delta \log \mathcal{L} \sim \chi^2_1$ in the null hypothesis, and thus we can reject the null hypothesis with 95% confidence (2σ) when $\Delta\mathcal{L} > 1.92$. None of the remaining models satisfy Wilks' Theorem when all parameters are allowed to vary. Nonetheless, for the remaining models, we may assume a χ^2 distribution in $\Delta \log \mathcal{L}$ to obtain approximate thresholds for 2σ evidence for the extra model component when compared to WN: BPL with two additional parameters is preferred when $\Delta \log \mathcal{L} > 3.0$, and Gauss is preferred at $\Delta \log \mathcal{L} > 3.91$ for three additional degrees of freedom.

We use the above thresholds to determine the fraction of DPEs and AGN which have significantly improved fits due to the extra model components. The cumulative distribution functions of $\Delta \log \mathcal{L}$ for 3 different model comparisons are shown in Figure 4.6. To determine the fraction of DPEs and AGN which have a significant high frequency turnover we may reference Figure 4.6 a), while the fraction of DPEs and AGN needing low frequency turnovers can be estimated from the BPL and Gauss models shown in Figures 4.6 b) and c).

In Table 4.2 we list the fraction of AGN or DPE power spectra with $> 2\sigma$ evidence for the model's extra component. We find that only a slightly higher fraction of DPEs require a high frequency turnover compared to the AGN control sample, and this difference is most prominent for the r-band light curves, where 8% of DPEs have evidence of an additional intrinsic white noise component compared to 5% of AGN. A slightly larger fraction of DPEs also show evidence of a low frequency turnover, with

20% of DPEs requiring a broken power law (in comparison to 13% of AGN) and 16% of DPE power spectra fits being improved by a Gaussian bump (in comparison to 11% of AGN). Ultimately, the CDFs in Figure 4.6 show only small differences between the two populations, indicating that DPEs are only slightly more likely to have high frequency or low frequency turnovers.

Table 4.2: Fractions of DPE and AGN populations with $> 2\sigma$ evidence for the first model over the second model listed in Column 1.

Model	DPE-g	DPE-r	AGN-g	AGN-r
WN vs PL	0.04	0.08	0.03	0.05
BPL vs WN	0.22	0.20	0.18	0.13
Gauss vs WN	0.15	0.16	0.14	0.11

4.3.3.3 Time series analysis

Our findings that DPEs have steeper power spectra and larger PSD amplitudes, and are slightly more likely to have both high and low frequency turnovers, are not necessarily consistent with the previous finding of Zhang & Feng (2017) that DPEs have characteristic timescales $\sim 2.7\times$ longer than other AGN from direct fitting of damped random walk models to light curves. In order to compare our results more directly with this study, we repeated the analysis demonstrated by Zhang & Feng (2017) for our ZTF dataset by fitting the g-band ZTF light curves with a damped random walk process to estimate the relaxation or characteristic timescale τ (the timescale at which the light curve becomes uncorrelated) and σ (the variance of the light curve at timescales shorter than τ) of the light curves. We used the MCMC–based `javelin` software[3], which has been used to

[3]https://github.com/legolason/javelin-1

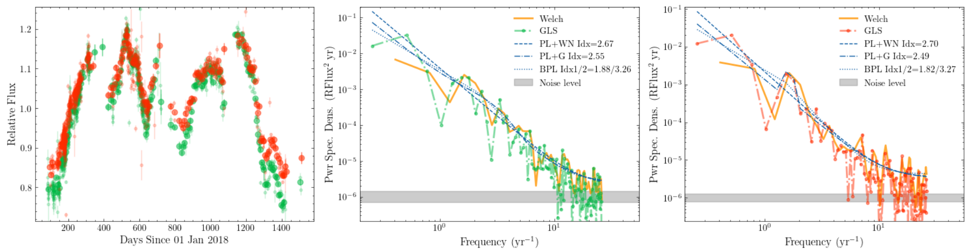

ZTF18aaymybb

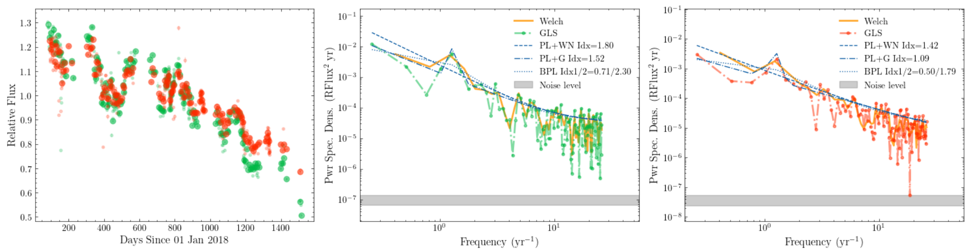

ZTF18aaadgxi

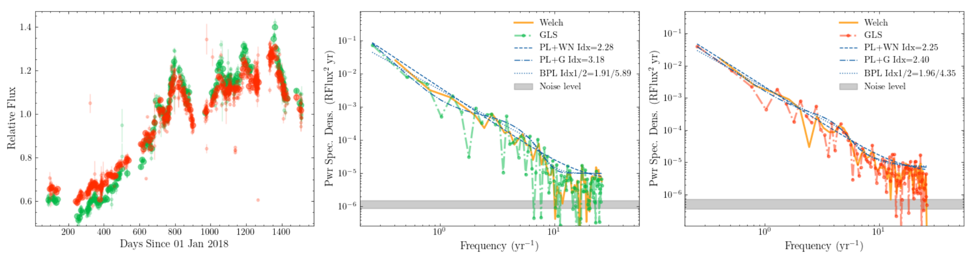

ZTF18aacjtlo

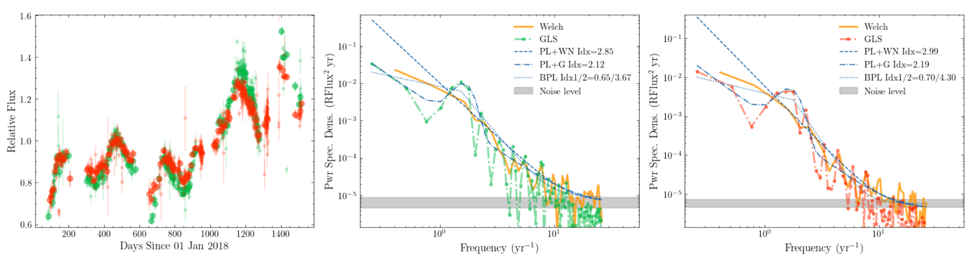

ZTF18aaklvii

Figure 4.3: Four DPE power spectra examples selected to display the range of power law spectral indices and high frequency turnovers observed in the sample. `Left`: The g- and r-band relative flux vs time from ZTF; `Center`: The power spectra of the g-band light curve (green), the Welch periodogram (orange), the best fit power law + white noise model (blue dashed), the best fit power law + Gaussian bump model (blue dot–dash), best fit broken power law model (blue dotted and noise range estimate (gray shaded); `Right`: The same as above but for the r-band light curve.

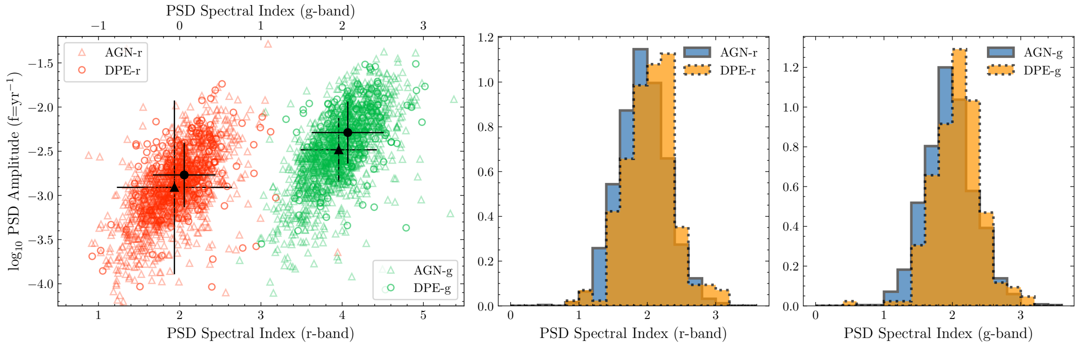

Figure 4.4: `Left`: Distribution of power law index and power spectral density amplitude at a 1 year period for the DPE and control AGN samples. DPEs are shown with circles while AGN are shown with triangles. The g-band spectral indices are shown on a different x–axis axis to the r-band spectral indices for clarity. `Right`: Distribution of power law index from the best-fit power law + white noise model for the DPE and AGN control samples based on separate analysis of the two bands. DPEs tend to have power spectral indices approximately 0.1 larger than the AGN control sample.

measure variability timescales of AGN light curves from OGLE, SDSS and CSS (Zhang & Feng, 2017; Zu et al., 2013). We implemented `javelin` continuum modelling with 200 walkers, 300 chains and 100 burn–in iterations for parameters in the range $0.01 < \tau < 2 \times 10^3$ days and $0 < \sigma < 1 \times 10^3$ mag days$^{-0.5}$ on the g-band ZTF lightcurves of the DPEs and the AGN control sample to find the posterior distributions for τ and σ.

The distributions of τ and σ for the two populations in ZTF based on the DRW fits are shown in Figure 4.7. We find that the ZTF DPE light curves have characteristic timescales slightly larger than the control sample on average, with median values of $\log \tau = 5.28 \pm 0.75$ and $\log \tau = 5.06 \pm 0.77$ respectively, where the uncertainties are given by the median absolute deviation of the parameter over the whole sample. The DPEs also have slightly larger variance at high frequencies of $\log \sigma = -1.50 \pm 0.32$ compared to the control sample variance of $\log \sigma = -1.71 \pm 0.36$. We note that the uncertainties

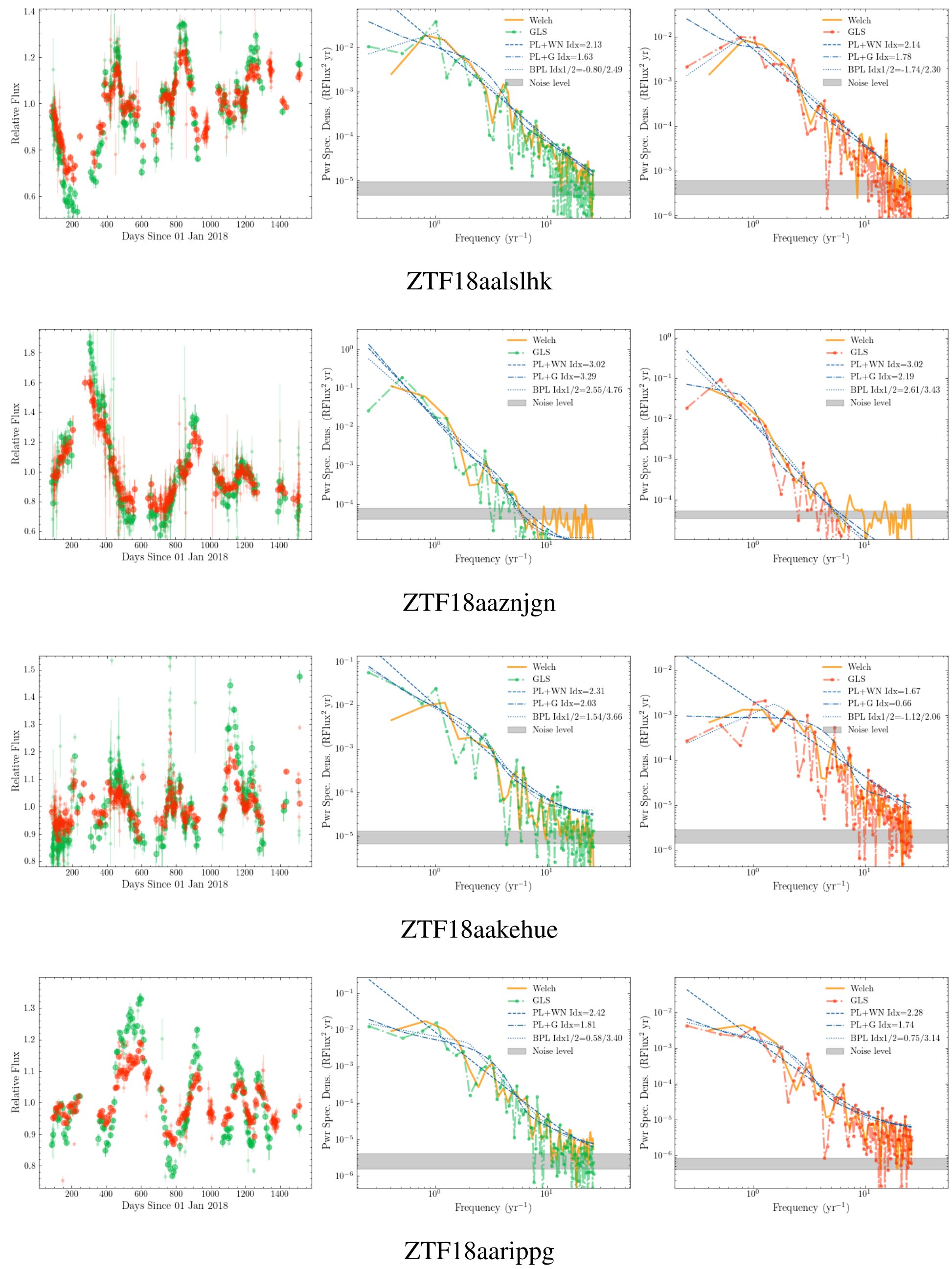

Figure 4.5: Four DPE examples selected to illustrate how low frequency turnovers arise for periodic and chirping sources, and how the Gaussian bump and broken power law models can pick up on these low frequency turnovers. `Left`: The g- and r-band relative flux vs time; `Center:` The power spectra of the g-band light curve (green), the Welch periodogram (orange), the best fit power law + white noise model (blue dashed), the best fit power law + Gaussian bump model (blue dot–dash), best fit broken power law model (blue dotted and noise range estimate (gray shaded); `Right:` The same as above but for the r-band light curve.

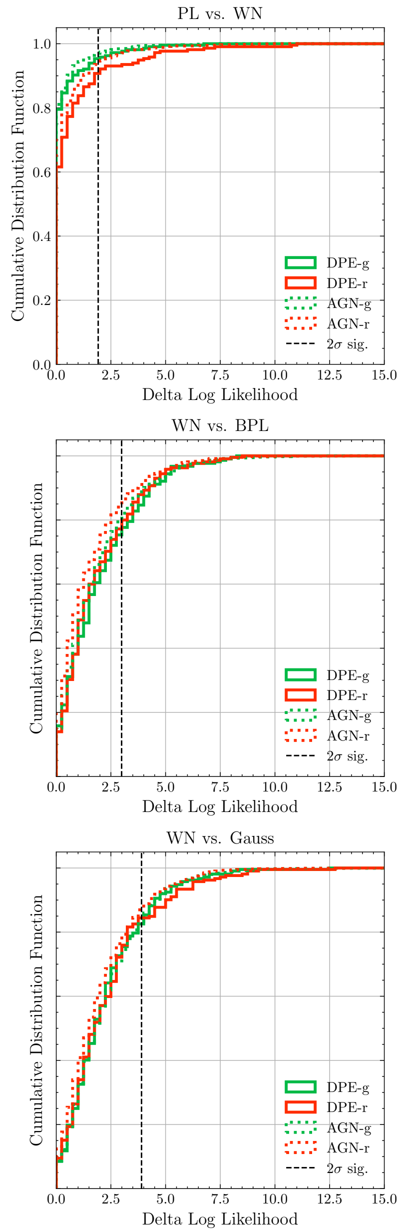

Figure 4.6: Cumulative distribution functions for the change in log likelihood when comparing the PL (power law), WN (power law + white noise), BPL (broken power law + white noise) and Gauss (power law + Gaussian bump) models. The solid lines show the DPE population fraction while the dotted lines show the AGN population fraction. Results are shown based on power spectra analysis and model fitting to g-band (green) and r-band (red) light curves. The gray dashed line shows the cutoff for the fraction of the population with a 2σ preference for the second model over the first.

are large here because the parameters have a large range of values over the populations, and that the histograms show the nature of the differences between the distributions more thoroughly. The differences in characteristic timescale that we observe between the two populations are much more modest than those found by Zhang & Feng (2017), where they measured typical DPE characteristic timescales of $\log \tau = 5.8$ and standard broad line AGN timescales of $\log \tau = 4.8$. The τ distributions of their DPE and AGN samples were much less consistent with each other than ours are (see Figure 5 from Zhang & Feng, 2017).

4.3.3.4 Impact of black hole mass on variability properties

There is well known positive correlation between AGN mass and characteristic timescale (see Section 1.2.6 Burke et al., 2021; Kelly et al., 2009). It is therefore important to determine if the longer characteristic timescales and steeper power spectra of the DPE light curve sample arises simply because they have larger masses than the control AGN sample. Virial mass measurements can be obtained from broad line AGN according to:

$$M_{\mathrm{BH}}(\mathrm{RM}) = f \frac{R(\delta V)^2}{G} \tag{4.1}$$

where R is the broad line radius, δV is the width of the broad line and f is a coefficient which depends on the kinematics and inclination angle of the broad line region. Unfortunately, it is challenging to measure δV, and therefore the virial masses of DPEs, as their broad lines are a mixture of a central wind component (from which masses are usually measured) and a broader disk component. The virial masses for

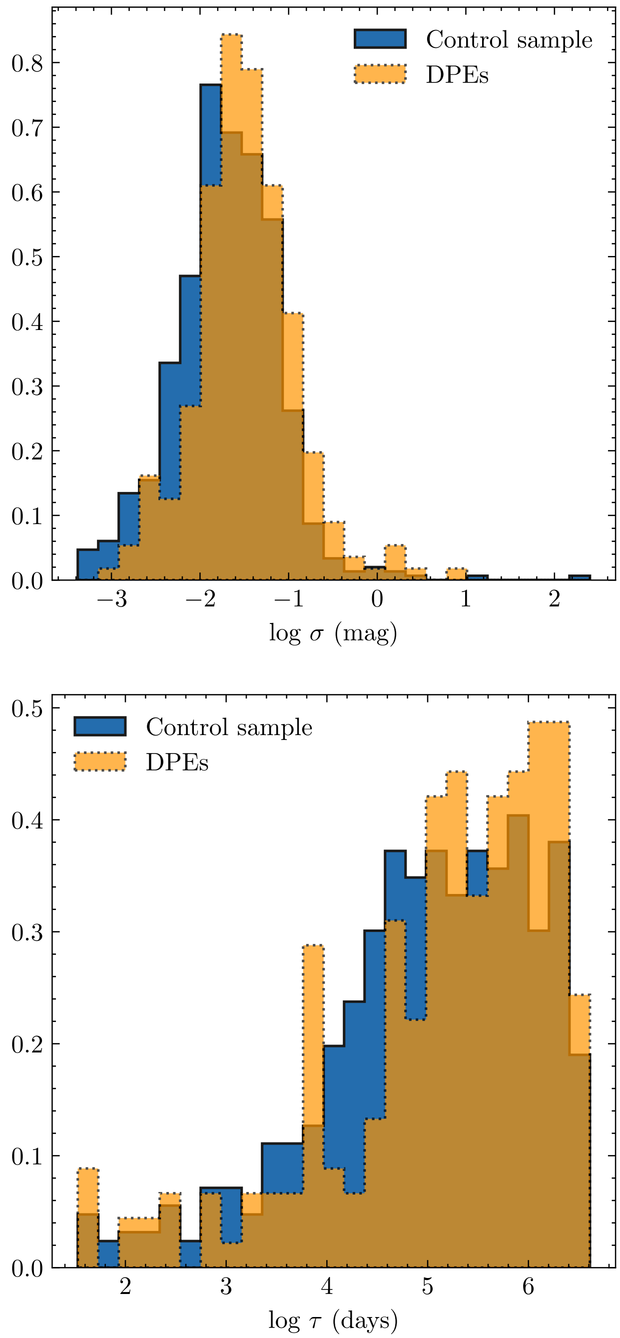

Figure 4.7: Distribution of damped random walk parameters τ (characteristic timescale) and σ (high frequency noise amplitude) from MCMC modeling of g-band ZTF light curves of the DPE and control AGN samples.

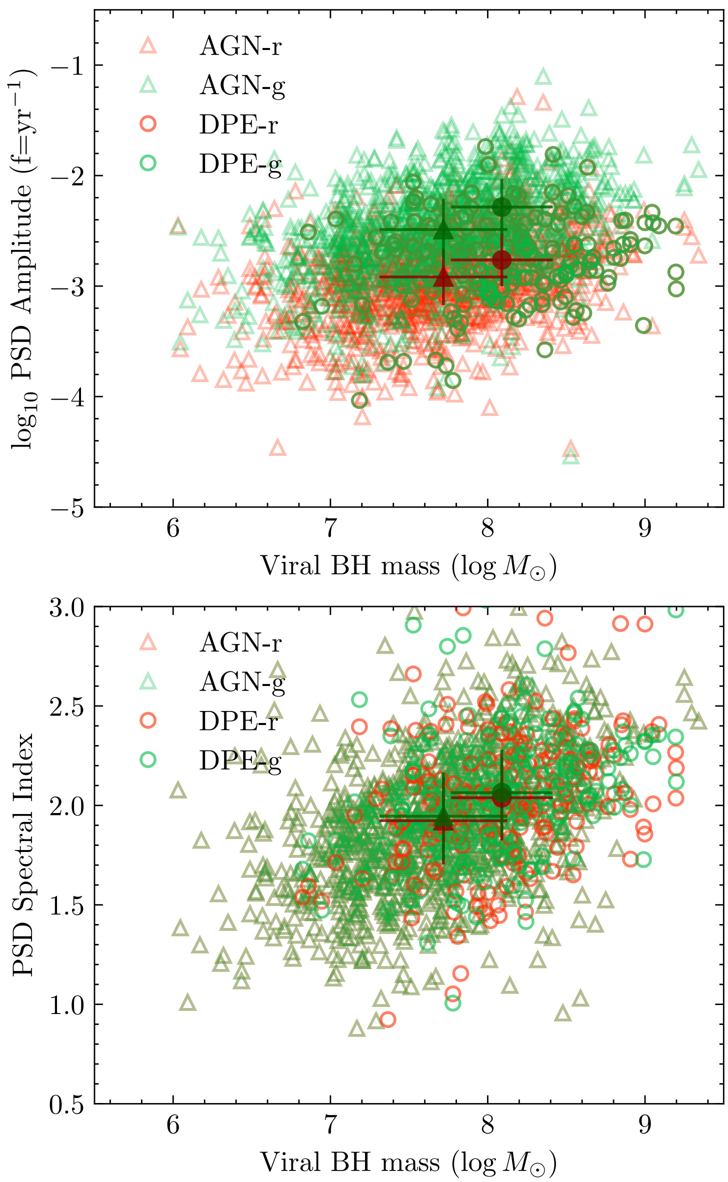

Figure 4.8: `Above:` Distributions of power spectral density amplitude (`above`) and power law index (`below`) vs estimated virial mass from Ho (2008) for the DPE sample and the broad line AGN control sample. DPEs are shown with circles while AGN are shown with triangles.

the two samples calculated by Ho (2008) and plotted in Figure 4.1 were obtained from broad line width measurements without consideration of the additional double–peaked component. As DPE broad line structures have twice the FWHM of radio–loud broad line AGN on average (Eracleous & Halpern, 1994; Eracleous et al., 1997b; Ho et al., 2000) the viral masses may therefore be overestimating the DPE mass by a factor of ~ 4. If this is the case for our ZTF DPEs, the mass distributions of the two samples would in fact have approximately the same distribution, and our findings of different characteristic timescales and power spectral indices between the two samples would not be attributable to mass differences alone. However, if we take the (Ho, 2008) mass measurements as is (without consideration of the broad double–peaked component's additional contribution to δV) and compare the distributions of τ and γ for a mass–matched control sample, the τ and σ differences between the two samples no longer hold (Figure 4.9). This finding differs from Zhang & Feng (2017), where they found that the substantially larger characteristic timescales of DPE light curves over control AGN light curves were maintained even when a mass–matched AGN control sample based on Ho (2008) mass estimates was used for comparison.

4.3.4 Spectroscopic monitoring of DPEs

We obtained follow–up spectra of 10 DPEs with the DeVeny spectrograph on the Lowell Discovery Telescope using a 1.5" slit, central wavelength of 5700 Å, a spectroscopic coverage of 3600–8000 Å and total exposure times ranging from 1000–3000 s. Comparisons between recent LDT and archival SDSS spectra, with time intervals

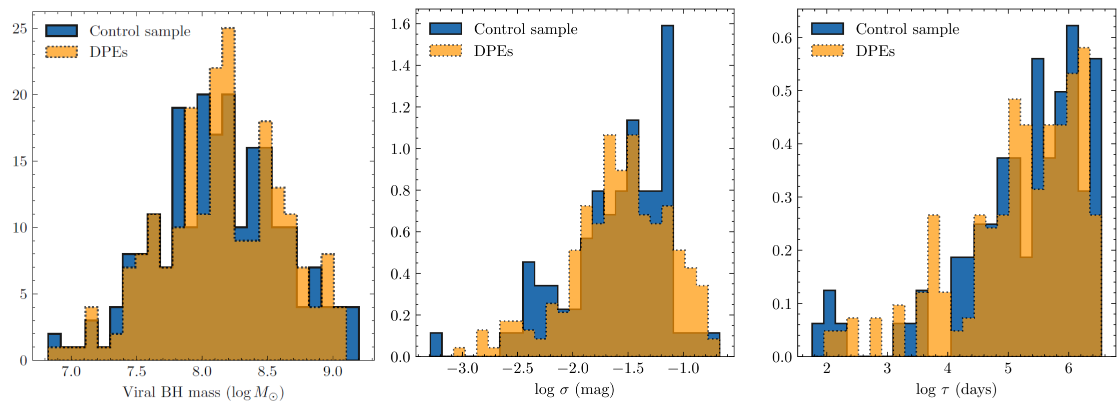

Figure 4.9: Distributions of virial black hole mass (left) and damped random walk parameters σ (high frequency noise amplitude, center) and τ (characteristic timescale, right) from MCMC modeling of DPE and a mass–matched control AGN sub–sample.

ranging from 13–18 years, are shown in Figure 4.10.

5 of the 10 objects show substantial changes in the relative fluxes of the two shoulders. ZTF19aarlffl, which had a bright blue shoulder in 2004, instead exhibited a prominent red shoulder in 2021. ZTF18aalslhl, which had a brighter red than blue shoulder in 2004, had a brighter blue shoulder in 2021. ZTF18aarywbt and ZTF18aalslhk, which had bright blue and red shoulders in 2005 and 2004 respectively, recently exhibited only blue shoulders with a smoother shape. ZTF18aarippg recently had prominent blue and red shoulders and high velocity when it previously only had a fainter blue shoulder, as noted by Jiang et al. (2022). Such substantial variations in relative flux of the blue and red shoulders have been noted in many other DPEs such as NGC 1097, NGC 7213, 3C 59 and 1E 0450.3–1817 and have been modeled by precession of hotspots and spiral arms (Gezari et al., 2007; Lewis et al., 2010; Schimoia et al., 2012, 2017; Storchi-Bergmann et al., 2002).

We took 4–6 LDT spectra each of ZTF18aaymybb, ZTF18abxxohm and ZTF19aagwzod during 2018 to 2021 to search for changes to the profiles on the timescales of months to a year. These spectra are shown in Figure 4.11. ZTF18aaymybb and ZTF19aagwzod do not show significant changes in the flux of the blue and red shoulders relative to one another or the narrow Hα and Hβ lines. In 2018 we observed small spiky structures on the red shoulder of ZTF18aaymybb, which may arise due to shocks are local disk motions (Gezari et al., 2007; Lewis et al., 2010). ZTF18abxxohm exhibited a gradual decrease in the broad shoulder fluxes relative to the narrow emission lines over an 18 month period. The peak velocities of the broad shoulders only vary by a few hundred km s^{-1} over the course of the 18 months. Velocity variations of this scale are attributable to radial velocity jitter arising from fluctuations in the continuum which illuminates the broad line gas (Barth et al., 2015; Doan et al., 2020; Guo et al., 2019).

The distributions of blue and red shoulder peak velocities obtained from archival SDSS spectra of the full DPE sample from ZTF are shown in Figure 4.12. Because we have included the 106 DPEs identified by eye as having strong red *or* blue shoulders, each distribution has values down to the narrow line rest velocity arising from candidates with only one prominent shoulder. The blue shoulder velocity of the population peaks at $\lambda_b \sim -1800$ while the red shoulder velocity peaks at $\lambda_r \sim 1000$. For comparison, we plot in the background the shoulder velocity distributions from another spectroscopically classified DPE sample (Strateva et al., 2003), which has a higher fraction of DPEs with > 3000 kms^{-1} shoulder velocities and a larger median red shoulder velocity. The smaller shoulder velocities of the ZTF DPE sample arise from our selection strategy, which was designed to find not only the classical LLAGN DPEs, but also the Seyfert 1 AGN with a

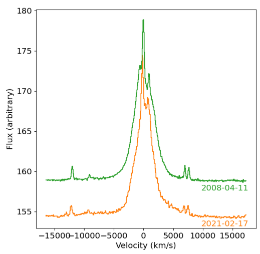

Hα: ZTF18aatxsvu

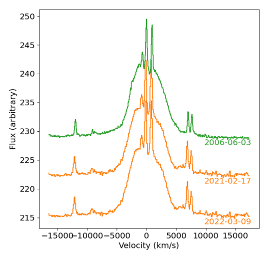

Hα: ZTF18aaylbyr

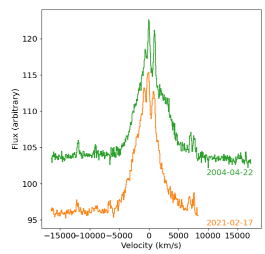

Hα: ZTF18aalslhk

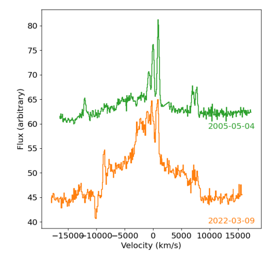

Hα: ZTF18aarippg

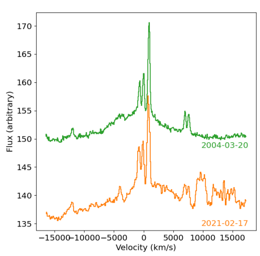

Hα: ZTF19aarlffl

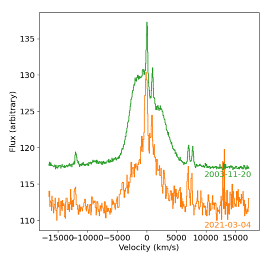

Hα: ZTF19acbvtcx

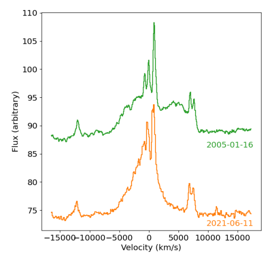

Hα: ZTF18aarywbt

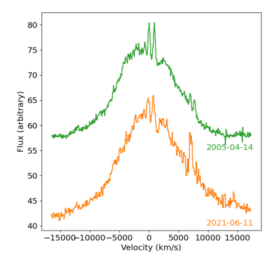

Hα: ZTF18acqtdnj

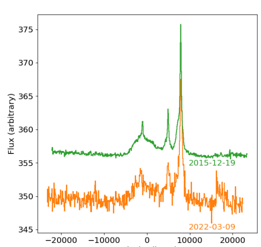

Hβ: ZTF18aaznjgn

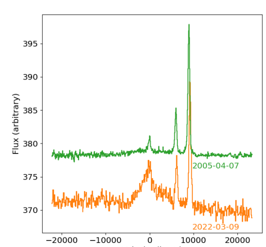

Hβ: ZTF18aaklvii

Figure 4.10: Comparison of Balmer broad line structures from recent Lowell Discovery Telescope spectra and archival SDSS spectra of 10 DPEs. Five of ten show changes in the relative fluxes of the blue and red shoulder.

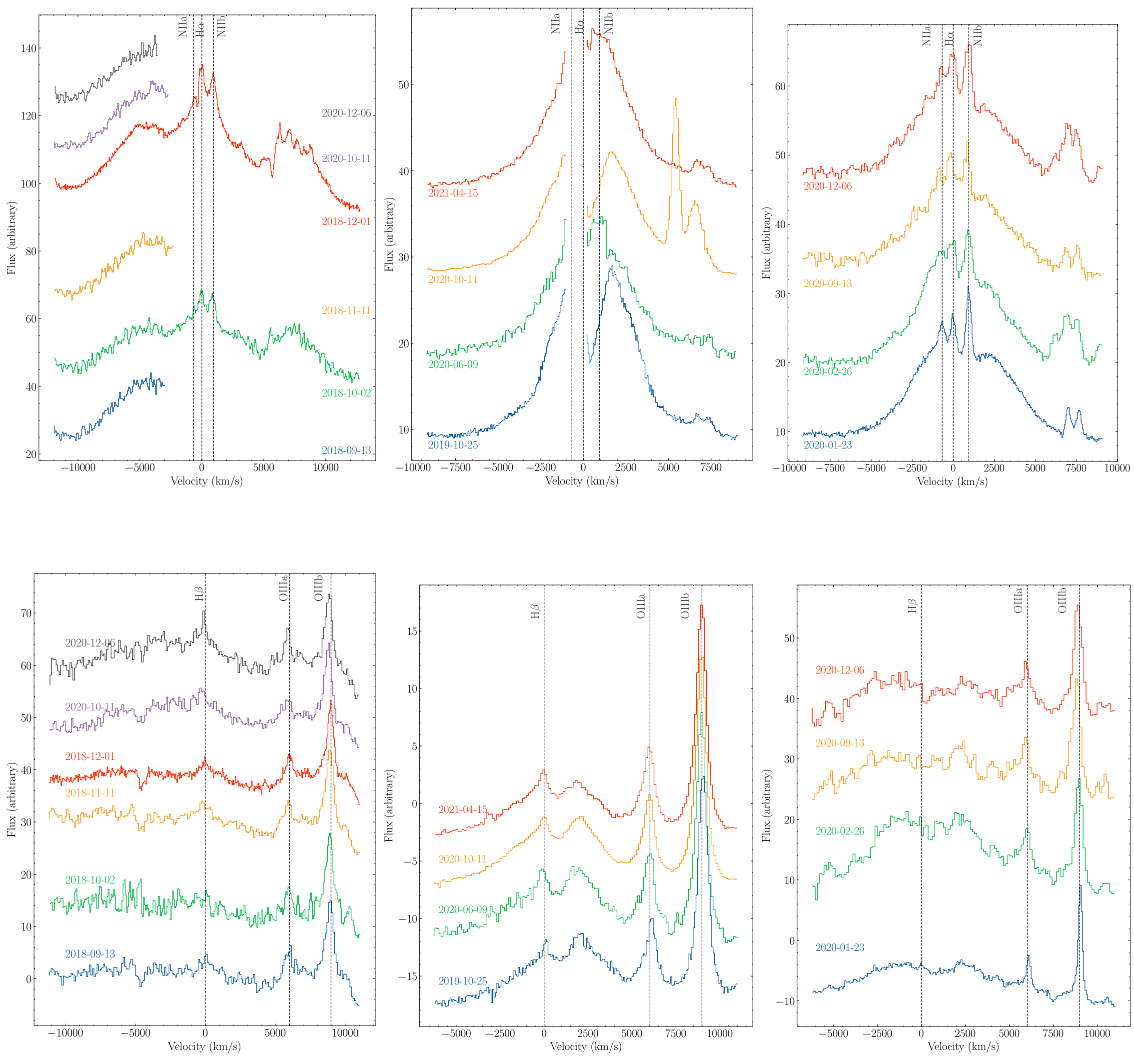

ZTF18aaymybb ZTF18abxxohm ZTF19aagwzod

Figure 4.11: Hα (`above`) and $H\beta$ (`below`) spectra from LDT monitoring of 3 new DPEs discovered during follow–up of variable DPEs from ZTF.

broad Gaussian wind component in addition to the double–peaked disk component, and with shoulders down to small disk inclination angles where the two peaks have smaller separations. On Figure 4.12 we also overplot the velocities measured from recent follow–up spectra of our three new DPEs and the inspiraling SMBH candidate ZTF19aarippg with vertical lines. We note that the velocities of ZTF18aaymybb ($\lambda_b \sim -4800$ and $\lambda_r \sim 7000$) and ZTF18aarippg ($\lambda_b \sim -4600$ and $\lambda_r \sim 4000$) are well in the tails of both the ZTF and Strateva et al. (2003) populations, and are more comparable to canonical LINER DPEs with a minimal central broad line component and large shoulder velocities. We note that the red shoulder velocity of ZTF18aaymybb is slightly larger than the highest shoulder velocity presented in the Strateva et al. (2003) sample.

After a number of follow–up spectra of flaring DPEs revealed that many had steep and blue optical continua, we undertook a comparison of the archival SDSS spectra of the DPE sample and the control AGN sample to see if there were any differences between the optical continua of the two populations. We first subtracted the emission lines fit by `pPXF` to obtain the continuum for each control AGN and DPE, and then fit the continuum with a power law model $F = C\nu^\alpha$ by directly minimizing the log likelihood between the model distribution and the data with a least squares method to fit for constant C and power law index α. The power law spectral index distributions obtained from the continuum fits of the two populations are shown in Figure 4.13. The power law fits to the DPE continua have a median spectral index value of $\alpha = -0.51$ while the control AGN continua have a median power law spectral index value of $\alpha = -0.32$. A larger fraction of DPEs had very large negative values, with 52% having $\alpha < -0.5$ (compared to 40% of control AGN) and 19% having $\alpha < -1.0$ (compared to 14% of control AGN), indicating that a

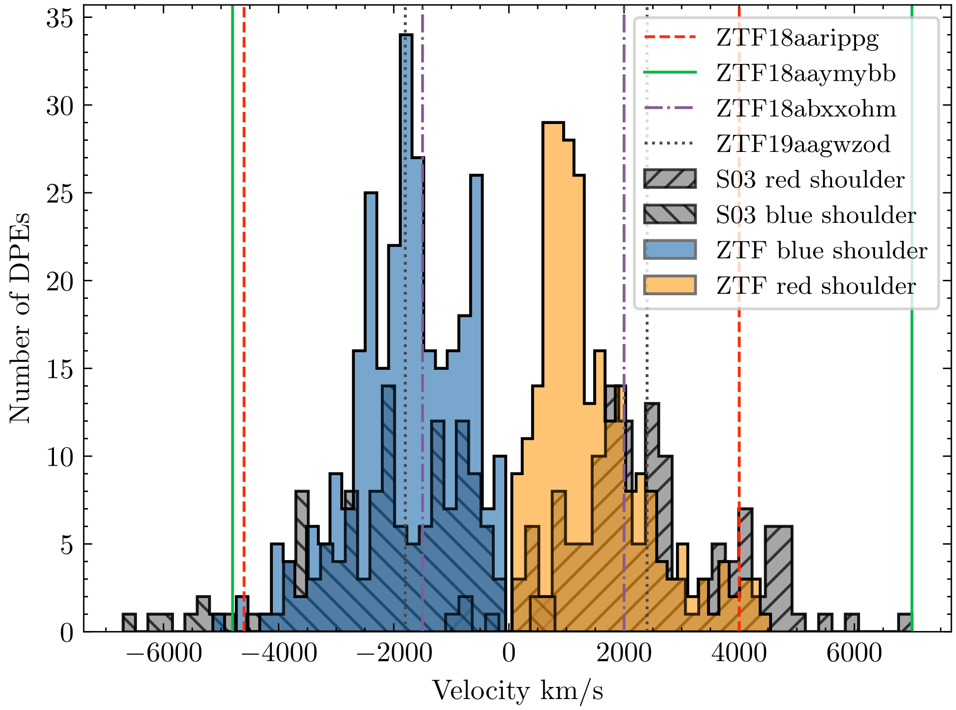

Figure 4.12: Distribution of velocities of red shoulder (orange) and blue shoulder (blue) from multi–Gaussian fitting of archival SDSS spectra of DPEs from the ZTF sample. We show in the background the shoulder velocity distributions of the Strateva et al. (2003, S03) DPE sample (gray, hatched). For the 3 DPEs without archival SDSS spectra (ZTF18aaymybb, ZTF18abxxohm and ZTF19aagwzod) and the more recent spectrum of the binary merger candidate (ZTF18aarippg) we show the the velocities from the more recent LDT spectra with vertical lines.

larger fraction of DPEs have steeper and bluer continua. We note that both populations have some AGN with red, shallow continua, where galaxy light dominates over the AGN ionizing continuum. This may be because many of the archival spectra from 10–20 years ago may capture the AGN in a less active state than the current state captured by the ZTF light curves.

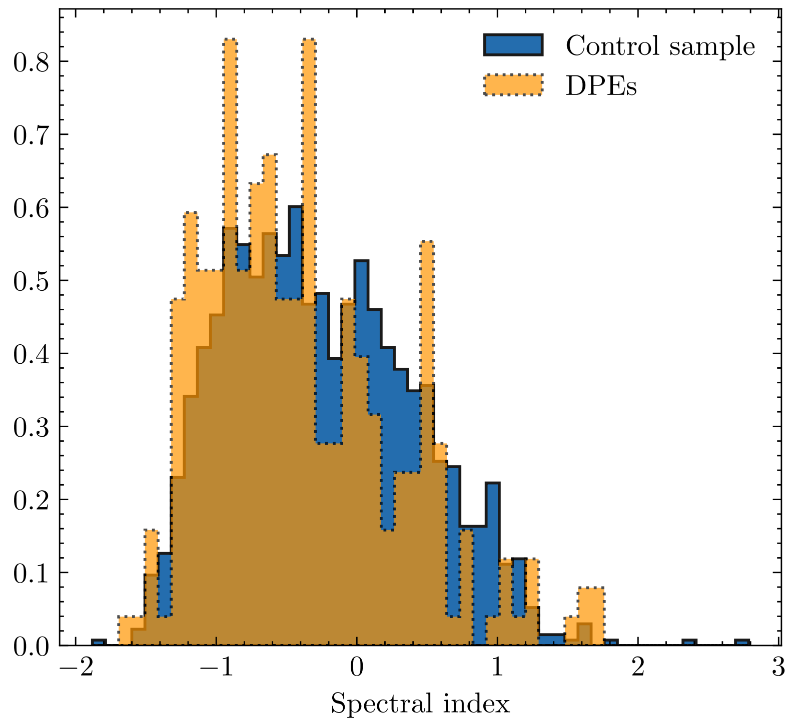

Figure 4.13: Distribution of the power law spectral index of the optical continua of the DPE and broad line AGN control samples. Results are shown based on archival SDSS spectra from 13–18 years prior to ZTF. Emission lines fit by `pPXF` were subtracted before the remaining continuum was fit with a power law to produce the above distributions.

4.3.5 Radio emission from DPEs

We undertook a search for radio emission from the DPEs and control AGN in the Karl G. Jansky Very Large Array Sky Survey (VLASS; Lacy et al., 2020). This survey covers a total of 33,885 deg^2 in the 2–4 GHz range with an angular resolution of $\sim$ 2".5 and will obtain a coadd 1σ sensitivity of 1 μJy/beam by survey end in 2024. We searched for crossmatches within 10" in Table 2 of the VLASS Epoch 1 Quick Look Catalogue which contains $\sim 700,000$ compact radio sources with > 1 mJy/beam detections associated with mid–IR hosts from the un*WISE* catalog (Gordon et al., 2021).

33 out of 245 DPEs in the VLASS region had significant radio emission, corresponding to 11% of DPEs. 91 out of 1323 broad line AGN from the control sample had radio emission, corresponding to 6.9% of control AGN.

4.4 Discussion

We have shown from power spectra analysis of ZTF light curves that variable DPEs have slightly steeper power spectra and higher PSD amplitudes than a comparative broad line AGN sample with the same redshift distribution. We have also shown that DPEs have slightly longer characteristic timescales and high frequency variance than the control sample. We have not, however, concluded that this is due to a physical difference in the accretion state, disk geometry or viewing angle between the DPEs and other broad–line AGN. Instead, we find that this could be entirely attributable to the higher masses of the DPEs given the known relationship between $M_{\rm BH}$ and τ and the relationship we find between $M_{\rm BH}$ and γ from our power law fits to the ZTF power spectra. Whether the

DPEs have higher masses because disk–emission is more likely to occur for high–mass AGN, or because selection effects make high–mass DPEs more easily spectroscopically classifiable, remains an open question.

Our time series modeling results are in contradiction to a previous study by Zhang & Feng (2017) which found that DPEs had typical characteristic timescales of 177 days, and that this was $2.7\times$ larger than a control AGN sample with a typical characteristic timescale of 65 days. For comparison, we find that the median τ for DPEs is 196 days: $1.2\times$ larger than the control AGN τ of 158 days. Most significantly, they found that the τ difference between the two samples held even for sub–samples of the same $M_{\rm BH}$ distribution, while we did not find this to be the case. We suggest two possible reasons for their larger and mass–independent τ difference between the two samples in comparison to our smaller, mass–dependent difference. Firstly, our τ measurements were based on modeling of ZTF light curves for both the DPE and control AGN samples, so that the two samples had consistent cadences and baselines of 3–4 years. By comparison, the Zhang & Feng (2017) paper compared Catalina Sky Survey Data Release 2 light curves of DPEs to SDSS Stripe 82 light curves of broad line AGN. Given that both CSS and Stripe 82 light curves have baselines of ~ 8 years, it is possible that the longer baselines allowed for improved measurement of the characteristic timescales compared to ZTF. However, given that the measured timescales are $\sim 60-200$ days, the ZTF baselines should be sufficient. Alternatively, the differing sensitivities, sampling rates, and central wavelengths of the CSS and Stripe 82 light curves may have produced apparent differences in the τ estimates between the two samples. Zhang & Feng (2017) argue that it is reasonable to compare the characteristic timescales between the two differing datasets because the mean ratio of

$\tau_{\rm SDSS}$ and $\tau_{\rm CSS}$ was 1.03 for a subset of 154 quasars with high quality light curves from the two surveys. However there is substantial scatter and an overall poor correlation between $\tau_{\rm SDSS}$ and $\tau_{\rm CSS}$ shown in Figure 9 of the paper, suggesting that light curve quality has a substantial impact on the accuracy of τ measurements from SDSS and CSS light curves.

The slightly higher fractions of the DPE population which have power spectra fits improved by a broken power law or Gaussian bump may imply that DPEs are slightly more likely to have low frequency turnovers than standard broad line AGN. Based on visual inspection of AGN and DPE light curves with apparently quasi–periodic or chirping behavior and the occurrance of low frequency turnovers in their power spectra, this result may also imply that DPEs are slightly more likely to exhibit periodic behaviour. This could be verified by systematically classifying which DPE light curves are periodic (based on comparisons of fits of sinusoidal and DRW models) and checking if the periodic lightcurves are more likely to have a low frequency turnover in the power spectrum. Regardless, the difference in low frequency turnover fraction between the DPE and control AGN populations is small and it is clear that DPEs are not substantially more likely to display periodic behaviour than normal broad line AGN.

We expect the periodic and chirping signals in most, if not all, DPE light curves to be 'phantom' periodicities arising naturally from the power spectra of the AGN, regardless of whether their variability are described by a damped random walk or another noise model. Simulations of light curves arising from DRW power spectra with $\tau = 200$ days and slopes of $\gamma = 2$ in 9–yr CRTS datasets found that $\sim$ 1–2 per 1000 light curves showed periodic behaviour well–fit by a sinusoidal model (Vaughan et al., 2016). In the simulations, most light curves had 1.5–2.5 cycles over the 9–yr baseline, corresponding to periods of 4.0–5.3 years. Furthermore, they found that the fraction with false periods increased to $\sim$ 1 in 200 when the spectral index of the PSD was increased from 2 to 3. Our finding that DPEs have slightly larger spectral indices than normal broad line AGN by ~ 0.1 may therefore result in a slightly increased probability of phantom periods arising in DPEs compared to other AGN. If the rate of AGN displaying phantom periods in ZTF is the same as the predicted rate for CRTS, we would expect to observe $\sim$2–4 AGN light curves which are well fit by a sinusoidal model in the combined AGN and DPE sample. The fraction of falsely periodic signals may be even larger for the ZTF light curves compared to CRTS, as 2–4 cycles need only arise over a 3–4 year baseline. The prediction that 2–4 falsely periodic light curves would arise within the entire AGN sample also does not include objects with apparently chirping signals like those of ZTF18aaznjgn and the inspiraling SMBH candidate ZTF18aarippg, which would not be fit well by a sinusoidal model with a single period. The presence of many periodic and chirping light curves shown in Figure 4.2 should therefore not be surprising for a sample of $\sim$2000 AGN varying according to a DRW spectrum.

Given that we observe quite a few examples of chirping and periodic signals across entire baselines (e.g. ZTF18aaznjgn, ZTF18aakehue) and within subsets (e.g. ZTF18aaylbyr, ZTF18aalslhk) of ZTF DPE light curves, and that $\sim 10-20\%$ of AGN and DPE light curves have evidence of a low frequency turnover which is associated with a periodic signal in many cases, it is worthwhile reconsidering whether the chirping signal of SDSSJ1430+2303 (ZTF18aarippg) is really the signature of an inspiraling SMBH. While it is well–fit by the Post–Newtonian orbital model of an eccentric system in Jiang et al. (2022), it could very well be a false positive arising from the phantom periodicities observed in large populations of time series well–described by a DRW. The existence of double–peaked broad Balmer emission lines in SDSSJ1430+2303, and the large change in relative flux of the blue and red peaks over a ~ 17 year period, are also not unusual for the optically variable broad–line AGN in ZTF, since 16% of variable AGN are DPEs and $\sim 50\%$ show changes in relative blue and red shoulder flux over decade–long timescales. While the shoulder velocities of ZTF18aarippg observed in 2022 spectra during the recent optical flaring are very large ($\lambda_r = 4600$ km s^{-1} and $\lambda_g = -4000$ km s^{-1}) and in the tail end of the velocity distribution seen from archival 13–18 year old SDSS spectra of the ZTF DPEs, the original velocity of $\lambda_g = -2400$ km s^{-1} observed in 2004 was more typical of the DPE population. The recently observed velocities of ~ 4000 km s^{-1} are also not unusual when compared to other DPE samples (see Figure 4.12 Strateva et al., 2003). We therefore caution that the light curve and spectra of SDSSJ1430+2303 may be more typical of the variable DPE population than originally considered. This observation, combined with the findings of recent theoretical SMBH binary population studies which paint a pessimistic picture for the existence of kinematically observable SMBH binaries (see Section 1.3.2; Kelley, 2020), lead us to predict that SDSSJ1430+2303 is likely to be a single disk–emitting AGN instead of an SMBH binary.

Our finding that ZTF DPEs are $1.6\times$ more likely to be radio emitters based on VLASS survey results is consistent with the FIRST detection rates of the Strateva et al. (2003) DPE population. Similarly, the higher fraction of DPEs with steep and blue continuum is consistent with previous studies of DPE host galaxies (Eracleous & Halpern, 1994). On the variability side, the relationships that we find between spectral index and black hole mass, and the larger spectral indices of DPE light curve power spectra compared to the control AGN population, is consistent with previous results which find that DPEs are more frequently observed from high–mass AGN. These consistencies with previous DPE population analyses suggest that variability–selected DPEs with a central wind contribution to the broad line region in addition to the disk–emitting component have similar physical properties to the classical disk–emission dominated DPEs in LINERs which dominate previous DPE studies.

4.5 Summary and conclusions

We have presented a population of 299 variable AGN with velocity–offset or double–peaked Hα and Hβ broad emission line profiles. By starting with a population of 1923 optically variable broad line AGN from ZTF and then searching for DPEs amongst the archival SDSS spectra of the variability–selected population, we find a rate of 16% for variable broad line AGN which are DPEs.

We have provided examples of DPE optical light curves from ZTF (Figure 4.2) which show apparently periodic or chirping signals in all or part of their variability history. A fraction of the light curves show comparable behavior to the previously reported inspiraling SMBH candidate SDSSJ1430+2303 (ZTF18aarippg) which we have included in our sample. We have also shown that approximately half of the DPE light curves have clear mid–IR dust echoes in WISE data with delays ranging from ~ 100 to > 1000 days.

We have generated power spectra of the DPE light curves as well as the remaining 1624 AGN light curves as a control sample, and fit those power spectra with 4 models

(Figures 4.3 and 4.5): a power law model (PL), a power law + high frequency turnover model to incorporate intrinsic white noise (WN), a model with a broken power law in addition to the white noise turnover (BPL) and a model with a Gaussian bump on top of a single power law with white noise (Gauss). The WN model fits were used to compare the power law spectral indices of the DPE and control AGN populations (Figure 4.4), and we find that DPEs typically have slightly steeper spectral indices ($\gamma_g = 2.07 \pm 0.35$ and $\gamma_r = 2.06 \pm 0.36$) than the control AGN ($\gamma_g = 1.96 \pm 0.36$ and $\gamma_r = 1.94 \pm 0.98$), where the uncertainties are the median absolute deviations describing the range of values over each sample. We found that the spectral index is steeper for higher mass AGN and DPEs (Figure 4.8) such that this difference may be attributable to the higher median masses of the DPE population compared to the control AGN population.

By comparing the goodness of fit of the PL and WN models to the DPE and AGN power spectra, we determined that 8% of DPEs have evidence of an additional intrinsic white noise component described by a high frequency turnover compared to 5% of AGN in the r-band data (Figure 4.6). By comparing the goodness of fit of the BPL and Gauss models to the WN model, we determined that 20% of DPE power spectra fits are improved by a broken power law over a single power law (in comparison to 13% of AGN) and 16% of DPE power spectra fits are improved by the addition of a Gaussian bump to the single power law (in comparison to 11% of AGN). These fractions indicate that DPEs are more likely to have detectable low frequency turnovers in their power spectra.

We modeled the ZTF time series with DRW models to measure their characteristic timescales τ and high frequency variance σ for comparison to previous findings that DPEs have timescales $2.7\times$ longer than standard AGN. The DPE and control AGN light curves in ZTF had a much more modest difference between their characteristic timescales compared to the previous study, with median values of $\log \tau = 5.28 \pm 0.75$ and $\log \tau = 5.06 \pm 0.77$ respectively (Figure 4.7). We attribute this contradictory finding to the use of a consistent ZTF data set for comparison of the two samples, rather than the use of two different surveys for each sample. The modest differences between τ for the two samples were not maintained when we instead compared the DPE population to a sub–sample of the control AGN with the same black hole mass distribution as the DPEs (Figure 4.9).

Analysis of archival SDSS spectra revealed that the ZTF DPEs have typical shoulder velocities of $\lambda_b \sim -1800$ and $\lambda_r \sim 1000$ but that these can be as high as ~ 5000 km s^{-1}. Our newly discovered DPE ZTF18aaymybb and the previously reported inspiraling binary candidate ZTF18aarippg have velocities in the tail end of the ZTF DPE distribution, but are not atypical for other spectroscopically–selected DPE populations reported in the literature (Figure 4.12). We find that a higher fraction of DPEs have steep blue continua (Figure 4.13), and that $\sim 50\%$ show significant changes in the relative fluxes of the blue and red shoulders over ~ 15 year timescales (Figure 4.10). Short term monitoring of newly discovered DPEs ZTF18aaymybb, ZTF18abxxohm, and ZTF18aagwzod did not reveal any major changes in the spectra over month to year long timescales, except for the appearance of small spikes in the red shoulder of ZTF18aaymybb (Figure 4.11).

In this chapter I have demonstrated that DPEs make up an important fraction of optically variable broad–line AGN, and that a large fraction display major changes in their double–peaked broad lines over decade–long timescales. The occurrance of periodic or chirping signals in the optical light curves is also not uncommon, and we have presented new examples of DPEs with variability properties comparable to the inspiraling SMBH candidate ZTF18aarippg. The population statistics presented in the chapter could be used to inform future calculation of false positive rates for variability and kinematic selection of SMBH binary candidates.

Our sample of DPEs has only minor differences in optical variability behavior compared to the remaining broad–line AGN in ZTF. The results of our spectroscopic and light curve analysis are consistent with the picture that DPEs do not have major physical differences to other broad line AGN, and have different observable properties arising from selection effects such as preferences for large black hole masses and intermediate disk viewing angles.

4.6 Supplementary Material

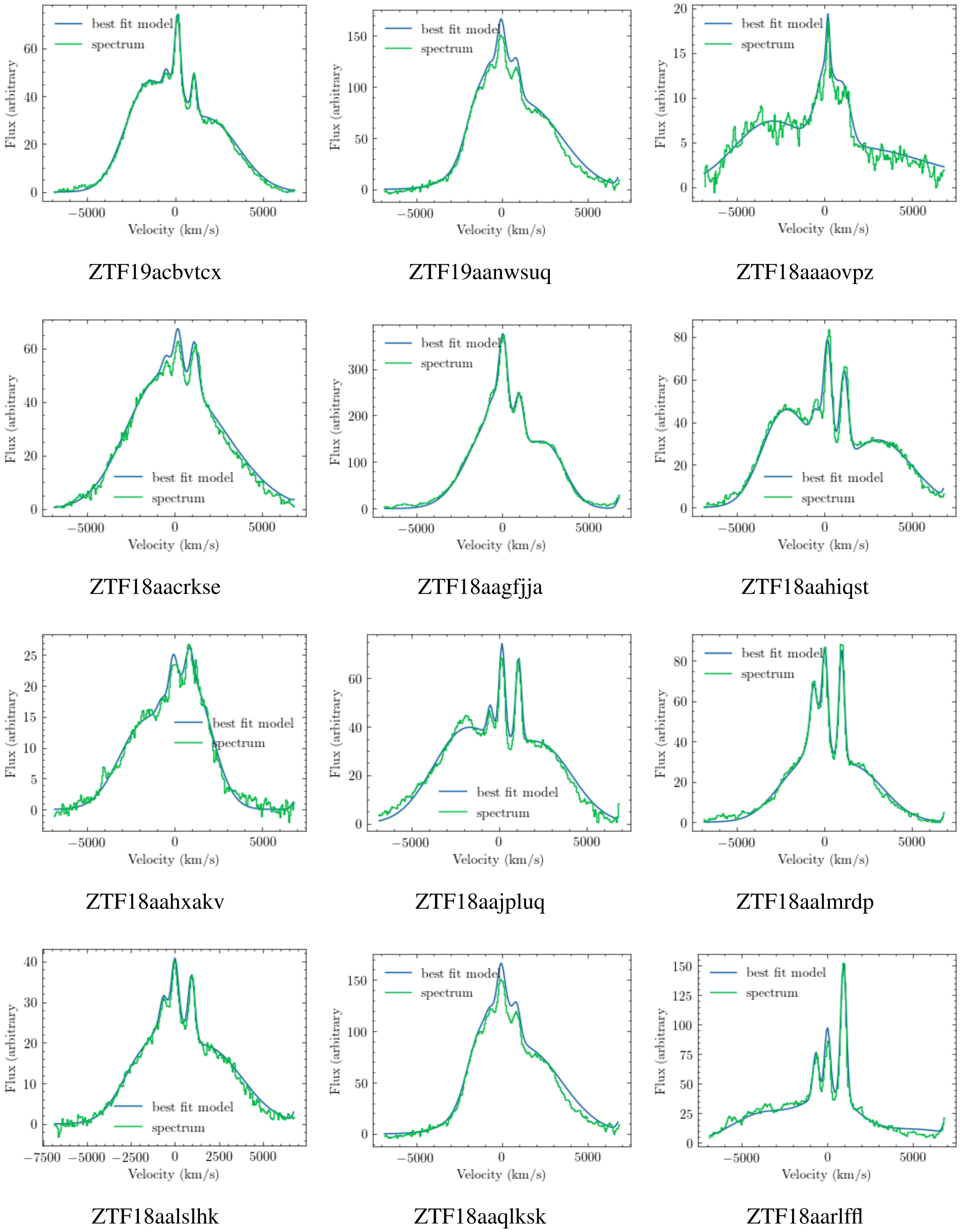

Figure 4.14: Examples of multi–Gaussian fits to the Hα spectra of the 33 DPEs with the brightest double–peaked broad lines relative to the flux of the Hα narrow line.

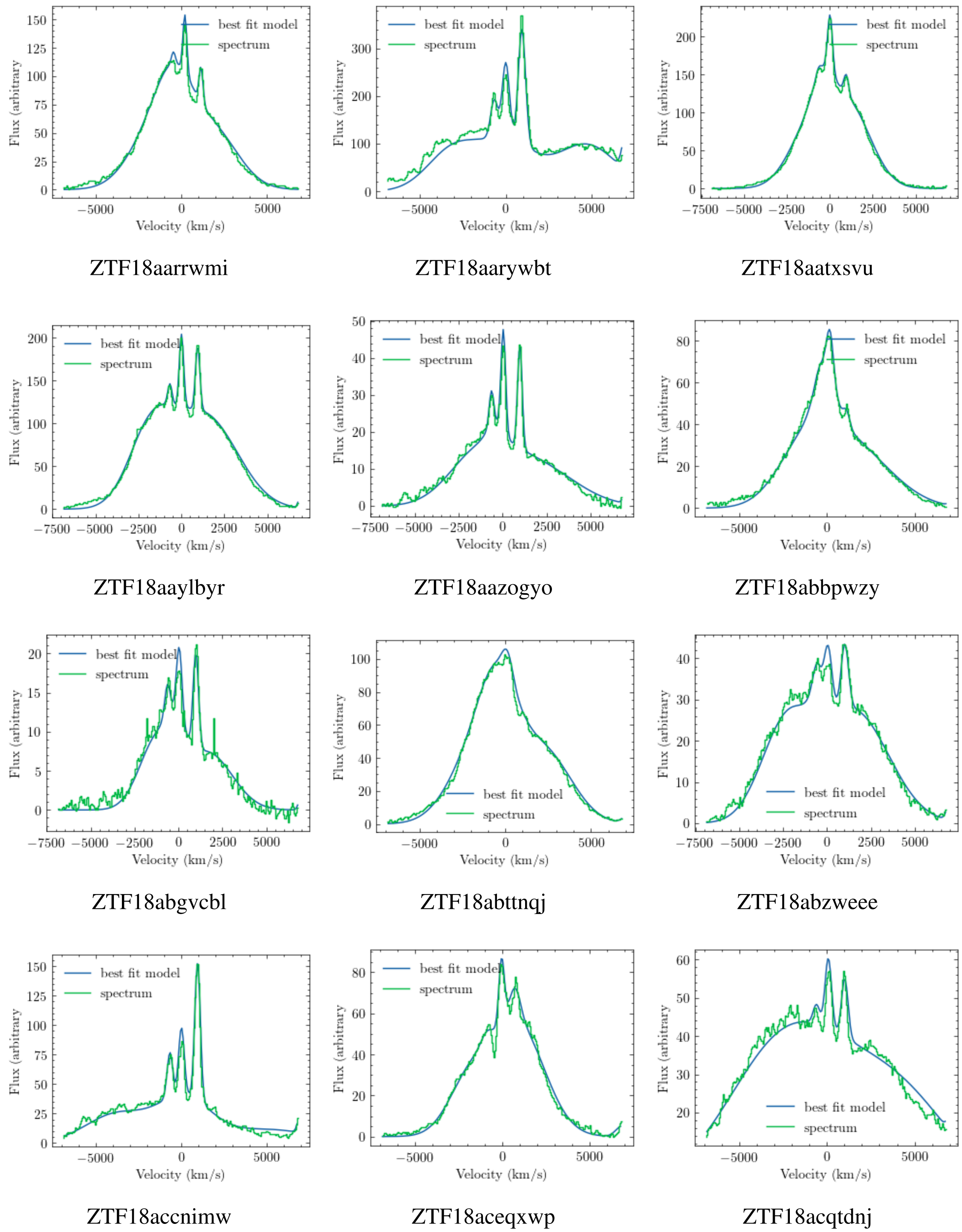

Figure 4.15: Examples of multi–Gaussian fits to the Hα spectra of the 33 DPEs with the brightest double–peaked broad lines relative to the flux of the Hα narrow line (continued).

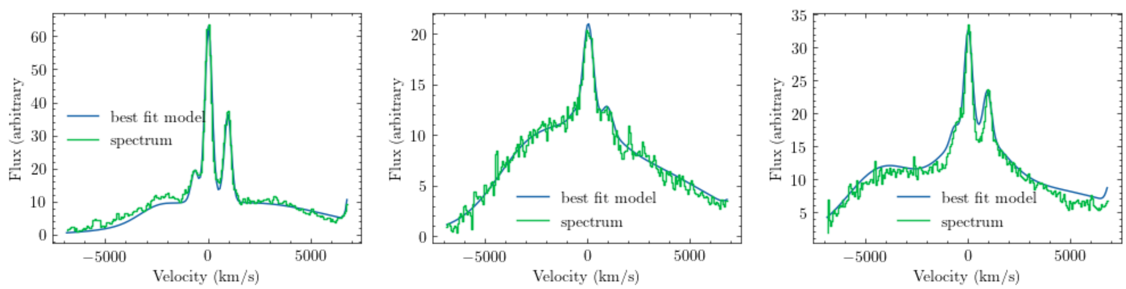

ZTF18acvcadu ZTF19aacixeg ZTF19aadgigp

Figure 4.16: Examples of multi–Gaussian fits to the Hα spectra of the 33 DPEs with the brightest double–peaked broad lines relative to the flux of the Hα narrow line (continued).

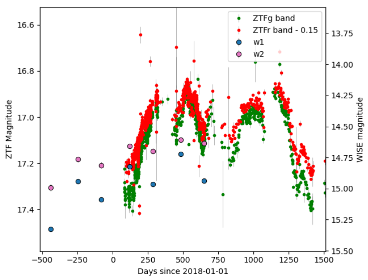

ZTF18aaymybb

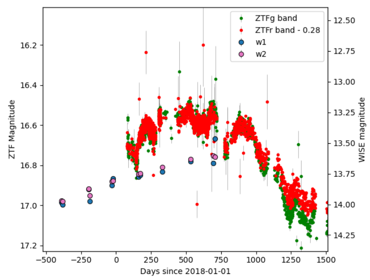

ZTF18abxxohm

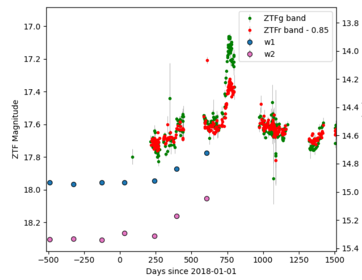

ZTF19aagwzod

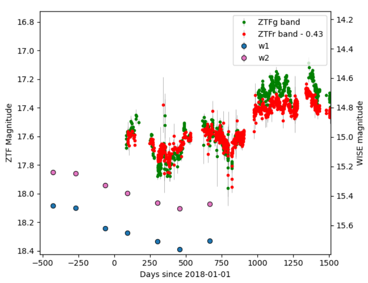

ZTF18aacrkse

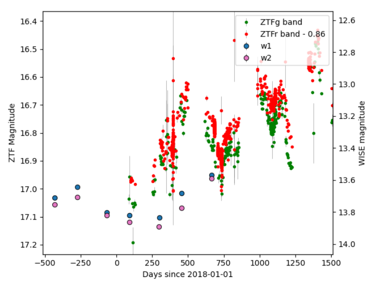

ZTF18aagfjja

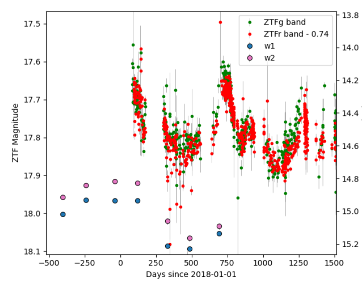

ZTF18aahiqst

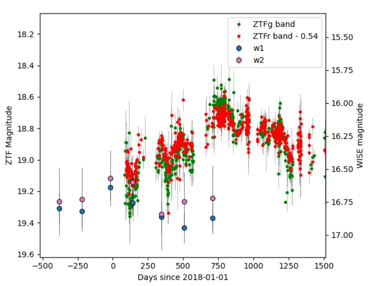

ZTF18aahxakv

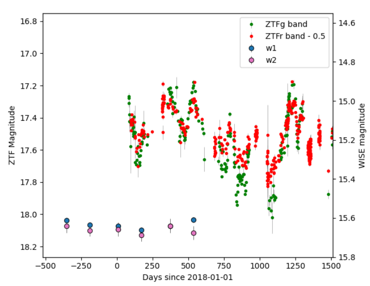

ZTF18aajpluq

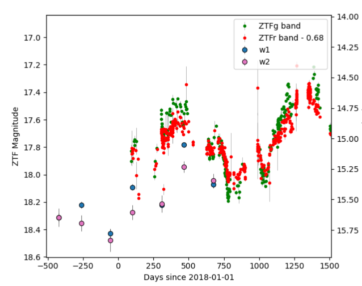

ZTF18aalmrdp

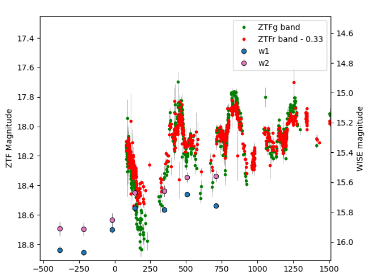

ZTF18aalslhk

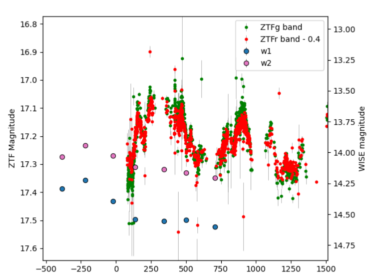

ZTF18aaqlksk

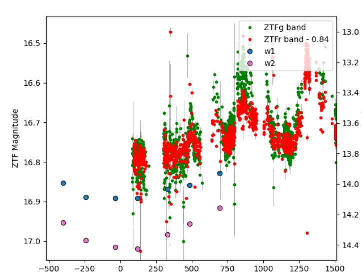

ZTF18aarlffl

Figure 4.17: ZTF and WISE optical and mid–IR light curves of the 26 DPEs with the brightest double–peaked broad lines relative to the flux of the Hα narrow line.

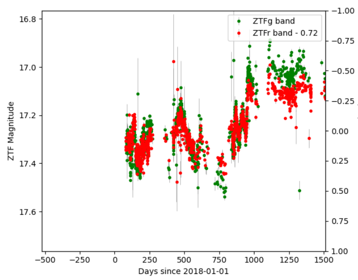

ZTF18aarrwmi

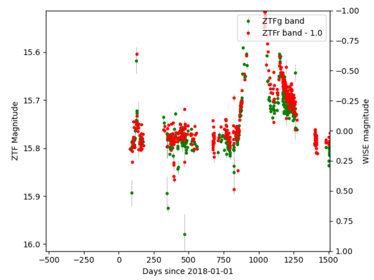

ZTF18aarywbt

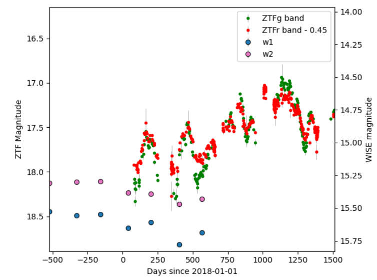

ZTF18aatxsvu

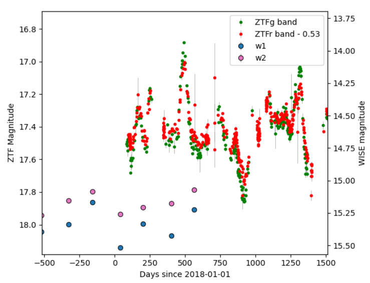

ZTF18aaylbyr

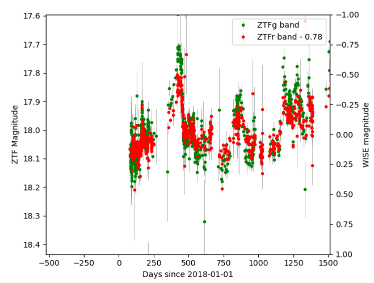

ZTF18aazogyo

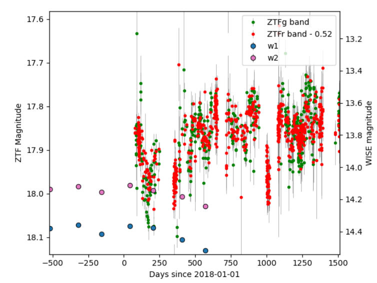

ZTF18abbpwzy

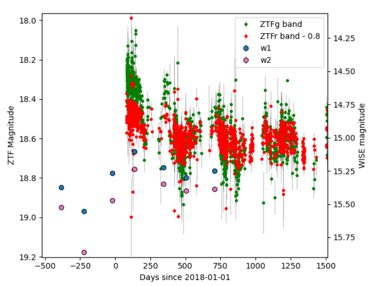

ZTF18abgvcbl

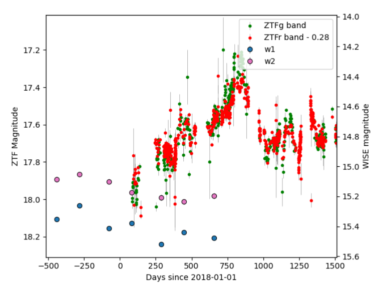

ZTF18abttnqj

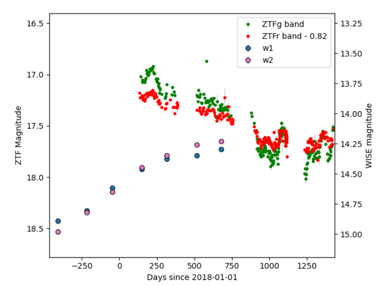

ZTF18abzweee

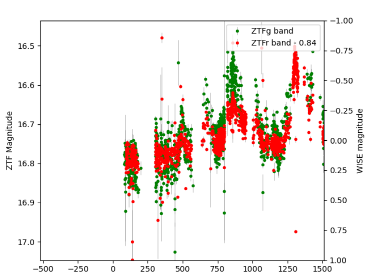

ZTF18accnimw

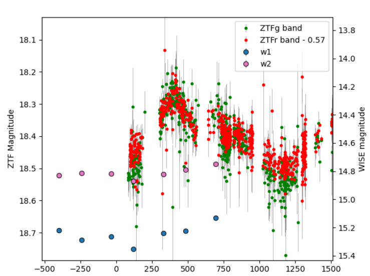

ZTF18aceqxwp

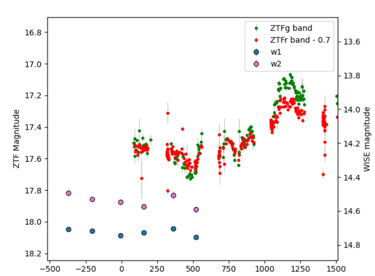

ZTF18acqtdnj

Figure 4.18: ZTF and WISE optical and mid–IR light curves of the 26 DPEs with the brightest double–peaked broad lines relative to the flux of the Hα narrow line (continued).

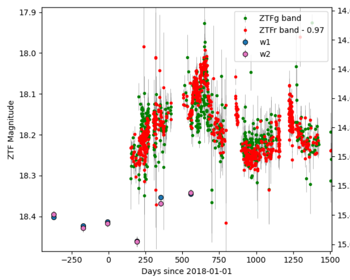

ZTF18acvcadu

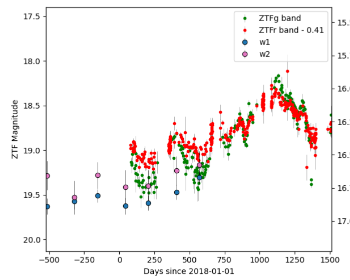

ZTF19aacixeg

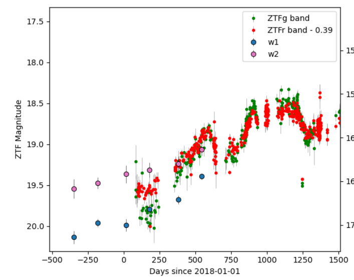

ZTF19aadgigp

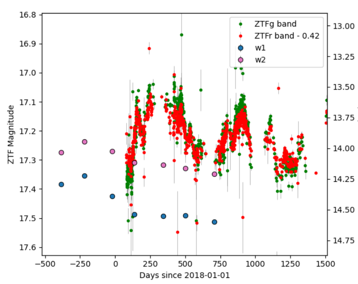

ZTF19aanwsuq

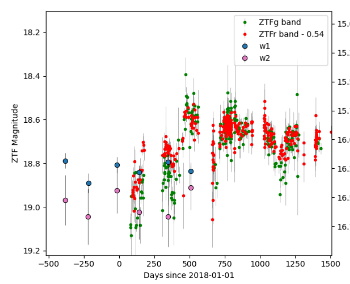

ZTF19aaoyjsq

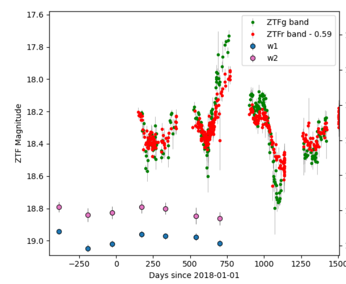

ZTF19aayrjsx

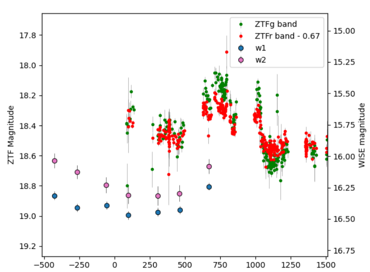

ZTF19acbvtcx

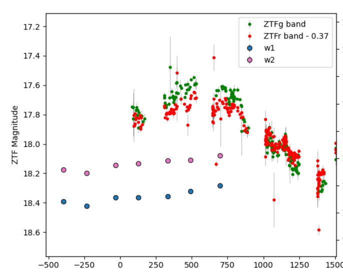

ZTF18aaaovpz

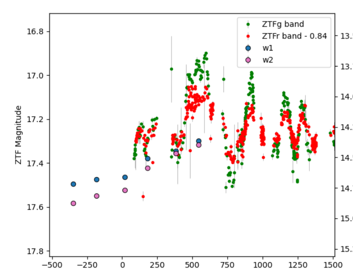

ZTF18aarippg

Figure 4.19: ZTF and WISE optical and mid–IR light curves of the 26 DPEs with the brightest double–peaked broad lines relative to the flux of the Hα narrow line (continued).

Chapter 5: Summary and Future Work

5.1 Summary

In this thesis I have demonstrated how time–domain survey data enable the discovery of three distinct and important AGN populations which shed light on the formation and merger–driven growth of massive black holes: off–nuclear AGN which may have been ejected from their host galaxies via gravitational wave recoil after merger; variable low–mass AGN in dwarf galaxies which are useful analogs to the first black hole seeds; and disk–emitting AGN which shed light on the disk–wind structure of AGN and which can mimic the kinematic and variability signatures of SMBH binaries. Discovery of these populations was enabled by the development of tailored software for the discovery of rare AGN amongst the millions of transients discovered by ZTF: image forward modeling code for analysis of transient objects in time–domain imaging datasets; a custom difference image photometry pipeline; and the implementation of a transient alert filter which incorporated light curve modeling and inbuilt catalog crossmatching. Spectroscopic follow–up and fitting of AGN emission line models to the data enabled the classification and analysis of the AGN discovered with ZTF. The systematic search strategies and modeling techniques presented in this thesis lay the groundwork for much more sensitive searches with the LSST dataset over the next decade.

In Chapter 2, I described a novel search strategy for the discovery of spatially offset AGN arising from GW recoil of SMBH merger remnants and ongoing galaxy mergers in ZTF. This strategy used ZTF difference imaging to find variable AGN and `Tractor` forward modeling to determine the AGN position by fitting data from multiple ZTF epochs and deep, high resolution Legacy Survey images. I presented a sample of 52 AGN in galaxy mergers and 9 off–nuclear AGN which are candidates for gravitational wave recoil. 5 of the 8 offset AGN for which I have spectra of the Hα or Hβ broad line regions were DPEs – much larger than the DPE fraction of 16% for broad line AGN in ZTF overall. If a subset of the offset AGN candidates are confirmed to be recoiling SMBHs, their large spatial offsets could show that SMBH binaries with misaligned spins exist and produce merger events. The off–nuclear AGN search also detected the previously discovered recoiling SMBH candidate SDSS1133 (Koss et al., 2014) when it re–brightened by 3 magnitudes in ZTF. Follow–up spectra showed the return of a blue continuum, blue–shifted absorption lines and [Fe II] λ7155 and [Ca II] $\lambda\lambda$ 7291, 7324 forbidden lines, suggesting that the source is likely a luminous blue variable star which continues to show non–terminal outbursts.

In Chapter 3, I presented a sample of variability–selected low–mass AGN within a parent sample of dwarf galaxies using optical photometry from ZTF and forward–modeled mid–IR photometry of time–resolved *WISE* coadded images. I found that 44 out of 25,714 dwarf galaxies had optically variable AGN candidates, and 148 out of 79,879 dwarf galaxies had mid–IR variable AGN candidates, corresponding to active fractions of $0.17 \pm 0.03\%$ and $0.19 \pm 0.02\%$ respectively. Of the 148 AGN which were variable in the mid–IR, 15 were also variable in the optical and 7 of these were broad line AGN. I found that spectroscopic approaches to AGN identification would have missed 81% of our ZTF IMBH candidates and 69% of our *WISE* IMBH candidates. Only 9 candidates had been detected previously in radio, X-ray, and variability searches for dwarf galaxy AGN. The IMBHs with broad Balmer lines had virial masses of $10^5 M_\odot < M_{\rm BH} < 10^7 M_\odot$ but for the rest of the sample, BH masses predicted from host galaxy mass ranged between $10^{4.8} M_\odot < M_{\rm BH} < 10^7 M_\odot$. I found that only 5 of 152 previously reported variability–selected AGN candidates from the Palomar Transient Factory in common with our parent sample were variable in ZTF. I also determined a nuclear supernova fraction of $0.05 \pm 0.01\%$ year^{-1} for dwarf galaxies in ZTF. Our ZTF and *WISE* IMBH candidates show the promise of variability searches for discovery of otherwise hidden low–mass AGN.

In Chapter 4, I presented a sample of 299 optically variable double–peaked emitter (DPE) AGN which have well–sampled optical light curves from ZTF. I described in further detail my methods for determining that 16% of variable broad line AGN in ZTF have double–peaked or velocity–offset broad lines and that these are 1.6 times more likely to have visible radio signatures at 2–4 GHz. I presented monthly monitoring of three new DPEs with shoulder velocities ranging from 2000–8000 km/s which had not previously been observed in the SDSS spectroscopic surveys. I showed that DPE light curves have slightly steeper power spectra than their standard broad line counterparts, with typical power law indices of 2.06 and 1.94 respectively. I showed that a number of DPEs exhibited apparently periodic and chirping behaviour in the optical and mid–IR and discuss how this arose naturally from their power spectra. I determined that 20% of DPE power spectra fits are improved by a broken power law over a single power law (in comparison to 13% of AGN) and 16% of DPE power spectra fits are improved by the addition of a Gaussian bump to the single power law (in comparison to 11% of AGN). I also modeled the ZTF time series with damped random walk models to test previous findings that DPEs have characteristic timescales τ which are $2.7\times$ longer than standard broad line AGN. Using consistent data sets to compare the two samples, I found that DPEs only have slightly longer τ ($\log \tau = 5.28 \pm 0.75$ vs $\log \tau = 5.06 \pm 0.77$) and that these differences may be entirely attributable to the higher average black hole mass of the DPEs. Finally, I presented spectroscopic follow–up of 10 optically variable DPEs and found that 5 showed dramatic changes in the relative fluxes of their red and blue peaks over 10–20 year timescales which can be explained by hotspot or spiral arm rotation. I showed that DPEs also tend to have steeper, bluer spectroscopic continua than standard broad line AGN. I compared the variability and spectroscopic properties of the ZTF DPE population with the recently discovered inspiraling SMBH binary candidate SDSSJ1430+2303 (ZTF18aarippg) and found that it is likely to be normal disk–emitting AGN. I concluded that the vast majority of variable DPEs in ZTF are from a population of disk–emitting AGN which have minor differences in their variability properties to their single broad line counterparts. The differences between the two populations may shed further light on why only a fraction of broad line AGN are disk–emitters.

5.2 Future Work

5.2.1 Multi–wavelength and spectroscopic follow–up of off–nuclear AGN

Further work is required to confirm if the 9 offset AGN presented in Chapter 2 are recoiling SMBHs, triple systems in which one SMBH was ejected (Kormendy & Richstone, 1995) or SMBHs in tidally stripped, compact dwarf galaxies (e.g. Afanasiev et al., 2018; Ahn et al., 2017, 2018; Seth et al., 2014; Voggel et al., 2019). To this end, the spatial resolution offered by HST and Chandra observations could be used to disentangle the optical and X-ray spectroscopic properties of the offset AGN and their host galaxies. A space-based spectrograph like STIS could be used to determine the relative positions and velocities of the broad and narrow line emission regions and classify the host galaxy type. This could be combined with Chandra observations to test for the presence of a second AGN in the systems and look for a redshifted broad Fe absorption line from the bright AGN indicating the presence of a relativistic inflow close to the SMBH (Chiaberge et al., 2017).

Space–based follow–up and analysis would allow us to test the effectiveness of the recoiling SMBH search strategy based on ZTF difference imaging and forward modeling. If the objects are confirmed as recoiling SMBHs, they could demonstrate the existence of SMBH binaries with misaligned spins and constrain spin alignment simulations of SMBH binaries. If they are instead triple systems or tidally stripped dwarf galaxies in a merger, the detailed X–ray and optical spectroscopic analysis could instead be used to investigate why we see such a high fraction of DPEs in the sample.

5.2.2 Searching for rare transients with The Legacy Survey of Space and Time

The superior resolution and depth offered by the upcoming Legacy Survey of Space and Time (LSST) at Vera C. Rubin Observatory (Ivezić et al., 2019) will provide a vastly more complete census of three distinct populations, two of which have already been explored in this thesis: low accretion rate IMBHs wandering in their galaxy haloes; supermassive black holes (SMBHs) which have been ejected from their host galaxies via gravitational wave (GW) recoil; and gravitationally lensed, multiply–imaged supernovae (gLSNe) and quasars (gLQSOs) from which we can measure H_0.

While ZTF produced an already substantial ∼100,000 – 1 million transient alerts per night, LSST will produce ∼10 million alerts per night and an estimated final source catalog of 20 billion galaxies and 17 billion stars. And while ZTF Phase I discovered 4000 supernovae (SNe, Perley et al., 2020), LSST is predicted to discover 10 million SNe along with ∼10 million AGN and QSOs (LSST Science Collaborations, 2009). It will be challenging to discover the small numbers of particularly rare and interesting objects amongst these enormous populations of transient and variable objects. For example, amongst the 10 million QSOs, it is predicted that 33 will be strongly lensed high redshift QSOs at $z \geq 3.5$ which we can use to study QSO formation and accretion in the early universe (Desira et al., 2021).

The LSST data volume will pose a range of computational challenges which must be overcome in order to discover these rare sources amongst the tens of millions of transients LSST will observe. Extending the alert filtering and forward modeling techniques demonstrated in this thesis to the LSST dataset will enable the discovery of substantially larger populations of rare AGN and other uncommon astrophysical phenomena with LSST than has been possible in previous time–domain surveys such as PTF and ZTF.

5.2.2.1 Searching for off–nuclear and low–mass AGN with LSST

LSST is designed to have single visit limiting magnitudes of $u \sim 23.9$, $g \sim 25.0$, $r \sim 24.7$, $i \sim 24.0$, $z \sim 23.3$ and $y \sim 22.1$, in comparison to ZTF's limiting magnitudes of $g, r \sim 21.0$. The sensitivity of LSST will allow it to detect variability from objects like the canonical $\sim 10^5\ M_{\odot}$ dwarf AGN NGC 4395, which varies at very low amplitudes of $\Delta g \sim 0.01$ magnitudes (Burke et al., 2020a; Edri et al., 2012). In Figure 5.1 we show the light curve of NGC4395 from the *Transiting Exoplanet Survey Satellite* (TESS; Ricker et al., 2014) presented in Burke et al. (2020a) and the equivalent g–band LSST light curve, calculated using the median TESS zeropoint of 20.44 e^{-} s^{-1} described in the TESS Instrument Handbook[1], the estimated LSST single exposure g-band limiting magnitude of 25.0 (Ivezić et al., 2019), and assuming a power law spectrum to convert from the TESS central wavelength of ~ 8000 Å to the LSST g-band central wavelength of ~ 4800 Å. Assuming a 3 day cadence, LSST can resolve the very faint variations in the optical flux from this low–mass AGN. Although more distant NGC4395–like AGN

[1]https://archive.stsci.edu/files/live/sites/mast/files/home/missions-and-data/active-missions/tess/_documents/TESS_Instrument_Handbook_v0.1.pdf

of mass $10^5\ M_\odot$ would need to exhibit larger variability amplitudes to be detectable by LSST, this prediction shows how powerful LSST will be even when compared to very sensitive space–based telescopes such as TESS. Greater sensitivity to variable AGN in dwarf galaxies will provide improved lower limits to black hole occupation fractions for galaxies of mass $< 10^9\ M_\odot$, allowing for comparison to cosmological simulations (Figure 5.2; Bellovary et al., 2021; Ricarte et al., 2021a) and improved constraints on BH seeding predictions.

The resolution of LSST, with pixel scales of 0.”2 in comparison to ZTF’s 1.”0, will enable improved measurements of spatial offsets between variable low–mass AGN and their host nuclei. By forward modeling LSST images we can measure the fraction of active IMBHs in dwarf galaxies which are wandering in their galaxy haloes, rather than occupying the nucleus. Observational findings can be compared to predicted offset distributions from cosmological simulations and test predictions that the majority of MBHs of mass $< 10^7 M_\odot$ are off–nuclear (Figure 5.3; Bellovary et al., 2018, 2021; Ricarte et al., 2021a). Since the majority of optically variable low–mass AGN do not appear in X-ray or radio wavelengths (see Chapter 3 and Baldassare et al., 2018, 2020b) it is highly advantageous to be able to model the AGN position using optical imaging alone. A population of variable low–mass AGN in dwarf galaxies from LSST could also become the subject of spectroscopic and multi–wavelength follow–up for characterization of the masses, SEDs, and accretion states of the dwarf galaxy AGN.

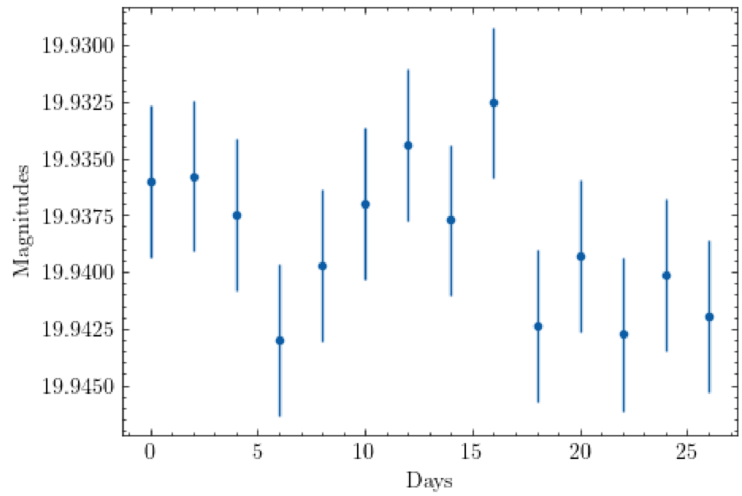

Figure 5.1: A simulated g–band LSST light curve of the $10^5 M_\odot$ AGN in NGC4395 based on conversion of the TESS light curve from Burke et al. (2020a) to the predicted limiting magnitude of LSST survey data.

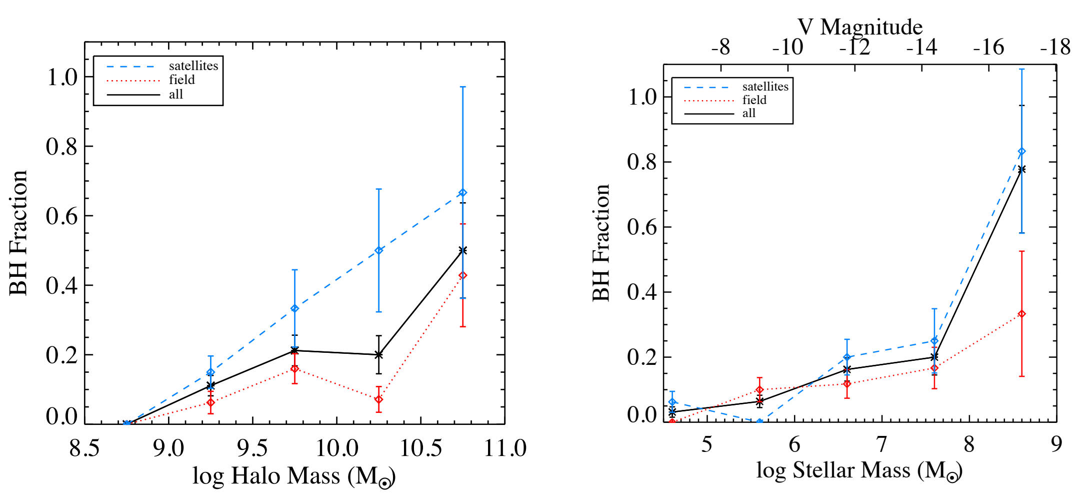

Figure 5.2: BH occupation fraction as a function of halo mass and stellar mass according to cosmological simulations, from Bellovary et al. (2018). Reproduced by permission of the authors.

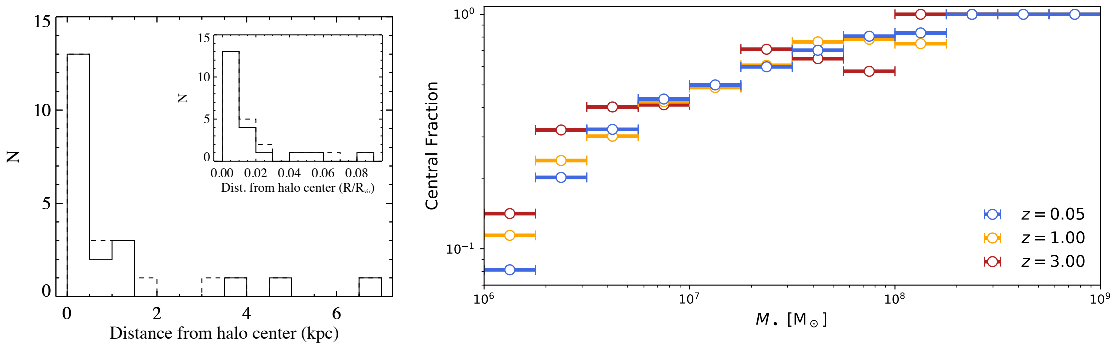

Figure 5.3: For IMBH populations in cosmological simulations: `Left:` distributions of distance from the halo center, from Bellovary et al. (2018). Reproduced by permission of the authors. `Right:` fraction of MBHs which are in galaxy nuclei (vs wandering) as a function of BH mass, from Ricarte et al. (2021b). Reproduced by permission of the authors and AAS.

5.2.2.2 Forward modeling analysis of strongly lensed supernovae and QSOs with LSST

Strong gravitational lensing of a supernova by a foreground galaxy can produce multiple, highly magnified images of the object with time delays which can be used to measure H_0. Very few gravitationally lensed SNe (gLSNe) have been resolved to date but LSST is predicted to find 1700 gLSNe over the survey lifetime (Goldstein et al., 2019). Pixel level simulations of the gLSNe population detectable by LSST show that the angular separations of most doubly–imaged SN will range from $\sim 0.03 - 3.0$” with a median of ~ 0.85”, and that most gLSNe in LSST will be unresolved or marginally resolved (Figure 5.4). Unresolved gLSNe can still be identified with LSST photometry by searching for SNe which appear to be hosted by elliptical galaxies and have magnitudes larger than expected for the galaxy's photometric redshift (Goldstein & Nugent, 2016).

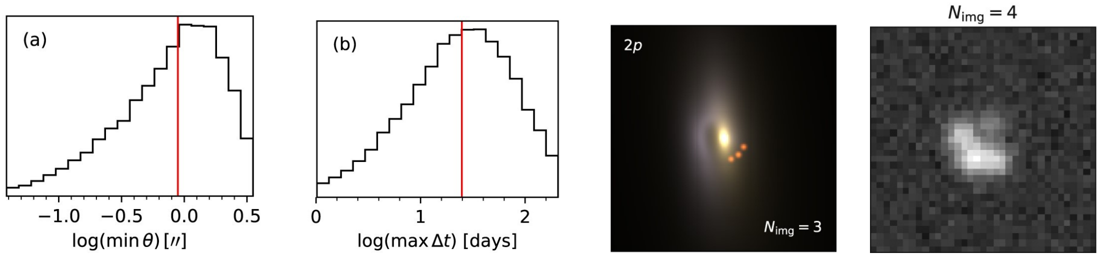

Figure 5.4: Simulations and histograms describing the gLSNe population that LSST will detect. `Left`: The minimum angular separations between multiply–imaged gLSNe in arcseconds. The red line shows the median. `Middle left`: The maximum time delay between two multiply–imaged gLSNe images. `Middle right`: A simulated multiply imaged gLSNe at the pixel size of HST's WFC3. `Right`: A simulated LSST image of a resolved multiply–imaged gLSNe. Adapted from Goldstein et al. (2019). Reproduced by permission of the authors and AAS.

LSST's capabilities for discovery of marginally resolved, multiply imaged gLSNe could be greatly enhanced by `Tractor` forward modeling of Rubin images of gLSNe candidates. The primary advantage of forward modeling is that it will improve measurements of time delays and angular separations from the fraction of the gLSNe population which are marginally resolved. We will also benefit from the ability to produce forward modeled photometry of the earliest imaging data to study the full development of the supernova. Secondly, if the foreground or host galaxy has a variable AGN or transient, we can incorporate this into the `Tractor` model to remove contamination. Finally, if gLSNe found by LSST are imaged at greater depth and resolution with another telescope, the positional constraints can be folded into the forward modeling for improved photometric sensitivity. With the planned launch of the Roman Space Telescope in the late 2020s, the forward modeling techniques developed in this thesis will enable combined analysis of high–resolution space–based imaging and time–domain information from surveys such as LSST for improved fitting of lensing parameters.

Chapter 6: Facilities and Software

6.1 Facilities

1. Lowell Discovery Telescope

   The Deveny Optical Spectrograph was used to obtain spectra of off–nuclear AGN (Chapter 2) and double–peaked emitters (Chapter 4).

2. W. M. Keck Observatory

   The Low Resolution Imaging Spectrometer (LRIS) was used by collaborators to obtain spectra of off–nuclear AGN (Chapter 2) and double–peaked emitters (Chapter 4).

3. The Zwicky Transient Facility

   Raw images from the Zwicky Transient Facility were obtained via the NASA/IPAC Infrared Science Archive (IRSA; Masci et al., 2019) for the purposes of direct modeling of image data (Chapter 2) and the production of difference photometry (Chapter 3). ZTF imaging data was also accessed via the GROWTH Marshal (Kasliwal et al., 2019) and the `fritz` *portal*[1].

4. SDSS DR16

   Archival spectra from SDSS DR16 (Ahumada et al., 2020) were accessed via

[1] https://fritz.science/sources

the DR16 SkyServer (`https://skyserver.sdss.org/dr16/en/home.aspx`) and the SQl query interface Casjobs (`https://skyserver.sdss.org/casjobs/`) for investigation of off–nuclear AGN broad line velocities (Chapter 2), emission line classifications of IMBHs (Chapter 3), and identification and analysis of double–peaked emitters (Chapter 4).

5. The Legacy Surveys Dr9

   Legacy Survey image and catalog data from the combined DECam Legacy Survey, Mayall z-band Legacy Survey, Beijing–Arizona Sky Survey and the Wide–field Infrared Survey Explorer (WISE) were accessed directly via the NERSC filesystem and via the online Skyviewer (`https://www.legacysurvey.org/viewer`) for modeling of off–nuclear AGN positions (Chapter 2) and analysis of mid–IR variability from dwarf galaxies and double–peaked emitters (Chapters 3 and 4).

6. National Energy Research Scientific Computing Center

   The supercomputing cluster cori (`https://www.nersc.gov/systems/cori/`), a large system with 12000 nodes and 30PB of scratch memory hosted by NERSC, was used for computationally intensive forward modeling of ZTF images (Chapter 2), image subtraction and photometry (Chapter 3) and AGN light curve modeling (Chapter 4).

6.2 Existing software applied to research presented in this thesis

1. AMPEL (Nordin et al., 2019a),

2. astropy (Price-Whelan et al., 2018; Robitaille et al., 2013),

3. Astromatic (`https://www.astromatic.net/`),

4. catsHTM (Soumagnac & Ofek, 2018),

5. extcats (`github.com/MatteoGiomi/extcats`),

6. GROWTH Marshal (Kasliwal et al., 2019),

7. Hotpants (`https://github.com/acbecker/hotpants`),

8. javelin (`https://github.com/legolason/javelin-1` Zhang & Feng, 2017; Zu et al., 2013),

9. qsofit (Butler & Bloom, 2011),

10. SNCOSMO (Barbary et al., 2016),

11. The Tractor (Lang et al., 2016)

6.3 New software developed for this thesis

1. I developed and implemented a new version of `The Tractor`[2] which is capable of producing models of variable sources and their host galaxies with improved astrometric and photometric precision (Ward et al., 2021a). I contributed forward modeling analyses to a number of papers to demonstrate the range of new capabilities offered by `The Tractor` for transient science: a search for prior outbursts in PTF data of a fast blue optical transient host galaxy (Coppejans et al., 2020); discovery of a nuclear optical transient within a candidate host galaxy of

[2]https://github.com/charlotteaward/tractor-1

a neutron star–black hole merger detected by LIGO (Andreoni et al., 2020; Dobie et al., 2019); determination of the position of the optical counterpart to an X-ray transient to confirm it as a likely TDE (Brightman et al., 2021); and demonstration of forward modeling of a ZTF–derived sky model to produce photometry of blended TESS sources (van Roestel et al., 2019). The implementation of this software to identify off-nuclear AGN was described in Chapter 2.

2. I developed an off–nuclear AGN filter for the `AMPEL` alert broker (Nordin et al., 2019b) during the beta–testing period[3]. Development of this filter involved adding new databases such as the Brescia AGN catalog (Brescia et al., 2015) to the `AMPEL` framework with `extcats`. This filter incorporated catalog crossmatching and implemented light curve modeling codes `SNCosmo` and `qsofit` at the filtering stage. This was described in Chapter 2.

3. I developed a new version of the Penalized Pixel Fitting (pPXF) code (Cappellari, 2017; Cappellari & Emsellem, 2004) which is capable of fitting AGN spectra with up to 3 Hα and Hβ broad line regions at different relative velocities to the narrow emission lines and comparing the goodness of fit to a single broad line model (Chapters 2 and 4).

4. A collaborator and I developed code to implement the generalized least squares method (Coles et al., 2011) for generating power spectra of ZTF light curves. The code included robust outlier rejection and treatment of unevenly sampled data, and was capable of determining best–fit parameters for different models of the PSD

[3]https://github.com/robertdstein/Ampel-contrib-ZTFbh

shape. It was described in Chapter 4.

5. I developed Python code to fit continuum–subtracted spectra of double–peaked broad Hα and Hβ line profiles with the circular and elliptical accretion disk models described in Section 1.4 (Chen & Halpern, 1989; Strateva et al., 2003). An original test case for both disk models is shown in Figure 6.1 for iPTF15ee. Example fit parameters for ZTF18aaymybb, which was presented as a new DPE in Chapter 4, and iPTF15ee are shown in Table 6.1.

Table 6.1: Best fit accretion disk parameters for circular and elliptical models of two double–peaked emitters from ZTF.

Source	Model	ξ_1 (R$_G$)	ξ_2 (R$_G$)	q	σ km/s	i (deg)	e	ϕ_0 (deg)
ZTF18aaymybb	Circular	252	586	1.0	409	29.3	0	0
ZTF18aaymybb	Elliptical	596	1395	2.44	403	50.39	0.11	17.7
iPTF15ee	Circular	292	444	3.0	630	89.44	0	0
iPTF15ee	Elliptical	216	424	3.0	775	89.79	0.67	16.9

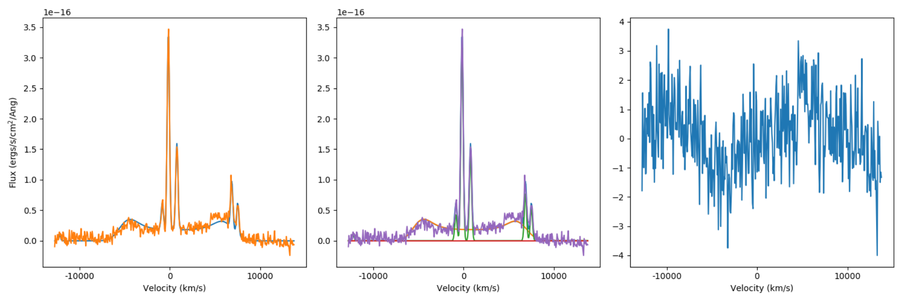

(a) Circular disk model of iPTF15ee

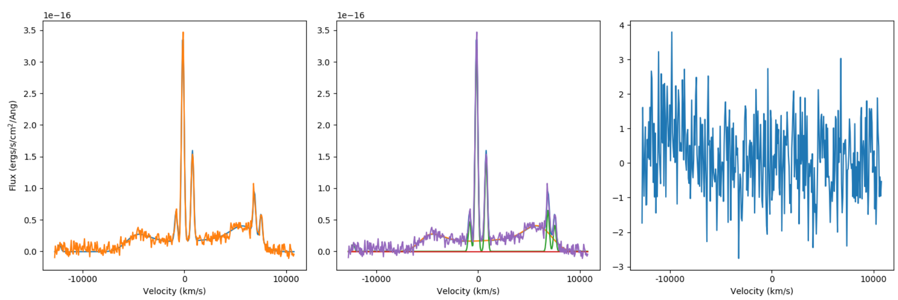

(b) Elliptical disk model of iPTF15ee

Figure 6.1: Fit of the double–peaked Hα region of iPTF15ee. The left images show the data and the best fit model. The middle images show the narrow line, broad line and disk components. The right images show the error normalized residuals.

Bibliography

Abajas, C., Mediavilla, E., Munoz, J. A., Popović, L. , & Oscoz, A. 2002, The Astrophysical Journal, 576, 640, doi: 10.1086/341793

Abramowicz, M. A., Czerny, B., Lasota, J. P., & Szuszkiewicz, E. 1988, The Astrophysical Journal, 332, 646, doi: 10.1086/166683

Afanasiev, A. V., Chilingarian, I. V., Mieske, S., et al. 2018, Monthly Notices of the Royal Astronomical Society, 477, 4856, doi: 10.1093/mnras/sty913

Ahn, C. P., Seth, A. C., Brok, M. d., et al. 2017, The Astrophysical Journal, 839, 72, doi: 10.3847/1538-4357/aa6972

Ahn, C. P., Seth, A. C., Cappellari, M., et al. 2018, The Astrophysical Journal, 858, 102, doi: 10.3847/1538-4357/aabc57

Ahumada, R., Prieto, C. A., Almeida, A., et al. 2020, The Astrophysical Journal Supplement Series, 249, 3, doi: 10.3847/1538-4365/ab929e

Allen, J. T., Schaefer, A. L., Scott, N., et al. 2015, Monthly Notices of the Royal Astronomical Society, 451, 2780, doi: 10.1093/mnras/stv1121

Andreoni, I., Goldstein, D. A., Kasliwal, M. M., et al. 2020, ApJ, 890, 131

Anglés-Alcázar, D., Faucher-Giguère, C. A., Quataert, E., et al. 2017, Monthly Notices of the Royal Astronomical Society: Letters, 472, L109, doi: 10.1093/mnrasl/slx161

Annuar, A., Gandhi, P., Alexander, D. M., et al. 2015, Astrophysical Journal, 815, doi: 10.1088/0004-637X/815/1/36

Annuar, A., Alexander, D. M., Gandhi, P., et al. 2017, The Astrophysical Journal, 836, 165, doi: 10.3847/1538-4357/836/2/165

Antonucci, R. 1993, Annual Review of Astronomy and Astrophysics, 31, 473, doi: 10.1146/annurev.aa.31.090193.002353

Assef, R. J., Stern, D., Kochanek, C. S., et al. 2013, Astrophysical Journal, 772, doi: 10.1088/0004-637X/772/1/26

Baldassare, V. F., Dickey, C., Geha, M., & Reines, A. E. 2020a, The Astrophysical Journal, 898, L3, doi: 10.3847/2041-8213/aba0c1

Baldassare, V. F., Geha, M., & Greene, J. 2018, The Astrophysical Journal, 868, 152, doi: 10.3847/1538-4357/aae6cf

—. 2020b, The Astrophysical Journal, 896, 10, doi: 10.3847/1538-4357/ab8936

Baldwin, J. A., Phillips, M. M., & Terlevich, R. 1981, Publications of the Astronomical Society of the Pacific, 93, 5, doi: 10.1086/130766

Bañados, E., Mazzucchelli, C., Momjian, E., et al. 2021, The Astrophysical Journal, 909, 80, doi: 10.3847/1538-4357/abe239

Banks, S., Lee, K., Azimi, N., et al. 2022, Monthly Notices of the Royal Astronomical Society, 512, 6007, doi: 10.1093/mnras/stac831

Bansal, K., Taylor, G. B., Peck, A. B., Zavala, R. T., & Romani, R. W. 2017, The Astrophysical Journal, 843, 14, doi: 10.3847/1538-4357/aa74e1

Barbary, K., rbiswas4, Goldstein, D., et al. 2016, sncosmo/sncosmo: v1.4.0, doi: 10.5281/zenodo.168220

Barth, A. J., & Stern, D. 2018, The Astrophysical Journal, 859, 10, doi: 10.3847/1538-4357/aab3c5

Barth, A. J., Bennert, V. N., Canalizo, G., et al. 2015, Astrophysical Journal, Supplement Series, 217, doi: 10.1088/0067-0049/217/2/26

Barvainis, R. 1992, The Astrophysical Journal, 400, 502, doi: 10.1086/172012

Begelman, M. C., Blandford, R. D., & Rees, M. J. 1980, Nature, 287, 307, doi: 10.1038/287307a0

Begelman, M. C., & Volonteri, M. 2017, Monthly Notices of the Royal Astronomical Society, 464, 1102, doi: 10.1093/mnras/stw2446

Bellm, E. C., Kulkarni, S. R., Graham, M. J., et al. 2019a, Publications of the Astronomical Society of the Pacific, 131, 018002, doi: 10.1088/1538-3873/aaecbe

Bellm, E. C., Kulkarni, S. R., Barlow, T., et al. 2019b, Publications of the Astronomical Society of the Pacific, 131, 68003, doi: 10.1088/1538-3873/ab0c2a

Bellovary, J. M., Cleary, C. E., Munshi, F., et al. 2018, Monthly Notices of the Royal Astronomical Society, 482, 2913, doi: 10.1093/mnras/sty2842

Bellovary, J. M., Governato, F., Quinn, T. R., et al. 2010, Astrophysical Journal Letters, 721, 148, doi: 10.1088/2041-8205/721/2/L148

Bellovary, J. M., Hayoune, S., Chafla, K., et al. 2021, Monthly Notices of the Royal Astronomical Society, 505, 5129, doi: 10.1093/mnras/stab1665

Berczik, P., Merritt, D., Spurzem, R., & Bischof, H.-P. 2006, The Astrophysical Journal, 642, L21, doi: 10.1086/504426

Bertin, E., & Arnouts, S. 1996, Astronomy and Astrophysics Supplement Series, 117, 393, doi: 10.1051/aas:1996164

Bertin, E., Mellier, Y., Radovich, M., et al. 2002, in Astronomical Society of the Pacific Conference Series, Vol. 281, Astronomical Data Analysis Software and Systems XI, ed. D. A. Bohlender, D. Durand, & T. H. Handley, 228

Blanton, M. R., Kazin, E., Muna, D., Weaver, B. A., & Price-Whelan, A. 2011, Astronomical Journal, 142, doi: 10.1088/0004-6256/142/1/31

Blanton, M. R., & Roweis, S. 2007, The Astronomical Journal, 133, 734, doi: 10.1086/510127

Blecha, L., Cox, T. J., Loeb, A., & Hernquist, L. 2011, Monthly Notices of the Royal Astronomical Society, 412, 2154, doi: 10.1111/j.1365-2966.2010.18042.x

Blecha, L., & Loeb, A. 2008, Monthly Notices of the Royal Astronomical Society, doi: 10.1111/j.1365-2966.2008.13790.x

Blecha, L., Sijacki, D., Kelley, L. Z., et al. 2016, Monthly Notices of the Royal Astronomical Society, 456, 961, doi: 10.1093/mnras/stv2646

Boco, L., Lapi, A., & Danese, L. 2020, The Astrophysical Journal, 891, 94, doi: 10.3847/1538-4357/ab7446

Bogdanović, T. 2015, 103–119, doi: 10.1007/978-3-319-10488-1{_}9

Bogdanović, T., Eracleous, M., Mahadevan, S., Sigurdsson, S., & Laguna, P. 2004, The Astrophysical Journal, 610, 707, doi: 10.1086/421758

Bogdanović, T., Reynolds, C. S., & Miller, M. C. 2007, The Astrophysical Journal, 661, L147, doi: 10.1086/518769

Bogdanović, T., Smith, B. D., Sigurdsson, S., & Eracleous, M. 2008, The Astrophysical Journal Supplement Series, 174, 455, doi: 10.1086/521828

Bohn, T., Canalizo, G., Veilleux, S., & Liu, W. 2021, The Astrophysical Journal, 911, 70, doi: 10.3847/1538-4357/abe70c

Boles, T. 2009, Central Bureau Electronic Telegrams, 1931, 1

Boller, T., Freyberg, M. J., Trümper, J., et al. 2016, Astronomy & Astrophysics, 588, A103, doi: 10.1051/0004-6361/201525648

Bon, E., Popović, L. , Gavrilović, N., Mura, G. L., & Mediavilla, E. 2009, Monthly Notices of the Royal Astronomical Society, 400, 924, doi: 10.1111/j.1365-2966.2009.15511.x

Bonning, E. W., Shields, G. A., & Salviander, S. 2007, The Astrophysical Journal, 666, L13, doi: 10.1086/521674

Boroson, T. A., & Lauer, T. R. 2009, Nature, 458, 53, doi: 10.1038/nature07779

Borucki, W. J., Koch, D., Basri, G., et al. 2010, Science, 327, 977, doi: 10.1126/science.1185402

Brescia, M., Cavuoti, S., & Longo, G. 2015, Monthly Notices of the Royal Astronomical Society, 450, 3893, doi: 10.1093/mnras/stv854

Brightman, M., Ward, C., Stern, D., et al. 2021, ApJ, 909, 102

Bruzual, G., & Charlot, S. 2003, Monthly Notices of the Royal Astronomical Society, 344, 1000, doi: 10.1046/j.1365-8711.2003.06897.x

Burke, C. J., Shen, Y., Chen, Y.-C., et al. 2020a, The Astrophysical Journal, 899, 136, doi: 10.3847/1538-4357/aba3ce

Burke, C. J., Baldassare, V. F., Liu, X., et al. 2020b, The Astrophysical Journal, 894, L5, doi: 10.3847/2041-8213/ab88de

Burke, C. J., Shen, Y., Blaes, O., et al. 2021, Science, 373, 789, doi: 10.1126/science.abg9933

Burke-Spolaor, S., Taylor, S. R., Charisi, M., et al. 2019, The Astronomy and Astrophysics Review, 27, 5, doi: 10.1007/s00159-019-0115-7

Butler, N. R., & Bloom, J. S. 2011, The Astronomical Journal, 141, 93, doi: 10.1088/0004-6256/141/3/93

Campanelli, M., Lousto, C., Zlochower, Y., & Merritt, D. 2007a, LARGE MERGER RECOILS AND SPIN FLIPS FROM GENERIC BLACK HOLE BINARIES, Tech. rep.

Campanelli, M., Lousto, C. O., Zlochower, Y., & Merritt, D. 2007b, Physical Review Letters, 98, 8, doi: 10.1103/PhysRevLett.98.231102

Canalizo, G., & Stockton, A. 2001, The Astrophysical Journal, 555, 719, doi: 10.1086/321520

Cann, J. M., Satyapal, S., Abel, N. P., et al. 2019, The Astrophysical Journal, 870, L2, doi: 10.3847/2041-8213/aaf88d

Cappellari, M. 2017, Monthly Notices of the Royal Astronomical Society, 466, 798, doi: 10.1093/mnras/stw3020

Cappellari, M., & Emsellem, E. 2004, Publications of the Astronomical Society of the Pacific, 116, 138, doi: 10.1086/381875

Chambers, K. C., Magnier, E. A., Metcalfe, N., et al. 2016, arXiv: 1612.05560. http://arxiv.org/abs/1612.05560

Chandra, P., Chevalier, R. A., Chugai, N., Fransson, C., & Soderberg, A. M. 2015, Astrophysical Journal, 810, 32, doi: 10.1088/0004-637X/810/1/32

Charisi, M., Bartos, I., Haiman, Z., et al. 2016, Monthly Notices of the Royal Astronomical Society, 463, 2145, doi: 10.1093/mnras/stw1838

Charisi, M., Haiman, Z., Schiminovich, D., & D'Orazio, D. J. 2018, Monthly Notices of the Royal Astronomical Society, 476, 4617, doi: 10.1093/mnras/sty516

Chen, K., & Halpern, J. P. 1989, The Astrophysical Journal, 344, 115, doi: 10.1086/167782

Chiaberge, M., Gilli, R., M. Lotz, J., & Norman, C. 2015, The Astrophysical Journal, 806, 147, doi: 10.1088/0004-637X/806/2/147

Chiaberge, M., Tremblay, G. R., Capetti, A., & Norman, C. 2018, The Astrophysical Journal, 861, 56, doi: 10.3847/1538-4357/aac48b

Chiaberge, M., Ely, J. C., Meyer, E. T., et al. 2017, Astronomy & Astrophysics, 600, A57, doi: 10.1051/0004-6361/201629522

Cid Fernandes, R., Stasińska, G., Mateus, A., & Vale Asari, N. 2011, Monthly Notices of the Royal Astronomical Society, 413, 1687, doi: 10.1111/j.1365-2966.2011.18244.x

Civano, F., Elvis, M., Lanzuisi, G., et al. 2010, Astrophysical Journal, 717, 209, doi: 10.1088/0004-637X/717/1/209

Coles, W., Hobbs, G., Champion, D. J., Manchester, R. N., & Verbiest, J. P. W. 2011, Monthly Notices of the Royal Astronomical Society, 418, 561, doi: 10.1111/j.1365-2966.2011.19505.x

Comerford, J. M., Barrows, R. S., Greene, J. E., & Pooley, D. 2017, The Astrophysical Journal, 847, 41, doi: 10.3847/1538-4357/aa876a

Comerford, J. M., & Greene, J. E. 2014, The Astrophysical Journal, 789, 112, doi: 10.1088/0004-637X/789/2/112

Comerford, J. M., Gerke, B. F., Newman, J. A., et al. 2009, Astrophysical Journal, 698, 956, doi: 10.1088/0004-637X/698/1/956

Condon, J. J., Cotton, W. D., Greisen, E. W., et al. 1998, The Astronomical Journal, 115, 1693, doi: 10.1086/300337

Condon, J. J., Darling, J., Kovalev, Y. Y., & Petrov, L. 2017, The Astrophysical Journal, 834, 184, doi: 10.3847/1538-4357/834/2/184

Congiu, E., Berton, M., Giroletti, M., et al. 2017, Astronomy & Astrophysics, 603, A32, doi: 10.1051/0004-6361/201730616

Coppejans, D. L., Margutti, R., Terreran, G., et al. 2020, ApJ, 895, L23

De Rosa, A., Vignali, C., Bogdanović, T., et al. 2019, New Astronomy Reviews, 86, 101525, doi: 10.1016/j.newar.2020.101525

Dekany, R., Smith, R. M., Riddle, R., et al. 2020, Publications of the Astronomical Society of the Pacific, 132, 038001, doi: 10.1088/1538-3873/ab4ca2

Denney, K. D., Peterson, B. M., Pogge, R. W., et al. 2010, Astrophysical Journal, 721, 715, doi: 10.1088/0004-637X/721/1/715

Desira, C., Shu, Y., Auger, M. W., et al. 2021, MNRAS, 509, 738

Dey, A., Schlegel, D. J., Lang, D., et al. 2019a, 168, doi: 10.3847/1538-3881/ab089d

Dey, L., Gopakumar, A., Valtonen, M., et al. 2019b, Universe, 5, 108, doi: 10.3390/universe5050108

Dickey, C. M., Geha, M., Wetzel, A., & El-Badry, K. 2019, The Astrophysical Journal, 884, 180, doi: 10.3847/1538-4357/ab3220

Dietrich, M., & Wagner, S. J. 1998, \Aap, 338, 405

Doan, A., Eracleous, M., Runnoe, J. C., et al. 2020, Monthly Notices of the Royal Astronomical Society, 491, 1104, doi: 10.1093/mnras/stz2705

Dobie, D., Stewart, A., Murphy, T., et al. 2019, The Astrophysical Journal, 887, L13, doi: 10.3847/2041-8213/ab59db

D'Orazio, D. J., & Haiman, Z. 2017, Monthly Notices of the Royal Astronomical Society, 470, 1198, doi: 10.1093/mnras/stx1269

D'Orazio, D. J., Haiman, Z., & MacFadyen, A. 2013, Monthly Notices of the Royal Astronomical Society, 436, 2997, doi: 10.1093/mnras/stt1787

D'Orazio, D. J., Haiman, Z., & Schiminovich, D. 2015, Nature, 525, 351, doi: 10.1038/nature15262

Drake, A. J., Djorgovski, S. G., Graham, M. J., et al. 2019, Monthly Notices of the Royal Astronomical Society, 482, 98, doi: 10.1093/mnras/sty2673

Drake, A. J., Djorgovski, S. G., Mahabal, A., et al. 2009, Astrophysical Journal, 696, 870, doi: 10.1088/0004-637X/696/1/870

Duev, D. A., Mahabal, A., Masci, F. J., et al. 2019, MNRAS, 489, 3582, doi: 10.1093/mnras/stz2357

Duffell, P. C., D'Orazio, D., Derdzinski, A., et al. 2020, The Astrophysical Journal, 901, 25, doi: 10.3847/1538-4357/abab95

Edri, H., Rafter, S. E., Chelouche, D., Kaspi, S., & Behar, E. 2012, The Astrophysical Journal, 756, 73, doi: 10.1088/0004-637X/756/1/73

Elitzur, M., & Ho, L. C. 2009, Astrophysical Journal, 701, doi: 10.1088/0004-637X/701/2/L91

Elitzur, M., Ho, L. C., & Trump, J. R. 2014, Monthly Notices of the Royal Astronomical Society, 438, 3340, doi: 10.1093/mnras/stt2445

Eracleous, M., & Halpern, J. P. 1994, The Astrophysical Journal Supplement Series, 90, 1, doi: 10.1086/191856

—. 2003, The Astrophysical Journal, 599, 886, doi: 10.1086/379540

Eracleous, M., Halpern, J. P., Gilbert, A. M., Newman, J. A., & Filippenko, A. V. 1997a, REJECTION OF THE BINARY BROAD-LINE REGION INTERPRETATION OF DOUBLE-PEAKED EMISSION LINES IN THREE ACTIVE GALACTIC NUCLEI, Tech. rep.

Eracleous, M., Halpern, J. P., M. Gilbert, A., Newman, J. A., & Filippenko, A. V. 1997b, The Astrophysical Journal, 490, 216, doi: 10.1086/304859

Eracleous, M., Lewis, K. T., & Flohic, H. M. 2009, New Astronomy Reviews, 53, 133, doi: 10.1016/j.newar.2009.07.005

Escala, A., Larson, R. B., Coppi, P. S., & Mardones, D. 2005, The Astrophysical Journal, 630, 152, doi: 10.1086/431747

Evans, I. N., Primini, F. A., Glotfelty, K. J., et al. 2010, Astrophysical Journal, Supplement Series, 189, 37, doi: 10.1088/0067-0049/189/1/37

Farrell, S. A., Webb, N. A., Barret, D., Godet, O., & Rodrigues, J. M. 2009, Nature, 460, 73, doi: 10.1038/nature08083

Farris, B. D., Duffell, P., Macfadyen, A. I., & Haiman, Z. 2014, Astrophysical Journal, 783, doi: 10.1088/0004-637X/783/2/134

Ferrarese, L., & Ford, H. 2005, Space Science Reviews, 116, 523, doi: 10.1007/s11214-005-3947-6

Ferrarese, L., & Merritt, D. 2000, The Astrophysical Journal, 539, L9, doi: 10.1086/312838

Filippenko, A. V. 1997, Annual Review of Astronomy and Astrophysics, 35, 309, doi: 10.1146/annurev.astro.35.1.309

Flesch, E. W. 2015, Publications of the Astronomical Society of Australia, 32, doi: 10.1017/pasa.2015.10

Foley, R. J., Berger, E., Fox, O., et al. 2011, The Astrophysical Journal, 732, 32, doi: 10.1088/0004-637X/732/1/32

Foreman, G., Volonteri, M., & Dotti, M. 2009, Astrophysical Journal, 693, 1554, doi: 10.1088/0004-637X/693/2/1554

Fransson, C., Ergon, M., Challis, P. J., et al. 2014, Astrophysical Journal, 797, doi: 10.1088/0004-637X/797/2/118

Frederick, S., Gezari, S., Graham, M. J., et al. 2019, The Astrophysical Journal, 883, 31, doi: 10.3847/1538-4357/ab3a38

Fryer, C. L., & Kalogera, V. 2001, The Astrophysical Journal, 554, 548, doi: 10.1086/321359

Fu, H., Myers, A. D., Djorgovski, S. G., & Yan, L. 2011a, Astrophysical Journal, 733, 1, doi: 10.1088/0004-637X/733/2/103

Fu, H., Zhang, Z. Y., Assef, R. J., et al. 2011b, Astrophysical Journal Letters, 740, 1, doi: 10.1088/2041-8205/740/2/L44

Geha, M., Blanton, M. R., Yan, R., & Tinker, J. L. 2012, Astrophysical Journal, 757, doi: 10.1088/0004-637X/757/1/85

Geha, M., Alcock, C., Allsman, R. A., et al. 2003, The Astronomical Journal, 125, 1, doi: 10.1086/344947

Gezari, S., Halpern, J. P., & Eracleous, M. 2007, The Astrophysical Journal Supplement Series, 169, 167, doi: 10.1086/511032

Glikman, E., Simmons, B., Mailly, M., et al. 2015, Astrophysical Journal, 806, 218, doi: 10.1088/0004-637X/806/2/218

Goldstein, D. A., & Nugent, P. E. 2016, ApJ, 834, L5

Goldstein, D. A., Nugent, P. E., & Goobar, A. 2019, ApJ Supplement Series, 243, 6

González-Martín, O., & Vaughan, S. 2012, Astronomy & Astrophysics, 544, A80, doi: 10.1051/0004-6361/201219008

Gordon, Y. A., Boyce, M. M., O'Dea, C. P., et al. 2020, Research Notes of the AAS, 4, 175, doi: 10.3847/2515-5172/abbe23

Gordon, Y. A., Boyce, M. M., O'Dea, C. P., et al. 2021, doi: 10.3847/1538-4365/ac05c0

Goulding, A. D., Alexander, D. M., Mullaney, J. R., et al. 2011, Monthly Notices of the Royal Astronomical Society, 411, 1231, doi: 10.1111/j.1365-2966.2010.17755.x

Goyal, A., Stawarz, , Zola, S., et al. 2018, The Astrophysical Journal, 863, 175, doi: 10.3847/1538-4357/aad2de

Graham, M. J., Djorgovski, S. G., Stern, D., et al. 2015a, Nature, 518, 74, doi: 10.1038/nature14143

—. 2015b, Monthly Notices of the Royal Astronomical Society, 453, 1562, doi: 10.1093/mnras/stv1726

Graham, M. J., Kulkarni, S. R., Bellm, E. C., et al. 2019, Publications of the Astronomical Society of the Pacific, 131, 1, doi: 10.1088/1538-3873/ab006c

Greene, J. E., Strader, J., & Ho, L. C. 2020, Annual Review of Astronomy and Astrophysics, 58, 257, doi: 10.1146/annurev-astro-032620-021835

Guo, H., Liu, X., Shen, Y., et al. 2019, Monthly Notices of the Royal Astronomical Society, 482, 3288, doi: 10.1093/mnras/sty2920

Habouzit, M., Volonteri, M., & Dubois, Y. 2017, Monthly Notices of the Royal Astronomical Society, 468, 3935, doi: 10.1093/mnras/stx666

Habouzit, M., Volonteri, M., Latif, M., et al. 2016, Monthly Notices of the Royal Astronomical Society, 456, 1901, doi: 10.1093/mnras/stv2740

Halpern, J. P., & Eracleous, M. 1994, The Astrophysical Journal, 433, L17, doi: 10.1086/187537

Halpern, J. P., Impey, C. D., Bothun, G. D., et al. 1986, The Astrophysical Journal, 302, 711, doi: 10.1086/164032

Helfand, D. J., White, R. L., & Becker, R. H. 2015, The Astrophysical Journal, 801, 26, doi: 10.1088/0004-637X/801/1/26

Hemberger, D. A., Lovelace, G., Loredo, T. J., et al. 2013, Physical Review D, 88, 064014, doi: 10.1103/PhysRevD.88.064014

Ho, L. C. 2008, Annual Review of Astronomy and Astrophysics, 46, 475, doi: 10.1146/annurev.astro.45.051806.110546

Ho, L. C., Filippenko, A. V., W Sargent, W. L., & Peng, C. Y. 1997, The American Astronomical Society. All rights reserved, Tech. rep.

Ho, L. C., & Kim, M. 2015, Astrophysical Journal, 809, 123, doi: 10.1088/0004-637X/809/2/123

Ho, L. C., Rudnick, G., Rix, H.-W., et al. 2000, DOUBLE-PEAKED BROAD EMISSION LINES IN NGC 4450 AND OTHER LINERs1, Tech. rep.

Holley-Bockelmann, K., Micic, M., Sigurdsson, S., & Rubbo, L. J. 2010, Astrophysical Journal, 713, 1016, doi: 10.1088/0004-637X/713/2/1016

Holley-Bockelmann, K., Gültekin, K., Shoemaker, D., & Yunes, N. 2008, The Astrophysical Journal, 686, 829, doi: 10.1086/591218

Hönig, S. F., & Kishimoto, M. 2011, Astronomy and Astrophysics, 534, doi: 10.1051/0004-6361/201117750

—. 2017, The Astrophysical Journal, 838, L20, doi: 10.3847/2041-8213/aa6838

Huang, Y., Liu, X. W., Yuan, H. B., et al. 2014, Monthly Notices of the Royal Astronomical Society, 439, 2927, doi: 10.1093/mnras/stu334

Hwang, H.-C., Shen, Y., Zakamska, N., & Liu, X. 2020, The Astrophysical Journal, 888, 73, doi: 10.3847/1538-4357/ab5c1a

Inayoshi, K., Haiman, Z., & Ostriker, J. P. 2016, Monthly Notices of the Royal Astronomical Society, 459, 3738, doi: 10.1093/mnras/stw836

Ivezić, v., Kahn, S. M., Tyson, J. A., et al. 2019, The Astrophysical Journal, 873, 111, doi: 10.3847/1538-4357/ab042c

Ivison, R. J., Smail, I., Amblard, A., et al. 2012, Monthly Notices of the Royal Astronomical Society, 425, 1320, doi: 10.1111/j.1365-2966.2012.21544.x

Jarrett, T. H., Chester, T., Cutri, R., et al. 2000, The Astronomical Journal, 119, 2498, doi: 10.1086/301330

Jiang, N., Yang, H., Wang, T., et al. 2022. http://arxiv.org/abs/2201.11633

Jonker, P. G., Torres, M. A., Fabian, A. C., et al. 2010, Monthly Notices of the Royal Astronomical Society, 407, 645, doi: 10.1111/j.1365-2966.2010.16943.x

Jovanović, P., Popović, L., Stalevski, M., & Shapovalova, A. I. 2010, Astrophysical Journal, 718, 168, doi: 10.1088/0004-637X/718/1/168

Ju, W., Greene, J. E., Rafikov, R. R., Bickerton, S. J., & Badenes, C. 2013, Astrophysical Journal, 777, doi: 10.1088/0004-637X/777/1/44

Jun, H. D., Stern, D., Graham, M. J., et al. 2015, Astrophysical Journal Letters, 814, doi: 10.1088/2041-8205/814/1/L12

Kaiser, N. 2004, 11, doi: 10.1117/12.552472

Kalfountzou, E., Lleo, M. S., & Trichas, M. 2017, The Astrophysical Journal, 851, L15, doi: 10.3847/2041-8213/aa9b2d

Kasliwal, M. M., Cannella, C., Bagdasaryan, A., et al. 2019, Publications of the Astronomical Society of the Pacific, 131, 038003, doi: 10.1088/1538-3873/aafbc2

Kauffmann, G., Heckman, T. M., Tremonti, C., et al. 2003, Monthly Notices of the Royal Astronomical Society, 346, 1055, doi: 10.1111/j.1365-2966.2003.07154.x

Keel, W. C., Bennert, V. N., Pancoast, A., et al. 2019, Monthly Notices of the Royal Astronomical Society, 483, 4847, doi: 10.1093/mnras/sty3332

Kellermann, K. I., Sramek, R., Schmidt, M., Shaffer, D. B., & Green, R. 1989, The Astronomical Journal, 98, 1195, doi: 10.1086/115207

Kelley, L. Z. 2020, doi: 10.1093/mnras/staa3219

Kelley, L. Z., Blecha, L., & Hernquist, L. 2017, Monthly Notices of the Royal Astronomical Society, 464, 3131, doi: 10.1093/mnras/stw2452

Kelley, L. Z., Blecha, L., Hernquist, L., Sesana, A., & Taylor, S. R. 2018, Monthly Notices of the Royal Astronomical Society, 477, 964, doi: 10.1093/mnras/sty689

Kelley, L. Z., Haiman, Z., Sesana, A., & Hernquist, L. 2019, Monthly Notices of the Royal Astronomical Society, 485, 1579, doi: 10.1093/mnras/stz150

Kelly, B. C., Bechtold, J., & Siemiginowska, A. 2009, Astrophysical Journal, 698, 895, doi: 10.1088/0004-637X/698/1/895

Kewley, L. J., Dopita, M. A., Sutherland, R. S., Heisler, C. A., & Trevena, J. 2001, The Astrophysical Journal, 556, 121, doi: 10.1086/321545

Kim, D.-C., Yoon, I., Privon, G. C., et al. 2017, The Astrophysical Journal, 840, 71, doi: 10.3847/1538-4357/aa6030

Klein, A., Barausse, E., Sesana, A., et al. 2015, doi: 10.1103/PhysRevD.93.024003

Kocevski, D. D., Brightman, M., Nandra, K., et al. 2015, Astrophysical Journal, 814, 104, doi: 10.1088/0004-637X/814/2/104

Komossa, S., Burwitz, V., Hasinger, G., et al. 2003, The Astrophysical Journal, 582, L15, doi: 10.1086/346145

Komossa, S., & Zensus, J. A. 2014, Proceedings of the International Astronomical Union, 10, 13, doi: 10.1017/S1743921315007395

Körding, E. G., Migliari, S., Fender, R., et al. 2007, Monthly Notices of the Royal Astronomical Society, 380, 301, doi: 10.1111/j.1365-2966.2007.12067.x

Kormendy, J., & Ho, L. C. 2013, Annual Review of Astronomy and Astrophysics, 51, 511, doi: 10.1146/annurev-astro-082708-101811

Kormendy, J., & Richstone, D. 1995, Annual Review of Astronomy and Astrophysics, 33, 581, doi: 10.1146/annurev.aa.33.090195.003053

Koshida, S., Minezaki, T., Yoshii, Y., et al. 2014, Astrophysical Journal, 788, doi: 10.1088/0004-637X/788/2/159

Koss, M., Mushotzky, R., Treister, E., et al. 2012, The Astrophysical Journal, 746, L22, doi: 10.1088/2041-8205/746/2/L22

—. 2011, Astrophysical Journal Letters, 735, doi: 10.1088/2041-8205/735/2/L42

Koss, M., Blecha, L., Mushotzky, R., et al. 2014, Monthly Notices of the Royal Astronomical Society, 445, 515, doi: 10.1093/mnras/stu1673

Koss, M. J., Blecha, L., Bernhard, P., et al. 2018, Nature, 563, 214, doi: 10.1038/s41586-018-0652-7

Koudmani, S., Sijacki, D., Bourne, M. A., & Smith, M. C. 2019, Monthly Notices of the Royal Astronomical Society, 484, 2047, doi: 10.1093/mnras/stz097

Kozłowski, S., Kochanek, C. S., Udalski, A., et al. 2010, The Astrophysical Journal, 708, 927, doi: 10.1088/0004-637X/708/2/927

Kristensen, M. T., Pimbblet, K. A., Gibson, B. K., Penny, S. J., & Koudmani, S. 2021, The Astrophysical Journal, 922, 127, doi: 10.3847/1538-4357/ac236d

Krolik, J. H., Volonteri, M., Dubois, Y., & Devriendt, J. 2019, The Astrophysical Journal, 879, 110, doi: 10.3847/1538-4357/ab24c9

La Mura, G., Di Mille, F., Ciroi, S., Popović, L. C., & Rafanelli, P. 2009, Astrophysical Journal, 693, 1437, doi: 10.1088/0004-637X/693/2/1437

Lacy, M., Baum, S. A., Chandler, C. J., et al. 2020, Publications of the Astronomical Society of the Pacific, 132, 1, doi: 10.1088/1538-3873/ab63eb

Lang, D. 2014, Astronomical Journal, 147, doi: 10.1088/0004-6256/147/5/108

Lang, D., Hogg, D. W., & Mykytyn, D. 2016, The Tractor: Probabilistic astronomical source detection and measurement, Astrophysics Source Code Library, ascl:1604.008

Lang, D., Hogg, D. W., & Schlegel, D. J. 2014, The Astronomical Journal, 151, 36, doi: 10.3847/0004-6256/151/2/36

Latimer, L. J., Reines, A. E., Hainline, K. N., Greene, J. E., & Stern, D. 2021, The Astrophysical Journal, 914, 133, doi: 10.3847/1538-4357/abfe0c

Law, N. M., Kulkarni, S. R., Dekany, R. G., et al. 2009, Publications of the Astronomical Society of the Pacific, 121, 1395, doi: 10.1086/648598

Lena, D., Robinson, A., Marconi, A., et al. 2014, The Astrophysical Journal, 795, 146, doi: 10.1088/0004-637X/795/2/146

Lewis, K. T., Eracleous, M., & Storchi-Bergmann, T. 2010, Astrophysical Journal, Supplement Series, 187, 416, doi: 10.1088/0067-0049/187/2/416

Liu, H.-Y., Liu, W.-J., Dong, X.-B., et al. 2019, The Astrophysical Journal Supplement Series, 243, 21, doi: 10.3847/1538-4365/ab298b

Liu, J., Eracleous, M., & Halpern, J. P. 2016a, The Astrophysical Journal, 817, 42, doi: 10.3847/0004-637x/817/1/42

Liu, T., Gezari, S., & Miller, M. C. 2018a, The Astrophysical Journal, 859, L12, doi: 10.3847/2041-8213/aac2ed

Liu, T., Gezari, S., Heinis, S., et al. 2015, Astrophysical Journal Letters, 803, doi: 10.1088/2041-8205/803/2/L16

Liu, T., Gezari, S., Burgett, W., et al. 2016b, The Astrophysical Journal, 833, 6, doi: 10.3847/0004-637x/833/1/6

Liu, W., Veilleux, S., Canalizo, G., et al. 2020, The Astrophysical Journal, 905, 166, doi: 10.3847/1538-4357/abc269

Liu, W.-J., Zhou, H.-Y., Jiang, N., et al. 2016c, The Astrophysical Journal, 822, 64, doi: 10.3847/0004-637x/822/2/64

Liu, X., Guo, H., Shen, Y., Greene, J. E., & Strauss, M. A. 2018b, The Astrophysical Journal, 862, 29, doi: 10.3847/1538-4357/aac9cb

Liu, X., Shen, Y., Bian, F., Loeb, A., & Tremaine, S. 2014, Astrophysical Journal, 789, doi: 10.1088/0004-637X/789/2/140

Liu, X., Shen, Y., Strauss, M. A., & Greene, J. E. 2010, Astrophysical Journal, 708, 427, doi: 10.1088/0004-637X/708/1/427

Liu, X., Shen, Y., Strauss, M. A., & Hao, L. 2011, The Astrophysical Journal, 737, 101, doi: 10.1088/0004-637X/737/2/101

Lodato, G., & Facchini, S. 2013, Monthly Notices of the Royal Astronomical Society, 433, 2157, doi: 10.1093/mnras/stt878

Lodato, G., & Natarajan, P. 2006, Monthly Notices of the Royal Astronomical Society, 371, 1813, doi: 10.1111/j.1365-2966.2006.10801.x

Loeb, A. 2007, Phys. Rev. Lett., 99, 41103, doi: 10.1103/PhysRevLett.99.041103

Loeb, A., & Rasio, F. A. 1994, The Astrophysical Journal, 432, 52, doi: 10.1086/174548

Lousto, C. O., & Zlochower, Y. 2011, doi: 10.1103/PhysRevLett.107.231102

LSST Science Collaborations. 2009, LSST Corporation, arXiv:0912

MacFadyen, A. I., & Milosavljević, M. 2008, The Astrophysical Journal, 672, 83, doi: 10.1086/523869

MacLeod, C. L., Ivezić, , Kochanek, C. S., et al. 2010, The Astrophysical Journal, 721, 1014, doi: 10.1088/0004-637X/721/2/1014

MacLeod, C. L., Brooks, K., Ivezic, Z., et al. 2011, The Astrophysical Journal, 728, 26, doi: 10.1088/0004-637X/728/1/26

Madau, P., Haardt, F., & Dotti, M. 2014, The Astrophysical Journal, 784, L38, doi: 10.1088/2041-8205/784/2/L38

Madau, P., & Rees, M. J. 2001, The Astrophysical Journal, 551, L27, doi: 10.1086/319848

Magorrian, J., Tremaine, S., Richstone, D., et al. 1998, The Astronomical Journal, 115, 2285, doi: 10.1086/300353

Mahabal, A., Rebbapragada, U., Walters, R., et al. 2019, Publications of the Astronomical Society of the Pacific, 131, 38002, doi: 10.1088/1538-3873/aaf3fa

Mainzer, A., Bauer, J., Grav, T., et al. 2011a, Astrophysical Journal, 731, doi: 10.1088/0004-637X/731/1/53

Mainzer, A., Grav, T., Bauer, J., et al. 2011b, The Astrophysical Journal, 743, 156, doi: 10.1088/0004-637X/743/2/156

Mainzer, A., Bauer, J., Cutri, R. M., et al. 2014, Astrophysical Journal, 792, doi: 10.1088/0004-637X/792/1/30

Martínez-Palomera, J., Lira, P., Bhalla-Ladd, I., Förster, F., & Plotkin, R. M. 2020, The Astrophysical Journal, 889, 113, doi: 10.3847/1538-4357/ab5f5b

Masci, F. J., Laher, R. R., Rusholme, B., et al. 2019, Publications of the Astronomical Society of the Pacific, 131, 1, doi: 10.1088/1538-3873/aae8ac

Massaro, E., Giommi, P., Leto, C., et al. 2009, Astronomy & Astrophysics, 495, 691, doi: 10.1051/0004-6361:200810161

Maza, J., Hamuy, M., Antezana, R., et al. 2009, Central Bureau Electronic Telegrams, 1928, 1

McHardy, I. M., Koerding, E., Knigge, C., Uttley, P., & Fender, R. P. 2006, Nature, 444, 730, doi: 10.1038/nature05389

McLure, R. J., & Dunlop, J. S. 2002, Monthly Notices of the Royal Astronomical Society, 331, 795, doi: 10.1046/j.1365-8711.2002.05236.x

Meisner, A. M., Lang, D., & Schlegel, D. J. 2017, The Astronomical Journal, 154, 161, doi: 10.3847/1538-3881/aa894e

—. 2018, The Astronomical Journal, 156, 69, doi: 10.3847/1538-3881/aacbcd

Melchior, P., Joseph, R., Sanchez, J., MacCrann, N., & Gruen, D. 2021, Nature Reviews Physics, 3, 712, doi: 10.1038/s42254-021-00353-y

Melchior, P., Moolekamp, F., Jerdee, M., et al. 2018, Astronomy and Computing, 24, 129, doi: 10.1016/j.ascom.2018.07.001

Merritt, D., & Milosavljević, M. 2005, Living Reviews in Relativity, 8, doi: 10.12942/lrr-2005-8

Mezcua, M., Civano, F., Marchesi, S., et al. 2018, Monthly Notices of the Royal Astronomical Society, 478, 2576, doi: 10.1093/mnras/sty1163

Mezcua, M., & Domínguez Sánchez, H. 2020, The Astrophysical Journal, 898, L30, doi: 10.3847/2041-8213/aba199

Miller, A. A., Kulkarni, M. K., Cao, Y., et al. 2017, The Astronomical Journal, 153, 73, doi: 10.3847/1538-3881/153/2/73

Miller, M. C., & Hamilton, D. P. 2002, Monthly Notices of the Royal Astronomical Society, 330, 232, doi: 10.1046/j.1365-8711.2002.05112.x

Milosavljević, M., & Merritt, D. 2001, The Astrophysical Journal, 563, 34, doi: 10.1086/323830

—. 2003, The Astrophysical Journal, 596, 860, doi: 10.1086/378086

Molina, M., Reines, A. E., Latimer, L., Baldassare, V., & Salehirad, S. 2021, The Astrophysical Journal, 922, 155, doi: 10.3847/1538-4357/ac1ffa

Mushotzky, R. F., Edelson, R., Baumgartner, W., & Gandhi, P. 2011, The Astrophysical Journal, 743, L12, doi: 10.1088/2041-8205/743/1/L12

Nguyen, K., & Bogdanović, T. 2016, The Astrophysical Journal, 828, 68, doi: 10.3847/0004-637x/828/2/68

Nguyen, K., Bogdanović, T., Runnoe, J. C., et al. 2018, The Astrophysical Journal, 870, 16, doi: 10.3847/1538-4357/aaeff0

Noble, S. C., Mundim, B. C., Nakano, H., et al. 2012, Astrophysical Journal, 755, doi: 10.1088/0004-637X/755/1/51

Nordin, J., Brinnel, V., van Santen, J., et al. 2019a, Astronomy & Astrophysics, 631, A147, doi: 10.1051/0004-6361/201935634

—. 2019b, Astronomy & Astrophysics, 631, A147, doi: 10.1051/0004-6361/201935634

O'Brien, P. T., Dietrich, M., Leighly, K., et al. 1998, The Astrophysical Journal, 509, 163, doi: 10.1086/306464

Osterbrock, D. E. 1989, Astrophysics of gaseous nebulae and active galactic nuclei

Pacucci, F., Loeb, A., Mezcua, M., & Martín-Navarro, I. 2018, The Astrophysical Journal, 864, L6, doi: 10.3847/2041-8213/aad8b2

Pacucci, F., Mezcua, M., & Regan, J. A. 2021, The Astrophysical Journal, 920, 134, doi: 10.3847/1538-4357/ac1595

Pacucci, F., Volonteri, M., & Ferrara, A. 2015, Monthly Notices of the Royal Astronomical Society, 452, 1922, doi: 10.1093/mnras/stv1465

Pastorello, A., Reguitti, A., Morales-Garoffolo, A., et al. 2019, Astronomy and Astrophysics, 628, 1, doi: 10.1051/0004-6361/201935420

Patterson, M. T., Bellm, E. C., Rusholme, B., et al. 2019, Publications of the Astronomical Society of the Pacific, 131, 18001, doi: 10.1088/1538-3873/aae904

Penny, S. J., Masters, K. L., Smethurst, R., et al. 2018, Monthly Notices of the Royal Astronomical Society, 476, 979, doi: 10.1093/mnras/sty202

Perley, D. A., Fremling, C., Sollerman, J., et al. 2020, ApJ, 904, 35

Perley, D. A., Ho, A. Y. Q., Yao, Y., et al. 2021, Monthly Notices of the Royal Astronomical Society, 508, 5138, doi: 10.1093/mnras/stab2785

Pflueger, B. J., Nguyen, K., Bogdanović, T., et al. 2018, The Astrophysical Journal, 861, 59, doi: 10.3847/1538-4357/aaca2c

Phillips, M. M. 1976, The Astrophysical Journal, 208, 37, doi: 10.1086/154578

Plotkin, R. M., Anderson, S. F., Hall, P. B., et al. 2008, The Astronomical Journal, 135, 2453, doi: 10.1088/0004-6256/135/6/2453

Polimera, M., Sarajedini, V., Ashby, M. L., Willner, S. P., & Fazio, G. G. 2018, Monthly Notices of the Royal Astronomical Society, 476, 1111, doi: 10.1093/MNRAS/STY164

Popovic, L. C. 2011, doi: 10.1016/j.newar.2011.11.001

Popović, L. C., Mediavilla, E., Bon, E., & Ilić, D. 2004, Astronomy and Astrophysics, 423, 909, doi: 10.1051/0004-6361:20034431

Popović, L. , Mediavilla, E. G., & Muñoz, J. A. 2001, Astronomy & Astrophysics, 378, 295, doi: 10.1051/0004-6361:20011169

Portegies Zwart, S. F., & McMillan, S. L. W. 2002, The Astrophysical Journal, 576, 899, doi: 10.1086/341798

Price-Whelan, A. M., Sipőcz, B. M., Günther, H. M., et al. 2018, The Astronomical Journal, 156, 123, doi: 10.3847/1538-3881/aabc4f

Ragusa, E., Lodato, G., & Price, D. J. 2016, Monthly Notices of the Royal Astronomical Society, 460, 1243, doi: 10.1093/mnras/stw1081

Rajagopal, M., & Romani, R. W. 1995, The Astrophysical Journal, 446, 543, doi: 10.1086/175813

Reines, A. E., & Comastri, A. 2016, Publications of the Astronomical Society of Australia, 33, e054, doi: 10.1017/pasa.2016.46

Reines, A. E., Condon, J. J., Darling, J., & Greene, J. E. 2020, The Astrophysical Journal, 888, 36, doi: 10.3847/1538-4357/ab4999

Reines, A. E., Greene, J. E., & Geha, M. 2013, The Astrophysical Journal, 775, 116, doi: 10.1088/0004-637X/775/2/116

Ricarte, A., & Natarajan, P. 2018, Monthly Notices of the Royal Astronomical Society, 481, 3278, doi: 10.1093/mnras/sty2448

Ricarte, A., Tremmel, M., Natarajan, P., & Quinn, T. 2021a, The Astrophysical Journal Letters, 916, L18, doi: 10.3847/2041-8213/ac1170

Ricarte, A., Tremmel, M., Natarajan, P., Zimmer, C., & Quinn, T. 2021b, Monthly Notices of the Royal Astronomical Society, 503, 6098, doi: 10.1093/mnras/stab866

Ricci, C., Bauer, F. E., Treister, E., et al. 2016, The Astrophysical Journal, 819, 4, doi: 10.3847/0004-637X/819/1/4

Ricci, C., Trakhtenbrot, B., Koss, M. J., et al. 2017, Nature, 549, 488, doi: 10.1038/nature23906

Ricker, G. R., Winn, J. N., Vanderspek, R., et al. 2014, Journal of Astronomical Telescopes, Instruments, and Systems, 1, 014003, doi: 10.1117/1.JATIS.1.1.014003

Robinson, A., Young, S., Axon, D. J., Kharb, P., & Smith, J. E. 2010, Astrophysical Journal Letters, 717, 122, doi: 10.1088/2041-8205/717/2/L122

Robitaille, T. P., Tollerud, E. J., Greenfield, P., et al. 2013, Astronomy and Astrophysics, 558, 1, doi: 10.1051/0004-6361/201322068

Rodriguez, C., Taylor, G. B., Zavala, R. T., et al. 2006, The Astrophysical Journal, 646, 49, doi: 10.1086/504825

Roedig, C., Zanotti, O., & Alic, D. 2012, Monthly Notices of the Royal Astronomical Society, 426, 1613, doi: 10.1111/j.1365-2966.2012.21821.x

Rosado, P. A., Sesana, A., & Gair, J. 2015, Monthly Notices of the Royal Astronomical Society, 451, 2417, doi: 10.1093/mnras/stv1098

Rots, A. H., & Budavári, T. 2011, Astrophysical Journal, Supplement Series, 192, 1, doi: 10.1088/0067-0049/192/1/8

Runnoe, J. C., Eracleous, M., Mathes, G., et al. 2015, Astrophysical Journal, Supplement Series, 221, doi: 10.1088/0067-0049/221/1/7

Salcido, J., Bower, R. G., Theuns, T., et al. 2016, Monthly Notices of the Royal Astronomical Society, 463, 870, doi: 10.1093/mnras/stw2048

Sánchez, P., Lira, P., Cartier, R., et al. 2017, The Astrophysical Journal, 849, 110, doi: 10.3847/1538-4357/aa9188

Satyapal, S., Ellison, S. L., McAlpine, W., et al. 2014, Monthly Notices of the Royal Astronomical Society, 441, 1297, doi: 10.1093/mnras/stu650

Satyapal, S., Secrest, N. J., Ricci, C., et al. 2017, The Astrophysical Journal, 848, 126, doi: 10.3847/1538-4357/aa88ca

Schimoia, J. S., Storchi-Bergmann, T., Nemmen, R. S., Winge, C., & Eracleous, M. 2012, Astrophysical Journal, 748, doi: 10.1088/0004-637X/748/2/145

Schimoia, J. S., Storchi-Bergmann, T., Winge, C., Nemmen, R. S., & Eracleous, M. 2017, Monthly Notices of the Royal Astronomical Society, 472, 2170, doi: 10.1093/mnras/stx2107

Schmidt, K. B., Marshall, P. J., Rix, H.-W., et al. 2010, The Astrophysical Journal, 714, 1194, doi: 10.1088/0004-637X/714/2/1194

Schnittman, J. D. 2013, Classical and Quantum Gravity, 30, 244007, doi: 10.1088/0264-9381/30/24/244007

Schutte, Z., Reines, A. E., & Greene, J. E. 2019, The Astrophysical Journal, 887, 245, doi: 10.3847/1538-4357/ab35dd

Secrest, N. J., & Satyapal, S. 2020, The Astrophysical Journal, 900, 56, doi: 10.3847/1538-4357/ab9309

Sergeev, S. G., Pronik, V. I., Peterson, B. M., Sergeeva, E. A., & Zheng, W. 2002, The Astrophysical Journal, 576, 660, doi: 10.1086/341791

Sesana, A., Haiman, Z., Kocsis, B., & Kelley, L. Z. 2018, The Astrophysical Journal, 856, 42, doi: 10.3847/1538-4357/aaad0f

Seth, A. C., Van Den Bosch, R., Mieske, S., et al. 2014, Nature, 513, 398, doi: 10.1038/nature13762

Shabala, S. S., Deller, A., Kaviraj, S., et al. 2017, Monthly Notices of the Royal Astronomical Society, 464, 4706, doi: 10.1093/mnras/stw2536

Shapovalova, A. I., Burenkov, A. N., Carrasco, L., et al. 2001, Astronomy & Astrophysics, 376, 775, doi: 10.1051/0004-6361:20011011

Shapovalova, A. I., Popović, L. , Burenkov, A. N., et al. 2013, Astronomy & Astrophysics, 559, A10, doi: 10.1051/0004-6361/201321781

Shappee, B., Prieto, J., Stanek, K. Z., et al. 2014, in American Astronomical Society Meeting Abstracts, Vol. 223, American Astronomical Society Meeting Abstracts #223, 236.03

Sharma, R., Brooks, A., Somerville, R. S., et al. 2019, arXiv, doi: 10.3847/1538-4357/ab960e

Shaya, E. J., Olling, R., & Mushotzky, R. 2015, Astronomical Journal, 150, 188, doi: 10.1088/0004-6256/150/6/188

Shen, Y., Hwang, H.-c., Zakamska, N., & Liu, X. 2019, The Astrophysical Journal, 885, L4, doi: 10.3847/2041-8213/ab4b54

Shen, Y., Liu, X., Loeb, A., & Tremaine, S. 2013, Astrophysical Journal, 775, doi: 10.1088/0004-637X/775/1/49

Shen, Y., & Loeb, A. 2010, Astrophysical Journal, 725, 249, doi: 10.1088/0004-637X/725/1/249

Shi, J. M., & Krolik, J. H. 2015, Astrophysical Journal, 807, doi: 10.1088/0004-637X/807/2/131

Shi, J. M., Krolik, J. H., Lubow, S. H., & Hawley, J. F. 2012, Astrophysical Journal, 749, doi: 10.1088/0004-637X/749/2/118

Shields, G. A., Bonning, E. W., & Salviander, S. 2009a, Astrophysical Journal, 696, 1367, doi: 10.1088/0004-637X/696/2/1367

Shields, G. A., Rosario, D. J., Smith, K. L., et al. 2009b, Astrophysical Journal, 707, 936, doi: 10.1088/0004-637X/707/2/936

Sicilia, A., Lapi, A., Boco, L., et al. 2022. http://arxiv.org/abs/2206.07357

Sillanpaa, A., Haarala, S., Valtonen, M. J., Sundelius, B., & Byrd, G. G. 1988, The Astrophysical Journal, 325, 628, doi: 10.1086/166033

Simm, T., Salvato, M., Saglia, R., et al. 2016, Astronomy & Astrophysics, 585, A129, doi: 10.1051/0004-6361/201527353

Skipper, C. J., & Browne, I. W. A. 2018, Monthly Notices of the Royal Astronomical Society, 475, 5179, doi: 10.1093/mnras/sty114

Smith, K. L., Mushotzky, R. F., Boyd, P. T., et al. 2018, The Astrophysical Journal, 857, 141, doi: 10.3847/1538-4357/aab88d

Smith, K. L., Shields, G. A., Bonning, E. W., et al. 2010, Astrophysical Journal, 716, 866, doi: 10.1088/0004-637X/716/1/866

Smitka, M. T. 2016, PhD thesis, Texas A\&M University

Solovyeva, Y., Vinokurov, A., Fabrika, S., et al. 2019, Monthly Notices of the Royal Astronomical Society: Letters, 484, L24, doi: 10.1093/mnrasl/sly241

Soumagnac, M. T., & Ofek, E. O. 2018, Publications of the Astronomical Society of the Pacific, 130, 1, doi: 10.1088/1538-3873/aac410

Steinhardt, C. L., Schramm, M., Silverman, J. D., et al. 2012, Astrophysical Journal, 759, 1, doi: 10.1088/0004-637X/759/1/24

Stern, J., & Laor, A. 2012, Monthly Notices of the Royal Astronomical Society, 426, 2703, doi: 10.1111/j.1365-2966.2012.21772.x

Stetson, P. B. 1987, Publications of the Astronomical Society of the Pacific, 99, 191, doi: 10.1086/131977

Stockton, A., & Farnham, T. 1991, The Astrophysical Journal, 371, 525, doi: 10.1086/169916

Stoll, R., Prieto, J. L., Stanek, K. Z., et al. 2011, The Astrophysical Journal, 730, 34, doi: 10.1088/0004-637X/730/1/34

Storchi-Bergmann, T., Baldwin, J. A., & Wilson, A. S. 2002, The Astrophysical Journal, 410, L11, doi: 10.1086/186867

Storchi-Bergmann, T., Schimoia, J. S., Peterson, B. M., et al. 2016, The Astrophysical Journal, 835, 1, doi: 10.3847/1538-4357/835/2/236

Storchi-Bergmann, T., Nemmen da Silva, R., Eracleous, M., et al. 2003, The Astrophysical Journal, 598, 956, doi: 10.1086/378938

Strateva, I. V., Strauss, M. A., Hao, L., et al. 2003, The Astronomical Journal, 126, 1720, doi: 10.1086/378367

Suberlak, K. L., Ivezić, , & MacLeod, C. 2021, The Astrophysical Journal, 907, 96, doi: 10.3847/1538-4357/abc698

Surace, J. A., Sanders, D. B., Vacca, W. D., Veilleux, S., & Mazzarella, J. M. 1998, The Astrophysical Journal, 492, 116, doi: 10.1086/305028

Tachibana, Y., & Miller, A. A. 2018, Publications of the Astronomical Society of the Pacific, 130, 128001, doi: 10.1088/1538-3873/aae3d9

Taggart, K., & Perley, D. A. 2021, Monthly Notices of the Royal Astronomical Society, 503, 3931, doi: 10.1093/mnras/stab174

Taylor, S. R., Vallisneri, M., Ellis, J. A., et al. 2016, The Astrophysical Journal, 819, L6, doi: 10.3847/2041-8205/819/1/L6

Tonry, J. L., Denneau, L., Heinze, A. N., et al. 2018, Publications of the Astronomical Society of the Pacific, 130, 064505, doi: 10.1088/1538-3873/aabadf

Treister, E., Schawinski, K., Urry, C. M., & Simmons, B. D. 2012, Astrophysical Journal Letters, 758, doi: 10.1088/2041-8205/758/2/L39

Tsai, C. W., Jarrett, T. H., Stern, D., et al. 2013, Astrophysical Journal, 779, doi: 10.1088/0004-637X/779/1/41

Ulrich, M.-H., Maraschi, L., & Urry, C. M. 1997, Annual Review of Astronomy and Astrophysics, 35, 445, doi: 10.1146/annurev.astro.35.1.445

Valtonen, M. J. 2007, The Astrophysical Journal, 659, 1074, doi: 10.1086/512801

Valtonen, M. J., Lehto, H. J., Nilsson, K., et al. 2008, Nature, 452, 851, doi: 10.1038/nature06896

van Roestel, J., Bellm, E. C., Duev, D. A., et al. 2019, Research Notes of the AAS, 3, 136, doi: 10.3847/2515-5172/ab459c

van Velzen, S., Gezari, S., Cenko, S. B., et al. 2019, The Astrophysical Journal, 872, 198, doi: 10.3847/1538-4357/aafe0c

van Velzen, S., Gezari, S., Hammerstein, E., et al. 2021, The Astrophysical Journal, 908, 4, doi: 10.3847/1538-4357/abc258

Van Wassenhove, S., Volonteri, M., Mayer, L., et al. 2012, Astrophysical Journal Letters, 748, 5, doi: 10.1088/2041-8205/748/1/L7

Vaughan, S., Uttley, P., Markowitz, A. G., et al. 2016, Monthly Notices of the Royal Astronomical Society, 461, doi: 10.1093/mnras/stw1412

Veilleux, S., & Osterbrock, D. E. 1987, The Astrophysical Journal Supplement Series, 63, 295, doi: 10.1086/191166

Voggel, K. T., Seth, A. C., Baumgardt, H., et al. 2019, The Astrophysical Journal, 871, 159, doi: 10.3847/1538-4357/aaf735

Volonteri, M. 2007, The Astrophysical Journal, 663, L5, doi: 10.1086/519525

Volonteri, M., & Begelman, M. C. 2010, Monthly Notices of the Royal Astronomical Society, 409, 1022, doi: 10.1111/j.1365-2966.2010.17359.x

Volonteri, M., Gültekin, K., & Dotti, M. 2010, Monthly Notices of the Royal Astronomical Society, 404, 2143, doi: 10.1111/j.1365-2966.2010.16431.x

Volonteri, M., & Madau, P. 2008, The Astrophysical Journal, 687, L57, doi: 10.1086/593353

Volonteri, M., Miller, J. M., & Dotti, M. 2009, Astrophysical Journal, 703, doi: 10.1088/0004-637X/703/1/L86

Volonteri, M., & Natarajan, P. 2009, Monthly Notices of the Royal Astronomical Society, 400, 1911, doi: 10.1111/j.1365-2966.2009.15577.x

Volonteri, M., & Perna, R. 2005, Monthly Notices of the Royal Astronomical Society, 358, 913, doi: 10.1111/j.1365-2966.2005.08832.x

Volonteri, M., & Reines, A. E. 2016, The Astrophysical Journal, 820, L6, doi: 10.3847/2041-8205/820/1/l6

Wang, J. M., Chen, Y. M., Hu, C., et al. 2009, Astrophysical Journal, 705, 76, doi: 10.1088/0004-637X/705/1/L76

Wang, L., Greene, J. E., Ju, W., et al. 2017, The Astrophysical Journal, 834, 129, doi: 10.3847/1538-4357/834/2/129

Ward, C., Gezari, S., Frederick, S., et al. 2021a, The Astrophysical Journal, 913, 102, doi: 10.3847/1538-4357/abf246

Ward, C., Gezari, S., Nugent, P., et al. 2021b. http://arxiv.org/abs/2110.13098

Weston, M. E., McIntosh, D. H., Brodwin, M., et al. 2017, Monthly Notices of the Royal Astronomical Society, 464, 3882, doi: 10.1093/mnras/stw2620

Woo, J.-H., Schulze, A., Park, D., et al. 2013, The Astrophysical Journal, 772, 49, doi: 10.1088/0004-637X/772/1/49

Wright, E. L., Eisenhardt, P. R., Mainzer, A. K., et al. 2010, Astronomical Journal, 140, 1868, doi: 10.1088/0004-6256/140/6/1868

Xu, D., & Komossa, S. 2009, Astrophysical Journal, 705, 20, doi: 10.1088/0004-637X/705/1/L20

Zackay, B., Ofek, E. O., & Gal-Yam, A. 2016, The Astrophysical Journal, 830, 27, doi: 10.3847/0004-637X/830/1/27

Zhang, X. G., & Feng, L. L. 2017, Monthly Notices of the Royal Astronomical Society, 464, 2203, doi: 10.1093/mnras/stw2489

Zu, Y., Kochanek, C. S., Kozłowski, S., & Udalski, A. 2013, Astrophysical Journal, 765, doi: 10.1088/0004-637X/765/2/106